

Properties of hot and dense matter created in relativistic heavy ion collisions

Ionut Cristian Arsene

Department of Physics

Faculty of Mathematics and Natural Sciences - University of Oslo



Dissertation presented for the degree of
Philosophia Doctor in Physics

Preface

Collisions of sub-atomic particles at relativistic energies give the possibility of studying the most intimate properties of nature in a "clean" environment and develop quantum field theories (QED and QCD). In the case of QCD however there are fundamental theoretical problems when trying to understand the physics of small momentum transfers ("soft" physics). The field of high energy heavy ion collisions came into play after the Nobel prize laureate T.D.Lee and a few other physicists published a series of papers in the 70's which predicted the existence of a new form of nuclear matter at very high temperatures and densities. In this new state of matter, named "Quark-Gluon Plasma"(QGP), the quarks and gluons are deconfined and the chiral symmetry is restored. This gives the possibility to study QCD in conditions which are not available in elementary particle interactions and motivated the development of heavy ion collisions culminating with the RHIC and the future LHC experiments. The rich new results discovered in this field over the past decades are a challenge for both theory and experimental developments.

This thesis tries to address only a small part of the wide field that heavy ion collisions is today. An introduction to some of the most prominent topics in the study of hot and dense nuclear matter with examples of experimental results and possible phenomenological interpretations is given in chapter 1. In Chapter 2, the equation of state of the nuclear matter is investigated in the framework of microscopical models without the assumption of the existence of a QGP phase. Chapter 3 describes the HYDJET++ model as a superposition of a soft state (hydro inspired parametrization) and a hard state which consists of hard jets quenched in the QGP. Two other models which use a microscopical transport approach are also briefly described. In chapter 4 the BRAHMS experimental setup is described while the data analysis for the Au+Au at $\sqrt{s_{NN}} = 62.4$ GeV run is addressed in detail in chapter 5. Chapter 6 summarizes the experimental results and in chapter 7, the experimental results are discussed based on comparisons with data at different energies and with theoretical calculations. The experimental results discussed are the identified particle yields and particle ratios as a function of rapidity, collision centrality and colliding species with a focus on strange particle ratios, K^-/K^+ and K/π ratios. Finally, chapter 8 contains a summary and the main conclusions of this thesis.

Acknowledgements

This thesis is the result of four years of hard work possible due to constant guidance from my supervisors and senior people from the collaborations i worked in. So first of all i am grateful to my supervisors from the University of Oslo, Prof.Larissa Bravina and Prof.Trine Tvetter. They gave me the opportunity to work in a very challenging and rewarding field. During all the time i spent in the heavy ion group from Oslo i received all their support both on scientific and personal level. I thank Prof.Trine Tvetter also for carefully reading this thesis and providing me with detailed comments and suggestions. I am also grateful to Prof.Dieter Röhrich from Bergen which supported me in many situations and helped me shaping many of the ideas presented in this thesis. I would like to mention here also the other senior people from our group, Prof.Gunnar Lovhoiden and Prof.Bernhard Skaali. During the past four years spent at the Physics Department in Oslo i got to know very nice people and made some good friends. I would like to thank my colleagues and friends Eugen Zabrodin, Konrad Tywoniuk, Jovan Milosevic, Atle Qviller, Svein Lindal, Mads Nilsson, Thomas Vik, Bjorn Samset for interesting discussions and great companionship during travels to conferences.

For my master degree and half of my doctoral studies i worked within the BRAHMS Collaboration. This meant a lot of work but also many travels for conferences, collaboration meetings and, ofcourse, to do shifts for data taking. It has been a lot to learn but also a lot of fun. I am deeply grateful to Flemming Videbaek, the spokesperson of BRAHMS Collaboration, from whom i always received feed-back for my work and good advices. I have to thank also to the other seniors of BRAHMS which helped me whenever i needed: Michael Murray, J.H. Lee, Pawel Staszal, Ian Bearden, Ramiro Debbe, Steve Sanders, Kris Hagel. I benefited a lot from the work of Peter Christiansen, Djamel Ouerdane, Claus Jorgensen, Christian Holm which made their Ph.D or master in BRAHMS before me and developed most of the analysis framework. BRAHMS is a very social and friendly collaboration where i enjoyed working or having a beer with friends like Hongyan Yang, Catalin and Oana Ristea, Truls Larsen, Hans Dalsgaard, Casper Nygaard, Radek Karabowicz.

The other half of my Ph.D was dedicated to working and developing simulation models. This was a great opportunity for me to learn about the theoretical aspects involved in heavy ion collisions. I am especially in debt to Nikolai Amelin, who unfortunately past away two years ago, for introducing me to the phenomenology and modeling behind the heavy ion event generators. I am grateful also to the members of the group from Moscow with whom i collaborated: Ludmila Malinina, Igor Lokhtin, Alexei Kaidalov, Alexander Snigirev.

I need to mention the people from Bucharest University, the place where i started learning physics. A special thank is for my old friend and colleague, Sorin Zgura, who introduced me to the heavy ion group from Bucharest. I am grateful also to my bachelor and master thesis coordinators, Prof.Alexandru Jipa and Prof.Calin Besliu. My life as

a physics student would have not been the same without my friends and colleagues from the Physics Faculty and the Institute for Space Sciences, Silviu, Vali, Daniel, Mihai, Ciprian, Sev, Ileana, Oana, Marius, Ionel, Mihai, Andrea and many others.

Finally, I am grateful to my family and friends. I especially thank my mother and father for their support and love during the time i spent abroad. My future wife, Adina, deserves also my gratitude for her patience during the late working days i spent in the last years. This thesis is dedicated to them.

Contents

1	Introduction	1
1.1	Elementary particles and QCD	1
1.2	Relativistic heavy ion collisions	6
1.2.1	Collision geometry and dynamics	6
1.2.2	Global measurements in relativistic collisions	7
1.3	Searching for the Quark Gluon Plasma	9
1.3.1	Electromagnetic probes	9
1.3.2	J/ψ suppression	11
1.3.3	High p_T suppression	13
1.3.4	In medium jet modification and correlations	15
1.3.5	Elliptic flow	18
1.3.6	Strangeness enhancement	20
1.3.7	The critical point	22
1.4	Kaon and pion production	24
1.4.1	Production mechanisms	25
1.4.2	Energy and rapidity dependence of yields and ratios	26
1.4.3	K/π ratios dependence on system size and geometry	28
2	Effective equation of state	31
2.1	Characteristics of UrQMD and QGSM	32
2.1.1	Similarities between the two models	32
2.1.2	Differences	33
2.2	Statistical model of an ideal hadron gas	34
2.3	Criteria of thermal and chemical equilibrium	35
2.4	Relaxation to equilibrium	36
2.4.1	Yields and energy spectra	36
2.4.2	Evolution of the cell characteristics	40
2.4.3	EOS in the cell	44
2.4.4	Early stage of the evolution	48
3	Theoretical models	51
3.1	UrQMD	51
3.2	AMPT	52
3.3	HYDJET++	53
3.3.1	Total particle multiplicities	54
3.3.2	Momentum distribution	56
3.3.3	Freeze-out surface modeling	58
3.3.4	Hard multi-jet production	65
3.3.5	Shadowing corrections	68

3.3.6	Final hadrons	70
4	Experimental apparatus	71
4.1	RHIC and the experiments	71
4.1.1	A short description	71
4.1.2	The heavy ion experiments	72
4.2	The BRAHMS experiment	74
4.2.1	Global detectors	75
4.2.2	The Spectrometers	76
4.2.3	Tracking components	78
4.2.4	PID devices	79
4.2.5	Triggers	80
4.2.6	Acceptance	82
5	Data analysis	85
5.1	Event characterization	85
5.1.1	Vertex determination	85
5.1.2	Centrality determination	87
5.2	Tracking	88
5.2.1	Local tracking	89
5.2.2	Matching and global tracking	89
5.2.3	Track cuts	93
5.3	Particle Identification	96
5.3.1	The time of flight PID	96
5.3.2	The Cerenkov PID	104
5.3.3	PID cuts	108
5.4	Building spectra	110
5.4.1	Corrections	111
5.4.2	Merging spectra	118
6	Experimental results	121
6.1	Invariant spectra	121
6.1.1	Fitting spectra	121
6.1.2	p_T integrated yields	127
6.2	Ratios	131
6.2.1	Anti-hadron to hadron ratios	131
6.2.2	K/π ratios	132
6.3	Systematic errors	132
7	Discussions and comparisons	137
7.1	Simulation procedures	137
7.1.1	HYDJET++	137
7.1.2	UrQMD	137
7.1.3	AMPT	138
7.2	Thermal fit of the mid-rapidity data using HYDJET++	139
7.3	Particle production in central Au+Au collisions	143
7.3.1	Integrated yields (dN/dy)	143
7.3.2	Particle ratios	145
7.4	Centrality dependent particle production	152

8 Summary and conclusions

List of Figures

1.1	Elementary particles in the Standard Model	2
1.2	$\alpha_S(Q)$ from theory and experiment.	3
1.3	Sketch of the deconfined nuclear matter.	4
1.4	ε/T^4 versus T/T_C from lattice QCD	4
1.5	(T, μ_B) phase diagram of nuclear matter	5
1.6	Perspective view of the nuclear collision geometry.	6
1.7	Schematic view of the nuclear collision time evolution	7
1.8	Net baryon and charged particles rapidity densities.	8
1.9	Anti-particle to particle ratios at $\sqrt{s_{NN}} = 200$ GeV	8
1.10	Photon invariant yields at RHIC energies	10
1.11	Invariant mass distribution for e^+e^- pairs	11
1.12	J/ψ suppression in d+Au, Au+Au and Cu+Cu collisions	12
1.13	J/ψ suppression in Au+Au compared to shadowing calculations.	12
1.14	Nuclear modification factor in d+Au and central Au+Au collisions	13
1.15	Nuclear modification factor in central and semi-peripheral Au+Au collisions at $\eta = 0.0$ and $\eta = 2.2$	14
1.16	Nuclear modification factor in d+Au collisions in four η intervals	14
1.17	Back-to-back correlation in Au+Au and p+p collisions	16
1.18	Energy density and energy flux profiles from AdS/CFT calculations	16
1.19	$(\Delta\eta, \Delta\phi)$ correlations - the ridge	17
1.20	Elliptic flow coefficient v_2 versus center of mass energy	18
1.21	v_2 versus transverse momentum and transverse kinetic energy	19
1.22	v_2 versus centrality and transverse momentum	20
1.23	Lowest order QCD diagrams for $s\bar{s}$ production	21
1.24	Energy dependence of strangeness to entropy ratio	21
1.25	QCD critical point in lattice QCD	22
1.26	The kink, the horn and the step	23
1.27	Phase trajectories $(\rho_B(t), \varepsilon(t))$ in central Au+Au collisions at $\sqrt{s_{NN}} = 2.36$ GeV	24
1.28	Energy systematics of the total yields of charged pions and kaons	26
1.29	π^\pm rapidity density distributions at AGS energies	27
1.30	Particle rapidity density distributions at SPS energies	28
1.31	K/π ratios at mid-rapidity in central A+A collisions as a function of energy	29
1.32	K/π ratios at mid-rapidity for different colliding systems at top AGS energy	29
1.33	K^-/π^- ratio versus centrality and energy	30
2.1	Pressure versus time in the central cell in UrQMD and QGSM	37

2.2	Time evolution of hadron yields at $E_{lab} = 40A\text{GeV}$	38
2.3	Energy spectra of produced hadrons.	39
2.4	Total energy density ε versus baryon density ρ_B in the central cell . . .	42
2.5	Net strangeness density and strangeness per baryon versus time	43
2.6	S/ρ_B evolution with time	44
2.7	Microscopic pressure P and energy density ε versus time	45
2.8	c_s^2 in central cell as a function of energy	46
2.9	Time evolution of the temperature T and baryon chemical potential μ_B . . .	49
3.1	m_T spectra versus centrality from FASTMC	57
3.2	Non-central collision transverse plane geometry	59
3.3	Schematic hydrodynamic evolution	60
3.4	Elliptic flow parameter in 20-30% Au+Au collisions	61
3.5	v_2 versus p_T in different centrality bins	62
3.6	HBT radii at $y = 0$ in central Au+Au	63
3.7	Azimuthal dependence of HBT radii at $y = 0$ in 20-30% Au+Au	64
3.8	R_{AA} and back-to-back correlations from HYDJET++	66
3.9	$dN/d\eta$ for charged hadrons in Au+Au versus centrality	67
3.10	Invariant spectra for π^+ in Au+Au from HYDJET++	68
3.11	Gluon shadowing versus x_g and impact parameter b	69
3.12	Gluon shadowing comparison with other calculations	69
4.1	RHIC view	72
4.2	Views of STAR and PHENIX experiments	73
4.3	View of PHOBOS experiment	73
4.4	View of BRAHMS experimental setup	74
4.5	Multiplicity Array	75
4.6	Beam-Beam Counters	76
4.7	Zero-Degree Calorimeters	77
4.8	Mid-Rapidity and Forward Spectrometers	77
4.9	Time-Projection and Drift Chambers	79
4.10	Time of Flight Wall	80
4.11	C1 and RICH detectors	81
4.12	BRAHMS design acceptance	83
5.1	BBC resolution and offsets	86
5.2	BBC and ZDC vertex measurements correlation	86
5.3	Mid-rapidity charged particle multiplicity from AMPT versus impact parameter	87
5.4	Centrality distribution using triggers 1 (BB) and 4 (ZDC)	88
5.5	Illustration of the track finding algorithm	89
5.6	$x - z$ view of the matching geometry	90
5.7	Track projection to the event vertex planes	92
5.8	Geometrical fiducial cut on D5 magnet	93
5.9	Track projection on the vertex plane	94
5.10	Track χ^2 distribution versus momentum	95
5.11	β^{-1} as a function of momenta \times charge	97
5.12	Measured m^2 as a function of momenta magnitude \times charge	98
5.13	m^2 distribution showing separable electrons, muons and pions	98
5.14	Fitted m^2 distributions in different momentum slices from TOFW	99

5.15	Fitted m^2 distributions in different momentum slices from H2	100
5.16	Fit parameters for TOFW	101
5.17	Fit parameters for H2	102
5.18	Fraction of the total yield lost due to PID cuts	103
5.19	RICH ring reconstruction efficiency	105
5.20	RICH ring radius as a function of momentum	106
5.21	RICH veto PID for protons	106
5.22	RICH veto PID for kaons	107
5.23	TOFW hits versus slat number and Δy distribution	108
5.24	PID cuts for TOFW and H2	109
5.25	PID cuts for RICH	110
5.26	Tracking efficiency for MRS and FS	112
5.27	H2 tracking efficiency	113
5.28	Decays, multiple scatterings and hadronic absorption correction	115
5.29	Acceptance correction	117
5.30	Normalization constants for 0-10% central Au+Au collisions	118
5.31	Consistency check between the settings and PID methods used	120
6.1	Invariant spectra in (y, p_T) coordinates	122
6.2	Fitted π^\pm invariant spectra	123
6.3	Fitted K^\pm invariant spectra	124
6.4	Fitted proton and anti-proton invariant spectra	125
6.5	Spectra fit quality check	126
6.6	Inverse slope from fits with m_T exponential function versus rapidity	127
6.7	Identified particle average transverse momentum $\langle p_T \rangle$ versus rapidity	128
6.8	p_T integrated yields dN/dy for pions and kaons	129
6.9	p_T integrated yields dN/dy for p and \bar{p}	130
6.10	Anti-particle to particle ratios versus rapidity	131
6.11	Interpolation of the dN/dy rapidity distribution for pions	132
6.12	K/π ratios versus rapidity in 0-10% central Au+Au collisions	133
6.13	Invariant p_T spectra for pions at mid-rapidity compared to STAR	134
7.1	Impact parameter distributions for UrQMD and AMPT	138
7.2	$dN/d\eta$ for charged particles from HYDJET++	139
7.3	Particle ratios at $y = 0$ in 0-10% central Au+Au from HYDJET++	140
7.4	Invariant spectra for π^\pm , K^\pm , p and \bar{p} from HYDJET++	141
7.5	Average $\langle p_T \rangle$ for π^\pm , K^\pm , p and \bar{p} in 0-10% Au+Au collisions at $\sqrt{s_{NN}} = 62.4$ GeV	142
7.6	Particle ratios as functions of centrality	143
7.7	dN/dy versus rapidity compared to UrQMD and AMPT	144
7.8	Like particle ratios versus rapidity in 0-10% Au+Au	145
7.9	Net protons versus rapidity	146
7.10	K/π ratios versus rapidity in central Au+Au collisions	147
7.11	K/π ratios and proton dN/dy at different energies	148
7.12	K/π ratios versus energy	148
7.13	K/π ratios versus \bar{p}/p ratio	149
7.14	K^-/K^+ ratio dependence on the \bar{p}/p ratio	150
7.15	Kaon slopes as a function of the \bar{p}/p ratio	151
7.16	$\langle p_T \rangle$ as a function of the participants number	152

7.17	Anti-particle to particle ratios versus N_{part}	154
7.18	K/π ratios as a function of N_{part}	155

List of Tables

2.1	Time evolution of the thermodynamic characteristics of hadronic matter in the central cell at 20A GeV	40
2.2	Time evolution of the thermodynamic characteristics of hadronic matter in the central cell at 40A GeV	41
3.1	Model parameters for FASTMC with single freezeout	61
3.2	Model parameters for FASTMC with double freezeout	62
4.1	Trigger definitions for the Au+Au at $\sqrt{s_{NN}}=62.4$ GeV run	81
5.1	Geometrical cuts on tracking detectors volumes	94
5.2	Parameters for the χ^2 cut functions	96
5.3	Spectrometer settings used in analysis	119
6.1	Functions used to fit the invariant differential spectra.	122
6.2	Extrapolated dN/dy yields for pions	128
6.3	Extrapolated dN/dy yields for kaons	129
6.4	Extrapolated dN/dy yields for protons and anti-protons	130
7.1	HYDJET++ relative impact parameter ranges	137
7.2	HYDJET++ parameters common to all centrality bins	141
7.3	HYDJET++ parameters for jets	142

Chapter 1

Introduction

The nuclear force is the strongest force in nature and it governs most of the interactions happening in the atomic nuclei. Initially this force was studied by using the radiations (α , β , γ) spontaneously emitted by certain nuclei. Later, the discovery of highly energetic cosmic rays and the first laboratory nuclear collisions opened a new domain for the sub-atomic physics and launched the development of underlying theories which today we call Quantum Electro-Dynamics (QED) and Quantum Chromo-Dynamics (QCD).

This chapter attempts to set the background for the subject of this thesis by making a brief review of our current understanding of the nuclear strong force and QCD, as the main theory which describes it. The necessity of high energy heavy ion collisions and the present status of this field are also discussed. Special attention will be given to the predicted and hunted new state of nuclear matter dubbed Quark-Gluon Plasma (QGP).

1.1 Elementary particles and QCD

Elementarity

The problem of elementarity, of the smallest bricks of matter, is at least two and a half millenia old. In the pre-Socratic Greek period, 420 B.C., Leukippos of Milet and his disciple Democritus of Abdere formulated the concept of atoms (*ἄτομο*, indivisible)¹. These atoms have the following properties:

- indivisible as their name says;
- in perpetual motion;
- invisible because of the extremely small size;
- solid because they have no void inside;
- eternal because they are perfect;
- surrounded by empty space to explain movement and changes in density;
- infinite number of shapes because of the diversity observed in nature.

¹The ideas of both Leukippos and Democritus are known only indirectly through the works of other greek philosophers, *e.g.* Diogenes Laertius, "Lives of the Philosophers".

Most of the properties imagined by Leukippos are still standing even with all the knowledge we have accumulated until today. Only the concepts of particles which were considered to be elementary changed with time. The first modern science atoms were the chemical elements classified by their atomic number in 1869 by the Russian chemist D. Mendeleev. In 1897, Thompson discovered a component part of the atom, the electron, which has negative electric charge. In 1912, E. Rutherford discovered that all the positive charge of the atom is concentrated in a very small region inside the atom. This observation was the basis of the atomic planetary model and the end of the chemical elements as indivisible particles. Later, it was found that the nucleus is composed of nucleons of two species, protons and neutrons.

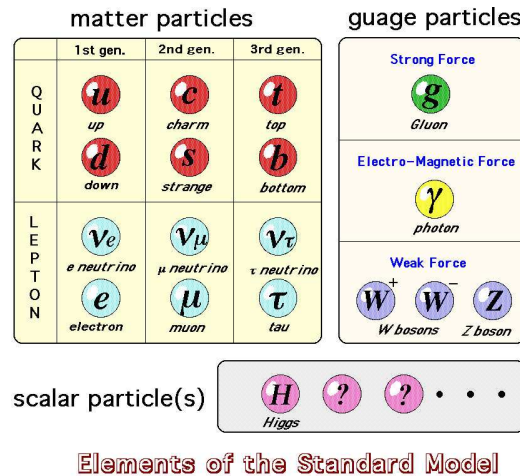


Figure 1.1: Elementary particles in the Standard Model. Figure taken from [1].

The picture we have today about the smallest parts of nature is contained in the Standard Model and is illustrated in figure 1.1. The Standard Model includes three generations of fermions, each generation being composed of two quarks and two leptons, exchange bosons corresponding to each of the three forces and the scalar particle called Higgs. The reason for the existence of only three generations of fermions is still an open issue of today's science. Quarks can interact through all the three forces included in the Standard Model while the leptons interact only through the electro-magnetic and nuclear weak force described by QED. The Higgs boson is still an hypothetical particle which interacts with particles based only on their mass.

Most of the ordinary matter is composed of only two quarks, u (up) and d (down), and the lightest massive lepton, the electron. The up and down quarks form the nucleons in the nuclei, while the electrons are orbiting around the atomic nucleus. The rest of the elementary particles are created for a short time during rare and highly energetic events (*e.g.* atomic and nuclear de-excitations, energetic astrophysical events like supernova explosions and gamma ray bursts, cosmic ray interactions in the upper atmosphere, man-made nuclear collisions, etc.).

Quantum Chromo-Dynamics

QCD is the theory which describes the interactions of hadrons through the strong nuclear force mediated by gluons. The word "chromo" comes from Greek and means color, and this is the charge carried by quarks and gluons. The color charge is of three

types dubbed red(R), green(G) and blue(B). The (anti-)quarks carry one unit of (anti-)color while gluons carry a non-neutral combination color/anti-color which leads to the existence of a gluon octet. The composed hadrons observed experimentally are all "white" (zero total color charge) and contain formations of three (anti-)quarks named (anti-)baryons or quark-antiquark pairs named mesons [2]. Data on exotic hadrons containing more quarks (pentaquarks, di-baryons) exist but is still inconclusive.

The fact that gluons, as force carriers, carry color charge make them able to interact with each other as opposed to the other force carriers which carry no charge with respect to the interaction they mediate (photons have no electric charge and W^\pm and Z^0 have no leptonic charge). This is a unique feature of QCD which has implications on the strength of the interactions between hadrons and on the structure of hadrons.

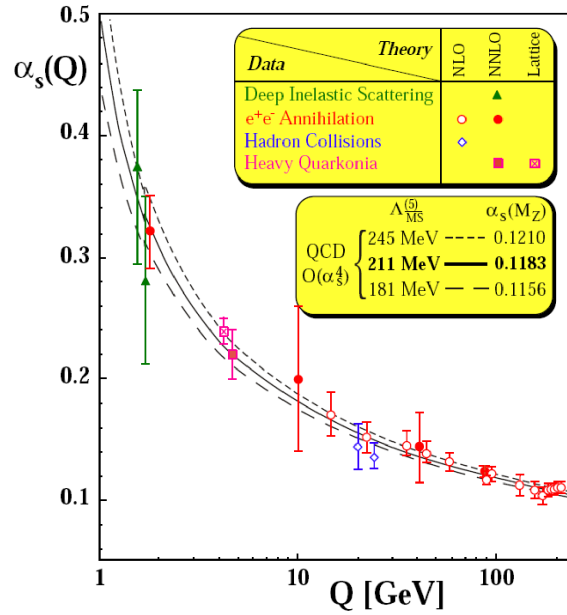


Figure 1.2: $\alpha_s(Q)$ from theory and experiment. Figure taken from [3]

The effective coupling constant of QCD, α_s , was found to be dependent on the momentum exchange Q between the interacting hadrons as shown in figure 1.2². This means that hadrons interact more strongly at small Q (or large distances) than at high Q (or small distances). One of the consequences is the quark confinement. In the string models, the interaction between quarks is viewed as an elastic potential proportional to the distance between them. When the quarks move apart, the string tension increases up to a limit where the string breaks into two strings and a quark-antiquark pair is formed between the two initial quarks. The process continues until the relative momenta between quarks from the string ends is less than the pair production threshold.

Another consequence of the running coupling constant is the behaviour of hadronic matter in the low coupling regime known also as the asymptotic freedom. At very high densities (higher than the normal nuclear matter or nucleon density) and temperatures, it was predicted that the hadronic matter cannot exist anymore in a bound state and the component quarks can move freely in a volume larger than the volume of the hadron

²For this discovery, D.J.Gross, H.D.Politzer and F.Wilczek were awarded with the 2004 Nobel Prize in physics.

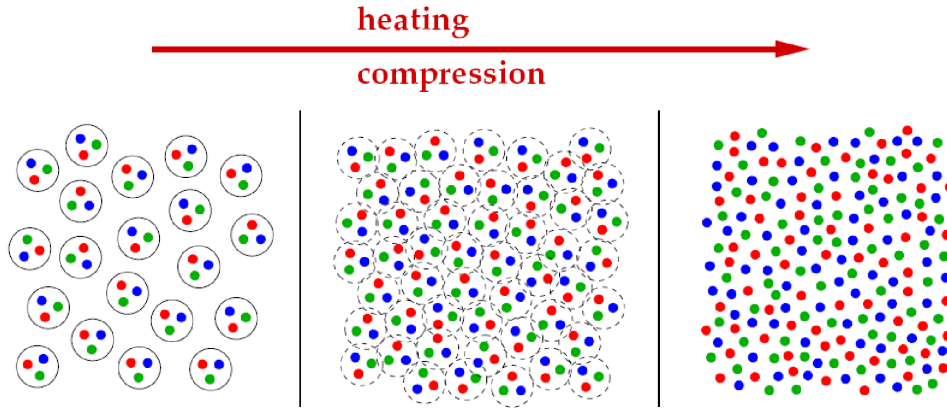


Figure 1.3: Illustration of the nuclear matter melting into QGP. Figure taken from [4]

it belongs to. This new state of matter was named Quark-Gluon Plasma³. It is obvious that the only way to obtain a QGP in the laboratory conditions is to collide heavy nuclei. The naive picture of how the quark-gluon plasma is to be formed is shown in figure 1.3.

In a very dense and hot medium, QCD predicts also that the chiral symmetry restoration will take place. Whether the deconfinement and the chiral symmetry restoration transitions coincide is still not clear with the existing data. One of the prime signals of the chiral symmetry restoration is the rest mass shift for very short lived vector bosons which are created and decay in the hot and dense nuclear medium, like the ρ meson [6, 7].

Lattice gauge QCD and the nuclear phase diagram

Lattice gauge QCD calculations confirmed the existence of a phase transition for the nuclear matter at a critical temperature T_C of approximately 170 MeV [8, 9, 10]. This

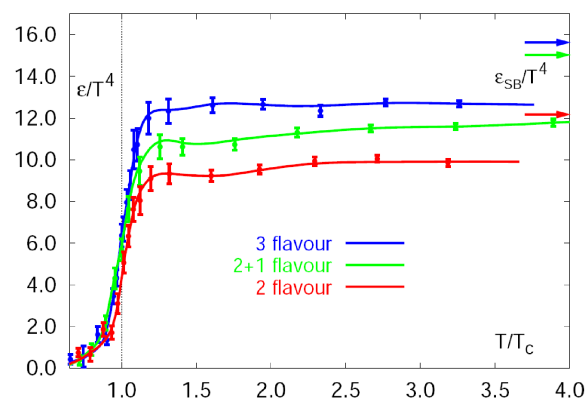


Figure 1.4: Energy density in units of T^4 as a function of the temperature normalized to the critical temperature T_C . The Stefan-Boltzmann limit is indicated by arrows for each of the three combinations of quark flavours considered. Figure taken from [8].

temperature is lower than the Hagedorn temperature [11] T_H estimated based on the

³The name was given first time by E.Shuryak in 1978 [5].

divergence of the hadronic resonance states at a certain temperature. The value of the Hagedorn temperature is considered to be today T_H 200 MeV from counting the hadron states as given by the Particle Data Book [2]. Figure 1.4 shows the dependence of the calculated energy density ε in units of temperature to the fourth power T^4 as a function of the temperature. The ε/T^4 quantity is proportional to the number of degrees of freedom in the system and shows a steep increase around $T = T_C$ which is an evidence of a phase transition from hadronic to partonic matter. At temperatures higher than T_C , the number of degrees of freedom saturates but at a value smaller than the Stefan-Boltzmann limit for an ideal gas. This is an indication of still strong interactions happening between quarks and gluons in the high energy density and temperature phase.

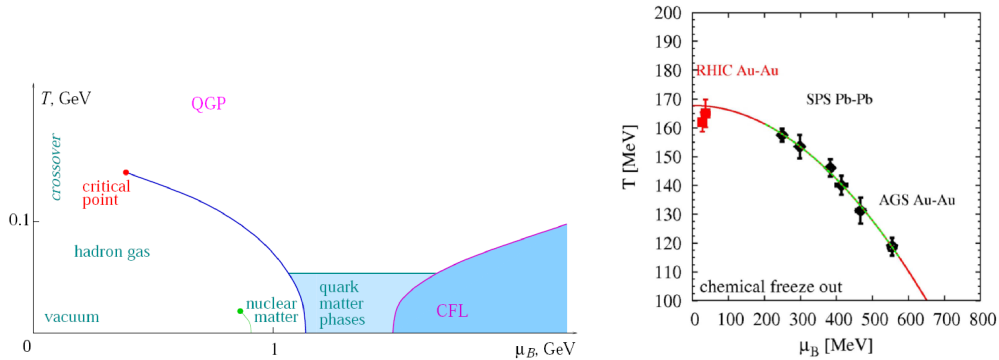


Figure 1.5: Left: (T, μ_B) phase diagram of nuclear matter. Figure taken from [12]. Right: Freeze-out points in the (T, μ_B) space obtained within statistical models from nucleus-nucleus collisions at AGS, SPS and RHIC energies. Figure taken from [13].

The left side of figure 1.5 is a sketch of the (T, μ_B) phase diagram, where μ_B is the baryo-chemical potential, of the nuclear matter as most physicists accept it today. The nuclear matter in its normal state is situated at $T = 0$ and $\mu_B = 937$ MeV. The dot at $\mu_B \sim 900$ MeV and small temperature at the bottom of the figure together with the small line represents the liquid-gas phase transition line. The hadron gas phase occupies the relatively low temperature and baryo-chemical potential region from the bottom left of the figure. The continuous line ending with a critical point is the first order phase transition line which separates the hadron gas phase from the QGP phase (at intermediate μ_B) or the quark dominated phases situated at low temperatures and high baryo-chemical potential. At low μ_B , it is thought today that the transition between the hadron gas phase and the deconfined QGP is of second order at the critical point and a smooth cross-over (high order phase-transition) at lower μ_B . [14]. The right side of figure 1.5 shows the temperatures and baryo-chemical potentials at the chemical freeze-out obtained from statistical model fits at various collision energies (AGS \rightarrow RHIC). The freeze-out (T, μ_B) points at AGS and low SPS energies are thought to be below the first order phase transition line calculated within lattice QCD [15]. At higher energies ($\sqrt{s_{NN}} > 7$ GeV) the freeze-out points tend to coincide with the cross-over phase transition line between QGP and hadron gas phase as obtained from lattice QCD.

The exact location of the critical point is the subject of intensive theoretical and experimental work (SPS experiments [16] and the future FAIR [17] and NICA [18] facilities).

1.2 Relativistic heavy ion collisions

Heavy ion collisions are the only way we can study in the laboratory the properties of nuclear matter in conditions other than the normal "ground" state. The colliding energies available for the relativistic nucleus-nucleus collisions grew very fast from $\sqrt{s_{NN}} \sim 2.3$ GeV at the Bevalac experiments, to $\sqrt{s_{NN}} = 5$ GeV at the AGS experiments from BNL and $\sqrt{s_{NN}} = 17.3$ GeV at the SPS experiments from CERN. To this date, the RHIC collider has been working for 8 years at center-of-mass energies approximately 10 times higher than SPS and the LHC experiments should start in the autumn of 2009 with a planned energy for the Pb+Pb system of $\sqrt{s_{NN}} \sim 5.5$ TeV.

One of the main goals of the heavy ion collision experiments at RHIC and LHC energies is the study of quark gluon plasma and the nuclear matter phase diagram. First, an overall description of the geometry and dynamics of the relativistic nuclear collisions will be given and then the main experimental facts accumulated up to now will be shortly introduced.

1.2.1 Collision geometry and dynamics

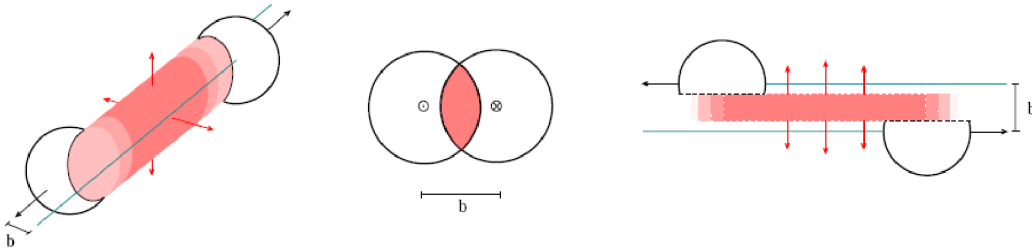


Figure 1.6: Perspective view of the nuclear collision geometry. Figure from [19].

Figure 1.6 contains views of the nuclear collision geometry from different angles. The nuclei, represented as spheres, collide at an impact parameter $b > 0$ (in the figure). The parts of the two nuclei which overlap/collide (colored in figure) form the so-called participant region while the rest of the nuclei is called the spectator region. At relativistic energies, the spectator parts of the nuclei move apart and fragment in a very narrow cone around their original direction. The participant region has a very different behaviour which is schematically illustrated in figure 1.7. There is not a clear delimitation for the steps in the evolution of the participant region from a nuclear collision but the sketch in figure 1.7 gives at least a temporal hierarchy.

Right before the collision, the two approaching Lorentz contracted nuclei are in a state which is still under vivid debates. The observed suppression of high transverse momentum particles seen at forward rapidity in d+Au collisions at $\sqrt{s_{NN}} = 200$ GeV [20] gave rise to the idea that the energetic incoming nuclei are in a state called Color Glass Condensate (CGC) [21]. In this state, due to the non-abelian nature of QCD, gluons self interact which results in nuclei containing a large number of low- x gluons⁴. At top RHIC energy the gluon density is believed to increase greatly forming a compact state thought to be responsible for the suppression of high p_T particles at forward

⁴ x is the fraction of the momentum of a hadron carried by a parton

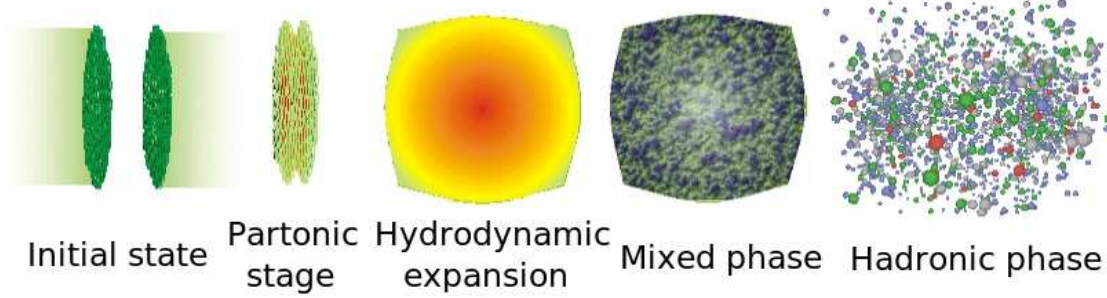


Figure 1.7: Schematic view of the nuclear collision time evolution. Art is courtesy of S.A.Bass.

rapidity. A different approach based on cold nuclear matter effects, like nuclear shadowing, was studied in [22, 23, 24, 25]. A more detailed description of this phenomenon is given in section 3.3.5.

The partonic stage occurs in the first instants of the collision. All the hard interactions between the incoming partons (quarks and gluons) take place now resulting in the production of high transverse momentum jets and heavy quarks. The multi-particle production leads to the formation of a very dense and hot medium with a mean free path much smaller than the nuclear radius. It is believed that this system thermalizes very quickly ($\tau \sim 1 \text{ fm}/c$) and starts to expand due to huge pressure gradients. This motivates the supposition that after the initial step, the nuclear fireball expands hydrodynamically. It is during this stage, which lasts for $\sim 10 \text{ fm}/c$, that the nuclear matter is expected to exist in the deconfined state named QGP.

After the nuclear fireball has expanded and cooled sufficiently, the lower densities force matter to hadronize (quarks get confined in bound states). Since at RHIC energies, this transition is expected to be a smooth cross over (second or higher order phase transition), there should be a stage when the nuclear matter exists in a phase which is a mixture between deconfined and confined matter. When the temperature lowers further, the nuclear matter hadronizes completely and after some time becomes a gas of free streaming particles.

1.2.2 Global measurements in relativistic collisions

One of the first questions that must be asked in relativistic heavy ion collisions is how much of the initial energy is available for particle production? This can be found by measuring the rapidity density of the number of baryons minus the number of anti-baryons. Knowing that initially all the baryons (protons and neutrons) had the beam rapidity and using the baryon number conservation law, one can extract the amount of stopping from the average rapidity loss. An illustration of the net-proton rapidity distributions at three colliding energies is shown in the left side of figure 1.8. It is very visible how the collision dynamics changed with energy. At AGS energies, the initial baryons lost almost all their initial momentum and were shifted to mid-rapidity. At top SPS energy, net proton distributions shows a double hump structure representing the fragmentation peaks of the two colliding nuclei. At top RHIC energy, the initial protons passed almost completely through each other leaving a net-baryon poor region at mid-rapidity. At this energy, $\sqrt{s_{NN}} = 200 \text{ GeV}$, it was found that as much energy

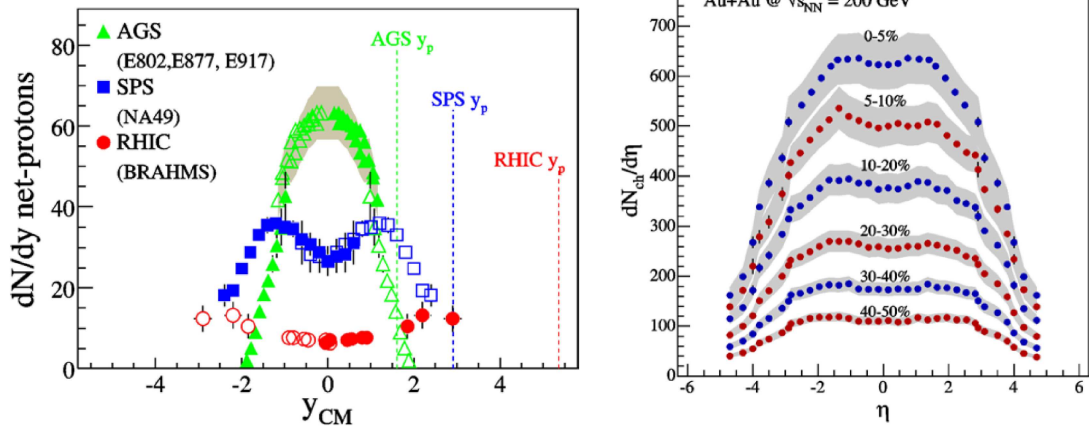


Figure 1.8: Left: Net-proton ($dN/dy(B) - dN/dy(\bar{B})$) rapidity density in central collisions at top AGS energy, top SPS energy and top RHIC energy. Figure from [26]. Right: Charged particle pseudo-rapidity density. Figure from [27].

as 73 ± 6 GeV per nucleon out of the initial 100 GeV is released in the collision region and is available for particle production [26].

By measuring the charged particle pseudo-rapidity density and the average transverse momentum one can calculate the energy density reached in the collision by using the Bjorken estimate [28]:

$$\epsilon = \frac{1}{\pi R^2 \tau} \frac{d\langle E_T \rangle}{dy}, \quad (1.1)$$

where R is the effective radius of the overlapping disk between the colliding nuclei, and τ is the formation time of the plasma, usually taken to be $1 \text{ fm}/c$ as a conservative estimate. In [27] it was estimated that in central Au+Au collisions at $\sqrt{s_{NN}} = 200$ GeV the energy density reached is at least $\epsilon \sim 5 \text{ GeV}/\text{fm}^3$ which is higher than the $\sim 1 \text{ GeV}/\text{fm}^3$ thought to be necessary for QGP formation. The obtained energy density is also 10 times higher than the energy density of a baryon and 30 times higher than the normal nuclear matter energy density.

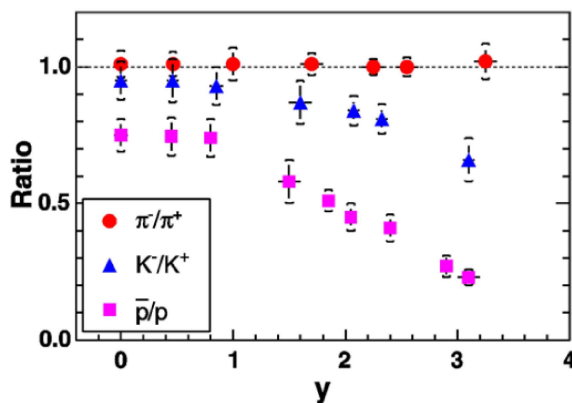


Figure 1.9: Anti-particle to particle ratios in central Au+Au collisions at $\sqrt{s_{NN}} = 200$ GeV. Figure from [29].

The anti-hadron to hadron ratios measured at the RHIC highest energy [29] and

shown in figure 1.9 are ~ 1 in the case of pions and approaching 1 for kaons and protons at mid-rapidity. This suggests that the particle production mechanism in the central region is mainly pair creation leading to a matter/anti-matter equilibrated medium with a vanishing number of net-baryons. These ratios together with the net-proton rapidity density shown in figure 1.8 supports the scenario of collision transparency proposed by Bjorken [28]. In this picture, the incoming nuclei pass through each other leaving between them a color field which produces pairs of particles from the highly excited vacuum.

1.3 Searching for the Quark Gluon Plasma

During the evolution of a heavy ion collision, the nuclear matter follows a trajectory in the (T, μ_B) space and if the colliding energy is sufficient it might cross from the hadronic phase into the deconfined phase. Subsequent cooling and expansion brings the matter back in the hadron phase. In the time nuclear matter is in the quark-gluon plasma state it is expected that the produced particles carry information about the medium in which they originated. Due to the complicated evolution and entangled processes involved in heavy ion collisions, it is accepted today that there is no single definitive observable which can demonstrate the existence of QGP. Instead, many possible signals are investigated. A very comprehensive review of most of the QGP predicted signals is given in [30].

1.3.1 Electromagnetic probes

Electromagnetic probes are represented by the photons and leptons which are created during the evolution of a nuclear collision. Their importance rely mainly on the fact that there is very little probability for these particles to rescatter after their original emission since they do not interact strongly. Hence these particles⁵ are carriers of unspoiled information about the thermodynamical conditions of the nuclear medium in which were created. Time evolution of the medium conditions is, in principle, also available since the direct probes are created throughout the collision lifetime.

The use of electromagnetic probes as indicators for the quark-gluon plasma formation has many difficulties due to the many sources which can produce photons or leptons. In the following, some of the main results on direct probes will be shown and discussed briefly.

Direct photons

Photons are produced in a QGP in annihilation processes ($q + \bar{q} \rightarrow \gamma + g$) or Compton like processes ($g + q(\bar{q}) \rightarrow \gamma + q(\bar{q})$). It has been shown theoretically (see [31] for a few reviews) that the momentum distribution of the γ photons emitted in these processes is strongly related to the corresponding distribution of the quarks and gluons from the plasma. Hence, the temperature of these photons is a good indicator of the QGP temperature. However there are many other photon sources which make the measurement of such an observable very difficult from both an experimental and theoretical point of view. Some of these are:

⁵Photons and lepton pairs are also called penetrating probes

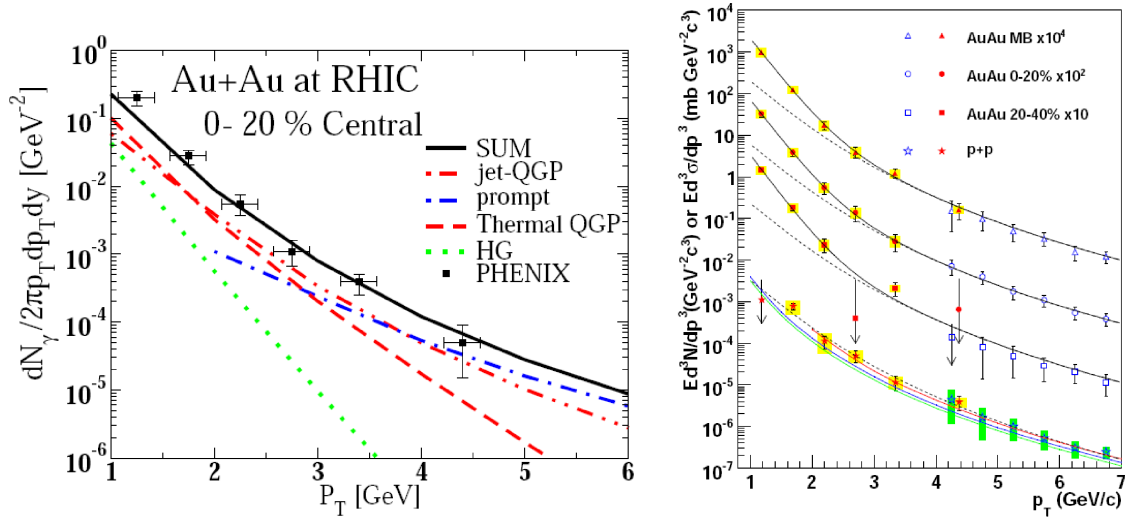


Figure 1.10: Left: Invariant photon yields measurement and comparison to theoretical calculations for the direct γ cocktail. Figure from [32]. Right: Invariant photon yields from $p+p$ and $Au+Au$ collisions at $\sqrt{s_{NN}} = 200$ GeV and comparison to NLO-pQCD calculations. Figure from [33].

hard scatterings of the initial partons ($q + \bar{q} \rightarrow \gamma + g$) produce photons with a distribution approximately proportional with the quark distribution in nucleons;

jet bremsstrahlung producing direct γ 's due to jet interaction within the dense hot plasma;

jet fragmentation outside the fireball;

hadron gas producing photons through channels like $\pi^+ + \pi^- \rightarrow \gamma + \rho^0$;

hadron decays (*e.g.* π^0 , ρ , η , ω) which dominate the inclusive photon spectrum.

In the left side of figure 1.10, the contributions from different sources to the total photon yield calculated theoretically [32] are illustrated and compared to experimental measurements from central Au+Au collisions at the RHIC top energy. It can be seen that the region where the contribution from QGP is important is at $p_T < 3$ GeV/c. The right part of figure 1.10 shows the photon yields from different Au+Au centrality ranges together with the ones from p+p collisions [33]. The dashed curves is a fit to the p+p data and is scaled so that it can be compared to the Au+Au yields. It is clear that in Au+Au collisions there is an excess of photons in the low p_T range where the contributions from QGP are expected to be strong.

Dileptons

Dileptons can be produced in QGP through the annihilation process $q + \bar{q} \rightarrow \gamma^* \rightarrow \ell^+ \ell^-$. The invariant mass of the lepton pair carries information about the quark distributions [34] meaning that, as in the photon case, these can be used to measure thermal properties of the plasma. The other sources which produce dileptons are annihilation processes with quarks from the initial nuclei⁶, hadronic scatterings like $\pi^+ + \pi^- \rightarrow \ell^+ \ell^-$ or decay

⁶This process of annihilation between a quark from the initial nucleons and a sea anti-quark is called a Drell-Yan process.

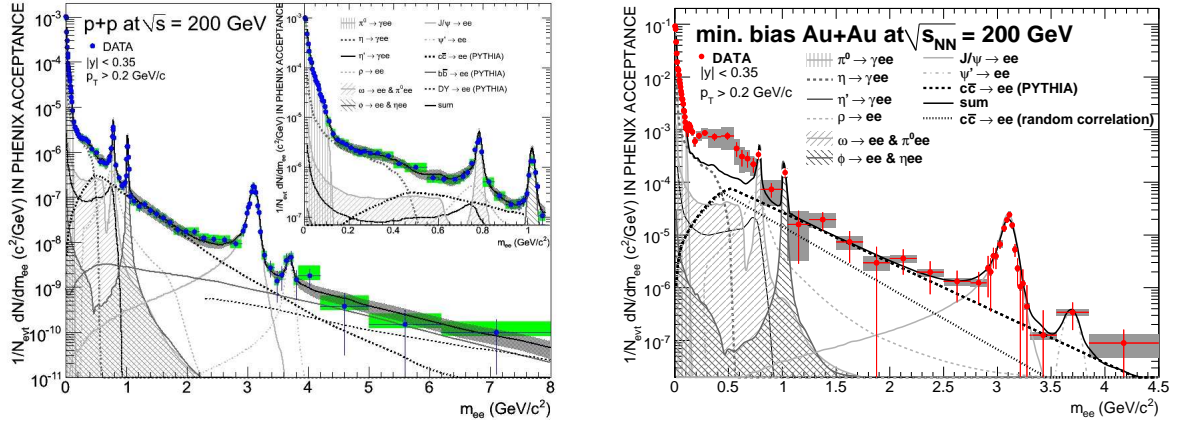


Figure 1.11: Invariant mass distribution for e^+e^- pairs measured by the PHENIX experiment at $\sqrt{s_{NN}} = 200$ GeV and the cocktail of contributions from known sources. Left: $p + p$ collisions from [35]. Right: Minimum bias $Au + Au$ collisions from [36].

of particles like π^0 , η , ρ , ω , ϕ , J/ψ , Ψ . At high invariant masses there is also a large background from correlated heavy quark decays. All these must be taken into account in order to see the net effect of the QGP. Figure 1.11 shows the invariant mass distribution of the e^+e^- pairs at $\sqrt{s_{NN}} = 200$ GeV in $p+p$ (left) and $Au+Au$ collisions (right) [35, 36]. The cocktail of contributions from the above mentioned dilepton sources are illustrated also. It was observed that the sum of non-QGP contributions is reproducing well the $p+p$ data. The $Au+Au$ results however show an excess of dielectron pairs in the range $0.2 < p_T < 0.8$ GeV/ c where it is expected for the QGP contribution to be most prominent.

1.3.2 J/ψ suppression

J/ψ particles are bound states of a c quark and a \bar{c} anti-quark. Since the charm quarks are heavy, they are likely to be produced in the initial moments of a collision mainly from hard parton scatterings. In $p+p$ or $p+A$ collisions, the created J/ψ 's would simply escape the collision region and be detected through their decay channels. In nucleus-nucleus collisions however, the J/ψ mesons need to pass through the extended hot and dense nuclear medium.

The J/ψ meson is a tightly bound particle but in a quark-gluon plasma environment the charm quarks are screened pretty much like in the analogous phenomenon called *Debye screening* from QED. Moreover, in a QGP the quarks and gluons are free and the string tension vanishes. In consequence, the interaction between the c and \bar{c} quarks is weakened to a point in which the J/ψ meson can dissociate leading to a suppression of the J/ψ yield compared to $p+p$ or $p+nucleus$ collisions [39]. The free charm and anti-charm quarks travel through the plasma until the system cools down and they can hadronize by combining with the more abundant u , d and s quarks and forming open charm particles like $D(c\bar{u}$ or $c\bar{d})$, $\bar{D}(\bar{c}u$ or $\bar{c}d)$, $D_s(c\bar{s})$ and $\bar{D}_s(\bar{c}s)$. If the density of charm quarks formed is high enough they can also recombine into J/ψ or excited states like ψ' and χ_C , thus complicating the signal.

Figure 1.12 shows the J/ψ nuclear modification factor⁷ in $d+Au$ collisions (left)

⁷Nuclear modification factor is the ratio of the yield in $p+A$ or $A+A$ collisions to the yield in $p+p$

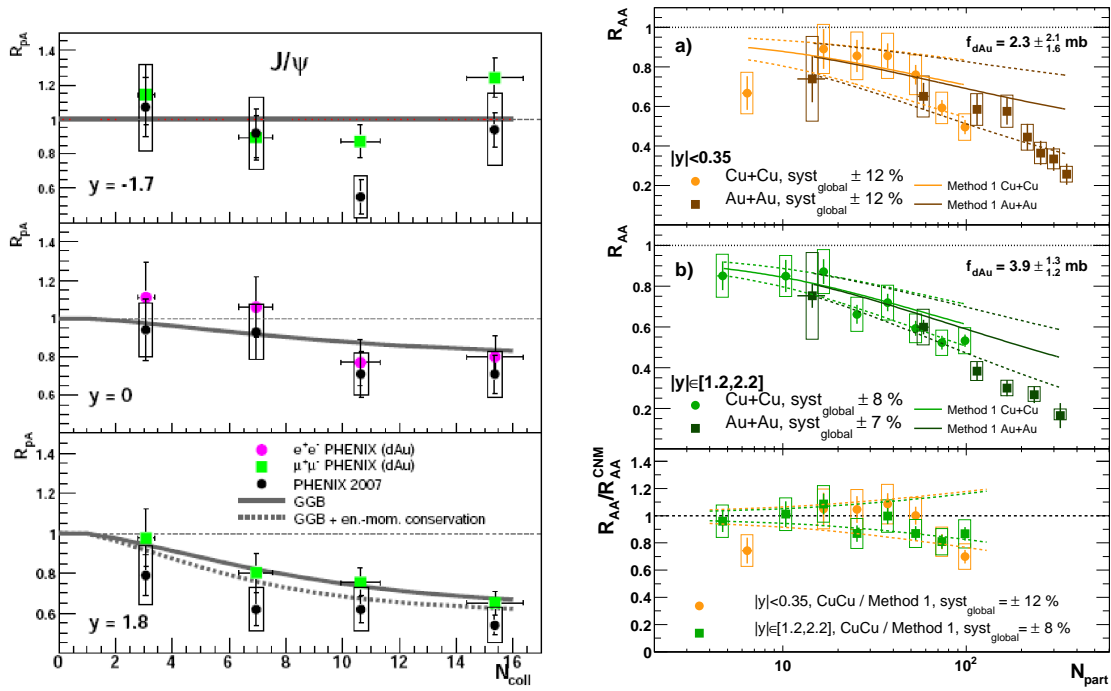


Figure 1.12: Left: J/ψ suppression in d+Au collisions at $\sqrt{s_{NN}} = 200$ GeV as a function of the number of binary collisions at $y = -1.7$, 0 and $+1.8$. The full curve accounts only for gluon shadowing calculated in a Glauber-Gribov approach. Figure from [37]. Right: J/ψ suppression in Au+Au and Cu+Cu collisions at $\sqrt{s_{NN}} = 200$ GeV as a function of the number of participant nucleons at $y = 0$ and $y \sim 2$. Figure from [38].

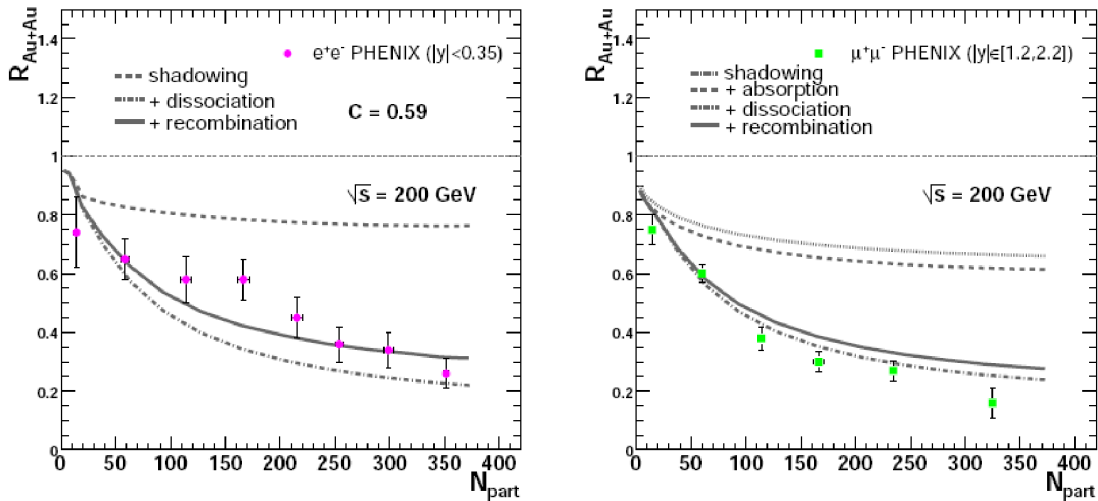


Figure 1.13: J/ψ suppression as a function of the number of participant nucleons in Au+Au collisions. The different curves account for contributions from shadowing, absorption, dissociation and recombination. Figure from [40]

and in Au+Au collisions (right). The suppression seen in d+Au collisions can be explained by using the cold nuclear matter effect called gluon shadowing which is calculated in the Glauber-Gribov approach [37]. At $y = 1.8$, in the Au fragmentation hemisphere, the energy-momentum conservation constraint becomes important and acts by increasing more the suppression given by shadowing. This means that there is no dissociation of the J/ψ 's formed in d+Au collisions. In the right side of figure 1.12 it can be seen that the suppression of J/ψ is very strong in central Au+Au collisions and decreases when the system gets smaller. It can also be observed that the suppression is stronger at more forward rapidity. In figure 1.13, the nuclear modification in Au+Au collisions is compared to a calculation which takes into account effects like gluon shadowing, absorption, dissociation and recombination [40]. It is clear that initial effects like gluon shadowing are not enough to explain all the suppression and the dissociation/recombination of J/ψ in the plasma must be taken into account. The higher suppression observed at $y \sim 2$ is explained partly through the rapidity evolution of shadowing but also through the absorption of $c\bar{c}$ pair. J/ψ suppression was studied also in the context of statistical hadronization models, *e.g.* in [41] leading to a good description of mid-rapidity $R_{AA}^{J/\psi}$ with centrality and rapidity.

1.3.3 High p_T suppression

This effect has been discovered for the first time at RHIC energies and is related to the suppression of the high transverse momentum particles in central Au+Au collisions as compared to the scaled spectra from p+p collisions. The suppression, originally proposed in [42, 43, 44], was explained through the large energy loss which high momentum partons suffer in a medium with high density of color charges. Figure 1.14

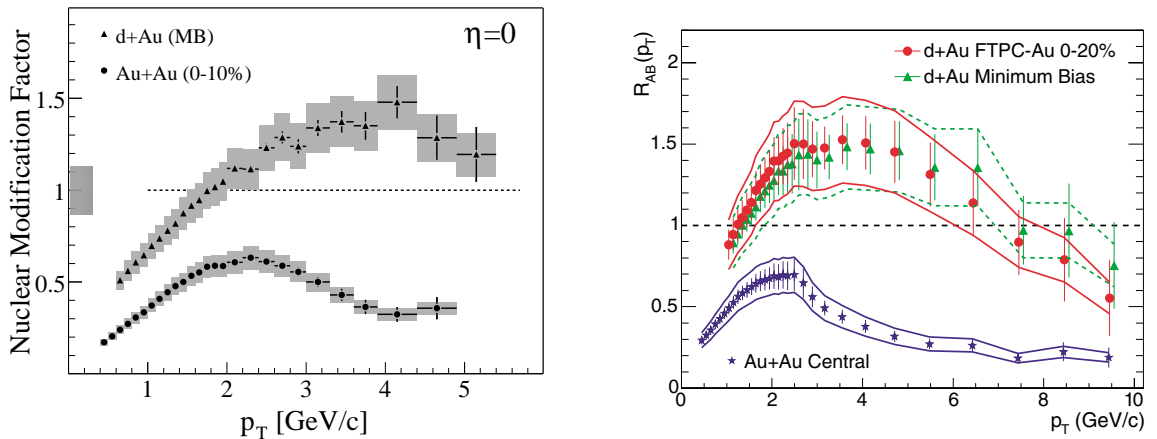


Figure 1.14: Nuclear modification factor in d+Au and central Au+Au collisions from BRAHMS (left) [45] and STAR (right) [46].

shows the nuclear modification factors R_{AA} and R_{dAu} for central Au+Au and minimum bias d+Au collisions respectively as a function of the transverse momentum at mid-rapidity. The nuclear modification factors are defined as

$$R_{AB} = \frac{d^2 N^{AB} / dp_T d\eta}{\langle N_{\text{bin}} \rangle d^2 N^{NN} / dp_T d\eta} \quad (1.2)$$

collisions scaled with a factor which accounts for the different number of binary collisions (see eq.1.2).

where $\langle N_{\text{bin}} \rangle$ is the average number of binary collisions in a A+B collision, $d^2N^{AB}/dp_T d\eta$ is the differential yield in the A+B collision and $d^2N^{NN}/dp_T d\eta$ is the differential yield in a nucleon-nucleon collision. In both sides of the figure it is visible that in Au+Au collisions the high p_T charged particles are suppressed compared to $p + p$ collisions. Moreover, in d+Au collisions where the formation of a QGP is not expected, an enhancement is actually seen, called the Cronin effect[47], confirming that the suppression in Au+Au collisions is not due to particular conditions of the colliding nuclei (initial state effect).

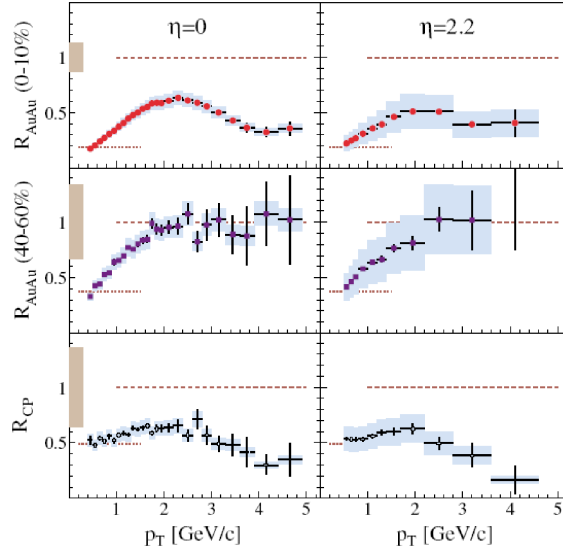


Figure 1.15: Nuclear modification factor in central and semi-peripheral Au+Au collisions at $\eta = 0.0$ and $\eta = 2.2$. Bottom row shows the R_{CP} factor which is defined as $R_{CP} = R_{AA}(\text{central})/R_{AA}(\text{peripheral})$. Figure from [45].

The R_{AA} factors were checked also in peripheral collisions (see an example in figure 1.15) and it was observed that the suppression is smaller than the one in central collisions. This fact is in agreement with models which explain the high p_T suppression through the energy loss of partons in the dense QGP medium. The longer the path length in plasma, the higher the suppression is.

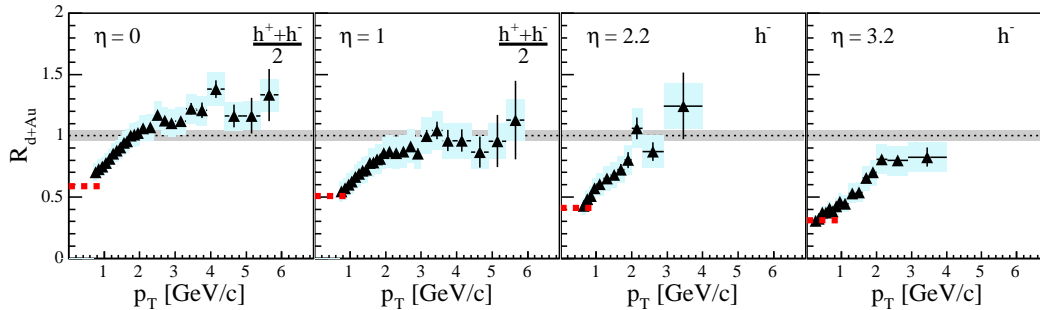


Figure 1.16: Nuclear modification factor for charged hadrons in d+Au collisions at $\eta = 0, 1, 2.2$ and 3.2 . Figure from [48].

The BRAHMS collaboration discovered that moving from mid-rapidity towards

high rapidity, the nuclear modification factor from d+Au collisions drops from Cronin enhancement at $\eta = 0$ to suppression at $\eta = 3.2$ (see figure 1.16) [48]. This was a novel observation and it was proposed that it is related to the initial conditions of the colliding d and Au nuclei. The most famous hypothesis was that prior to collision the colliding nuclei exist in a state called color-glass condensate (CGC) [21] (see section 1.2.1). Other explanations consider cold nuclear matter effects like gluon shadowing which take into account the modification of nucleonic parton distribution functions in nuclei compared to the ones in free nucleons.

1.3.4 In medium jet modification and correlations

Particle correlations are a very important tool in studying the interaction of high momentum partons with the nuclear medium providing a tomography of the hot and dense fireball. In the previous section it was shown that high p_T particles are suppressed in Au+Au collisions at $\sqrt{s_{NN}} = 200$ GeV and that this suppression is stronger in central collisions than in peripheral collisions.

The high momentum partons or jets are created normally in $2 \rightarrow 2$ processes which involve two jets being emitted back-to-back. It was proved that at RHIC top energy, only jets created at the edge of the fireball can escape meaning that the associated jet, emitted azimuthally opposite to the trigger jet, will traverse through the QGP medium and will be strongly modified. Figure 1.17 shows a summary of the back-to-back hadron-hadron correlations. In the left side it can be observed that in p+p collisions the di-hadron correlations show a pronounced peak at $\Delta\phi = 0$ ⁸ (near side peak), which represents the trigger particle, and another peak (away side peak) at $\Delta\phi = \pi$ representing the associated jet. Although the away side peak is slightly broader than the near side peak, it can be approximated that both of the jets survive and fragment in vacuum. In central Au+Au collisions the near side peak is visible as in the p+p collisions but the away side peak disappears meaning that the associated jet was absorbed in the medium. Moving towards peripheral collisions the away side increases due to shrinking of the path length traversed by the associated parton.

The right hand side of figure 1.17 shows di-hadron back-to-back correlations in p+p and central Au+Au collisions by using different momenta ranges for the trigger and associated particles. It has been observed that the away side in Au+Au collisions develops a double hump structure at certain trigger-associated momentum ranges which is consistent with the associated jet emitting particles conically. In figure 1.18 are shown calculations of a quark jet moving through a strongly coupled $N = 4$ supersymmetric Yang-Mills plasma by using the gauge/string duality [51]. The energy density and energy flux flow profiles are analogous to a Mach wake for objects traveling with velocities higher than the speed of sound. Particles are emitted in a cone with an opening of about 50° but also parallel to the direction of the associated parton. Attempts to model the effect of fast moving jets on the QGP medium have been made also by using ideal hydrodynamics and different jet energy momentum deposition models [52] which give rise to a Mach cone that might explain the double hump structure seen in the di-hadron correlations.

Another important observation made at RHIC was the near-side $\Delta\eta$ versus $\Delta\phi$ correlations also called the "ridge" [53]. Figure 1.19 shows these correlations in four centrality bins. In central Au+Au collisions, the near side "ridge" ($\phi_\Delta \sim 0$) exhibits a

⁸ ϕ is the azimuthal angle

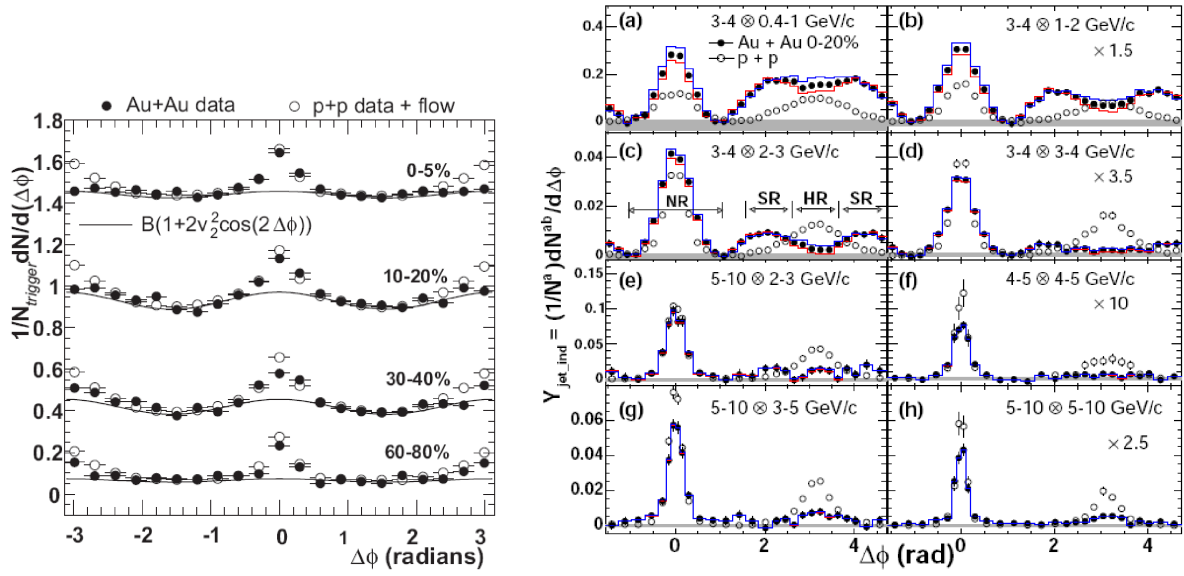


Figure 1.17: Left: Centrality dependent back-to-back di-hadron correlation functions from Au+Au collisions at $\sqrt{s_{NN}} = 200$ GeV compared to p+p collisions. Figure from [49]. Right: Back-to-back di-hadron correlations in p+p and central Au+Au collisions with different $(p_T^{trig}, p_T^{assoc})$ range combinations. Figure from [50].

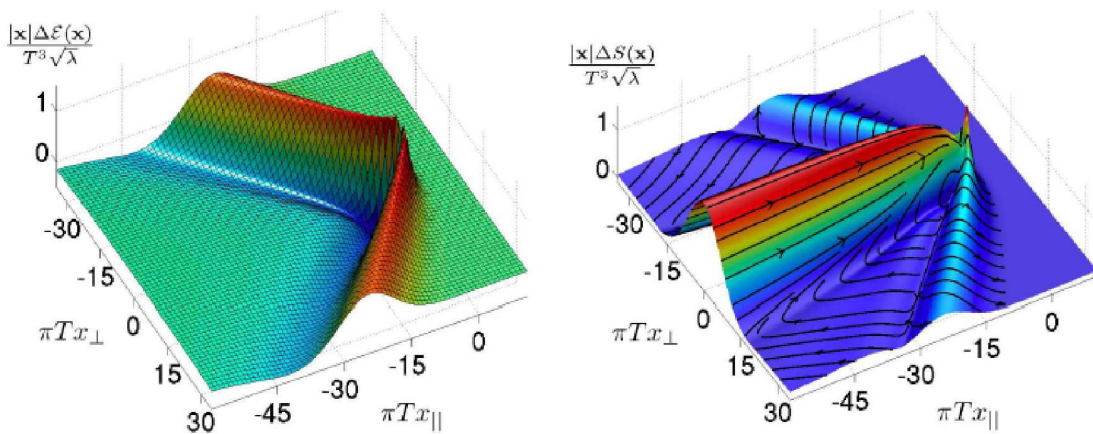


Figure 1.18: Energy density (left) and energy flux (right) profiles from AdS/CFT calculations. Figure from [51].

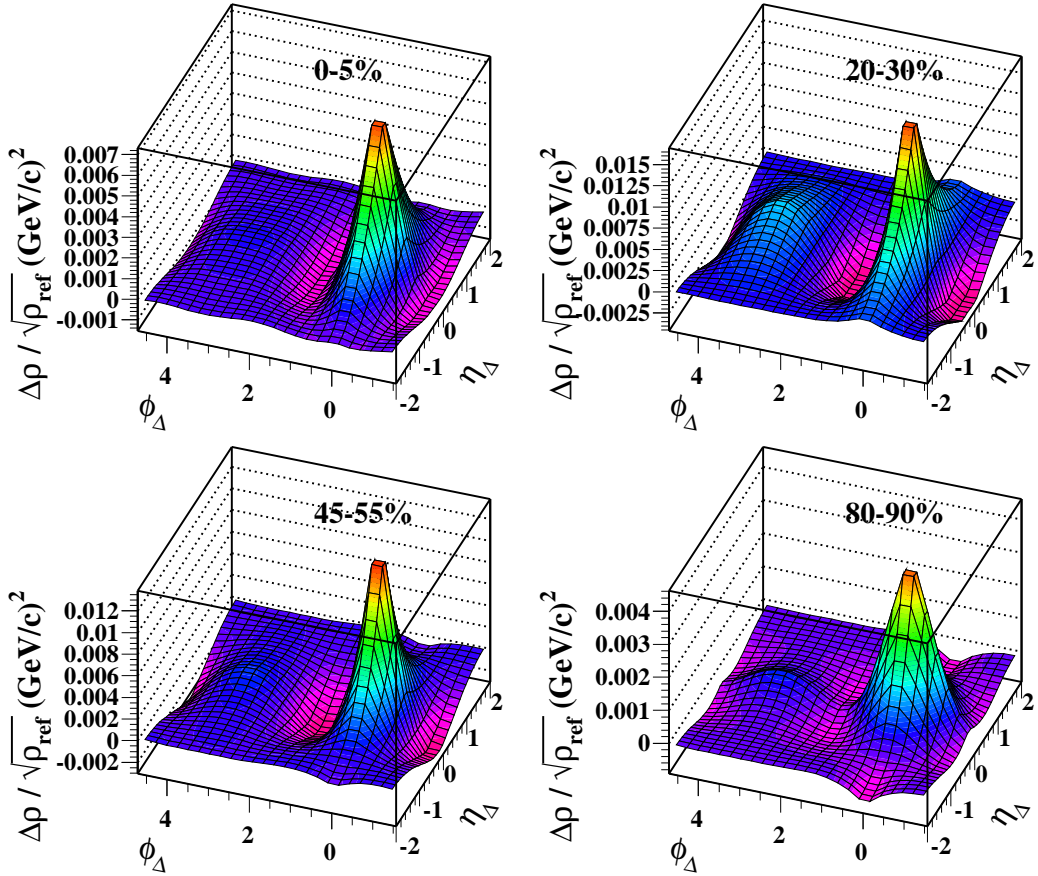


Figure 1.19: Distributions of the $\Delta\rho/\sqrt{\rho_{\text{ref}}}(\eta_\Delta, \phi_\Delta)$ density ratio which estimates the p_T covariance per particle for a given separation on η, ϕ , averaged over acceptance. Figure from [53].

structure peaked around $\eta_\Delta = 0$ (the trigger jet) but with a wide extension in pseudo-rapidity. At lower centralities, this structure gradually changes until it becomes a narrow structure in rapidity around the trigger particle which is consistent with free streaming jets. It is also observed that in semi-central collisions, the correlation density ratio is more concentrated in the reaction plane. A summary of most of the many tentative explanations for the ridge structure can be found in [54].

1.3.5 Elliptic flow

Elliptic flow is an important observable for the evolution of nuclear collisions. A comprehensive description of the elliptic flow history and analysis methods can be found in [55] and this subject is treated also in chapter 3.3. In short, the elliptic flow coefficient v_2 is a measure of the azimuthal anisotropy of particles momenta. It is defined as

$$v_2 = \langle \cos[2(\phi - \Psi_r)] \rangle \quad (1.3)$$

where $\langle \rangle$ indicates particle-wise average, ϕ is the azimuthal angle of a given particle and Ψ_r is the event reaction plane azimuthal angle. If one knows the reaction plane, then the reference system can be rotated around the beam axis so that the x and z axes will be in the event reaction plane. In this reference system, the v_2 coefficient becomes

$$v_2 = \left\langle \frac{p_x^2 - p_y^2}{p_x^2 + p_y^2} \right\rangle \quad (1.4)$$

where p_x and p_y are the x and y components of momentum vector in the rotated reference system. The reason for the anisotropy is different depending on energy and it reflects reaction dynamics. Figure 1.20 shows the evolution of the v_2 coefficient with the

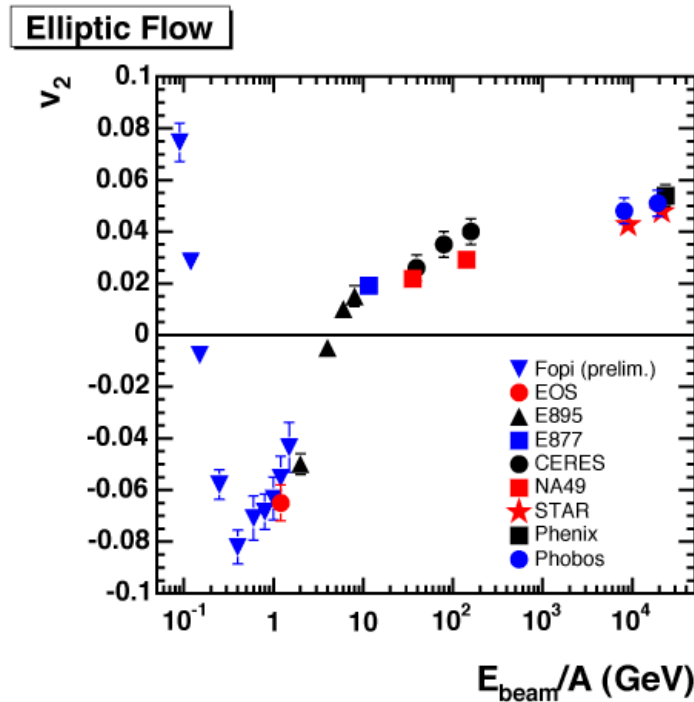


Figure 1.20: Elliptic flow coefficient versus center of mass energy. Figure from [55].

center of mass energy calculated for the 25% most central nucleus-nucleus collisions⁹. This is a very explanatory picture for the evolution of the reaction dynamics. At very low energies, $E_{beam} < 150$ MeV/A, the positive elliptic flow reflects the in plane momentum anisotropy due to the strong orbital momentum of the nuclear fragments created in collision. The v_2 coefficient is dropping with energy and at $E_{beam} \sim 150$ MeV/A becomes negative and continues to drop down to a minimum at $E_{beam} \sim 400$ MeV/A. This behaviour was explained through the increasingly distinct participant and spectator regions which start to form with growing energy. The participant-spectator picture was described in section 1.2.1 for high energy nuclear collisions. At low energies, the

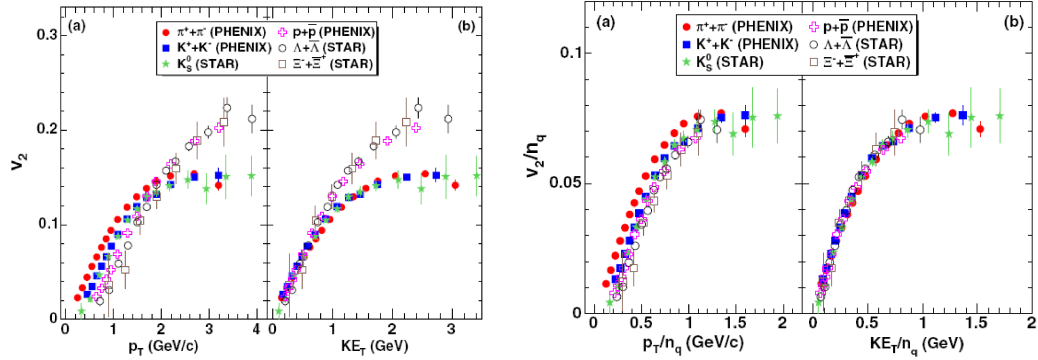


Figure 1.21: Left: v_2 versus p_T and transverse kinetic energy KE_T . Right: v_2/n_q versus p_T/n_q and KE_T/n_q where n_q is the number of constituent quarks for each of the particle species considered. Figure from [56].

spectator part does not exit the collision region fast enough and block in-plane emission from the nuclear overlap zone so that particles emitted from the participant region are bounced out of plane resulting in negative v_2 coefficient. With increasing energy the bouncing off-plane dynamics becomes less and less important because the spectator region move faster and escape from the collision region. At the same time, at energies higher than $E_{beam} \sim 400$ MeV/A, pressure gradients start to develop in the collision region preferentially in-plane giving positive contributions to v_2 . The two mechanisms are competing with each other leading to a monotonic increase of the elliptic flow coefficient with energy. At $E_{beam} \sim 4$ GeV/A, v_2 changes sign again and becomes positive signifying that the pressure gradient driven elliptic flow starts to dominate. At RHIC energies, v_2 is almost saturated suggesting that there is no more influence from the spectator region and that the elliptic flow is due only to the initial spatial eccentricity of the collision region which transforms into a momentum space azimuthal eccentricity (see figure 3.3 for a schematic hydro evolution of the collision).

One of the main observations at RHIC was the fact that the elliptic flow v_2 divided by the number of constituent quarks n_q as a function of the kinetic transverse energy also divided by the number of quarks has a common behaviour for many particle

⁹In order to understand this data some collision geometrical details must be explained. The reaction plane is the plane formed by the line joining the centers of the two nuclei (impact parameter vector - defined as x axis) with the beam axis (z -axis). The y axis is the axis perpendicular to the reaction plane. A positive v_2 coefficient means that the momentum azimuthal anisotropy drives particles preferentially towards the reaction plane and is also called *in-plane* flow, while when v_2 is negative, the flow is called *out-of-plane* because the momentum anisotropy drives particles preferentially perpendicular to the reaction plane.

species. Figure 1.21 shows this behaviour for a selection of non-strange and strange mesons and baryons (the 4th plot). The conclusion drawn from this data was that the flow is developed at very early stages and that the matter at RHIC energies flows at partonic level. This implies the formation of deconfined nuclear matter [56].

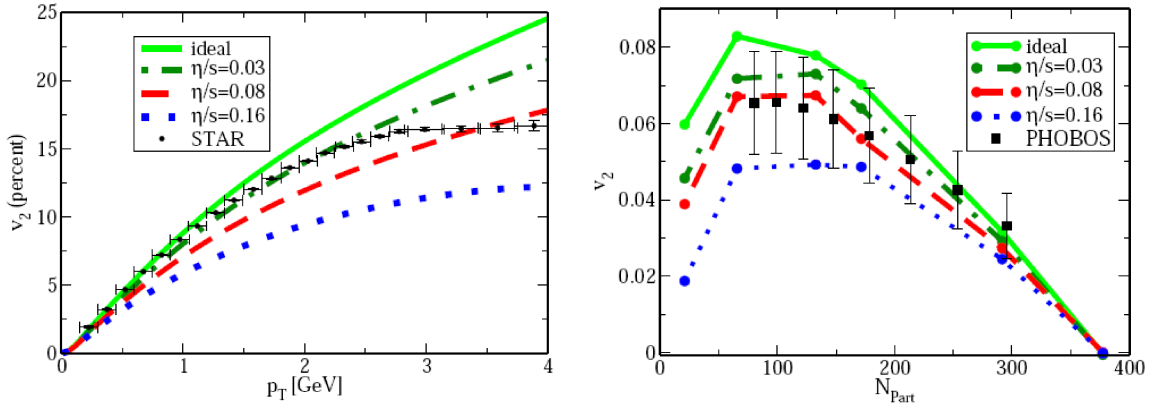


Figure 1.22: Figure is from [57], PHOBOS experimental data from [58] and STAR experimental data from [59].

In the left part of figure 1.22 it is shown that calculations within the framework of ideal hydrodynamics (zero viscosity) do not explain the v_2 coefficient at transverse momenta higher than 1.5-2 GeV/c. Calculations made using hydrodynamics with non-zero shear viscosity η [57] explain the trend of v_2 at higher p_T but do not quite describe data in the entire p_T range. The azimuthal anisotropy at higher p_T might also be due to non-flow effects but to path length dependent energy loss of partons. The same calculation model was used to describe the centrality dependence of the p_T integrated v_2 (see right side of figure 1.22). The conclusion of this calculation was that, in terms of viscosity, the fluid formed at RHIC is close to the lower bound conjectured in the AdS/CFT theory to be $\eta/s \geq 1/4\pi$ [60].

1.3.6 Strangeness enhancement

Strangeness enhancement refers to the increased production of strange particles in nuclear collisions due to the opening of new production channels in quark-gluon plasma. This signal was first predicted in [61] and explained through interactions between partons in the dense and hot QGP. At low energy, strange particles are produced mainly in hadronic channels but in a QGP environment processes like quark anti-quark annihilation and gluon fusion produce an excess of strange quark pairs (see figure 1.23). It is expected that for a high enough temperature, $T \geq 160$ MeV, the strangeness abundance saturates in the plasma in a very short time $\sim 10^{-23}$ sec and will lead to an enhanced production of strange and multi-strange particles. This enhancement was observed at the top SPS energy for strange hyperons like Λ , Ξ , Ω , in nucleus-nucleus collisions compared to small interacting systems like proton-nucleus collisions (see figure 1.23). Moreover, in nucleus-nucleus collisions, the enhancement grows with the number of wounded nucleons (or reaction centrality) but also with the number of component strange quarks. This is consistent with the QGP creation hypothesis.

In order to observe experimentally the strangeness enhancement one needs to measure in principle all the strange particles and compare with the number of non-strange

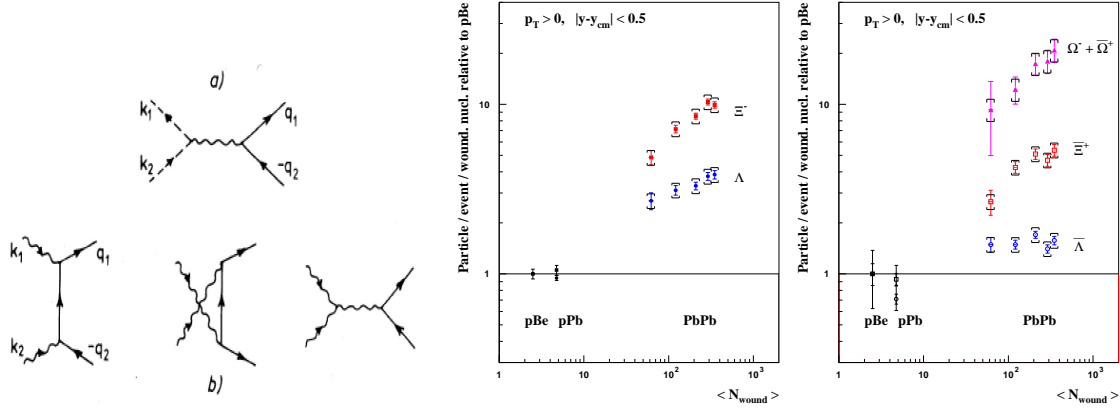


Figure 1.23: Left: Lowest order QCD diagrams for $s\bar{s}$ production from $q\bar{q}$ annihilation (a) and gluon fusion (b). Figure from [61]. Right: Hyperon enhancements as a function of the number of wounded nucleons in p+Be, p+Pb and Pb+Pb collisions at $\sqrt{s_{NN}} = 17.3$ GeV. Figure from [62]

ones. This has been done by using a relative strangeness production observable E_S defined in [63] as:

$$E_S = \frac{2 \times (K^+ + K^-) + 1.54 \times (\Lambda + \bar{\Lambda})}{1.5 \times (\pi^+ + \pi^-) + 2 \times \bar{p}}. \quad (1.5)$$

The factor 2 which multiplies the kaon yield takes into account the K^0 yield, the factor 1.54 for Λ s accounts for the Σ^\pm hyperons (deduced from model calculations), the factor 1.5 for pions accounts for the π^0 yield while the factor 2 for \bar{p} accounts for the protons produced in the collision (excludes the initial protons). The definition of E_S can slightly

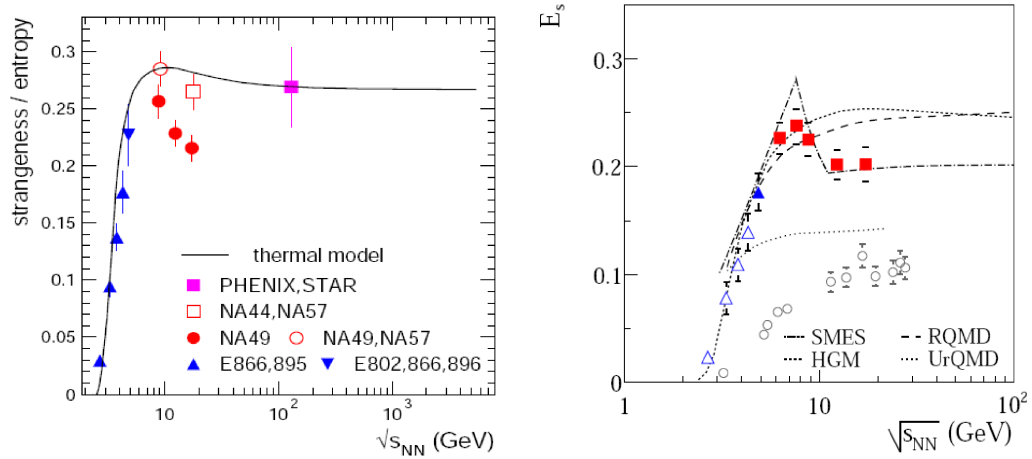


Figure 1.24: Energy dependence of strangeness to entropy ratio. Figures are from [63] (left) and [64] (right).

vary from case to case due to the possible inclusion of multiple strange hyperons like Ξ , Ω or ϕ mesons but their contribution to the total strangeness ratio is small. The numerator of the r.h.s. in equation 1.5 is also called total strangeness production while the denominator is often referred to as entropy production. A detailed discussion on the construction of this observable is given in [65, 63]. Figure 1.24 shows the energy

dependence of E_S . The data in the two sides was extracted in [63] (left) and [64] (right) and both show a steep increase in strangeness production up to $\sqrt{s_{NN}} \sim 6$ GeV where E_S seems to saturate. It should be noted that the E_S factor calculated in [64](right panel) is constructed slightly different than in the left panel (without the 1.54 factor, etc.). The thermal model used in [63] gives a good description of the data showing that the strangeness ratio saturates in the range $5 < \sqrt{s_{NN}} < 10$ GeV. The statistical model of early stage (SMES) described in [66] which assumes the formation of QGP at low SPS energies gives also a good description of the strangeness production ratio but exhibits a sharp "horn"¹⁰ peaked at $\sqrt{s_{NN}} \sim 8$ GeV. The hadron gas model and the hadronic cascade model RQMD predict a saturation of the strangeness ratio in the SPS energy region but at a higher value than what is seen experimentally.

From the right side of figure 1.24 it can also be seen that E_S is significantly enhanced in nucleus-nucleus collisions as compared to p+p collisions even at energies close to the strangeness production threshold.

1.3.7 The critical point

It is generally agreed that a phase transition line separating bound hadronic matter from deconfined matter which starts from $(T \sim 0, \mu_B > m_N)$ and meets the zero μ_B axis at a critical temperature T_C in the range 170–190 MeV (see left side of figure 1.5). Lattice QCD calculations [67] show that at $\mu = 0$, the order of the phase transition depends on the light and strange quark masses as shown in the left side of figure 1.25. At small and very high u, d and s masses the phase transition is of the first order while

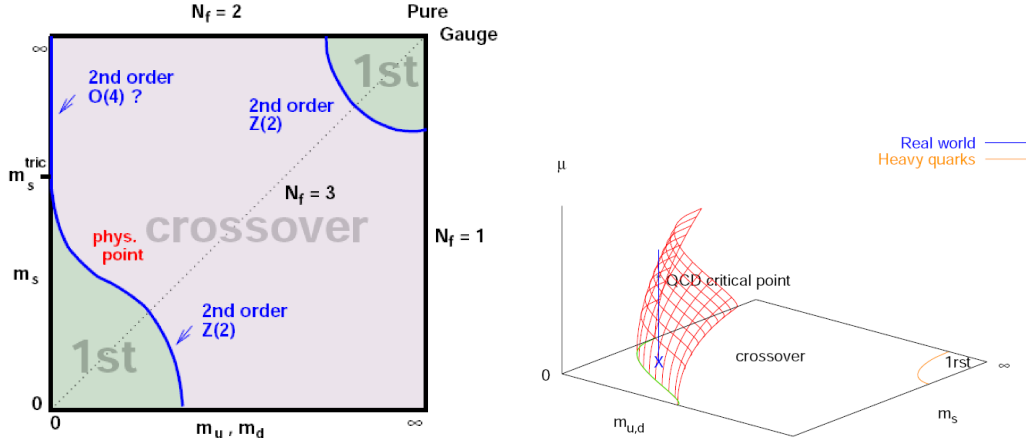


Figure 1.25: Left: Schematic phase transition behaviour of $N_f = 2 + 1$ flavour QCD as a function of quark masses $(m_{u,d}, m_s)$ at $\mu = 0$ [67]. Right: $(m_{u,d}, m_s)$ first order phase transition line evolution with the chemical potential [68].

at intermediate masses the transition is continuous (higher order). All existing lattice calculations at zero chemical potential suggest a continuous transition (the physical point is marked on the figure). See [67] for a review on lattice results for heavy ion collisions. Recent studies with non-vanishing chemical potential [68] suggest that the $(m_{u,d}, m_s)$ phase transition line moves towards higher quark masses and at some critical μ_C it reaches the physical quark masses point (see right part of figure 1.25). For $\mu > \mu_C$,

¹⁰Also known as "Marek's horn"

the physical point for quark masses falls inside the first order phase transition region. This would determine the existence of a critical point (T_C, μ_C) which separates a first order phase transition region at $\mu > \mu_C$ and a smooth cross-over region at $\mu < \mu_C$.

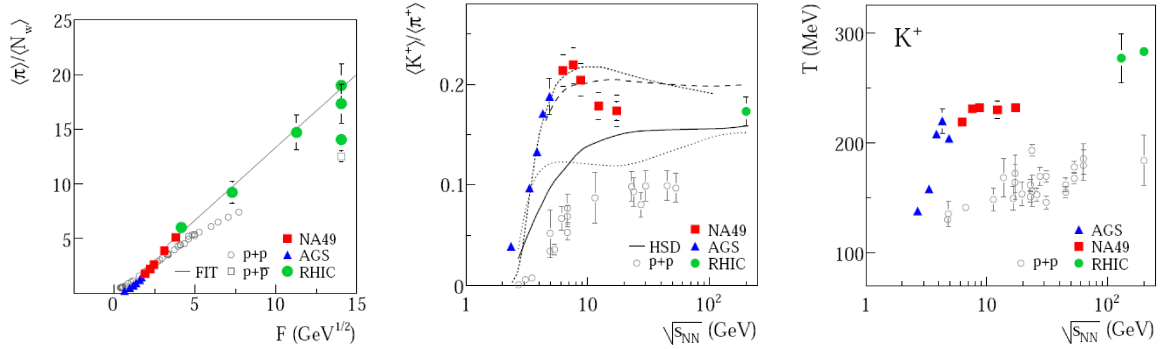


Figure 1.26: Left: Energy dependence of the mean pion multiplicity per wounded nucleon (the *kink*). Middle: Energy dependence of the $\langle K^+ \rangle / \langle \pi^+ \rangle$ ratio (the *horn*). Right: Energy dependence of the inverse slope parameter T for K^+ spectra (the *step*). Figures and data are from [64] and references therein.

The exact location of the critical point is not yet known but it has been speculated that it lies in the phase space reachable at lower SPS energies ($5 < \sqrt{s_{NN}} < 8$ GeV). Lattice QCD calculations suggest that the critical chemical potential μ_C might be approximately $\mu_C = 360$ MeV [69] or $\mu_C = 470$ MeV [70] which might be reachable at the above mentioned energies. Figure 1.26 suggest discontinuities in the excitation functions of hadronic observables measured in nucleus-nucleus collisions compared to the nucleon-nucleon collisions [64]. The 4π pion yield normalized to the number of participant(wounded) nucleons, proportional to the entropy production, is at AGS energies lower for A+A collisions than for N+N collisions. The slope in the energy dependence is however steeper for A+A collisions so that at $\sqrt{s_{NN}} \sim 7$ GeV the $\langle \pi \rangle / \langle N_w \rangle$ ratio becomes higher than the one for N+N collisions. The excitation function of the $\langle K^+ \rangle / \langle \pi^+ \rangle$ ratio, and also the strangeness ratio E_S (see figure 1.24) show a steep increase with a sharp maximum at $\sqrt{s_{NN}} \sim 7$ GeV followed by a decrease and a flattening behaviour toward RHIC energies. The inverse slopes of kaons show a sharp increase at AGS energies, then a flat region at SPS followed by another increase in temperature at RHIC energies. This behaviour resembles the behaviour of intensive thermodynamical quantities at a phase transition in a macroscopic system.

Although evidence of the collision energy range where the critical point might be accessible exist, its exact location in the phase diagram is still unclear from both a theoretical and experimental point of view. The search for the critical point is limited experimentally due to the fixed dynamical phase trajectories available in heavy ion collisions. An attempt to find the optimum collision energy where the decomposed nuclear matter spends maximum time in the phase coexistence region has been carried out in [72] by using a large variety of theoretical models. It was found that despite of the very different theoretical approaches the models are in good agreement on the energy and baryonic densities reached during nuclear collisions (see figure 1.27). The main conclusion was that the optimal conditions for exploring the hadronization phase transition and the critical point lies in the energy range $3.6 < \sqrt{s_{NN}} < 6.4$ GeV.

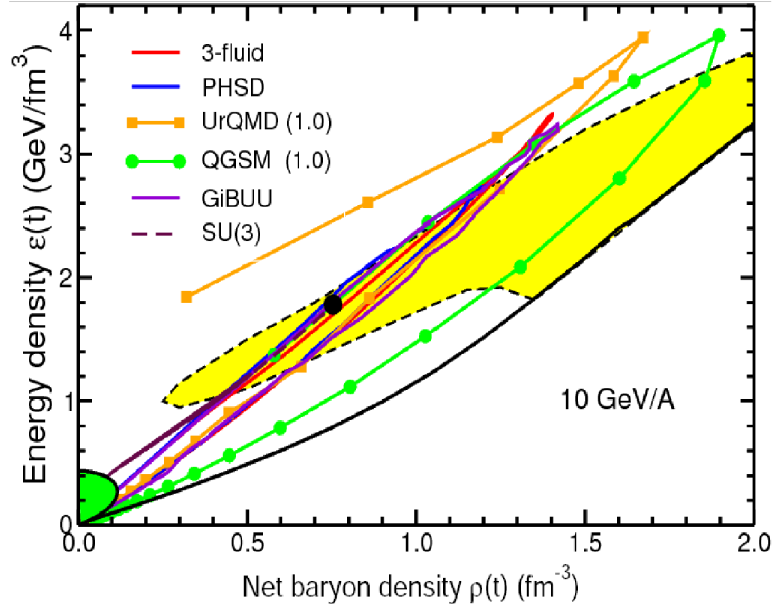


Figure 1.27: Phase trajectories $(\rho_B(t), \varepsilon(t))$ at the center of head-on Au+Au collisions at $\sqrt{s_{NN}} = 4.7$ GeV from several dynamical models. The hadronic freeze-out is indicated at the lower left of the figure while the dashed contour denotes the phase coexistence region as obtained in reference [71]. The markers in the figure represent time steps in the collision evolution starting with 1 fm/c and continuing up to 12 fm/c with 1 fm/c time intervals. Figure from [72].

1.4 Kaon and pion production in relativistic nuclear collisions

The production of mesons is an important observable in nuclear collisions at all energies. At intermediate to high energies, the production of kaons and pions play a key role in describing the hot and dense fireball created during the collision. The strange quark has a mass comparable to the characteristic temperatures of the nuclear fireball ($m_s = 104_{-34}^{+26}$ MeV) [2] so it is the only quark except u and d quarks to be produced copiously. The kaons are the main strange quark carriers and pions are the main light quark carriers (u and d) at these energies so they are important for finding one of the predicted signals of the formation of quark-gluon plasma, strangeness enhancement (described in section 1.3.6). The $\langle K \rangle / \langle \pi \rangle$, K/π , $\langle \pi \rangle / N_W$ ratios dependence on energy and system size but also their event-by-event fluctuations [73] are important tools for the search of the critical point in the QCD phase diagram.

The experimental part of this thesis is dedicated to the measurement of rapidity and collision centrality dependent meson ratios in Au+Au collisions at $\sqrt{s_{NN}} = 62.4$ GeV. The measurements were made using the BRAHMS experimental setup which will be presented in chapter 4. Hence, it is useful to review the context in which these data appears. Previous data from lower AGS and SPS experiments together with data from top RHIC energy will be summarized in the remainder of this chapter.

1.4.1 Production mechanisms

In order to understand the excitation function of kaon and pion yields together with their ratios, it is useful to disentangle some of the production mechanisms. The observed meson yields and their ratios are a superposition of the contributions of each of these mechanisms.

Hadronic scatterings

At intermediate energies, e.g. $\sqrt{s_{NN}} \sim 5$ GeV, a big share of mesons are produced through hadronic scatterings. Since the nuclei are composed of neutrons and protons the dominant reactions are the ones producing pions like

$$N + N \rightarrow \text{pions/kaons} + X.$$

In a heavy nucleus there are more neutrons(udd) than protons(uud) (e.g. $Z(\text{Au})=79$, $A(\text{Au})=197$) which means that the production of negatively charged pions($d\bar{u}$) is favoured compared to the positive pions($u\bar{d}$). At lowest AGS energy, $E_{lab} = 2A\text{GeV}$, the measured $\langle\pi^-\rangle/\langle\pi^+\rangle$ ratio is 1.81 [74] which is very close to the theoretical limit, 1.95, calculated from the neutron excess in Au+Au collisions combined with the pions branching ratios [75]. Going higher with energy, the contribution of this effect¹¹ decreases so that it should asymptotically reach 1.

Kaons can be produced through hadronic channels like

$$\begin{aligned} N + N &\rightarrow K^+ + \Lambda(\Sigma) + N \quad (\text{associated production}) \\ N + N &\rightarrow K^+ + K^- + N + N \quad (\text{pair production}) \end{aligned}$$

$K^+(\bar{s}u)$ mesons require only an $s\bar{s}$ pair and recombination of quarks to be formed while $K^-(s\bar{u})$ mesons need an additional $u\bar{u}$ pair. Moreover, in baryon rich environments, the negative kaons can be absorbed through a strangeness exchange reaction ($K^- + n \rightarrow \pi^- + \Lambda$) while for the positive kaons this is more difficult since anti-baryons are more scarce. This means that in hadronic scatterings in matter with a positive net-baryon content there will always be an asymmetry leading to an enhancement of K^+ mesons compared to K^- mesons.

Resonance decay

During the evolution of a nuclear collision, a large number of resonances are formed as a consequence of both quark gluon plasma decay through coalescence of quarks and hadronic scatterings. All of the unstable resonances produce pions giving significant contributions to the pion yields especially at low transverse momentum [76]. The most abundant resonances are mesonic resonances like ρ , η , ω , ϕ , η' , $K(892)$ or baryonic resonances like Δ , N^* , Λ , Σ , Ξ , Ω with their excited states. There are very few decay channels producing kaons, e.g. $\Omega^- \rightarrow \Lambda + K^-$.

QGP decay and jet fragmentation

At higher SPS and RHIC energies, the densities and temperatures reached during the collision evolution are expected to be high enough for a deconfined state of nuclear

¹¹Also called *isospin effect*

matter to be formed. In consequence many degrees of freedom are opened increasing the phase space available for particle creation and the number of produced mesons greatly surpasses the number of baryons. At $\sqrt{s_{NN}} = 200$ GeV at mid-rapidity a nearly perfect particle/anti-particle symmetry was observed suggesting that the big majority of particles are produced through pair creation from the chromo-electric fields or strings. Models describing the fragmentation of strings into sub-strings and (di-)quark pairs can be found in [77, 78]. The effect of isospin asymmetry for pions or the asymmetry in kaon production are nearly vanishing at this energy ($\pi^-/\pi^+ = 1$, $K^-/K^+ \sim 0.95$ at mid-rapidity [76]). At higher rapidity ($y = 3$), where the net-baryon content increases to $dN/dy(B - \bar{B}) \sim 25$ [26] and the density of the fireball decreases ($N_\pi(y=0)/N_\pi(y=3) \sim 2.5$), the K^-/K^+ ratio drops to a value of ~ 0.7 [29].

Particles can be also formed from the fragmentation of jets either in vacuum or in medium. Since the particles created from in-medium jet fragmentation are thermalized, most of the "visible"¹² jet contribution to particle yields comes from jets being emitted from the surface of the fireball or from un-thermalized N+N collisions from the nuclear periphery. The jet contribution is expected to give different particle ratios and yields, similar or close to p+p collisions. See references [79] for more on core-corona models.

1.4.2 Energy and rapidity dependence of yields and ratios

As the collision energy has increased with the advent of newer relativistic heavy-ion accelerators, from AGS energies ($\sqrt{s_{NN}} \sim 4$ GeV) to those achieved with the SPS ($\sqrt{s_{NN}} \leq 17.3$ GeV) and now with RHIC ($\sqrt{s_{NN}} \leq 200$ GeV), the fireball generated in heavy-ion collisions has been found to evolve from one that is baryon rich to one dominated by mesons [80, 81, 82, 76]. This change is evident in the rapid increase

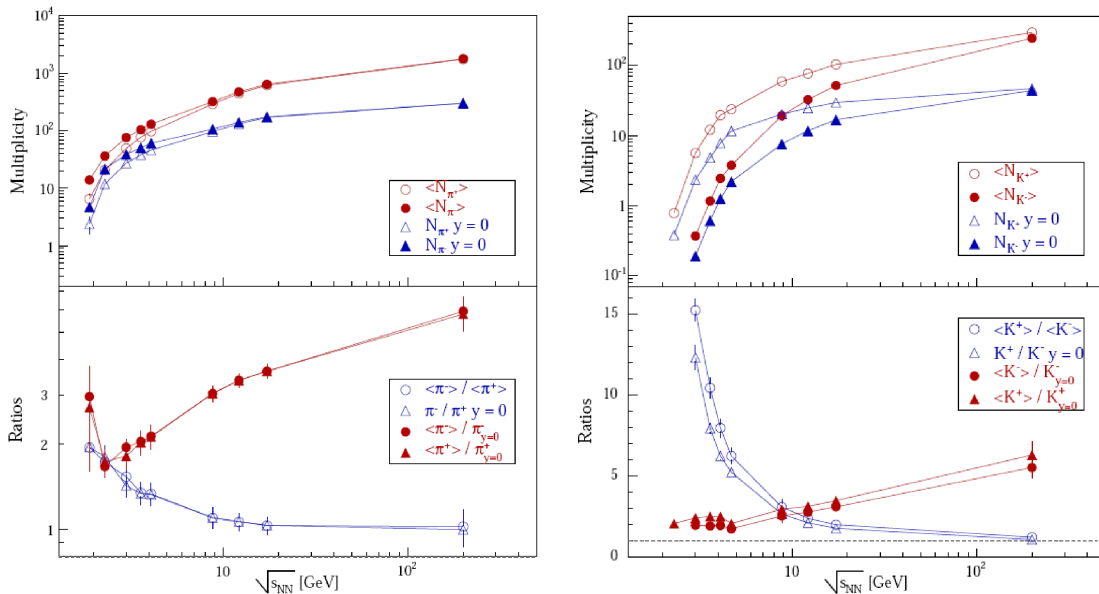


Figure 1.28: Energy systematics of charged pions (left) and kaons (right). Pion data is from [74] (AGS), [82] (SPS) and [76] (RHIC-BRAHMS). Kaon data is from [83, 84, 85] (AGS), [82] (SPS) and [76] (RHIC-BRAHMS). The figure is from [86].

¹²By "visible" jet contribution one can understand those particles which keep some kinematic memory of their creation which is reflected in particle correlations, e.g. back-to-back correlations

of central rapidity densities of emitted mesons and the concurrent change of the net-baryon peak (see left panel of figure 1.8), which gradually moves from mid-rapidity (AGS and SPS) [87, 88] towards forward rapidity (RHIC) [26], leaving a relatively net-baryon poor region at mid-rapidity at the highest RHIC energy. Figure 1.28 shows the increase of both mid-rapidity densities and 4π integrated yields of mesons with energy.

The particle/anti-particle ratios for mesons (see figure 1.28) have a drastic change with energy as well. At AGS energies, the isospin effect in the production of charged pions is dominant leading to a $\pi^-/\pi^+ \sim 2$. The asymmetry in the production of charged pions gradually diminishes with increasing energy so that at top SPS energy the π^-/π^+ ratio is already almost 1. The K^+/K^- ratio measured at mid-rapidity shows also a steep decrease from ~ 15 at lowest AGS energy to ~ 1.05 at top RHIC energy. This is an indication that the dominant production mechanism is pair creation.

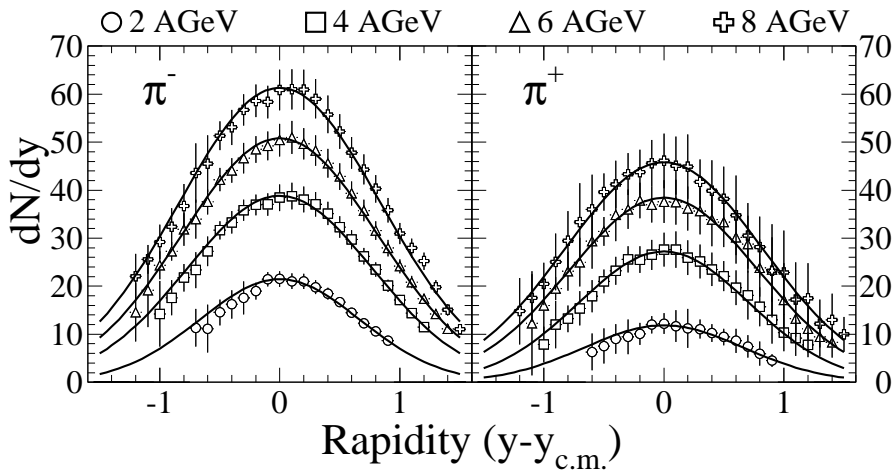


Figure 1.29: π^\pm rapidity density distributions at AGS energies. Fits are Gaussian parametrizations. Figure from [74]

The rapidity density of produced particles reflects the collision dynamics but also the energy densities reached in central region. From AGS to SPS energies, the dN/dy rapidity distributions for most of the newly created particles are almost Gaussian shaped and centered on mid-rapidity (see figures 1.29 and 1.30). The width and the amplitude of the distributions for a given particle species is increasing with energy meaning that more and more energy is deposited in the collision region and made available for particle creation. At the same time, the protons, as carriers of the initial beam energy, have decreasing densities at mid-rapidity leaving, at top RHIC energy, an almost net-baryon free region at mid-rapidity (see figure 1.8).

It is interesting to observe that at a given energy the shape of the dN/dy distribution is different for different particle species. In figure 1.30 it can be seen that in the whole range of SPS energies, the width of K^+ particles is always larger than the width of K^- or ϕ particles. This is because K^+ particles are created also through the associated production mechanism in a dense baryon environment which, at SPS energies, shifts toward high rapidities. The K^- and ϕ particles are composed only of newly created quarks so their production rate dramatically decreases when moving away from the hot and dense region found at mid-rapidity. The rapidity density of Λ baryons has a suggestive behaviour also. Their rapidity density profile is strongly correlated with the

baryon rapidity density profile. Λ baryons carry an s quark and a di-quark ud which is more probable to be picked up from a region with high baryon densities.

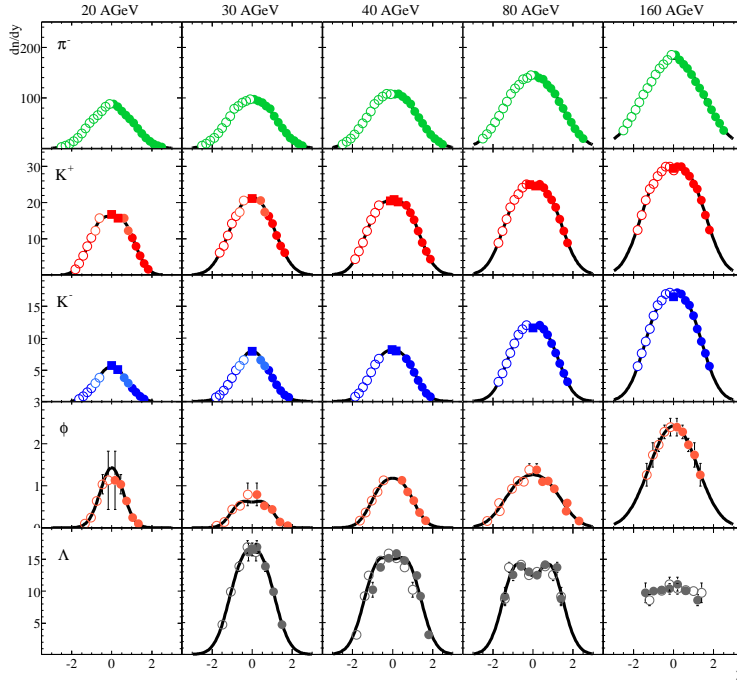


Figure 1.30: Particles rapidity density distributions at AGS energies. Figure from [89].

The K/π ratios are an important observable for studying strangeness creation. Assuming approximate charge symmetry,

$$\langle K^+ \rangle + \langle K^- \rangle = \langle K^0 \rangle + \langle \bar{K}^0 \rangle, \quad (1.6)$$

and the fact that most of the anti-strange quarks form kaons it is straightforward to see that the yield of K^+ kaons is approximately proportional to the total strangeness created in a system. The approximation is worsening with increasing energies due to increasing yields of strange anti-baryons. Figure 1.31 shows the evolution of the charged K/π ratios measured at mid-rapidity. The K^-/π^- ratio has a monotonic increase with energy almost reaching the value of its positive counterpart at top RHIC energy. K^+/π^+ ratio increases sharply between the kaon production threshold energy and low SPS energies where it has a maximum at ~ 0.25 and then falls smoothly towards RHIC energies. The peak at low SPS energies was interpreted as a signal of the onset of deconfinement as described in the previous section.

1.4.3 K/π ratios dependence on system size and geometry

The ratio of strange to non-strange particles measured in all A+A collisions shows an enhancement compared to the N+N reactions considered at the same energy. This enhancement depends on energy [90, 88], system size [81, 91] and collision geometry [92, 91].

Figure 1.32 shows the K/π ratios measured in a range around mid-rapidity in different colliding systems starting from p+Be, the lightest, up to Au+Au, the heaviest. The energy is $E_{beam} = 11.6 A \text{ GeV}/c$ for Au+Au collisions and $E_{beam} = 14.6 A \text{ GeV}/c$

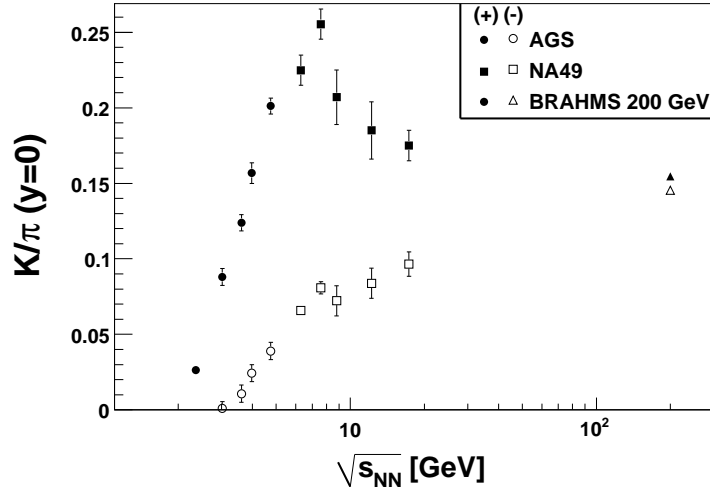


Figure 1.31: K/π ratios at mid-rapidity in central nucleus-nucleus collisions as a function of energy.

for the other systems. The K^+/π^+ ratio shows quite a steep increase with the system size. There is also a hint that the K^-/π^- ratio might also show a rise with system size. These facts were interpreted as the result of many hadronic rescatterings in a baryon rich medium which increases the yields of strange particles [81].

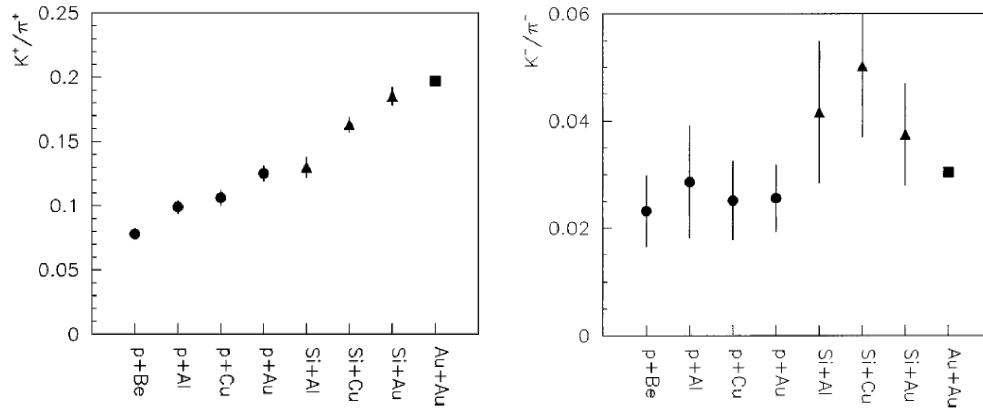


Figure 1.32: K/π ratios at mid-rapidity for different colliding systems at top AGS energy. The Au+Au data is at $E_{beam} = 11.6A\text{GeV}/c$ while p+A and Si+A data is at $E_{beam} = 14.6A\text{GeV}/c$. Figures are from [81].

Figure 1.33 shows a wide selection of data on mid-rapidity K^-/π^- ratios as a function of both number of participants and energy. There are a few remarkable things which can be noticed in this plot. **First** of all one can see that in the most central collisions of the heaviest systems (Au+Au and Pb+Pb) there is a definite *monotonic increase of the K^-/π^- with energy*. **Secondly**, at the same energy and colliding system, the K^-/π^- ratio *increases with the number of participant nucleons*, that is participant volume size. And **thirdly**, at the same number of participants and the same energy the K^-/π^- ratio *depends on the geometry of the collision*, e.g., the K/π ratios measured in peripheral Pb+Pb collisions at top SPS energy are lower than the

same ratios measured at the same energy and number of participants in central C+C or Si+Si collisions where the number of binary collisions per participant is higher.

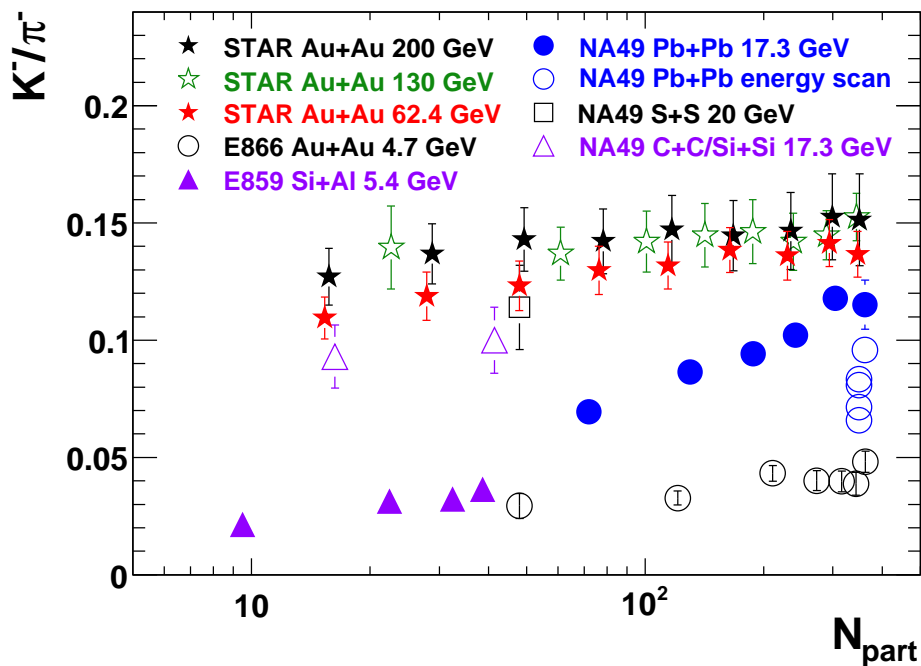


Figure 1.33: K^-/π^- ratio at mid-rapidity as a function of the number of participants and energy. Figure and data from [93] and references therein.

Most of the already know experimental facts described in this section will be discussed in chapter 7 together with the results obtained in the present work.

Chapter 2

Effective equation of state in microscopic transport models

This chapter is based on the work published in [94] and is dedicated to the study of the formation of locally equilibrated hot and dense nuclear matter in heavy ion collisions at beam energies from $11.6A$ GeV up to $160A$ GeV in the fixed target reference system. The study is made within the approach of the microscopical transport models UrQMD [95, 96] and QGSM [97].

The collisions at top RHIC energy, $\sqrt{s_{NN}} = 200$ GeV, or at the energy of CERN's Large Hadron Collider (LHC) $\sqrt{s_{NN}} = 5.5$ TeV probe the domain of high temperatures and low net baryon densities, while lower temperatures and much higher baryon densities should be produced in heavy-ion collisions at relatively moderate energies around $E_{lab} = 30A$ GeV, accessible for future GSI's Facility for Antiproton and Ion Research (FAIR) accelerator [98]. It is most likely, that the matter under such extreme conditions is composed of partons, *i.e.* quarks and gluons, in the phase of quark-gluon plasma (QGP), colored tubes of chromo-electric field (or strings), hadrons and their resonances. The question about the equation of state (EOS) of such a substance remains still open.

The highly anticipated transition between the hot hadron gas (HG) and the QGP is of first order for relatively dense baryonic substances only. With rising temperature and dropping baryon density and baryo-chemical potential the transition becomes of second order at the so-called tricritical point (TCP). After that it is transformed to a smooth crossover. Although the theory cannot localize the position of the TCP on T - μ_B plane, lattice quantum chromodynamic (LQCD) calculations indicate that it might be somewhere between the points with $T \approx 160$ MeV and $\mu_B = 360$ MeV [69] or $\mu_B = 470$ MeV [70]. These values are close to the chemical freeze-out parameters obtained from the analysis of heavy-ion collisions at energies between $E_{lab} = 11.6A$ GeV and $E_{lab} = 40A$ GeV within the statistical models [99, 63, 100]. They are close also to the temperatures and baryo-chemical potentials in the central zone of heavy-ion reactions generated by microscopic transport models [101, 102, 103, 104, 105]. Another interesting feature of the collisions at bombarding energies around $40A$ GeV is the transition from a baryon-dominated matter to a meson-dominated one. According to microscopic models, in Au+Au collisions at top AGS energy nearly 70% of the total available energy is deposited in the baryonic sector. At top SPS energy mesons are carrying 70% of the total energy, and at $E_{lab} \approx 40A$ GeV the energy parts of mesons and baryons are roughly the same. Hence the particle composition of the fireball is changing with center-of-mass energy.

Two transport Monte Carlo models were employed: the ultrarelativistic quantum molecular dynamics (UrQMD) model and the quark-gluon string model (QGSM). The models use different mechanisms of string excitation and fragmentation. UrQMD relies on the longitudinal excitation, while the color exchange scheme is employed in QGSM. Central gold-gold collisions with zero impact parameter $b = 0$ fm were simulated at bombarding energies $E_{lab} = 11.6, 20, 30, 40, 80$ and 160 AGeV. Microscopic parameters related to quantities conserved in strong interactions, namely, the total energy, the net baryon charge, and the net strangeness extracted for a certain volume of the reaction were inserted into a system of nonlinear equations to obtain temperature, baryon chemical potential and strangeness chemical potential of an ideal hadron gas in equilibrium as described later in this chapter. If the yields and transverse momentum spectra of particles obtained in microscopic simulations are close to those provided by the statistical model, the matter in the cell is considered to be in the vicinity of equilibrium. Then its equation of state and other thermodynamic characteristics can be derived and studied.

Relaxation of hot matter to equilibrium in the central cell of central heavy-ion collisions has been studied within the UrQMD model in [101, 102, 103, 104, 105] for energies ranging from $E_{lab} = 11.6$ AGeV at AGS to $\sqrt{s_{NN}} = 200$ GeV at RHIC, and, partially, within the QGSM [106, 107]. The size of the cell once chosen has been fixed throughout the system evolution. In the present work the analysis of the early stage is modified in order to trace the expansion of an initially small volume of homogeneity just after its formation. The central volume was further sub-separated into smaller cells embedded within each other ("russian-doll" structure). The transition of analysis from the smaller cell to the larger one was allowed if, and only if, the energy densities in both cells were the same. Regardless of the microscopic model applied for the actual calculations, the formation of (quasi)equilibrated state in the central cell at all bombarding energies in question is observed. The matter in the cell expands isentropically with constant entropy-per-baryon ratio. The isentropic regime arises even before the chemical and thermal equilibration takes place. Due to coarse-graining of the central volume characteristic, kinks in the temperature versus baryochemical potential phase diagrams are found for both model simulations. This feature has not been seen in the previous studies because of the averaging of energy and baryon densities, in fact non-isotropically distributed within the relatively large volume.

2.1 Characteristics of UrQMD and QGSM

2.1.1 Similarities between the two models

Both UrQMD and QGSM are formulated as Monte-Carlo event generators allowing to perform a careful analysis of the measurable quantities by introducing all necessary experimental cuts. The models are designed to describe hadronic, hadron-nucleus, and nuclear collisions in a broad energy range. In the hadronic sector both models treat the production of new particles via formation and fragmentation of specific colored objects, strings. Strings are uniformly stretched, with constant string tension $\kappa \approx 1$ GeV/fm, between the quarks, diquarks and their antistates. The excited string is fragmenting into pieces via the Schwinger-like mechanism of $q\bar{q}$ and $qq - \bar{q}\bar{q}$ pair production, and the produced hadrons are uniformly distributed in the rapidity space.

To describe hadron-nucleus ($h + A$) and nucleus-nucleus ($A + A$) collisions the

momenta and positions of nucleons in the nuclei are generated according to the Fermi momentum distribution and the Wood-Saxon density distribution, respectively. The black disk approximation is adopted as criterion of interaction. It means that two hadrons can interact both elastically and inelastically if the distance d between them is smaller than $\sqrt{\sigma/\pi}$, where σ is the total cross section. Tables of the experimentally available information, such as hadron cross sections, resonance widths and decay modes, are implemented in the models. If this information is lacking, the one-boson exchange model, detailed balance considerations and isospin symmetry conditions are employed. The propagation of particles is governed by Hamilton equation of motion, and both models use the concept of hadronic cascade for the description of $h + A$ and $A + A$ interactions. Note that such a rescattering procedure is very important in the case of relativistic heavy-ion collisions and is necessary for the thermalization of the fireball. Due to the uncertainty principle newly produced particles can interact further only after a certain *formation time*. However, hadrons containing valence quarks can interact immediately with the reduced cross section $\sigma = \sigma_{qN}$. The Pauli principle is taken into account via the blocking of the final state, if the outgoing phase space is occupied. The Bose enhancement effects are not implemented yet.

2.1.2 Differences

Differences between the two models for hadronic interactions exists in three collision stages. The first stage is the formation of strings. UrQMD belongs to the group of models which are based on the classical FRITIOF model [108], while QGSM uses the Gribov Reggeon field theory (RFT) [109, 110]. In the FRITIOF model the longitudinal excitation of strings is employed, and the string masses arise from momentum transfer. In the Gribov-Regge models the string masses appear due to the color exchange mechanism, and strings are stretching between the constituents belonging to different hadrons. Longitudinal excitation of strings is also possible in the QGSM. This mechanism describes the processes of single and double diffraction.

The second stage concerns the string fragmentation. The Lund JETSET routine [78], used in the UrQMD, assumes that the string always breaks into a sub-string and a particle on a mass shell. In the QGSM the Field-Feynman algorithm [77] with independent jets is applied. Therefore, the fragmentation functions which determine the energy, momentum, and the type of the hadrons produced during the string decay, are different in the models.

Last but not least, the two models do not use the same tables of hadrons, chosen as discrete degrees of freedom. Whereas the UrQMD contains 55 baryon and 32 meson states together with their anti-states and isospin projections, the QGSM takes into account octet and decuplet baryons, and nonets of vector and pseudoscalar mesons, as well as their anti-particles. Further details can be found in [95] and [97]. Recently, the QGSM has been extended by the implementation of a parton recombination mechanism [107]. Since parton recombination plays a minor role for nuclear collisions at intermediate energies, the whole analysis of the relaxation process is done for the standard QGSM. The basic underlying principles and designs of the models are quite far from each other. By using both the UrQMD and QGSM for studies of the relaxation process in a broad energy range one can expect that the model-dependent effects, caused by application of a particular event generator, will be significantly reduced.

2.2 Statistical model of an ideal hadron gas

For our analysis of the thermodynamic conditions in the cell we use a conventional statistical model (SM) of an ideal hadron gas formulated in pioneering works of Fermi [111] and Landau [112]. The statistical approach was successfully applied to the description of particle production in heavy-ion collisions from AGS to RHIC energies (see [63] and references therein). In chemical and thermal equilibrium the distribution functions of hadron species i at temperature T read (in units of $c = k_B = \hbar = 1$)

$$f(p, m_i) = \left[\exp \left(\frac{\epsilon_i - \mu_i}{T} \right) \pm 1 \right]^{-1}, \quad (2.1)$$

where p , m_i , $\epsilon_i = \sqrt{p^2 + m_i^2}$, and μ_i are the full momentum, mass, energy, and the total chemical potential of the hadron, respectively. The "+" sign is for fermions and the "-" sign for bosons. Since in equilibrium the chemical potentials associated to nonconserved charges vanish, the total chemical potential assigned to the i -th hadron is a linear combination of its baryon chemical potential μ_B and strangeness chemical potential μ_S

$$\mu_i = B_i \mu_B + S_i \mu_S, \quad (2.2)$$

with B_i and S_i being the baryon charge and the strangeness of the particle, respectively. The isospin chemical potential (or, alternatively, chemical potential associated with electric charge) is usually an order of magnitude weaker than μ_B and μ_S . Therefore, the dependence on this potential is disregarded in eq. (2.2). Then, particle number density n_i and energy density ϵ_i are simply moments of the distribution function

$$n_i = \frac{g_i}{(2\pi)^3} \int f(p, m_i) d^3p, \quad (2.3)$$

$$\epsilon_i = \frac{g_i}{(2\pi)^3} \int \sqrt{p^2 + m_i^2} f(p, m_i) d^3p, \quad (2.4)$$

with g_i being the spin-isospin degeneracy factor of hadron i . The partial hadron pressure given by the statistical model reads

$$P_i = \frac{g_i}{(2\pi)^3} \int \frac{p^2}{3(p^2 + m_i^2)^{1/2}} f(p, m_i) d^3p. \quad (2.5)$$

The integrals in Eqs. (2.3)–(2.5) can be calculated numerically. Another way is to use a series expansion of Eq. (2.1) in the form [112]

$$f(p, m_i) = \sum_{n=1}^{\infty} (\mp 1)^{n+1} \exp \left(-n \frac{\epsilon_i - \mu_i}{T} \right), \quad (2.6)$$

which is inserted into Eqs. (2.3)–(2.5). After some straightforward calculations one gets

$$n_i = \frac{g_i m_i^2 T}{2\pi^2} \sum_{n=1}^{\infty} \frac{(\mp 1)^{n+1}}{n} \exp \left(\frac{n\mu_i}{T} \right) K_2 \left(\frac{nm_i}{T} \right), \quad (2.7)$$

$$\begin{aligned} \epsilon_i &= \frac{g_i m_i^2 T^2}{2\pi^2} \sum_{n=1}^{\infty} \frac{(\mp 1)^{n+1}}{n^2} \exp \left(\frac{n\mu_i}{T} \right) \\ &\times \left[3K_2 \left(\frac{nm_i}{T} \right) + \frac{nm_i}{T} K_1 \left(\frac{nm_i}{T} \right) \right], \end{aligned} \quad (2.8)$$

$$P_i = \frac{g_i m_i^2 T^2}{2\pi^2} \sum_{n=1}^{\infty} \frac{(\mp 1)^{n+1}}{n^2} \exp \left(\frac{n\mu_i}{T} \right) K_2 \left(\frac{nm_i}{T} \right), \quad (2.9)$$

where K_1 and K_2 are modified Hankel functions of first and second order, respectively. The first terms in Eqs. (2.7)–(2.9) correspond to the case of Maxwell-Boltzmann statistics, which neglects the ± 1 term in the particle distribution function (2.1).

The entropy density in the cell is represented by a sum over all particles of the product $f(p, m_i) [1 - \ln f(p, m_i)]$ integrated over all possible momentum states

$$s = - \sum_i \frac{g_i}{2\pi^2} \int_0^\infty f(p, m_i) [\ln f(p, m_i) - 1] p^2 dp. \quad (2.10)$$

According to the presented formalism, the hadron composition and energy spectra in equilibrium are determined by just three parameters, namely, the temperature, the baryon chemical potential, and the strangeness chemical potential. In order to define values of T , μ_B , and μ_S one has to obtain the total energy density ε , baryon density ρ_B and strangeness density ρ_S for a given volume from microscopic model calculations, and insert them as input parameters into the system of nonlinear equations

$$\rho_B = \sum_i B_i n_i(T, \mu_B, \mu_S), \quad (2.11)$$

$$\rho_S = \sum_i S_i n_i(T, \mu_B, \mu_S), \quad (2.12)$$

$$\varepsilon = \sum_i \varepsilon_i(T, \mu_B, \mu_S), \quad (2.13)$$

where $n_i(T, \mu_B, \mu_S)$ and $\varepsilon_i(T, \mu_B, \mu_S)$ are given by Eqs. (2.3)–(2.4). Since the particle data tables implemented in the microscopic models contain different numbers of hadrons, two versions of the SM with properly adjusted lists of hadron species are used, i.e. the number of hadronic degrees of freedom in the macroscopic model should correspond to that in the microscopic model. To decide whether or not the equilibrium is reached, the criteria of the equilibrated state for open systems, discussed in the next section, should be applied.

2.3 Criteria of thermal and chemical equilibrium

Criteria of local equilibrium for open systems were formulated in [102], and we recall them briefly. Compared to a non-equilibrium state, the equilibrium is characterized by the absence of collective effects, like flow of matter or flow of energy. The fireball produced in heavy-ion collisions is always expanding both radially and longitudinally. Therefore, the centrally placed symmetric cell is chosen to diminish effects caused by nonzero collective velocity of any asymmetric or asymmetrically located cell. The cell should be neither too small to allow for the statistical treatment, nor too large, - otherwise the homogeneous distribution of matter may not be reached. Previous studies [101, 102, 103, 104, 106] found that the cubic cell of volume $V = 125 \text{ fm}^3$ centered around the center-of-mass of colliding gold-gold or lead-lead nuclei is well suited for such an analysis. Clearly, the relaxation to local equilibrium cannot occur earlier than at a certain time needed for the Lorentz contracted nuclei to pass through each other and leave the cell

$$t^{eq} \geq \frac{2R}{\gamma\beta} + \frac{\Delta z}{2\beta}. \quad (2.14)$$

Here R is the nuclear radius, Δz is the cell length in longitudinal direction, β is the velocity of nuclei in the center of mass frame, and $\gamma = (1 - \beta^2)^{-1/2}$. Quite unexpectedly,

the reduction of the longitudinal size of the cell from 5 fm to 1 fm does not automatically imply a faster equilibration in the smaller cell: the transition times are practically the same [103]. This means that the transition to equilibrium takes place simultaneously within a relatively large volume along the beam axis.

Isotropy of the pressure gradients is a necessary condition for kinetic equilibration. Diagonal elements of the pressure tensor $P_{\{x,y,z\}}$ are calculated from the virial theorem [113]

$$P_{\{x,y,z\}} = \frac{1}{3V} \sum_{i=h} \frac{p_{i\{x,y,z\}}^2}{(m_i^2 + p_i^2)^{1/2}}, \quad (2.15)$$

where V , m_i and p_i are the volume of the cell, the mass and the momentum of the i th hadron, respectively. Figure 2.1 depicts the convergence of the transverse pressure in the cell to the longitudinal one in the UrQMD and the QGSM calculations. Both models claim that the pressure becomes isotropic at $t \leq 10$ fm/ c after beginning of the collision. The time of convergence decreases with rising bombarding energy. The pressure calculated according to the statistical model is plotted onto the results of microscopic simulations also. The agreement between microscopic and macroscopic calculations is good for a period of about $t = 8 - 10$ fm/ c . Then the matter in the cell becomes quite dilute, and the collision rate is not sufficiently high to maintain equilibrium anymore. However, the isotropy of pressure can be obtained, for instance, in a spherically expanding system of non-interacting particles. To exclude such a situation from the analysis one has to impose two additional criteria concerning thermal and chemical equilibrium.

For a closed system in equilibrium the distribution functions of particles are given by eq. (2.1) with an unique temperature, so the hadron composition and energy spectra are fixed. In open systems neither the energy density nor the number of particles is conserved. Therefore, the snapshots of hadron abundances and energy spectra obtained at a certain time t should be compared with those corresponding to an ideal gas in equilibrium. The technical procedure is simple. At the very beginning, the pressure gradients in transverse and longitudinal directions are considered. If the pressure isotropy is restored, say, within 10%-limit of accuracy, the densities of conserved quantities, *i.e.* energy, baryon charge, and strangeness, determined microscopically, (i) should be used as an input to Eqs. (2.11)-(2.13). The solution of this system of equations (ii) provides us with values of the chemical temperature, baryon chemical potential, and strangeness chemical potential which fully determine the composition and spectra of particles. By (iii) a comparison of microscopic and macroscopic yields of the most abundant hadronic species one can decide whether or not the chemical equilibrium occurs, whereas (iv) the energy spectra of these hadrons should possess a common slope corresponding to $1/T$ (thermal equilibrium). The similarity of the particle distributions means that our system is in the vicinity of equilibrium. At each subsequent time step the procedure described by (i)-(iv) is repeated.

2.4 Relaxation to equilibrium

2.4.1 Yields and energy spectra

The yields of main hadron species, *i.e.* $N, \Delta, \Lambda + \Sigma, \pi, K$ and \bar{K} in the central cell are shown in figure 2.2 for central Au+Au collisions at $E_{lab} = 40A$ GeV. For all particles, except pions, the agreement between the microscopic and macroscopic estimates

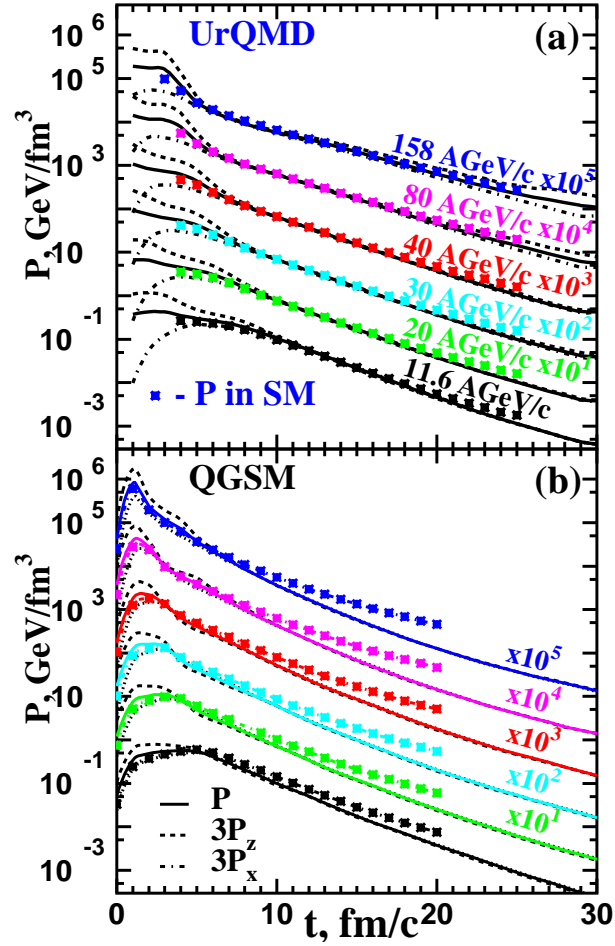


Figure 2.1: The longitudinal ($3P_z$, dashed curves) and the transverse ($3P_x$, dash-dotted curves) diagonal components of the microscopic pressure tensor in the central 125 fm^3 cell in (a) UrQMD and (b) QGSM calculations of central Au+Au collisions at energies from 11.6 AGeV to 158 AGeV . Asterisks indicate the pressure given by the statistical model and solid lines show the total microscopic pressure.

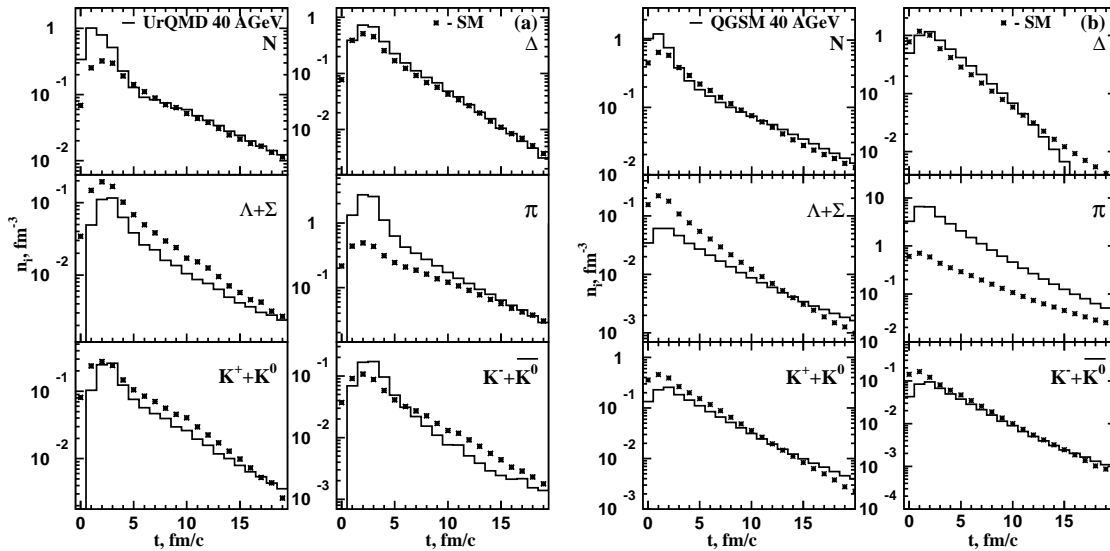


Figure 2.2: Evolution of yields of hadron species in the central cell of volume $V = 125 \text{ fm}^3$ in (a) UrQMD and (b) QGSM calculations (histograms) of central Au+Au collisions at 40A GeV. Asterisks denote the results of the statistical model.

at $t \geq 9 \text{ fm}/c$ is good. Compared to the microscopic models, the number of pions is underestimated in the SM. The pion excess comes from the many-body decaying resonances, such as N^* , Δ^* , Λ^* , ω , etc, and strings. After $t = 10 - 13 \text{ fm}/c$ the many-body processes play just a minor role, and the pion multiplicity slowly converges to the equilibrium value. It looks like all species of the hadronic cocktail, except pions, are not far from the chemical equilibrium. It is well-known that the pure statistical model of an ideal hadron gas, which does not include effective chemical potential for pions or weak decays, systematically underestimates the pion yields compared to experimental data. Nevertheless, the excess of pions in a model with short table of resonances, QGSM, is quite significant. This circumstance should affect the thermal spectra of all hadrons, provided the thermalization is reached.

To verify how well the temperature is reproduced, the energy spectra $dN/4\pi p E dE$ are displayed in figure 2.3. The Boltzmann fit to particle distributions is performed, and the SM calculations are plotted onto the microscopic results also. Both in UrQMD and in QGSM the energy spectra agree well with the exponential form of the Boltzmann distributions. Despite the good quality of the fit, the abundance of pions in particle spectrum leads to significant reduction of the effective temperature of the system within the QGSM calculations. Analytical estimates of the temperature drop are close to the temperatures extracted from the fit. It would be possible to diminish the pion yield by taking into account larger part of the resonance states, but our intention is to check the principal occurrence of the (quasi)equilibrium states in different microscopic models and to define the limits imposed on the effective equation of state. Note also, that a significant part of the pion spectrum seems to be softer compared to other hadronic species. These pions are coming mainly from the decays of resonances and experience too few elastic collisions, that are necessary for their thermalization. Since the hadronic matter in the central cell reaches the state of thermal equilibrium, one can apply the mathematical apparatus formulated in section 2.2 and, finally, obtain the anticipated EOS.

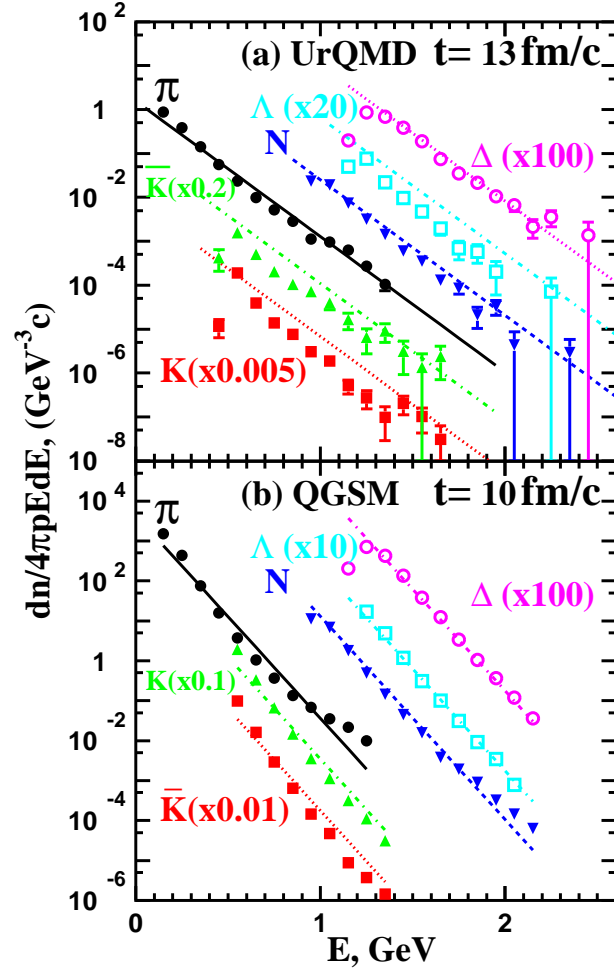


Figure 2.3: Energy spectra of N (\blacktriangledown), Λ (\square), π (\bullet), \bar{K} (\blacktriangle), K (\blacksquare), and Δ (\circ) in the central 125 fm^3 cell in (a) UrQMD and (b) QGSM calculations of central Au+Au collisions at 40 AGeV at $t = 13 \text{ fm}/c$ and $t = 10 \text{ fm}/c$, respectively. Lines show the results of the fit to Boltzmann distribution.

2.4.2 Evolution of the cell characteristics

According to the information provided by figures 2.1 - 2.3, the appropriate time to start the study of thermodynamic conditions in the cell is $t = 11$ fm/c for the reactions at $E_{lab} = 20$ AGeV and $t = 9$ fm/c for $E_{lab} = 40$ AGeV. The input parameters obtained in the microscopic model analysis are listed in tables 2.1 and 2.2 together with the

Time fm/c	$\varepsilon^{\text{cell}}$ MeV/fm ³	ρ_B^{cell} fm ⁻³	ρ_S^{cell} fm ⁻³	T MeV	μ_B MeV	μ_S MeV	P MeV/fm ³	s fm ⁻³	s/ρ_B^{cell}
11	464.2	0.210	-0.0143	144.5	450.5	92.7	59.6	2.97	14.16
	522.6	0.257	-0.0059	150.2	487.8	116.1	73.8	3.13	12.19
12	343.2	0.160	-0.0115	137.9	459.2	86.4	44.0	2.27	14.18
	385.7	0.197	-0.0051	141.9	498.1	109.4	53.1	2.40	12.16
13	255.2	0.124	-0.0093	131.5	469.5	80.4	32.6	1.75	14.15
	286.9	0.153	-0.0046	134.0	609.5	103.1	38.5	1.85	12.09
14	189.9	0.096	-0.0072	124.9	481.7	75.8	24.1	1.34	14.06
	214.2	0.117	-0.0035	127.2	515.9	97.1	28.2	1.43	12.22
15	143.9	0.075	-0.0064	119.2	492.8	68.6	18.1	1.05	13.97
	162.3	0.091	-0.0028	121.0	522.3	91.5	20.1	1.12	12.35
16	108.8	0.059	-0.0052	113.7	502.5	62.7	13.6	0.82	13.97
	125.4	0.072	-0.0025	115.4	529.2	85.4	15.9	0.89	12.43
17	83.6	0.046	-0.0043	108.7	511.0	57.0	10.4	0.65	14.02
	98.3	0.058	-0.0022	110.4	535.9	80.1	12.3	0.72	12.52
18	65.0	0.037	-0.0035	103.5	523.7	52.4	8.0	0.52	13.88
	78.1	0.047	-0.0019	105.9	541.3	75.4	9.6	0.59	12.66
19	50.9	0.030	-0.0029	98.8	534.5	47.6	6.2	0.41	13.82
	62.9	0.039	-0.0016	101.1	552.7	72.2	7.6	0.49	12.52
20	40.6	0.025	-0.0027	94.6	544.2	38.9	4.8	0.34	13.76
	51.0	0.033	-0.0014	97.0	560.1	67.4	6.0	0.40	12.54

Table 2.1: Time evolution of the thermodynamic characteristics of hadronic matter in the central cell of volume $V = 125\text{fm}^3$ in central Au+Au collisions at bombarding energy 20 AGeV. The temperature, T , baryochemical potential, μ_B , strange chemical potential, μ_S , pressure, P , entropy density, s , and entropy density per baryon, s/ρ_B , are extracted from the statistical model of ideal hadron gas, using the microscopically evaluated energy density, $\varepsilon^{\text{cell}}$, baryonic density, ρ_B^{cell} , and strangeness density, ρ_S^{cell} , as input. Of each pair of numbers, the upper one corresponds to the UrQMD calculations, and the lower one to the QGSM calculations.

output thermodynamic characteristics given by the SM. Because of the different number of hadronic states employed by QGSM and UrQMD, the tables of available hadronic degrees of freedom in the statistical model are adjusted properly. The only objects not taken into account in the SM are strings. The detailed analysis done in [114, 115] shows that string processes play only a minor role at such late times in the central part of the reaction. Less than 5% of the total amount of hadronic collisions result in formation of strings. The strings produced at late time stages are quite light, and usually just one extra-particle, most commonly a pion, is produced after the string fragmentation. This circumstance, however, may account for the pion overproduction (see figure 2.2), since the inverse reactions such as $3(\text{or more}) \rightarrow 2$ are not incorporated in the employed

Time	$\varepsilon^{\text{cell}}$	$\rho_{\text{B}}^{\text{cell}}$	$\rho_{\text{S}}^{\text{cell}}$	T	μ_{B}	μ_{S}	P	s	$s/\rho_{\text{B}}^{\text{cell}}$
fm/c	MeV/fm ³	fm ⁻³	fm ⁻³	MeV	MeV	MeV	MeV/fm ³	fm ⁻³	
9	662.3	0.226	-0.0181	160.2	341.6	75.5	91.8	4.23	18.69
	732.3	0.290	-0.0050	167.2	401.9	105.3	113.5	4.36	15.01
10	492.2	0.175	-0.0145	153.2	354.2	71.6	68.3	3.25	18.60
	524.3	0.219	-0.0041	157.1	417.9	100.4	79.3	3.26	14.85
11	369.4	0.135	-0.0113	146.8	363.7	67.4	51.5	2.53	18.73
	384.5	0.170	-0.0045	148.1	434.5	94.7	56.7	2.48	14.61
12	276.2	0.104	-0.0094	140.5	374.7	62.4	38.7	1.96	18.80
	282.7	0.130	-0.0033	140.0	447.2	90.0	40.9	1.90	14.60
13	205.7	0.081	-0.0075	134.0	390.1	58.0	28.8	1.51	18.66
	211.5	0.101	-0.0030	132.6	460.3	85.0	30.0	1.47	14.53
14	155.6	0.064	-0.0060	128.0	404.0	54.9	21.8	1.18	18.59
	158.4	0.077	-0.0023	126.3	465.9	79.4	22.2	1.15	14.85
15	118.9	0.050	-0.0051	122.3	419.0	50.8	16.6	0.93	18.43
	120.4	0.060	-0.0018	120.5	471.9	74.4	16.8	0.90	15.16
16	90.5	0.040	-0.0041	117.2	426.6	46.3	12.8	0.74	18.81
	93.2	0.047	-0.0013	115.2	479.7	71.2	12.9	0.72	15.38
17	69.9	0.032	-0.0034	112.0	441.0	42.3	9.9	0.59	18.69
	73.8	0.038	-0.0012	110.2	489.8	67.2	10.1	0.59	15.39
18	55.0	0.026	-0.0028	107.0	457.3	39.2	7.6	0.47	18.40
	59.0	0.031	-0.0006	105.7	499.7	70.0	7.9	0.49	15.48
19	43.3	0.021	-0.0025	102.4	469.8	34.2	6.0	0.39	18.34
	47.8	0.026	-0.0006	101.2	512.1	65.7	6.3	0.40	15.31

Table 2.2: The same as table 2.1 but for 40A GeV.

versions of both microscopic models.

For both energies the baryon density in the cell at the beginning of the equilibrium phase is about 30% larger than the normal baryon density $\rho_0 = 0.16 \text{ fm}^{-3}$ in the UrQMD calculations. Whereas QGSM allows for the production of hot equilibrated matter with a density of $\rho_B = 1.8 \rho_0$, much higher nuclear densities obtained in microscopic simulations have been reported [72]. One has to bear in mind two important things concerning such density estimates. Firstly, they are very sensitive to the volume of the test-system, especially at the initial stage of the collision. As seen in the top left panel and top right panels of figure 2.4, the baryon density in both models cannot

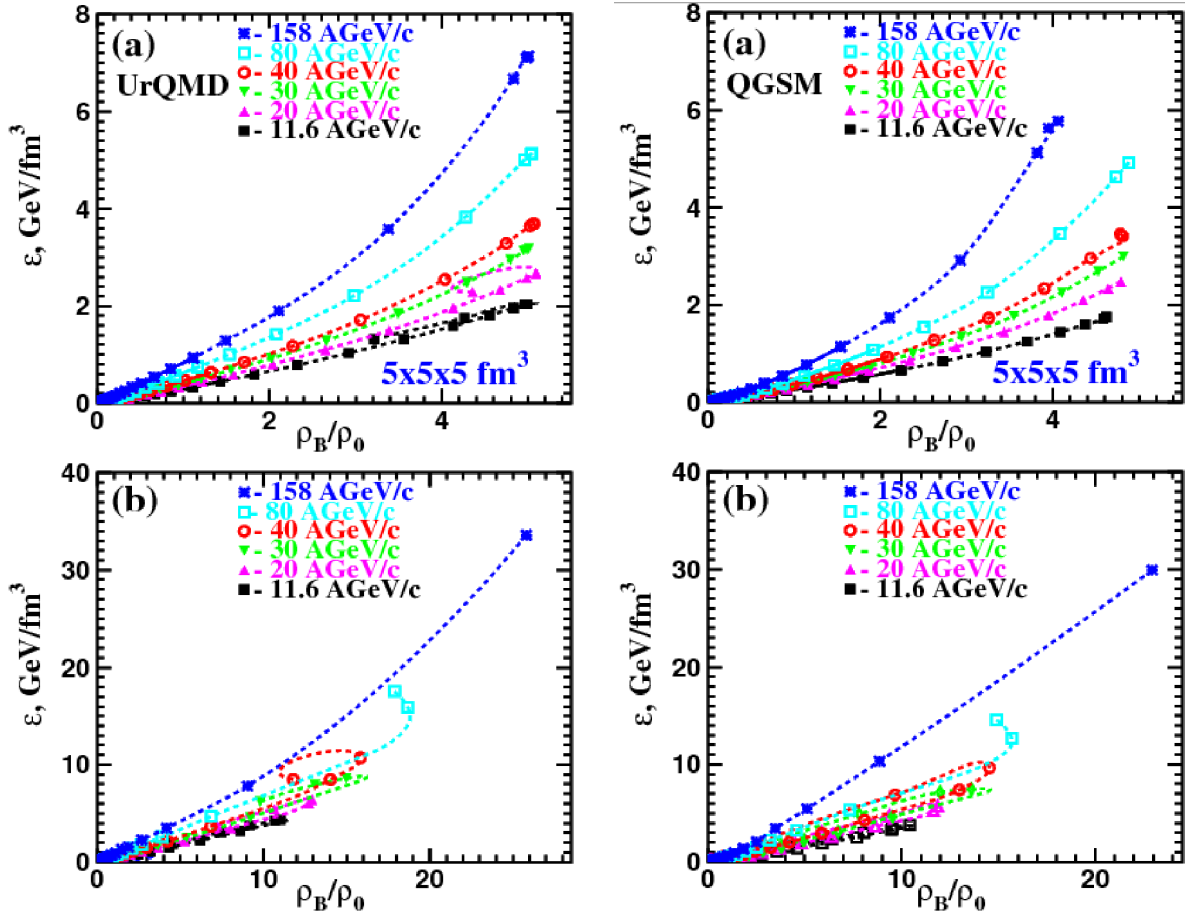


Figure 2.4: The total energy density ϵ versus baryon density ρ_B obtained in the central cell of volume (a) $V = 125 \text{ fm}^3$ and (b) $V = 0.125 \text{ fm}^3$ during the time evolution of central Au+Au collisions at energies from 11.6 AGeV to 158 AGeV. Dashed lines correspond to the non-equilibrium stage of the reaction, solid lines represent the equilibrium phase. Left panels are for UrQMD and right panels for QGSM calculations.

exceed $5 \rho_0$ in the central cubic cell with volume $V = 5 \times 5 \times 5 \text{ fm}^3$ regardless of the bombarding energy, while for the smaller cell with volume $V_{small} = 0.5 \times 0.5 \times 0.5 \text{ fm}^3$ the baryon density can be as high as $20 \rho_0$ in the calculations within the same microscopic models, see bottom panels of figure 2.4. Secondly, such high values of the ρ_B should be treated with great care. The accelerated cold nuclear matter is automatically "compressed" in the calculations by the γ -factor. At the initial stage of a nuclear collision one deals with two opposite fluxes of Lorentz-contracted nucleons which just start to interact with their counterparts. Although the calculated baryon

densities are huge, especially for the small cell, this is a purely kinematic effect, since the system is far from local equilibrium. The numbers become meaningful only when the equilibration takes place.

Another interesting effect is the negative (though small) net strangeness density in the cell throughout the evolution of the system depicted in the left panels of figure 2.5. The result is pretty insensitive to the size of test-volume and can be explained

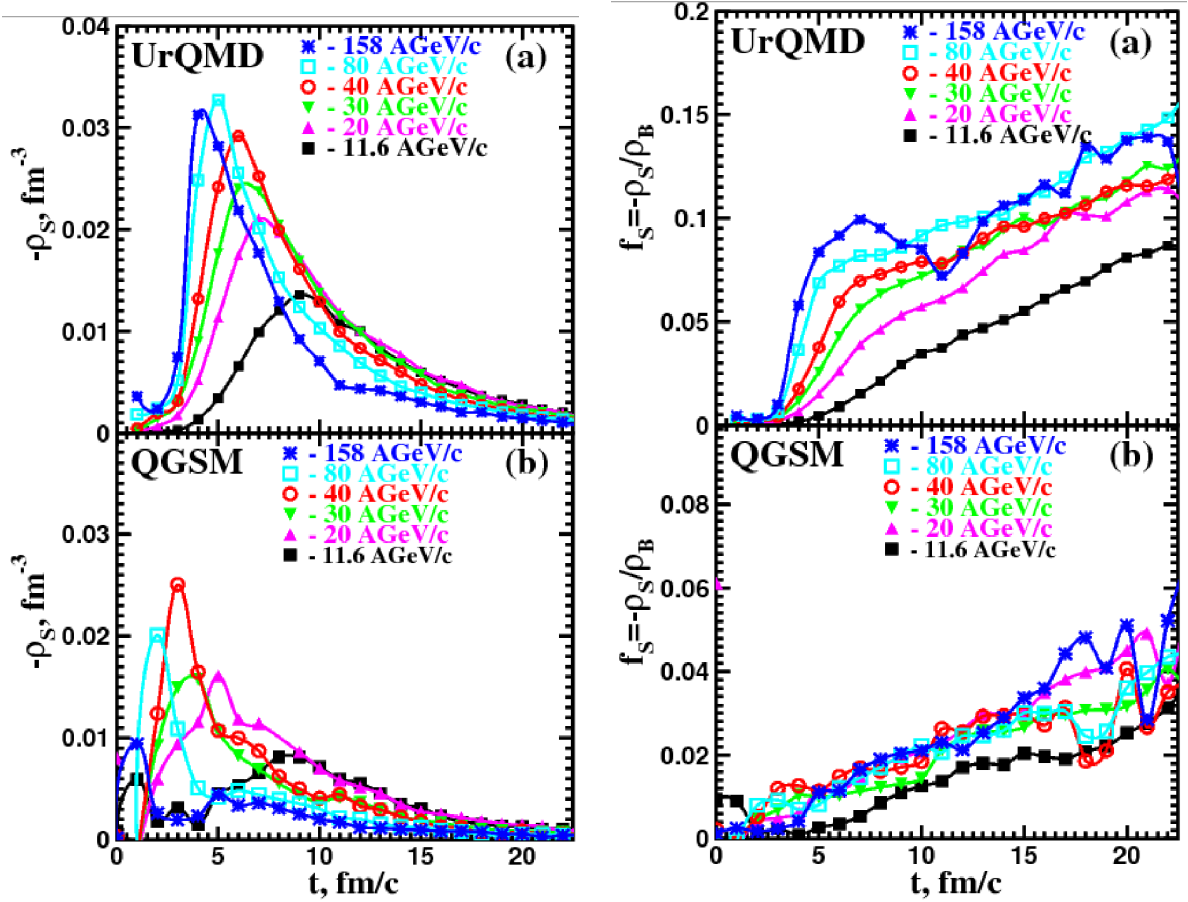


Figure 2.5: Left panels: Time evolution of net strangeness density in the central 125 fm^3 cell in (a) UrQMD and (b) QGSM calculations of central Au+Au collisions at energies from $11.6A$ GeV to $158A$ GeV. Right panels: The same as in left panels but for strangeness per baryon, $f_s = -\rho_S/\rho_B$

as follows. Strange particles are always produced in pairs, so the net ρ_S is zero. At energies about $40A$ GeV and below kaons emerge predominantly with lambdas and antikaons. Because of the \bar{s} -quark in its composition, kaons have significantly smaller interaction cross-section with baryons at $p \leq 2 \text{ GeV}/c$ compared to antikaons, which carry the s -quark. Therefore, K leave the central cell with positive net baryon charge easier than Λ or \bar{K} thus resulting to negative net strangeness. At RHIC energies the $B - \bar{B}$ asymmetry in the cell is much less pronounced, and the net ρ_S is very close to zero [104, 100].

Here we distinctly see the role of hadronic degrees of freedom. Despite the net baryon density is about 15% larger in the QGSM calculations than in the UrQMD ones, the absolute value of the net strangeness density is almost 30% higher in the UrQMD cell as compared to that in the QGSM. Extra-strangeness is deposited in the

resonance sector, mainly in Λ^* and K^* . Although the net ρ_S in the cell shown in figure 2.5 quickly drop almost to zero after $t = 6 \text{ fm}/c$, its relaxation proceeds slower than that of the net baryon density. The right panels of figure 2.5 display the instant rise of the ratio $f_s = -\rho_S/\rho_B$ with time t attributed to both microscopic models. The role of the small non-zero net strangeness is not negligible. The difference in particle spectra and, especially, in particle ratios can be about 15% [102] if one performs the SM calculations with essentially zero net strangeness.

2.4.3 EOS in the cell

Isentropic expansion of relativistic fluid is one of the main postulates of Landau hydrodynamic theory [112] of multiparticle production. We cannot prove or disprove this assumption in microscopic simulations for the whole system, simply because a global equilibrium is not attained. Though conditions in the cell are instantly changing, it is possible to check the behavior of the entropy per baryon. Within the 5% accuracy limit, this ratio is nearly conserved in the equilibrium phase of the expansion, see figure 2.6. The entropy densities obtained for the cell in both models are very close to each

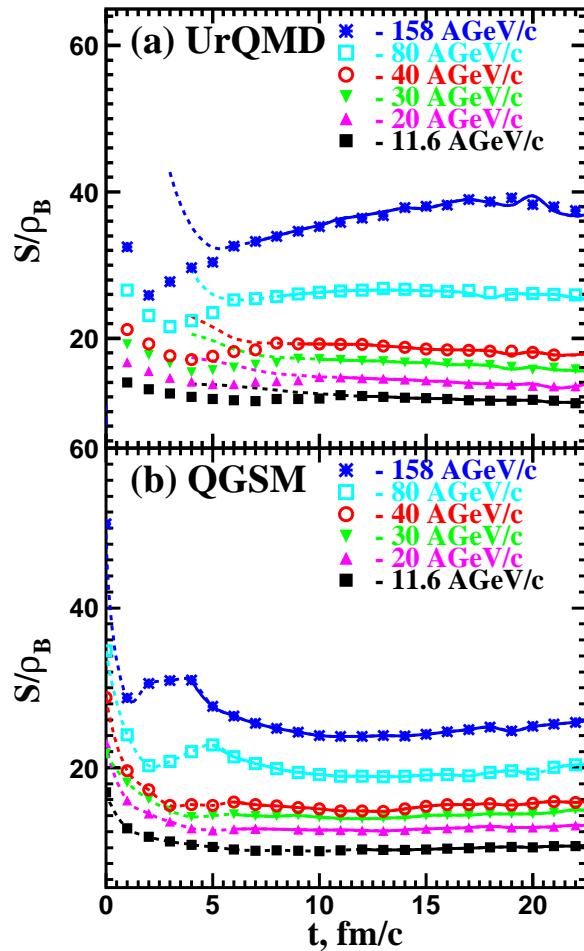


Figure 2.6: Time evolution of entropy per baryon S/ρ_B in the central 125 fm^3 cell in (a) UrQMD and (b) QGSM calculations of central Au+Au collisions at energies from 11.6 AGeV to 158 AGeV. Dashed lines correspond to the non-equilibrium stage of the reaction, solid lines represent the equilibrium phase.

other, but, because of the difference in net-baryon sector, the ratio s/ρ_B in UrQMD is about 15-20% larger than that in QGSM. Together with the pressure isotropy, the conservation of entropy per baryon supports the application of hydrodynamics.

Any hydrodynamic model relies on the equation of state, which links the pressure of the system to its energy density. Otherwise, the system of hydrodynamic equations is incomplete. The corresponding plot with microscopic pressures $P_{mic}(\varepsilon)$ is presented in the left panels of figure 2.7, whereas the macroscopic pressures obtained from the SM

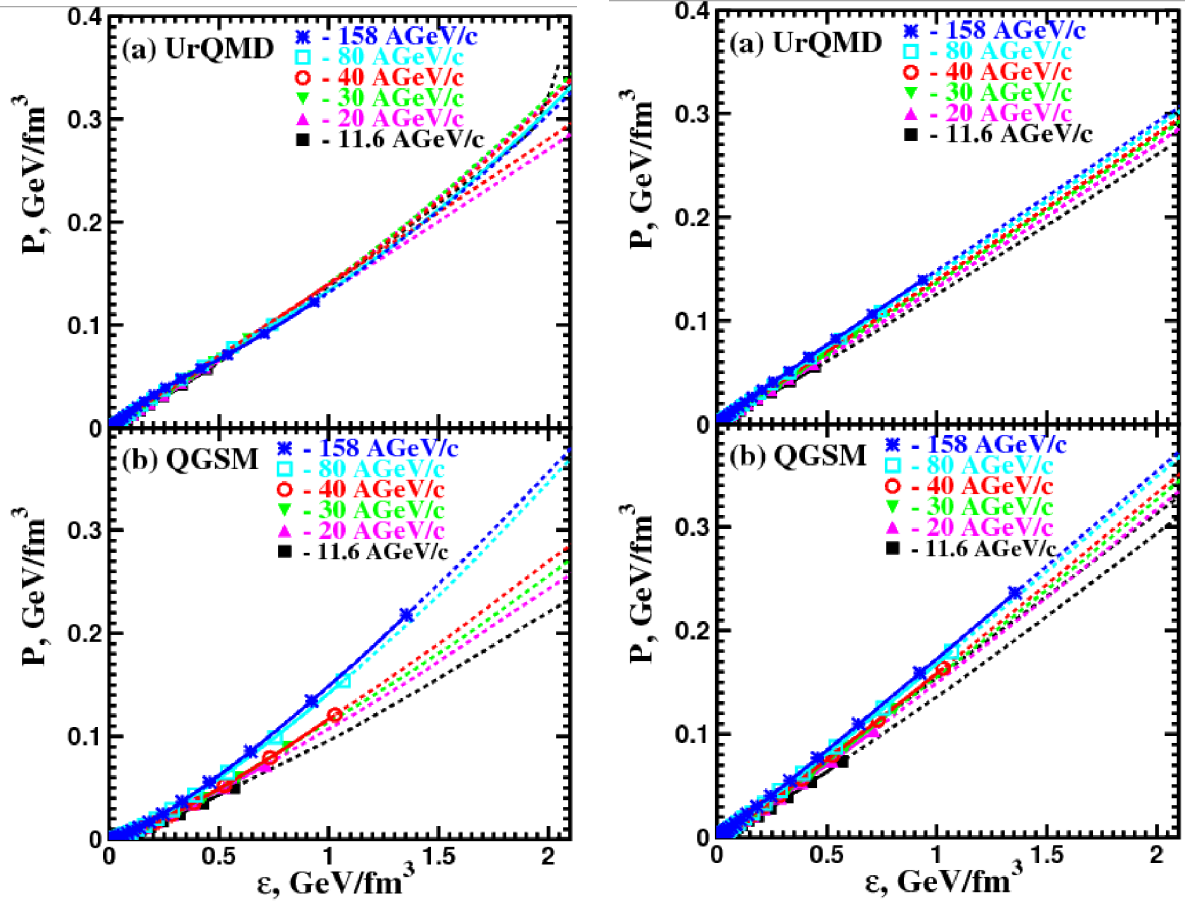


Figure 2.7: Left panels: Time evolution of the microscopic pressure P and the energy density ε in the central 125 fm³ cell in (a) UrQMD and (b) QGSM calculations of central Au+Au collisions at energies from 11.6A GeV to 158A GeV. Dashed lines correspond to the non-equilibrium stage of the reaction, solid lines represent the equilibrium phase. Right panels: Same as left panels but for macroscopic pressure P extracted from the SM fit to microscopic data.

fit are shown in the right panels of same figure. In the SM fit panels, the dependence of pressure on energy density is remarkably linear for both models for all energies in question. Thus the EOS has a rather simple form

$$P(\varepsilon) = c_s^2 \varepsilon , \quad (2.16)$$

where the sonic velocity in the medium $c_s = (dP/d\varepsilon)^{1/2}$ is fully determined by the slopes of the distributions $P(\varepsilon)$. However, if the pressure is determined microscopically and not via the distribution function, the fall-off of pressure with decreasing energy density proceeds slightly nonlinearly. This feature can be seen distinctly for top SPS

energy in the QGSM calculations. Therefore, for both models we averaged the slopes of the P versus ε distributions over the whole period of the equilibrated phase (see figure 2.7). It should be noted that due to the averaging over time, respectively energy density, the values do not represent the maximal values for c_s^2 which are reached in the corresponding reactions. They are actually lower, since also energy densities below the critical energy density of about $0.8 \text{ GeV}/\text{fm}^3$ contribute to the average.

The extracted values of the c_s^2 are presented in figure 2.8. For the UrQMD cal-

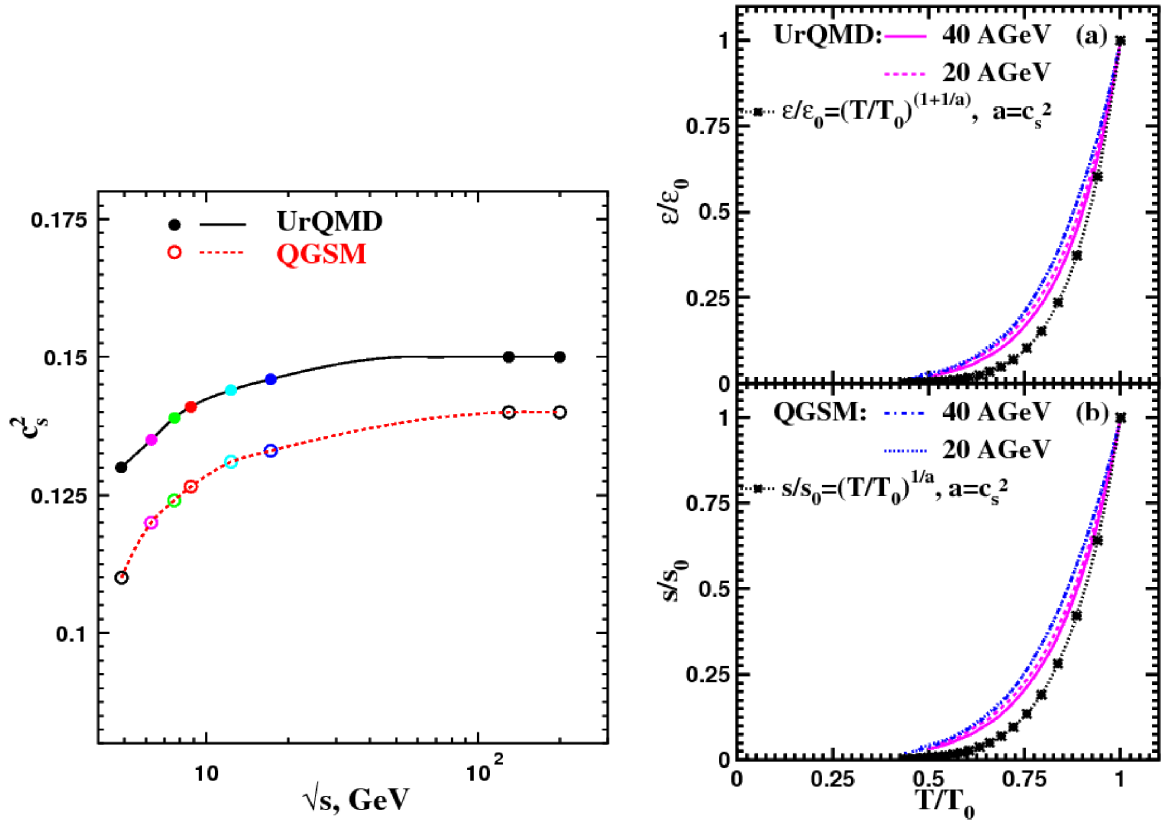


Figure 2.8: Left: The ratio $P/\varepsilon = c_s^2$, where P is defined microscopically, in the central cell of volume $V = 125 \text{ fm}^3$ as a function of center of mass energy \sqrt{s} in UrQMD (solid symbols) and in QGSM (open symbols) calculations. Lines are drawn to guide the eye. Right: (a) Ratio of energy densities $\varepsilon/\varepsilon_0$ vs. T/T_0 in the central $V = 125 \text{ fm}^3$ cell. Dashed line and solid line represent UrQMD calculations of central Au+Au collisions at 20 AGeV and 40 AGeV , respectively, whereas dotted line and dash-dotted line show the QGSM results for these reactions. Asterisks depict the analytic calculations given by eqs. 2.19-2.20 with $\mu = 0$ and $a = c_s^2 = 0.14$. (b) The same as (a) but for the ratio of entropy densities s/s_0 .

culations the velocity of sound increases from 0.13 at $E_{lab} = 11.6 \text{ AGeV}$ to 0.146 at $E_{lab} = 158 \text{ AGeV}$, and saturates at $c_s^2 = 0.15$ for RHIC energies, $\sqrt{s} = 130 \text{ AGeV}$ and $\sqrt{s} = 200 \text{ AGeV}$ [104]. In QGSM calculations the averaged sound velocity is about 0.015 units smaller due to the pion excess. For instance, it reaches $c_s^2 = 0.127$ at $E_{lab} = 40 \text{ AGeV}$. Both models indicate that at the energy around $E_{lab} = 40 \text{ AGeV}$ the slope of the $c_s^2(\sqrt{s})$ distribution is changing, and the velocity of sound becomes less sensitive to rising bombarding energy.

Let us discuss the obtained values of the c_s^2 . For the ultrarelativistic gas of light

particles the well-known theoretical result is $c_s = 1/\sqrt{3}$ of the speed of light [116]. As shown in [117], the presence of resonances in particle spectrum generates the decrease of the sonic speed. Employing the empirical dependence [11]

$$\rho(m) \propto m^{\alpha'} \quad (2 \leq \alpha' \leq 3), \quad (2.17)$$

where $\rho(m) dm$ denotes the number of resonances with masses from m to $m + dm$, one arrives to the equation of state in the form [117]

$$\varepsilon = (\alpha' + 4) P, \quad (2.18)$$

i.e., $\frac{1}{7} \leq c_s^2 \leq \frac{1}{6}$. This trend is reproduced in microscopic models.

Since neither energy density nor pressure can be directly measured in the central area of heavy-ion collisions, the experimental evaluation of the c_s is more difficult. One may rely on the hydrodynamic calculations, which claim that the magnitude of the so-called elliptic flow v_2 depends on the speed of sound c_s [118]. Using the estimates, obtained for fixed impact parameter $b = 8$ fm under assumption of constant c_s throughout the system expansion, PHENIX collaboration reported the value $c_s \approx 0.35 \pm 0.05$ [119], *i.e.* $c_s^2 \approx 0.12 \pm 0.3$, for gold-gold collisions at top RHIC energy $\sqrt{s} = 200A$ GeV. This value is close to our results and also implies rather soft effective EOS.

Lattice calculations [120] predict an asymptotic value of $c_s^2 \sim 0.3$ slightly below the Stefan-Boltzmann limit of $c_s \sim 1/\sqrt{3}$ which indicates the appearance of a strongly coupled partonic medium. Recombination processes decrease the mean free path of the particles and lower thus the viscosity of the medium. By including such processes the sonic speed can be increased above the critical energy density thus coming closer to the lattice predictions [107].

The velocity of sound defines the change of entropy and energy densities with decreasing temperature, provided that local equilibrium is maintained during the expansion. The analytic expressions, which can be derived, *e.g.*, for a gas of non-strange mesons with zero chemical potential, read

$$\varepsilon = \varepsilon_0 \left(\frac{T}{T_0} \right)^{\frac{1+a}{a}}, \quad (2.19)$$

$$s = s_0 \left(\frac{T}{T_0} \right)^{\frac{1}{a}}. \quad (2.20)$$

where $a = c_s^2$. The ratios $\varepsilon/\varepsilon_0$ and s/s_0 as functions of T/T_0 obtained from model calculations at $E_{lab} = 20A$ GeV and $40A$ GeV are plotted in the right panels of figure 2.8 together with results for $\mu = 0$ given by eqs. (2.19)-(2.20). Although the hadron gas in the cell represents a cocktail of species with different chemical potentials, that can be either zero, positive or negative in case of anti-particles, the curves calculated by the UrQMD and QGSM are not far from the ideal ones. Moreover, there is just a very weak difference between the UrQMD and QGSM curves for both energies. If one formally fits these distributions to eqs. 2.19-2.20 using the velocity of sound as fitting parameter, one gets $a = 0.2$ exactly. It would be nice to check whether the deceleration of energy(entropy) density falloff with dropping temperature could be charged solely to the presence of hadrons with non-zero chemical potential. One way to do this is to perform a similar analysis of the cell conditions at RHIC (or higher) energies. Here strange hadrons, baryons and their resonances are still present [104], but both chemical

potentials, μ_B and μ_S , are quite small. Therefore, one may expect that the microscopic results would be closer to those presented by eqs. (2.19)-(2.20).

Note also, that pressure in the cell changes with energy density quite smoothly, and no peculiarities which can be attributed to first-order phase transition are seen in the early stage of the reaction. Here we simply extend the formalism of extraction of the thermodynamic parameters to the non-equilibrium phase, where one cannot trust the obtained values anymore. This was done merely in order to find any traces of the transition related to the onset of equilibrium and to changes of the effective EOS in the models. However, the analysis is performed for the fixed cubic cell of relatively large volume $V = 125 \text{ fm}^3$, where the matter is distributed non-homogeneously at early times. To get rid of the evident ambiguities, the scheme is properly modified.

2.4.4 Early stage of the evolution

The central cell is further subdivided into the smaller ones, embedded one into another. The size of the initial test-volume is just $V_{init} = 0.125 \text{ fm}^3$, and the energy density ε of the cells becomes the main parameter now. If the ε of the inner cell is not the same (within the 5% limit of accuracy) as the energy density of the outer one, the SM analysis of the thermodynamic conditions is performed for the inner cell. If the energy density is uniformly distributed within the outer cell, the latter becomes a new test-volume, and so on. In the latter case it appears (see figure 2.6) that the onset of the isentropic expansion regime in the central area occurs significantly earlier than the formation of equilibrated matter. Moreover, at the collision energies below 80 AGeV entropy per baryon ratio seems to be quite stable almost from the beginning of the reaction.

Evolutions of the temperature and baryon chemical potential both in the central cell of the fixed volume $V = 125 \text{ fm}^3$ and in the expanding energy area are depicted in figure 2.9. One sees that the transition to equilibrium proceeds quite smoothly if the analysis is performed for the fixed cell (upper plot). In contrast, in the area with uniformly distributed energy the transition to the equilibrated phase is characterized by a kink distinctly seen in each of the phase diagrams in both microscopic models. Although this effect takes place along the lines of the constant entropy per baryon, it should not be automatically linked to the highly anticipated quark-hadron phase transition. The reason is simple, - extraction of the thermodynamic parameters, such as T , P , μ_B and μ_S (but not the entropy density, which is determined microscopically), by means of the equilibrium statistical model is doubtful for the non-equilibrium phase. On the other hand, the formation of the kink may not be accidental. It is correlated with the significant reduction of the number of processes going via the formation and fragmentation of strings, and, therefore, with the inelastic (chemical) freeze-out of particles. In both models the matter, produced in a central area in central heavy-ion collisions at energies between AGS and SPS, is dominated by (pseudo)elastic collisions after $t \approx 6 \div 8 \text{ fm}/c$ [121, 122, 123]. In the fixed-cell analysis all parameters within the cell are averaged and the transition is smeared out. The observed phenomenon can easily mimic the signature of the QCD phase transition in the T - μ_B plane, found in lattice QCD calculations [124] also along the lines of the constant entropy per baryon.

Figure 2.9 demonstrates also that thermodynamic characteristics of the fixed-size cell and the instantly growing energy-homogeneous area coincide completely during the equilibrium stage. In accord with earlier observation [103], neither the mechanical reduction of the test-volume in longitudinal direction nor the criterion of uniformly

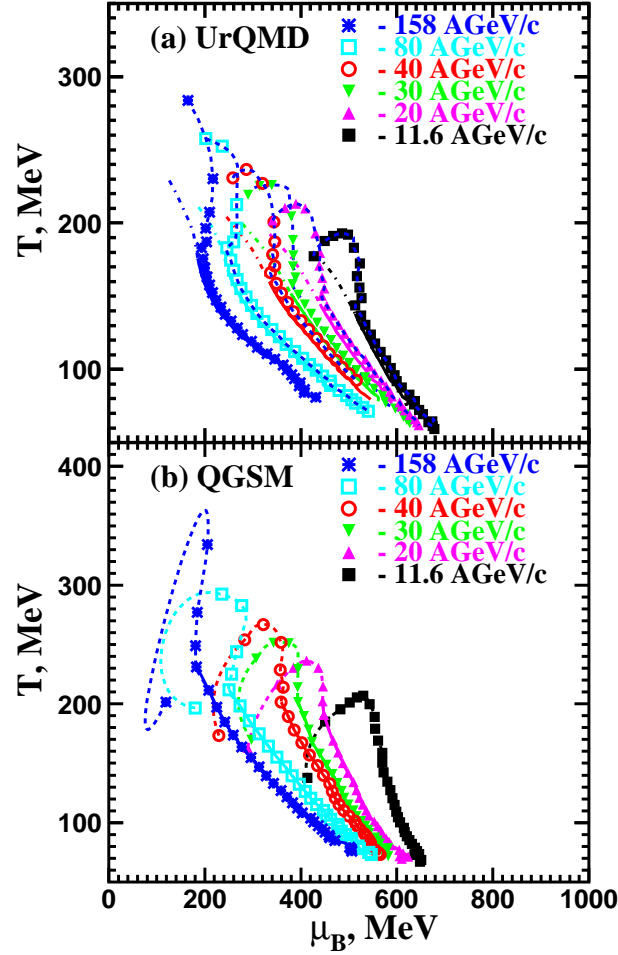


Figure 2.9: The evolution of the temperature T and baryon chemical potential μ_B in the central cell of central Au+Au collisions at energies from $11.6A$ GeV to $158A$ GeV. Both parameters are extracted from the fit to the SM. Symbols and dashed lines show the evolution of these quantities in a cell of instantly increasing volume ($V_{init} = 0.125 \text{ fm}^3$), while dash-dotted (upper plot) and full (both plots) lines are related to calculations with the fixed volume $V = 125 \text{ fm}^3$.

distributed energy density alone can help us in searching for quick equilibration in the central zone of relativistic heavy-ion collisions. Criteria of local thermal and chemical equilibrium described in section 2.3 are fulfilled after the chemical freeze-out in the test-volume, when the production of new particles in the system is ceased.

Chapter 3

Theoretical models

In the field of high energy heavy ion collisions there are still many theoretical questions due to intrinsic problems like non-perturbativity of QCD in the strong coupling limit but also due to the complexity of the many-body system evolution during the collision. As a consequence there is a cornucopia of ideas and theories which are usually materialized in the form of Monte-Carlo codes which try to model the nuclear collisions. The theoretical models vary largely in sophistication and physical features but it seems that up to now none of them describe accurately all the existing experimental data. However, as more and more experimental results become available, the theories become more precise and their predictive power increases or they are ruled out.

The Monte-Carlo codes or theoretical calculations can be classified in many ways according to their physical models, energy range where these are applicable and others. Some of the codes use models which are closer to the first principles, *e.g.* lattice QCD calculations [125, 126] and perturbative QCD models [127], but most contain phenomenological assumptions, approximations and tuning based on experimental data. There are models which focus on collective phenomena, like thermal [128, 129] and hydro [130] models, and models which treat microscopical phenomena like the parton scattering, jet quenching, string fragmentation, etc [95, 131]. Another classification can be made according to the stage of the collision on which a model is focusing, like initial state models (Glauber [132], CGC [133, 134]), partonic interactions and cascades [135], hydrodynamic expansion models [136, 137], hadronization models [138, 139] and hadron cascade models [140, 141]. There is also a large variety of hybrid codes which incorporate more than one of the models described above in order to make a realistic approach to the simulation of nuclear collisions through all stages of the reaction. [95, 142].

In the remainder of this chapter, the models selected for comparison with the data are briefly described.

3.1 Ultra Relativistic Quantum-Molecular Dynamics (UrQMD)

UrQMD [95, 96] is a microscopical model based on a phase space description of the reaction. It implements a wide range of phenomena and contains many unknown parameters which have to be fixed by experimental data or by model assumptions. It contains both hadronic and partonic interactions through string formation and fragmentation and there is no *a priori* supposition of the existence of a stage with deconfined partons.

The UrQMD collision term contains 55 baryon mass states (up to $2.25 \text{ GeV}/c^2$) and 32 meson mass states plus their corresponding anti-particle and all isospin-projected states. All these states can either be produced in string decays, s-channel collisions between hadrons or resonance decays. At low energies, up to beam energies of 8-10 GeV/nucleon the particle production is dominated by meson- or baryon-resonance decays. At higher energies, string excitation and fragmentation are the most important mechanisms for particle creation.

The elementary cross sections are fitted to the available proton-proton, proton-neutron or pion-proton data and isospin symmetry is used when possible. When no experimental data on cross sections exists (*e.g.* hyperon-baryon resonance scattering) some assumptions must be made. Such an assumption is the additive quark model where the cross sections depend only on the quark content of the colliding hadrons [143] as given in the empirical formula:

$$\sigma_{tot} = 40 \left(\frac{2}{3}\right)^{n_M} (1 - 0.4x_1^s)(1 - 0.4x_2^s) \text{ [mb]} \quad (3.1)$$

$$\sigma_{el} = 0.039\sigma_{tot}^{2/3}. \quad (3.2)$$

Here $n_M = 0, 1, 2$ is the number of colliding mesons and x_i^s is the ratio of strange to non-strange quarks in the i -th hadron. There is no energy or momentum dependence in these cross sections and they agree well with experimentally known hadron-hadron cross sections at high energies. Another assumption made is the detailed balance which is based on the time-reversal invariance of the matrix element of the reaction:

$$\sigma_{f \rightarrow i} = \frac{\mathbf{p}_i^2 g_i}{\mathbf{p}_f^2 g_f} \sigma_{i \rightarrow f}. \quad (3.3)$$

Here the g factors represent the spin-isospin degeneracy factors for the initial, i , and final, f state.

The inelastic hadron-hadron interactions at high energies are modeled through the string excitation-fragmentation mechanism. In baryon-baryon (meson-meson) interactions strings are formed between the quark and diquark (antiquark) from the same hadron. The strings are then stretched and longitudinal momenta is assigned to the constituent quarks according to the structure functions of hadrons. The Lund JET-SET routine [78], used in the UrQMD, assumes that the string always breaks into a sub-string and a particle on a mass shell.

UrQMD uses a set of empirical suppression factors to control the production of certain meson or baryon species. The s -quark suppression factor is very sensitive with regard to kaon production while the diquark suppression factor plays an important role for the anti-nucleon production. The standard values used in the model are:

$$u : d : s : qq = 1 : 1 : 0.35 : 0.1 . \quad (3.4)$$

These values can be tuned by using the model parameters but in this work the default values were used.

3.2 A Multi-Phase Transport model (AMPT)

AMPT [142] is, like UrQMD, a microscopical transport model designed for the energies available at the Relativistic Heavy Ion Collider. AMPT includes a partonic cascade

model for the initial interactions (ZPC [135]) which uses as input the parton distribution from the HIJING model [131]. The ZPC model is extended to include the transition from quark-gluon to hadronic matter. The final state interactions are based on the ART model [140].

In the AMPT model, the initial parton momentum distributions are generated from the HIJING model. In HIJING the nucleus-nucleus collision is treated as a superposition of many binary nucleon-nucleon collisions at impact parameters generated by assuming a Wood-Saxon nuclear density distribution. The probability for a collision to occur is calculated by using the eikonal formalism. Nuclear effects in hard interactions are taken into account by using an impact parameter dependent parton distribution function based on the Mueller-Qiu [144] parametrization of nuclear shadowing. Afterwards, PYTHIA [145] routines are called to describe hard interactions, while soft interactions are treated according to the Lund model [108].

The partons given by HIJING have a finite formation time during which they do not rescatter, being considered part of the coherent cloud of parent nucleons. After the partons are formed, their positions are calculated and then the ZPC model is employed for the parton cascade. After the partons stop interacting, they are converted into hadrons using the HIJING fragmentation scheme with some modifications. The main modification is the possibility to produce diquark-antidiquark pairs which helps giving a good description of the net baryon rapidity distribution in Pb+Pb collisions at 158 GeV/nucleon.

For the evolution of hadrons, the ART model is used [140]. In order to extend the validity of ART to RHIC energies new channels have been added like nucleon-antinucleon annihilation channels, inelastic interactions of kaons and antikaons, and neutral kaon production. The detailed balance is also taken into account.

3.3 HYDroynamics plus JETs model (HYDJET++)

The HYDJET++ Monte-Carlo model [146, 147, 148] was developed for the study of hadron production in central and non-central ultra-relativistic heavy ion collisions at RHIC and LHC energies. It is composed of a part for soft particle production and a part for the study of hard physics, *i.e.* jet quenching, shadowing, etc.

The soft part, also called FASTMC, is a statistical model and the particles are generated on a chemical or thermal freeze-out hypersurface which is a parametrization or a numerical solution of relativistic hydrodynamics with given initial conditions and equation of state. The main assumption of the model is that the hadronic matter created in a nuclear collision reaches a local equilibrium after a short period of time (typically less than 1 fm/ c) and then expands hydrodynamically with the equation of state of an ideal hadron gas. The chemical freeze-out takes place at a constant temperature which generates a hypersurface where all the particle ratios are frozen with the exception of hadronic decays. The experimental data and hydrodynamics suggest that at this stage the hadron densities are still too high to consider all particles as free streaming [149] so FASTMC assumes a later thermal freeze-out where the system decouples. In between the two freeze-outs the system expands hydrodynamically with frozen chemical composition, cools down and when the thermal freeze-out temperature is reached, the hadrons stream freely. .

The hard part of the model uses PYQUEN (PYthia QUENched) model [150] which modifies a jet event obtained with the PYTHIA generator [145]. PYQUEN generates

binary nucleonic collision vertices according to Glauber at a given impact parameter. PYTHIA is then used to simulate the NN collision, but only events with a generated total transverse momentum higher than a certain p_T^{min} value are further evolved. Events with lower created p_T are considered to be taken over by the soft part of the model. The p_T^{min} value becomes in this way a matching parameter between the soft fireball and the hard part of the event. Jets created in hard partonic collisions according to parton distribution functions are evolved through a deconfined medium. The nuclear shadowing of parton distribution functions is also taken into account by using an impact parameter dependent parametrization obtained in the framework of Glauber-Gribov theory [25]. The jets produced by PYTHIA are then transported in the hot and dense QCD medium where these lose energy through collisions and the gluon radiation associated with each parton scattering. After this, the modified jets and the additionally created gluons are added back to PYTHIA's particle list which performs the hadronization using the Lund string model. Finally the list of resulted hadrons is added to the list of the soft fireball.

3.3.1 Total particle multiplicities

The mean number \bar{N}_i of particles of a given species i crossing the space-like freeze-out hypersurface $\sigma(x)$ in Minkowski space can be computed as [151]:

$$\bar{N}_i = \int_{\sigma(x)} d^3\sigma_\mu(x) j_i^\mu(x). \quad (3.5)$$

The four vector $d^3\sigma_\mu(x) = n_\mu(x)d^3\sigma(x)$ is the freeze-out hypersurface element directed along the hypersurface normal unit-vector $n^\mu(x)$ with a positively defined time component ($n^0(x) > 0$). The four vector $j_i^\mu(x)$ is the current of particle specie i defined as:

$$j_i^\mu(x) = \int \frac{d^3\vec{p}}{p^0} p^\mu f_i(x, p), \quad (3.6)$$

where $f_i(x, p)$ is the Lorentz invariant particle distribution function which depends on the four-coordinate $x = \{x^0, \vec{x}\}$ and four-momentum $p = \{p^0, \vec{p}\}$. By considering that the system is locally equilibrated, the distribution function can be expressed as

$$f_i(x, p) = f_i^{\text{eq}}(p \cdot u(x); T(x), \mu(x)) = \frac{1}{(2\pi)^3} \frac{g_i}{\exp([p \cdot u(x) - \mu_i(x)]/T(x)) \pm 1} \quad (3.7)$$

where $p \cdot u \equiv p^\mu u_\mu$ is the "thermal four-energy" of the fluid element, $g_i = 2J_i + 1$ is the spin degeneracy factor, $T(x)$ and $\mu_i(x)$ are the local temperature and chemical potential, respectively, $u(x) = \gamma\{1, \vec{v}\}$ is the local collective four-velocity, $\gamma = (1 - v^2)^{-1/2}$, $u^\mu u_\mu = 1$. The signs \pm in the denominator account for the proper statistics (Fermi-Dirac or Bose-Einstein).

The local particle density is defined as:

$$\rho_i(x) = u_\mu(x) j_i^\mu(x) = \int \frac{d^3\vec{p}}{p^0} p_\mu u^\mu(x) f_i(x, p). \quad (3.8)$$

For convenience, we choose the fluid element rest frame where $u^{*\mu} = \{1, 0, 0, 0\}$ and for a system in local thermal equilibrium the particle density depends only on the local temperature $T(x^*)$ and local chemical potential $\mu_i(x^*)$:

$$\rho_i^{\text{eq}}(T(x^*), \mu_i(x^*)) = u_\mu^* j_i^{\mu, \text{eq}}(x^*) = \int d^3\vec{p}^* f_i^{\text{eq}}(p^{*0}; T(x^*), \mu_i(x^*)). \quad (3.9)$$

The star denotes the four-vectors in the fluid element rest frame.

In the case of local equilibrium, the particle current is proportional to the fluid element four-velocity, $j_i^{\mu,\text{eq}}(x) = \rho_i^{\text{eq}}(T(x), \mu_i(x))u^\mu(x)$ and thus the mean multiplicity of the i^{th} species can be expressed directly through the equilibrated density:

$$\bar{N}_i = \int_{\sigma(x)} d^3\sigma_\mu(x) u^\mu(x) \rho_i^{\text{eq}}(T(x), \mu_i(x)). \quad (3.10)$$

For the case of constant temperature and chemical potential, $T(x) = T$ and $\mu_i(x) = \mu_i$, the mean multiplicity becomes

$$\bar{N}_i = \rho_i^{\text{eq}}(T, \mu_i) \int_{\sigma(x)} d^3\sigma_\mu(x) u^\mu(x) = \rho_i^{\text{eq}}(T, \mu_i) V_{\text{eff}}. \quad (3.11)$$

In this approximation, the total yield of a given species depends only on the freeze-out temperature T , the chemical potential μ and on the total comoving volume V_{eff} [152, 149], also named *effective volume*. The effective volume conveniently absorbs the collective velocity profile and the form of the hypersurface and always cancels out in particle ratios. Also it can be used to calculate the hadronic composition at both chemical and thermal freeze-outs.

The chemical potential for a particle specie i is determined by its charges and by the chemical potentials per unit charge, *i.e.* baryon number, strangeness, electric charge, charm number, etc.

$$\mu_i = B_i\mu_B + S_i\mu_S + Q_i\mu_Q + C_i\mu_C + \dots \quad (3.12)$$

Taking into account that the net-strangeness generated in the collision must remain zero and that the electrical charge is conserved, the strangeness chemical potential μ_S and the electric chemical potential μ_Q can be expressed through the baryonic chemical potential μ_B . Therefore the mean multiplicities for all particles and resonances at freeze-out can be determined solely by the temperature T and baryonic chemical potential μ_B .

In practice the particle densities from Eq.(3.9) becomes

$$\rho_i^{\text{eq}}(T, \mu_i) = 4\pi \int_0^\infty dp^* p^{*2} f_i^{\text{eq}}(p^{*0}; T, \mu_i) \quad (3.13)$$

where the equilibrium distribution function in the fluid element rest frame is

$$f_i^{\text{eq}}(p^{*0}; T, \mu_i) = \frac{1}{(2\pi)^3} \frac{g_i}{\gamma_S^{-(s_i+\bar{s}_i)} \exp([p^{*0} - \mu_i]/T) \pm 1}. \quad (3.14)$$

where the ”-” sign is for fermions and the ”+” sign is for bosons. The γ_S is a phase space occupancy factor which accounts for the suppression of strange particles possibly due to incomplete strangeness saturation in the QGP phase [153] while s_i and \bar{s}_i are the number of component strange and anti-strange quarks of a given species, respectively. By using the expansion

$$f_i^{\text{eq}}(p^{*0}; T, \mu_i) = \frac{g_i}{(2\pi)^3} \gamma_S^{(s_i+\bar{s}_i)} \sum_{k=1}^{\infty} (\mp)^{k+1} \exp(k \frac{\mu_i - p_i^{*0}}{T}), \quad (3.15)$$

the particle density can be expressed as a sum of modified Bessel functions of the second kind:

$$\rho_i^{\text{eq}}(T, \mu_i) = \frac{g_i}{2\pi^2} m_i^2 T \gamma_S^{(s_i + \bar{s}_i)} \sum_{k=1}^{\infty} \frac{(\mp)^{k+1}}{k} \exp\left(\frac{k\mu_i}{T}\right) K_2\left(\frac{km_i}{T}\right). \quad (3.16)$$

Using the particle density from (3.16) together with (3.11) one can calculate now the mean multiplicity of particles at the chemical freeze-out. However if it is assumed that the chemical freeze-out and the thermal one do not coincide, a more complicated procedure must be taken into account since the effective volume changes between the two freeze-outs and the chemical potential cannot be calculated through (3.12) which is valid only for chemically equilibrated systems. To solve this, an effective pion chemical potential μ_π^{eff} at thermal freezeout was introduced. By using this and the fact that the particle ratios are frozen after the chemical freeze-out (3.17),

$$\frac{\rho_i^{\text{eq}}(T^{\text{ch}}, \mu_i^{\text{ch}})}{\rho_\pi^{\text{eq}}(T^{\text{ch}}, \mu_\pi^{\text{ch}})} = \frac{\rho_i^{\text{eq}}(T^{\text{th}}, \mu_i^{\text{th}})}{\rho_\pi^{\text{eq}}(T^{\text{th}}, \mu_\pi^{\text{eff th}})} \quad (3.17)$$

the chemical potentials at thermal freeze-out can be calculated for all species (3.18).

$$\mu_i^{\text{th}} = T^{\text{th}} \ln \left(\frac{\rho_i^{\text{eq}}(T^{\text{ch}}, \mu_i^{\text{ch}})}{\rho_i^{\text{eq}}(T^{\text{th}}, \mu_i = 0)} \frac{\rho_\pi^{\text{eq}}(T^{\text{th}}, \mu_\pi^{\text{eff th}})}{\rho_\pi^{\text{eq}}(T^{\text{ch}}, \mu_\pi^{\text{ch}})} \right) \quad (3.18)$$

3.3.2 Momentum distribution

As it was mentioned before, the hydrodynamic expansion of the fireball ends by a sudden system decoupling at a given temperature and chemical potentials. If we assume that the momentum distribution of the produced hadrons keeps the thermal character given by (3.7), then this distribution can be calculated according to the Cooper-Frye prescription [138]:

$$p^0 \frac{d^3 \bar{N}_i}{d^3 p} = \int_{\sigma(x)} d^3 \sigma_\mu(x) p^\mu f_i^{\text{eq}}(p \cdot u(x); T, \mu_i). \quad (3.19)$$

The integral can be calculated in a similar way to the Eqs.(3.5) and (3.6) by using the invariant weight

$$W_{\sigma,i}(x, p) \equiv p^0 \frac{d^6 \bar{N}_i}{d^3 \sigma d^3 \vec{p}} = n_\mu(x) p^\mu f_i^{\text{eq}}(p \cdot u(x); T, \mu_i) \quad (3.20)$$

and the fluid element rest frame where, *e.g.*

$$n^{*0} = n^\mu u_\mu = \gamma(n^0 - \vec{v}\vec{n}), \quad (3.21)$$

$$\vec{n}^* = \vec{n} - \gamma(1 + \gamma)^{-1}(n^{*0} + n^0)\vec{v}. \quad (3.22)$$

In the simple case when the normal four-vector $n^\mu(x)$ coincides with the fluid element flow velocity $u^\mu(x)$, $n^{*\mu} = u^{*\mu} = \{1, 0, 0, 0\}$, the weight $W_{\sigma,i}^*(x^*, p^*) = p^{*0} f_i^{\text{eq}}(p^{*0}; T, \mu)$ becomes independent of x and isotropic in the three-momentum \vec{p}^* . The most important consequence is that the simulation procedure in this frame becomes simple and 100% efficient. The particles initialized in this frame are boosted afterwards to the fireball rest frame by using the velocity field $\vec{v}(x)$. There are very well known examples of models where the normal four-vector is collinear with the

fluid element velocity, in central collisions, like the Bjorken model with hypersurface $\tau_B = (t^2 - z^2)^{1/2} = \text{const}$ and zero transverse flow or the Hubble-like models with hypersurface $\tau_H = (t^2 - x^2 - y^2 - z^2)^{1/2} = \text{const}$ and spherically symmetric flow. However, in general the two four-vectors are not collinear even in the fluid element rest frame.

It is well known that the Cooper-Frye model is not valid where the freeze-out hypersurface is characterized by a space-like normal four-vector because the quantity $p^\mu n_\mu < 0$ for some momenta which leads to negative contributions to the particle numbers. Usually the negative contributions are rejected but this violates the continuity condition of the flow through the freeze-out hypersurface. In order to cure this caveat one can use a generalized form of Eq.(3.19) [154]:

$$p^0 \frac{d^3 \bar{N}_i}{d^3 p} = \int_{\sigma(x)} d^3 \sigma_\mu(x) \pi^\mu(x, p) f_i^{\text{eq}}(T(x), \mu_i(x)), \quad (3.23)$$

where the generalized four-momentum π^μ is defined as:

$$\pi^\mu(x, p) = p^\mu \theta(1 - |\bar{\lambda}(x, p)|) + u^\mu(x) (p \cdot u(x)) \theta(|\bar{\lambda}(x, p)| - 1), \quad (3.24)$$

$$\bar{\lambda}(x, p) = 1 - p \cdot n(x) [(p \cdot u(x))(n(x) \cdot u(x))]^{-1}, \quad (3.25)$$

and $\theta(x)$ is the Heaviside step function.

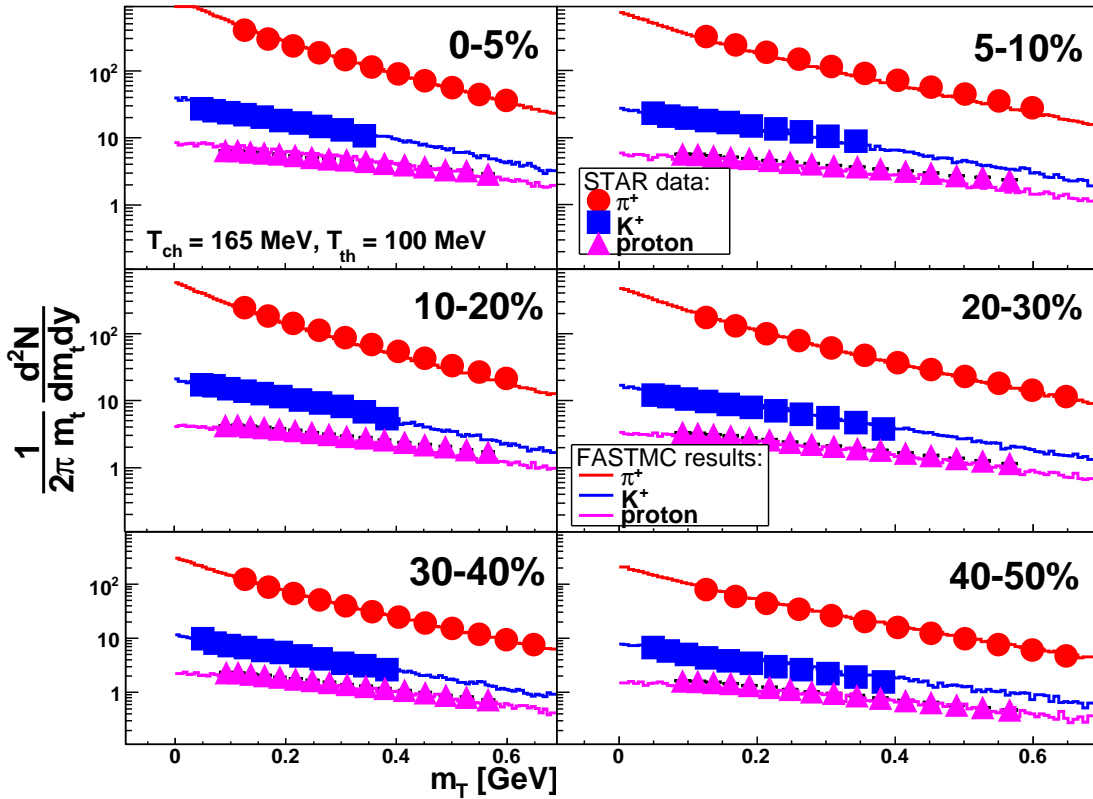


Figure 3.1: m_T spectra at different centralities in Au+Au at 200 AGeV as measured by STAR [155] (solid points) and from the FASTMC calculation [147].

By using the fluid element rest frame for the quantities in Eq.(3.23) one can obtain the same form for the particle flow four-vector $j^\mu(x)$ as in the case with time-like normal four-vector $n^\mu(x)$:

$$j^\mu(x) = \int \frac{d^3 \vec{p}}{p^0} \pi^\mu(x, p) f_i^{\text{eq}}(T(x), \mu_i(x)) = \rho_i^{\text{eq}}(T(x), \mu_i(x)) u^\mu(x). \quad (3.26)$$

Therefore the factorization of the freeze-out details in the effective volume is still valid in the case of constant temperature and chemical potentials. The invariant weight in the fluid element rest frame becomes:

$$W_{\sigma,i}^*(x^*, p^*) = \left[p^{*\mu} n_\mu^* \theta \left(1 - \left| \frac{(\vec{p}^* \vec{n}^*)}{p^{*0} n^{*0}} \right| \right) + p^{*0} n^{*0} \theta \left(\left| \frac{(\vec{p}^* \vec{n}^*)}{p^{*0} n^{*0}} \right| - 1 \right) \right] f_i^{\text{eq}}(p^{*0}; T, \mu_i) \quad (3.27)$$

and reduces to the above calculated one for a time-like normal four-vector.

In Fig.3.1 the invariant spectra at mid-rapidity for π^+ , K^+ and protons are shown for different centralities in Au+Au collisions at $\sqrt{s_{NN}} = 200$ GeV in comparison with the results from STAR Collaboration [155]. The double freeze-out scenario was used with a chemical freeze-out temperature $T^{\text{ch}} = 165$ MeV and a thermal freeze-out temperature $T^{\text{th}} = 100$ MeV. The other model parameters are given in table 3.1.

3.3.3 Freeze-out surface modeling

In the previous sections of this chapter it has been shown how the integrated and differential multiplicities are calculated but avoiding the calculation of the comoving effective volume V_{eff} . It has been showed that the geometry of the freeze-out hypersurface can be factorized out within the assumption of constant temperature and chemical potentials. In this section we will focus on modeling the freeze-out hypersurface for the case of central to semi-peripheral nucleus-nucleus collisions by considering a Bjorken-like freeze-out parametrizations model and calculate the total comoving volume.

In the Bjorken formalism [28] it is more convenient to substitute the Cartesian coordinates t and z by

$$\tau = (t^2 - z^2)^{1/2}, \quad \eta = \frac{1}{2} \ln \frac{t+z}{t-z}, \quad (3.28)$$

and work with the radial vector $\vec{r} \equiv \{x, y\} = \{r \cos \phi, r \sin \phi\}$. The coordinate four-vector becomes

$$x^\mu = \{\tau \cosh \eta, r \cos \phi, r \sin \phi, \tau \sinh \eta\}. \quad (3.29)$$

The freeze-out hypersurface is generally represented by a equation of the type $\tau = \tau(\eta, r, \phi)$ and the hypersurface element in terms of η and polar coordinates has the form

$$d^3 \sigma_\mu = \epsilon_{\mu\alpha\beta\gamma} \frac{dx^\alpha}{d\eta} \frac{dx^\beta}{dr} \frac{dx^\gamma}{d\phi} d\eta dr d\phi, \quad (3.30)$$

where $\epsilon_{\mu\alpha\beta\gamma}$ is the completely antisymmetric Levy-Civita tensor in four dimensions with $\epsilon^{0123} = -\epsilon_{0123} = 1$. It is frequent that the freeze-out happens on a surface of constant proper time so in this case we can consider $\tau = \text{const}$. After straightforward calculations, the hypersurface element becomes

$$d^3 \sigma_\mu = \tau d^2 \vec{r} d\eta \{\cosh \eta, 0, 0, -\sinh \eta\} = n_\mu d^3 \sigma, \quad (3.31)$$

$$d^3 \sigma = \tau d^2 \vec{r} d\eta, \quad (3.32)$$

$$n^\mu = \{\cosh \eta, 0, 0, \sinh \eta\}. \quad (3.33)$$

In non-central collisions the shape of the particle emission region can be approximated by an ellipse in the transverse plane ($x - y$) (see Fig.3.2). The ($z - x$) plane coincides with the reaction plane. At a given impact parameter b , the ellipse radii

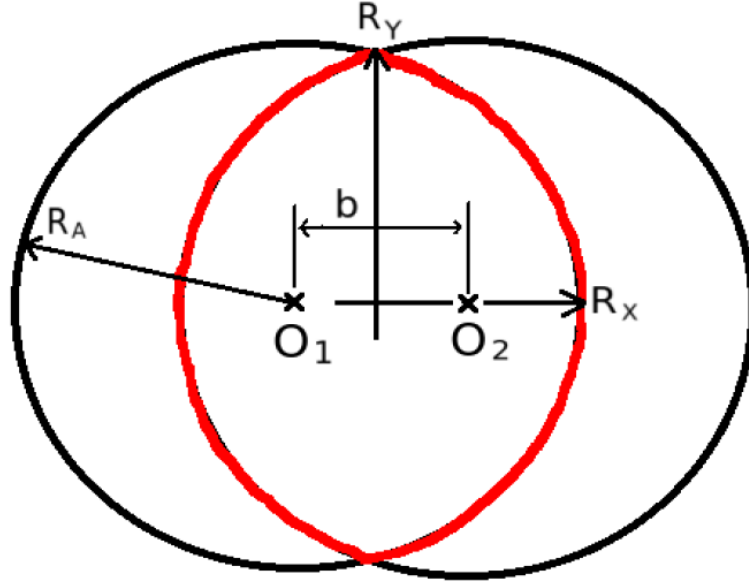


Figure 3.2: Non-central collision transverse plane geometry.

$R_x(b)$ and $R_y(b)$ can be parametrized in terms of the spatial anisotropy or eccentricity $\epsilon(b) = (R_y^2 - R_x^2)/(R_x^2 + R_y^2)$ and a scale factor $R_S(b) = [(R_x^2 + R_y^2)/2]^{1/2}$, so that

$$R_x(b) = R_S(b)\sqrt{1 - \epsilon(b)}, \quad R_y(b) = R_S(b)\sqrt{1 + \epsilon(b)}. \quad (3.34)$$

From the ellipse equation $x^2/R_x^2 + y^2/R_y^2 = 1$ follows the explicit dependence of the fireball transverse radius $R(b, \phi)$ on the azimuthal angle ϕ :

$$R(b, \phi) = R_S(b) \frac{\sqrt{1 - \epsilon^2(b)}}{\sqrt{1 + \epsilon(b)\cos 2\phi}}. \quad (3.35)$$

In the following we use a simple scaling option [150]

$$R_S(b) = R_S(b=0)\sqrt{1 - \epsilon_S(b)}, \quad (3.36)$$

where $R_S(b=0) \equiv R$ is the fireball freeze-out transverse radius in central collisions. It means that the dimensionless ratio $R_S(b)/R_S(0)$ at the freeze-out moment depends on the collision energy, the radius R_A of the colliding (identical) nuclei and on the impact parameter b through a dimensionless quantity only, namely $\epsilon_S(b)$. The effective eccentricity $\epsilon_S(b)$ and the fireball freeze-out eccentricity $\epsilon(b)$ are determined by the eccentricity $\epsilon_0(b) = b/(2R_A)$ of the elliptical overlap of the colliding nuclei at the initial moment, when

$$\frac{R_S(b)}{R_S(b=0)} \Big|_{\epsilon(b)=\epsilon_0(b)} \equiv \frac{R_S(b)_{\text{initial}}}{R_A} = \sqrt{1 - \epsilon_0(b)}. \quad (3.37)$$

Since $\epsilon_S(0) = \epsilon(0) = \epsilon_0(0) = 0$, one can assume that $\epsilon_S(b) \simeq \epsilon(b)$ at sufficiently small impact parameters. From the comparison with data, it appears that by using this approximation the absolute normalization of spectra can be achieved up to $b \simeq R_A$.

In the hydrodynamic evolution of the fireball the expansion is stronger in the direction of the short ellipse (in the reaction plane) because of higher pressure gradients [156]. The typical hydrodynamic evolution is shown in Fig.3.3. During the evolution,

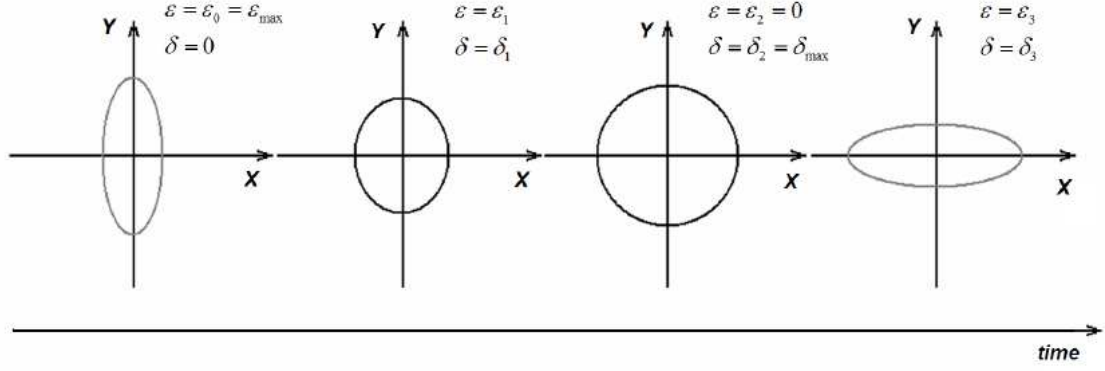


Figure 3.3: Schematic hydrodynamic evolution.

the initial system coordinate anisotropy $\epsilon_0(b)$ is transformed into momentum anisotropy $\delta(b)$. According to the hydrodynamical calculations, the spatial eccentricity almost disappears and the momentum anisotropy saturates rather early before freeze-out. Since in this model the hydrodynamical evolution is not traced, the spatial and momentum anisotropies $\epsilon(b)$ and $\delta(b)$ at freeze-out are considered as free parameters but are motivated by realistic hydrodynamics.

For central collisions the fluid flow four-velocity $u^\mu(t, \vec{x}) = \gamma(t, \vec{x})\{1, \vec{v}(t, \vec{x})\}$ at a point \vec{x} and time t was parametrized (see [146]) in terms of the longitudinal and transverse fluid flow rapidities

$$\eta_u(t, \vec{x}) = \frac{1}{2} \ln \frac{1 + v_z(t, \vec{x})}{1 - v_z(t, \vec{x})}, \quad \rho_u(t, \vec{x}) = \frac{1}{2} \ln \frac{1 + v_\perp(t, \vec{x}) \cosh \eta_u(t, \vec{x})}{1 - v_\perp(t, \vec{x}) \cosh \eta_u(t, \vec{x})}, \quad (3.38)$$

where $v_\perp = |\vec{v}_\perp|$ is the magnitude of the transverse component of the flow three-velocity $\vec{v} = \{v_\perp \cos \phi_u, v_\perp \sin \phi_u, v_z\}$, *i.e.*,

$$u^\mu(t, \vec{x}) = \{\cosh \rho_u \cosh \eta_u, \sinh \rho_u \cos \phi_u, \sinh \rho_u \sin \phi_u, \cosh \rho_u \sinh \eta_u\} \quad (3.39)$$

$$= \{(1 + u_\perp^2)^{1/2} \cosh \eta_u, \vec{u}_\perp, (1 + u_\perp^2)^{1/2} \sinh \eta_u\}, \quad (3.40)$$

where $\vec{u}_\perp = \gamma \vec{v}_\perp = \gamma_\perp \cosh \eta_u \vec{v}_\perp$, $\gamma_\perp = \cosh \rho_u$. However, unlike the transverse isotropic parametrization ($\phi_u = \phi$) valid for central collisions, in non-central collisions the azimuthal angle ϕ_u of the fluid velocity vector is not identical to the spatial azimuthal angle ϕ , because of the non-zero flow anisotropy parameter $\delta(b)$ [157, 158]:

$$u^\mu(t, \vec{x}) = \{\gamma_\phi \cosh \tilde{\rho}_u \cosh \eta_u, \sqrt{1 + \delta(b)} \sinh \tilde{\rho}_u \cos \phi, \quad (3.41)$$

$$\sqrt{1 - \delta(b)} \sinh \tilde{\rho}_u \sin \phi, \gamma_\phi \cosh \tilde{\rho}_u \sinh \eta_u\}, \quad (3.42)$$

where

$$\gamma_\phi = \sqrt{1 + \delta(b) \tanh^2 \tilde{\rho}_u \cos 2\phi}, \quad (3.43)$$

$$\tan \phi_u = \sqrt{\frac{1 - \delta(b)}{1 + \delta(b)}} \tan \phi. \quad (3.44)$$

The transverse flow rapidity ρ_u is related to $\tilde{\rho}_u$ by:

$$u_\perp = \sinh \rho_u = \sqrt{1 + \delta(b) \cos 2\phi} \sinh \tilde{\rho}_u. \quad (3.45)$$

The elliptic flow parameter calculated with this model for different sets of δ and ϵ parameters for 20%-30% central Au+Au collisions at $\sqrt{s_{NN}}=200$ GeV are shown in Fig.3.4 in comparison with experimental data [159] where a common chemical and thermal freeze-out at $T^{\text{ch}} = T^{\text{th}} = 165$ MeV was assumed. The data is not well described over the p_T range shown by any of sets of eccentricity parameters. By using separated

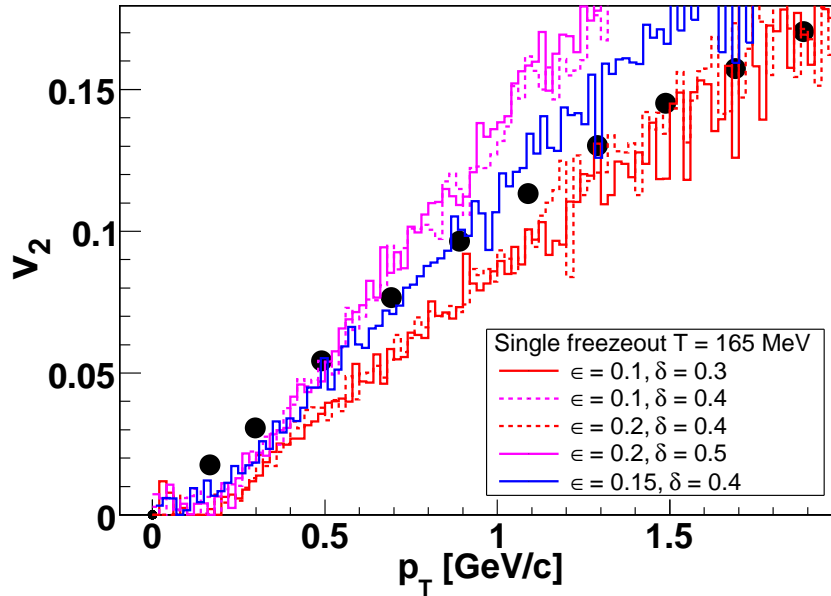


Figure 3.4: Elliptic flow parameter calculated in 20%-30% semi-central Au+Au collisions at $\sqrt{s_{NN}}=200$ GeV in the single freeze-out scenario for different sets of δ and ϵ parameters. The solid points are STAR data [159].

chemical and thermal freeze-outs the experimental elliptic flow coefficient is described much better for a wide range of centralities (see Fig.3.5).

T^{th} [MeV]	τ [fm/c]	$\Delta\tau$ [fm/c]	$R(b=0)$ [fm]	$\rho_u^{\text{max}}(b=0)$	$\mu_\pi^{\text{eff th}}$
165	7.0	2.0	9.0	0.65	0.0
100	8.0	2.0	10.0	1.1	0.11

Table 3.1: Model parameters for central Au+Au collisions at $\sqrt{s_{NN}}=200$ GeV. The chemical freeze-out parameters are $T^{\text{ch}} = 165$ MeV, $\mu_B = 28$ MeV, $\mu_S = 7$ MeV and $\mu_Q = -1$ MeV. The strangeness occupancy factor γ_S was set to 1.

In the Bjorken scenario [28] it is assumed that at mid-rapidity the system is boost invariant but in this model one can allow for a small violation of the boost invariance by introducing a Gaussian weight, $\exp(-\eta^2/2\Delta\eta^2)$, to the rapidity distribution in the interval $[-\eta_{\text{max}}, +\eta_{\text{max}}]$. The presence of the "oscillation term" $\sqrt{1 + \delta(b)\cos 2\phi}$ in the transverse component of the fluid flow velocity in Eq.(3.45) allows the use of a simple linear profile for transverse flow rapidity $\tilde{\rho}_u$

$$\tilde{\rho}_u = \frac{r}{R_S(b)} \rho_u^{\text{max}}(b=0), \quad (3.46)$$

where $\rho_u^{\text{max}}(b=0)$ is the maximal transverse flow rapidity for central collisions.

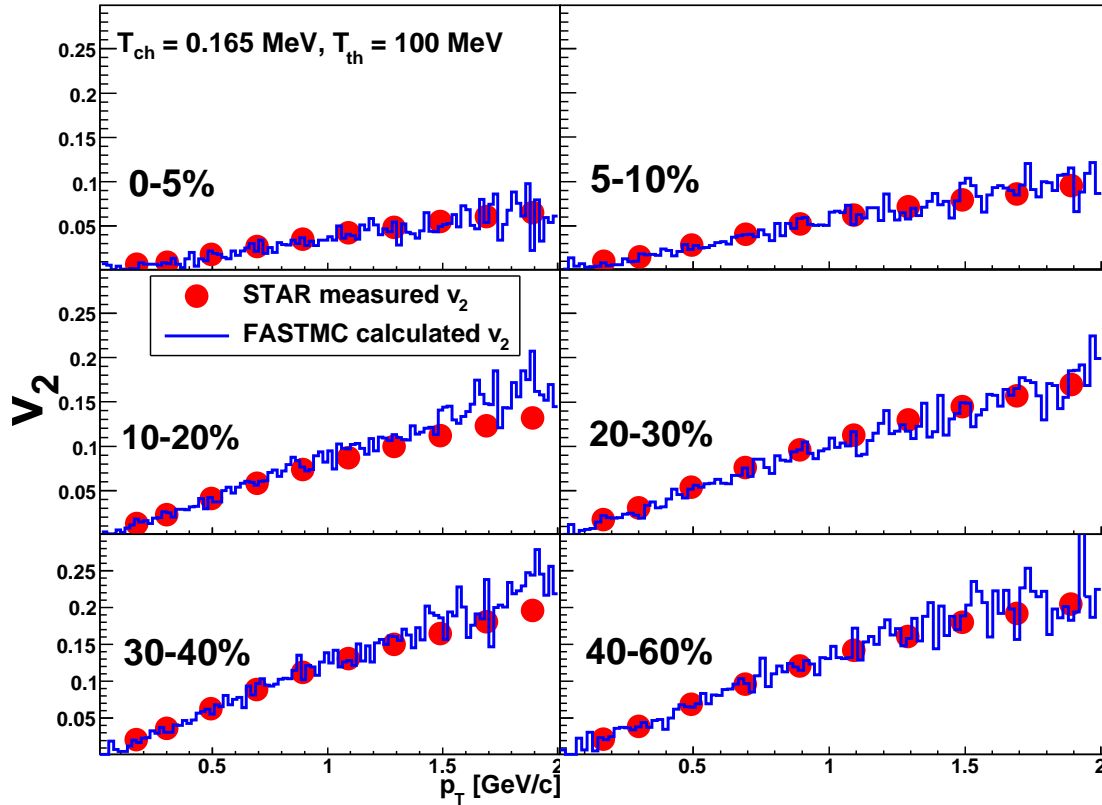


Figure 3.5: Elliptic flow parameter dependence on p_T for different centrality intervals. The parameters used for this calculation are given in table 3.1 and table 3.2. Data is from [159].

centrality	0-5%	5-10%	10-20%	20-30%	30-40%	40-60%
b_{\min}/R_A	0.0	0.447	0.632	0.894	1.095	1.265
b_{\max}/R_A	0.447	0.632	0.894	1.095	1.265	1.549
ϵ	0	0	0	0.1	0.15	0.15
δ	0.05	0.08	0.12	0.25	0.34	0.36

Table 3.2: Model parameters for central Au+Au collisions at $\sqrt{s_{NN}} = 200$ GeV at different centralities. The thermal freeze-out temperature is $T^{\text{th}} = 100$ MeV and the other parameters are the ones defined in Table 3.1.

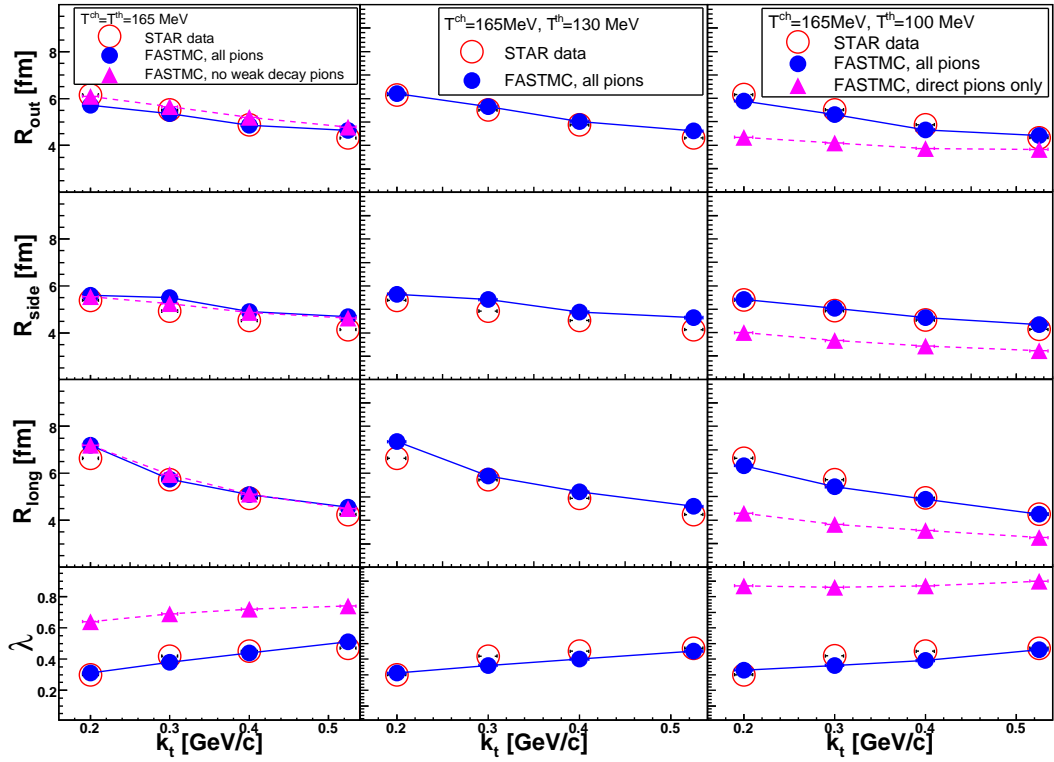


Figure 3.6: The π^+ correlation radii at midrapidity in central Au+Au collisions at $\sqrt{s_{NN}} = 200$ GeV. The model parameters are the ones listed in Table 3.1. The chemical freeze-out temperature is $T^{ch} = 165$ MeV and the thermal is varied between $T^{th} = 165$ MeV (left), $T^{th} = 130$ MeV (middle) and $T^{th} = 100$ MeV (right). Both HBT radii from direct pions and from all pions are shown.

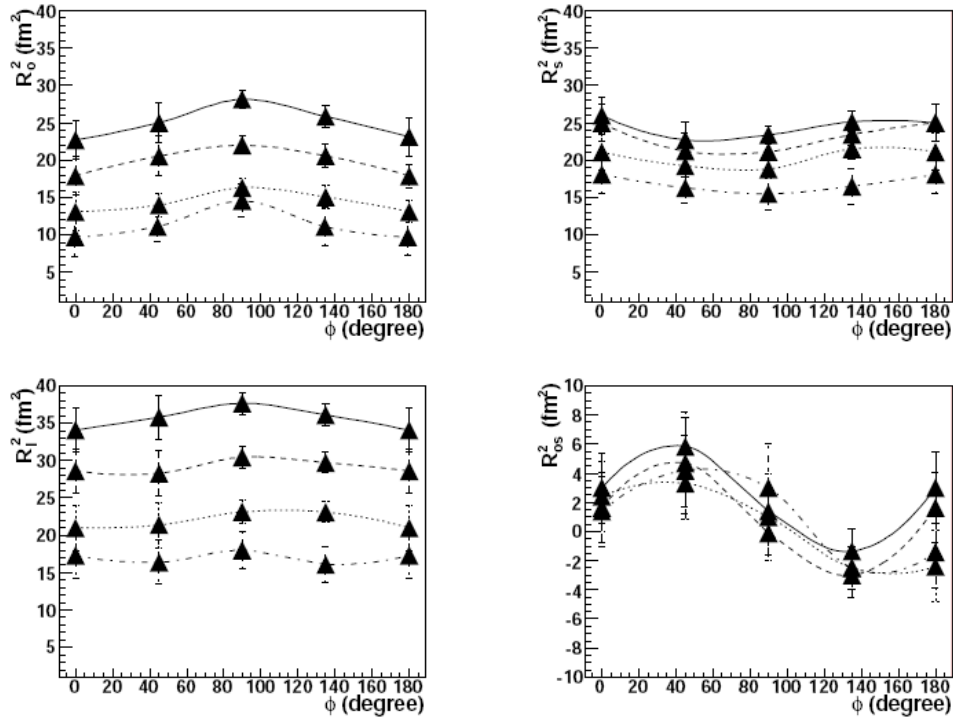


Figure 3.7: Azimuthal dependence of midrapidity $\pi^+\pi^+$ HBT radii in 20-30% semi-central Au+Au collisions at $\sqrt{s_{NN}} = 200$ GeV calculated with FASTMC and compared to data in different k_T intervals: $0.15 < k_T < 0.25$ (solid line), $0.25 < k_T < 0.35$ (dashed line), $0.35 < k_T < 0.45$ (dotted line) and $0.45 < k_T < 0.60$ (dotted-dashed line). This simulation was made with a special set of parameters: $T^{th} = 0.1$ GeV, $\rho_u^{max}(b=0) = 1$, $R(b=0) = 11.5$ fm, $\tau = 7.5$ fm/c, $\Delta\tau = 0$ fm/c, $\epsilon = 0.1$ and $\delta = 0.25$. Weak decays were not taken into account.

Now we can finally calculate the effective volume for particle production in the case of central and noncentral collisions by solving the integral

$$V_{\text{eff}} = \int_{\sigma(t, \vec{x})} d^3\sigma_{\mu}(t, \vec{x}) u^{\mu}(t, \vec{x}) = \tau \int_0^{2\pi} d\phi \int_0^{R(b, \phi)} (n_{\mu} u^{\mu}) r dr \int_{\eta_{\text{min}}}^{\eta_{\text{max}}} d\eta, \quad (3.47)$$

where $(n_{\mu} u^{\mu}) = \cosh \tilde{\rho}_u \sqrt{1 + \delta(b) \tanh^2 \tilde{\rho}_u \cos 2\phi}$.

The midrapidity HBT radii of the particle emitting source in Au+Au collisions at $\sqrt{s_{NN}} = 200$ GeV are illustrated in Fig.3.6. The radii R_{out} , R_{side} and R_{long} are obtained by fitting the three-dimensional correlation function with the Gaussian formula

$$CF(p_1, p_2) = 1 + \lambda \exp(-R_{\text{out}}^2 q_{\text{out}}^2 - R_{\text{side}}^2 q_{\text{side}}^2 - R_{\text{long}}^2 q_{\text{long}}^2), \quad (3.48)$$

where λ is the chaoticity factor or correlation strength and $\vec{q} = \vec{p}_1 - \vec{p}_2 = (q_{\text{out}}, q_{\text{side}}, q_{\text{long}})$ is the relative three momentum of two identical particles with four-momenta p_1 and p_2 . In the reference system where the reaction plane coincide with the $x - z$ plane, the "out", "side" and "long" subscripts correspond to the y , x and z directions, respectively. The radii shown take into account only $\pi^+ \pi^+$ HBT correlations and show a good agreement between the model calculation and experimental data. Furthermore, in Fig.3.7, the model calculation for the dependence of the HBT radii on the azimuthal angle ϕ show a good agreement with the experiment in different k_T intervals.

3.3.4 Hard multi-jet production

The model for the hard multi-parton production is based on the PYTHIA generator [145] for production of multi-jets and on PYQUEN [150, 148] for the scatterings of jets in the dense QCD-matter. The hard partons multiple scatterings are based on the cumulative energy loss via the gluon radiation associated with each scattering in the expanding quark-gluon fluid. The basic kinetic integral equation for the energy loss ΔE as a function of initial energy E and path length L has the form

$$\Delta E(L, E) = \int_0^L dl \frac{dP(l)}{dl} \lambda(l) \frac{dE(l, E)}{dl}, \quad \frac{dP(l)}{dl} = \frac{1}{\lambda(l)} \exp(-l/\lambda(l)), \quad (3.49)$$

where l is the transverse coordinate of a parton, dP/dl is the scattering probability density, dE/dl is the energy loss per unit length, $\lambda = 1/(\sigma\rho)$ is the in-medium mean free path, $\rho \propto T^3$ is the medium density at temperature T and σ is the integral cross section for the parton interaction in the medium. Both collisional and radiative energy loss are taken into account in the model. In Fig.3.8 are shown calculations for nuclear modification factor (left) and back-to-back correlations (right) with the HYDJET model for jet energy loss. A good agreement with data is observed.

The partonic collisional energy loss due to elastic scatterings is treated in the high momentum transfer limit [161, 162, 163]:

$$\frac{dE^{\text{col}}}{dl} = \frac{1}{4T\lambda\sigma} \int_{\mu_D^2}^{t_{\text{max}}} dt \frac{d\sigma}{dt} t, \quad (3.50)$$

where the dominant contribution to the differential scattering cross section is

$$\frac{d\sigma}{dt} \simeq C \frac{2\pi\alpha_S^2(t)}{t^2} \frac{E^2}{E^2 - m_p^2}, \quad \alpha_S = \frac{12\pi}{(33 - 2N_f)\ln(t/\Lambda_{\text{QCD}}^2)} \quad (3.51)$$

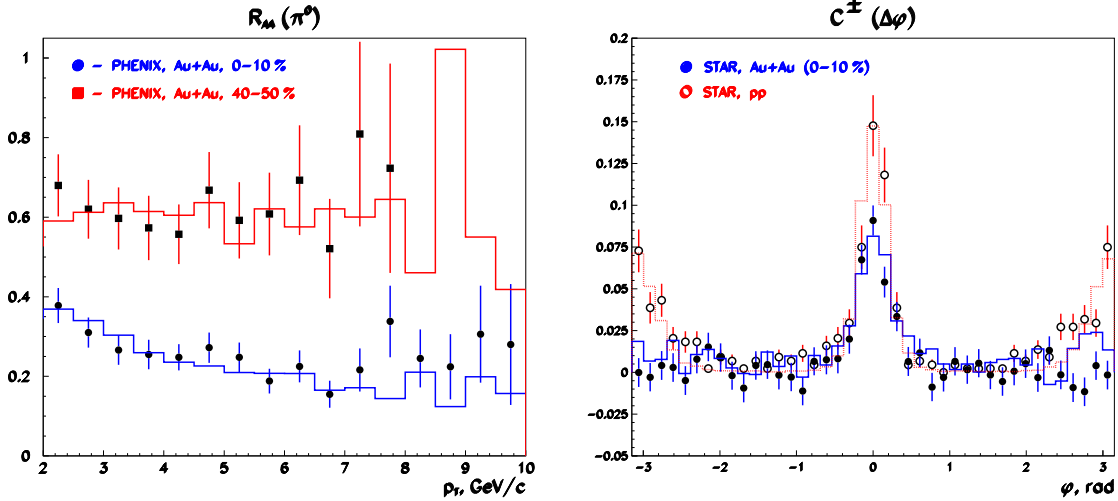


Figure 3.8: Left: Nuclear modification factor for π^0 in 0-10% and 40-50% central Au+Au collisions at $\sqrt{s_{NN}}=200$ GeV calculated with HYDJET(histogram) and compared to PHENIX measurements (solid symbols)[160]. Right: Back-to-back correlations in 0-10% central Au+Au and p+p collisions at $\sqrt{s_{NN}}=200$ GeV from HYDJET calculation(histogram) and STAR measurements (solid symbols) [49].

for the scattering of a hard parton with energy E and mass m_p off the "thermal" parton with energy (or effective mass) $m_0 \sim 3T \ll E$. Here $C = 9/4, 1, 4/9$ for gg, gq and qq scatterings respectively, α_S is the QCD running coupling constant for N_f active flavours, and Λ_{QCD} is the QCD scale which is of the order of the critical temperature of quark-hadron phase transition, $\Lambda_{\text{QCD}} \simeq T_c \simeq 200$ MeV. μ_D is the Debye screening mass $\mu_D^2(T) \simeq 4\pi\alpha_S T^2(1 + N_f/6)$ and is used for infrared regularization.

The partonic radiative energy loss is treated in the framework of the BDMS formalism [164, 165]. The energy spectrum of the coherent medium-induced gluon radiation and the corresponding radiative energy loss is:

$$\frac{dE^{\text{rad}}}{dl} = \frac{2\alpha_S(\mu_D^2)C_R}{\pi L} \int_{\omega_{\min}}^E d\omega \left[1 - y + \frac{y^2}{2} \right] \ln|\cos(\omega_1\tau_1)|, \quad (3.52)$$

$$\omega_1 = \sqrt{i \left(1 - y + \frac{C_R}{3}y^2 \right) \bar{k} \ln \frac{16}{k}} \quad \text{with} \quad \bar{k} = \frac{\mu_D^2 \lambda_g}{\omega(1-y)}, \quad (3.53)$$

where $\tau_1 = L/(2\lambda_g)$, $y = \omega/E$ is the fraction of the hard parton energy carried away by the radiated gluon, and $C_R = 4/3$ is the quark color factor. In this treatment, possible effects like double parton scattering and thermal gluon absorption are not considered. The angular spectrum of the emitted gluons used is a simple "small-angle" parametrization of the form

$$\frac{dN^g}{d\theta} \propto \sin\theta \exp\left(-\frac{(\theta - \theta_0)^2}{2\theta_0^2}\right), \quad (3.54)$$

where $\theta_0 \sim 5^\circ$ is the typical angle of the coherent gluon radiation estimated in [166]. Two other parametrizations ("wide-angle" $dN^g/d\theta \propto 1/\theta$ and "collinear" $dN^g/d\theta = \delta(\theta)$) can be also used as an option of the model.

The medium where partonic rescatterings occur is treated as a boost invariant longitudinally expanding quark-gluon fluid, and the partons are being produced on a hypersurface of equal proper times τ .

The mean number of jets produced in a nucleus-nucleus collision at a given impact parameter b is determined as

$$N_{AA}^{\text{jet}}(b, \sqrt{s}, p_T^{\text{min}}) = \int_{p_T^{\text{min}}} dp_T^2 \int dy \frac{d\sigma_{NN}^{\text{hard}}(p_T, \sqrt{s})}{dp_T^2 dy} \int_0^{2\pi} d\psi \int_0^\infty r dr \quad (3.55)$$

$$T_A(r_1)T_A(r_2)S(r_1, r_2, p_T, y), \quad (3.56)$$

where ψ is the azimuthal angle and $d\sigma_{NN}^{\text{hard}}(p_T, \sqrt{s})/dp_T^2 dy$ is calculated with PYTHIA and represents the differential cross section of a hard process in an NN collision with a minimum transverse momentum transfer of p_T^{min} . In HYDJET++ framework the

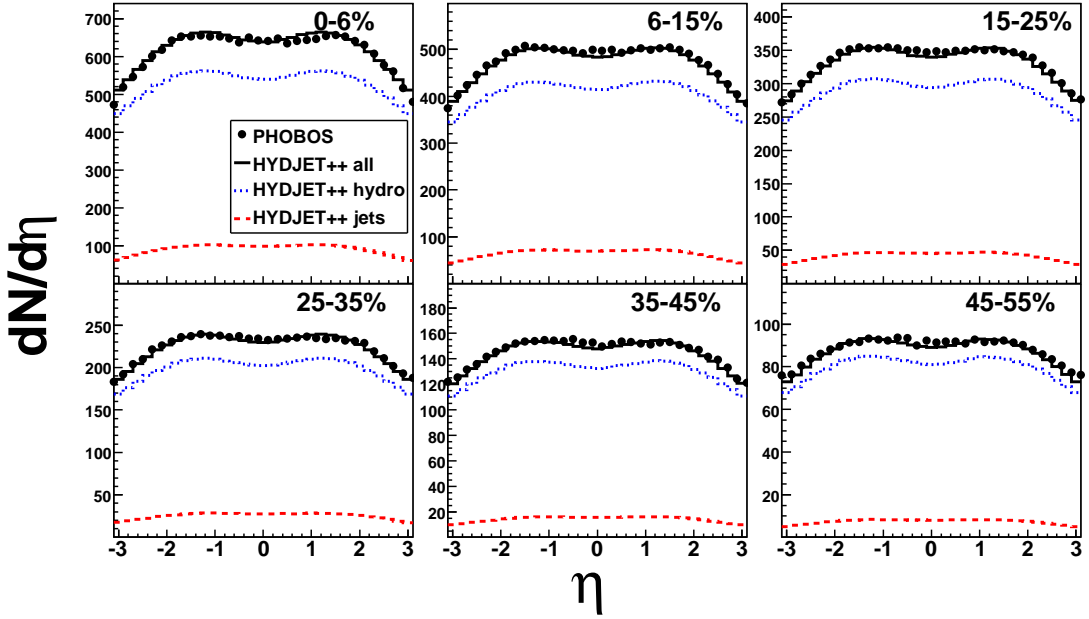


Figure 3.9: $dN/d\eta$ for charged hadrons in Au+Au collisions at $\sqrt{s_{NN}} = 200$ GeV for six centralities. The points are PHOBOS data [167] and histograms are HYDJET++ calculations.

partons produced in (semi)hard processes with momentum transfers lower than p_T^{min} are considered as being "thermalized", so their hadronization products are included in the soft part of the event. The soft and hard contributions to the total charged particle yields and to the invariant p_T spectra are shown in Fig.3.9 and Fig.3.10 respectively. The calculations are made for Au+Au collisions in different centrality intervals at $\sqrt{s_{NN}} = 200$ GeV. The factor $S \leq 1$ in Eq.(3.56) takes into account the effect of nuclear shadowing on parton distribution functions. It can be written as a product of shadowing factors for both of the colliding nuclei as

$$S(r_1, r_2, p_T, y) = S_A^i(x_1, Q^2, r_1)S_A^j(x_2, Q^2, r_2), \quad (3.57)$$

where $S_A^{i,j}$ is the ratio of nuclear to nucleon parton distribution functions for the parton of type $\{i, j\}$ (light quark or gluon), $x_{1,2}$ are the momentum fractions of the initial partons from the incoming nuclei which participate in the hard scattering characterized

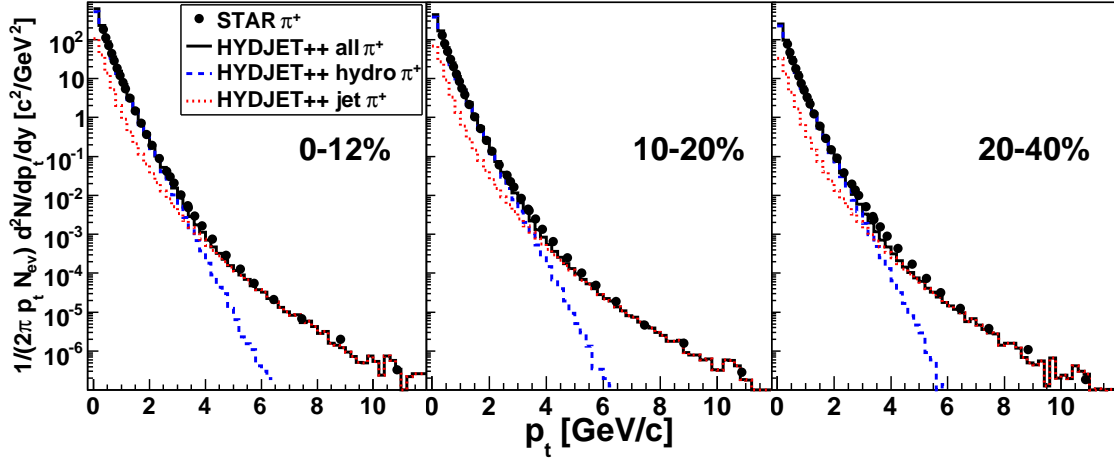


Figure 3.10: Invariant spectra for π^+ in Au+Au collisions at $\sqrt{s_{NN}} = 200$ GeV. The points are STAR data [168] and histograms are HYDJET++ calculations.

by the scale $Q^2 = x_1 x_2 s$, and $r_{1,2}$ are the transverse coordinates of the partons in their respective nuclei, so that $r_1 + r_2 = b$. This nuclear effect reduces the number of partons in the incoming hadronic wave-function of both the nuclei and thus reduces the total jet production cross section.

3.3.5 Shadowing corrections

The shadowing effect included in the model was estimated by using the Glauber-Gribov theory [169] where this phenomenon arises from coherent interaction of the projectile fluctuation on the target constituents and is closely related to the diffractive structure function of the nucleon. Due to the factorization theorem for hard processes in QCD, S_A^i describes the modifications of nuclear parton distribution functions such that:

$$f_{i/A}(x, Q^2, b) = f_{i/N}(x, Q^2) S_i(A, b, x, Q^2). \quad (3.58)$$

From summation of Pomeron fan diagrams the shadowing factor is found to be $S_A^i = 1/(1 + F^i(x, Q^2)T_A(b))$, where the effective cross section for quarks and gluon, respectively, is found to be

$$F^i(x, Q^2) = 4\pi \int_x^{0.1} dx_P \Pi(x_P) \begin{cases} \beta \Sigma^{\mathcal{D}}(\beta, Q^2) / \Sigma(x, Q^2) \\ \beta g^{\mathcal{D}}(\beta, Q^2) / g(x, Q^2) \end{cases}, \quad (3.59)$$

$$\Pi(x_P) = B(x_P) f_P(x_P) F_A^2(-x_P^2 m_N^2), \quad (3.60)$$

where $\Sigma^{\mathcal{D}}$ and $g^{\mathcal{D}}$ denote the quark-singlet and gluon diffractive parton distribution functions, Σ and g are the normal parton distribution functions, B and f_P are the slope of diffractive distribution and the Pomeron flux factor respectively, F_A is the nuclear form factor and x_P is the fraction of hadron momentum carried out by the Pomeron. The quark and gluon diffractive distributions are taken from the most recent experimental parametrizations by the H1 Collaboration [173], and the resulting shadowing factors are calculated in [25] and are implemented in the model (see figures 3.11 and 3.12).

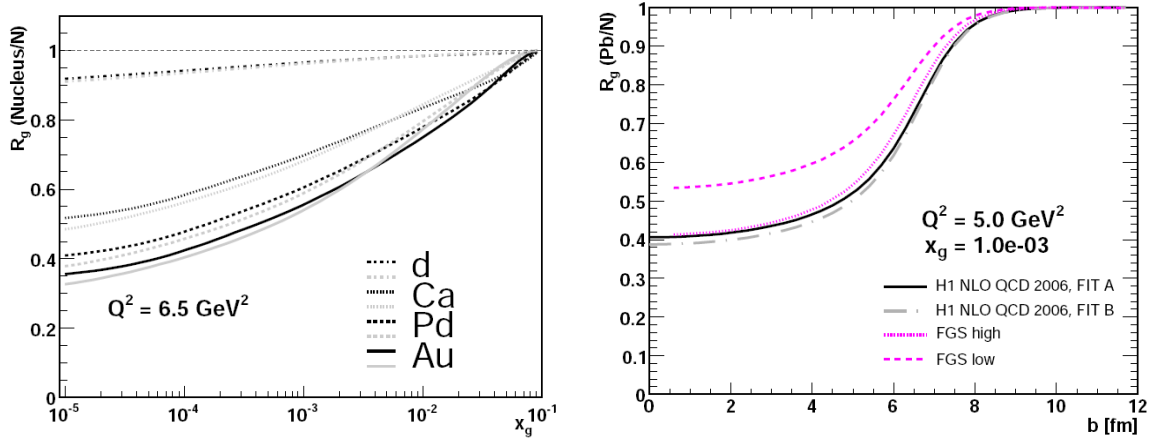


Figure 3.11: Left: Gluon shadowing dependence on x_g at a virtuality of $Q^2 = 6.5 \text{ GeV}^2$ for deuteron (dash-dotted curves), Ca (dotted curves), Pd (dashed curves) and Au (solid curves) [25]. Right: Impact parameter dependence of gluon shadowing in the Glauber-Gribov model [25] compared to the calculations of FGS [170].

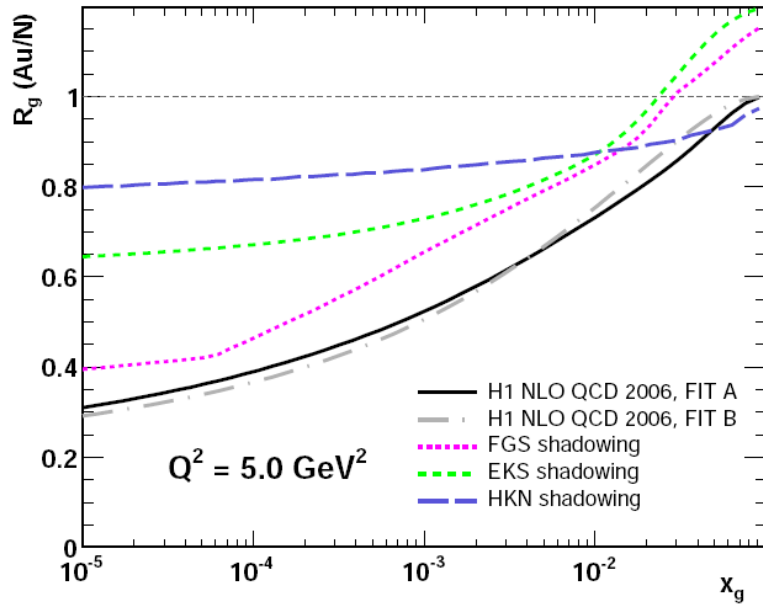


Figure 3.12: Comparison of the results of the Glauber-Gribov model with FGS model [170], EKS [171] and HKM [172] parametrizations.

3.3.6 Final hadrons

After all the hadrons are created, the decay of unstable particles is performed. The hadronic state in HYDJET++ consists of stable hadrons and resonances from the SHARE particle table [128] which contains 360 particles, excluding the not well established resonance states. The decay of unstable particles occur with a probability density of $\Gamma \exp(-\Gamma\tau)$ in the particle rest frame. Resonances are given the mass distribution according to a non-relativistic Breit-Wigner distribution

$$P(m)dm \propto \frac{1}{(m - m_0)^2 + \Delta m^2/2} dm, \quad (3.61)$$

where m_0 and Δm are the resonance nominal mass and width respectively. The Breit-Wigner shape is truncated symmetrically, $|m - m_0| < \Delta m$, with Δm taken for each particle from PYTHIA [145] ($\Delta m = 0$ for some narrow resonances not included in PYTHIA). The decay products are then boosted to the reference frame in which the freeze-out hypersurface was defined. The space-time coordinates of the decaying particle are shifted from the creation space/time point by their decay length/time. The branching ratios are also taken from the SHARE tables [128]. Only two and three body decays are taken into account in the model. The cascade decays are also possible.

Chapter 4

Experimental apparatus

The experimental results presented in this thesis were collected using the Broad Range Hadron Magnetic Spectrometer (BRAHMS) during the 62.4 GeV Au+Au run at the Relativistic Heavy Ion Collider. This chapter will give a description of BRAHMS experimental setup and also of the RHIC accelerator and the other three experiments.

4.1 RHIC and the experiments

The Relativistic Heavy Ion Collider is, at the moment, the newest working accelerator complex for heavy ion collisions and has the capability of delivering nucleus-nucleus collisions at a maximum energy of $\sqrt{s_{NN}}=200$ GeV, the highest energy available for heavy nucleus collisions. The previous heavy ion accelerators were using a single ion beam so only fixed target experiments have been possible. The most remarkable heavy ion experiments were built at GSI laboratory (Heavy Ion Synchrotron), at BNL (Alternating Gradient Synchrotron) and at CERN (Super Proton Synchrotron) sweeping a large interval of beam momentum ($1 < p_{\text{LAB}} < 158$ GeV/ c) but a relatively small center of mass energy ($1.9 < \sqrt{s_{NN}} < 17.3$ GeV).

4.1.1 A short description

The collider systems accelerate two beams in opposite directions and collide them at very precise locations where experimental setups are placed (interaction regions). This kind of design made possible a more than ten times leap in center of mass energy at RHIC.

RHIC [174] uses two ion beams ("blue" and "yellow") accelerated at a maximum beam energy of $E_{\text{LAB}} = 100$ GeV. A schematic view of RHIC is shown in Fig. 4.1. The RHIC ring has a circumference of about 3.8 km and consists of super-conducting quadrupole magnets for beam steering and radio frequency cavities for beam acceleration. The accelerator complex includes an ion source which produces partially electron stripped ions, a series of electron stripping devices and preaccelerators:

- Tandem accelerator which accelerates the beam up to 1 MeV/u;
- A Booster which injects the beam into AGS at 95 MeV/u; and
- AGS which accelerates the beam up to 10.8 GeV/u and injects it into RHIC.

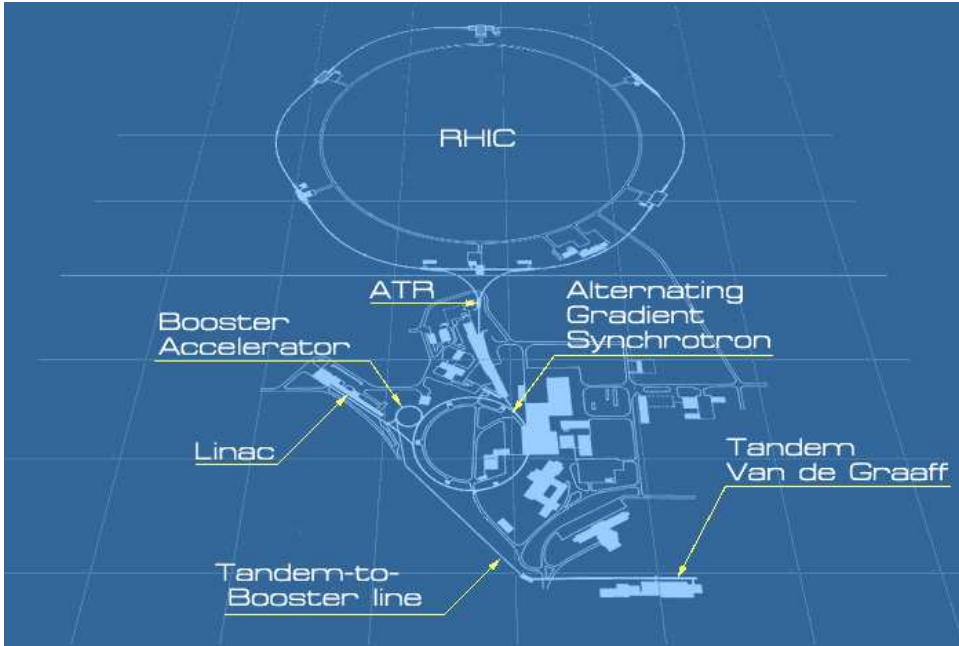


Figure 4.1: The Relativistic Heavy Ion Collider (RHIC) accelerator complex [174] at Brookhaven National Laboratory(BNL).

At the AGS/RHIC injection point the ions are divided into two beams circulating in opposite directions which intersect at six locations where the experiments are placed. Each beam contains up to 60 bunches with $\sim 10^9$ ions each. The design luminosity is $\mathcal{L} = 2 \cdot 10^{26} \text{cm}^{-2}\text{s}^{-1}$ and the reaction rate is $R = \mathcal{L} \times \sigma \simeq 1200 \text{ Hz}$ which gives a probability for collision overlapping smaller than 0.03% per collision event. The systems accelerated up to now by RHIC are Au+Au, d+Au, p+p and Cu+Cu at $\sqrt{s_{NN}} = 200, 130, 62.4$ and 22 GeV.

4.1.2 The heavy ion experiments

RHIC provides 6 beam intersection regions but only 4 are occupied by heavy ion experiments. The two largest experiments, STAR and PHENIX, are located at 6 and 8 o'clock respectively. The other two experiments, PHOBOS and BRAHMS, are located at 10 and 2 o'clock respectively.

Solenoidal Tracker at RHIC (STAR)

The STAR experimental setup [175] was designed for measurements of hadron production over a large solid angle. It consists of detector systems for charged particle tracking (Silicon Vertex Tracker(SVT) and a large Time Projection Chamber (TPC)), momentum measurements (a room temperature solenoidal magnet) and particle identification (TPC, Cherenkov detector, Time of Flight (TOF) detector). The STAR setup acceptance extends continuously in a large interval around mid-rapidity ($|\eta| \leq 1.8$ with TPC only) and has full azimuthal coverage which makes it particularly well suited for event-by-event characterization of heavy ion collisions. The measurement of multi-strange hyperons is also possible with its silicon pixel tracker (SVT).

be done by using two midrapidity spectrometer arms composed of silicon pad detectors and a time-of-flight wall to extend the particle identification. PHOBOS has also the unique capability of measuring the charged particles at very low transverse momenta ($p_T < 100\text{MeV}$).

4.2 The BRAHMS experiment

The BRAHMS experiment [178] was designed for detailed measurements of charged hadrons over a wide range of rapidity and transverse momentum. The experiment consists of a set of global detectors for event characterization and two movable spectrometer arms for momentum measurements and particle identification (PID) over a wide phase space region. A schematic picture of BRAHMS experimental design is shown in Fig. 4.4. BRAHMS has the unique feature at RHIC of identifying charged particles up to very forward rapidities ($y \sim 3.5$) and high transverse momenta due to its Ring Imaging Cherenkov (RICH) detector [179]. This section gives a review of BRAHMS components.

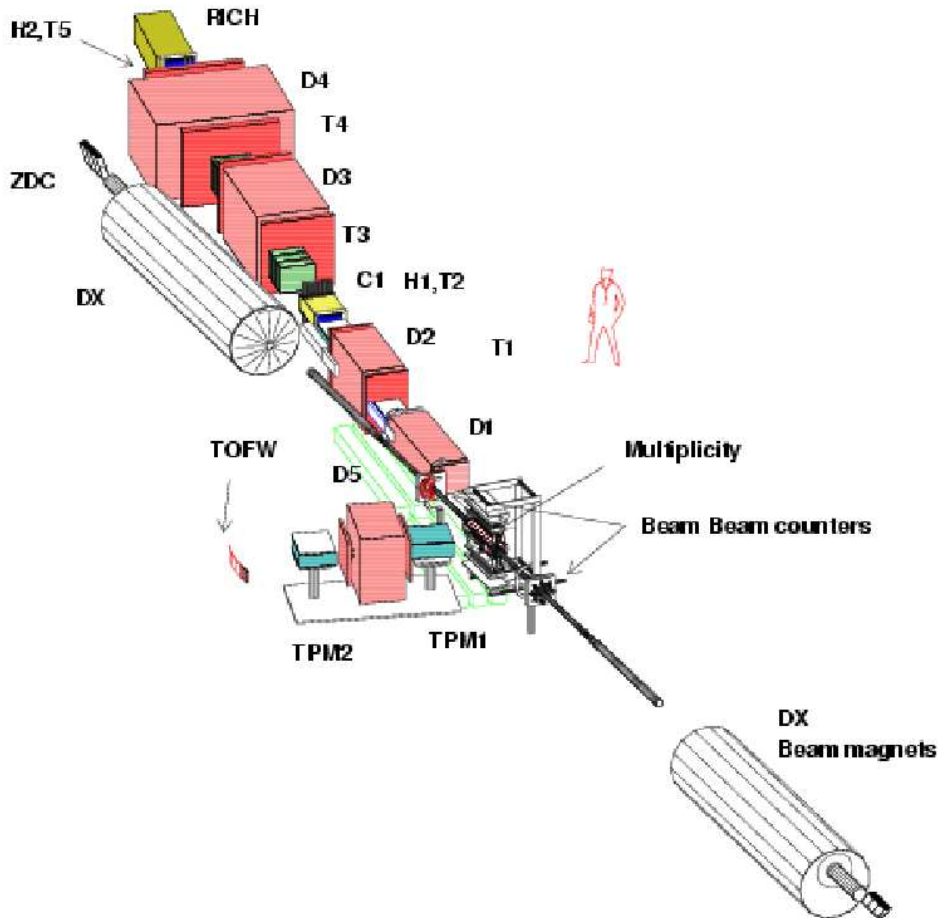


Figure 4.4: The BRAHMS experiment detector system [178].

4.2.1 Global detectors

The global detectors are used for general event characterization, *i.e.* centrality, triggering, vertex measurement. BRAHMS is composed of three sets of global detectors: the multiplicity array(MA) for multiplicity measurement around mid-rapidity, the beam-beam counters (BBC) for start-time, vertex and multiplicity measurements, and the zero-degree-calorimeters (ZDC) for spectator multiplicity measurement.

Multiplicity Arrays

The MA detector is composed of two sets of detectors arranged as hexagonal barrels around the beam axis (see Fig. 4.5). The inner barrel is made of Si strip detectors (SMA) while the outer one is made of scintillator tiles (TMA). These detectors are capable of measuring the energy lost by the passing charged particles which gives a measure for the multiplicity. The multiplicity measured event-by-event with this detector is used to estimate the collision centrality. The segmentation of the detector allows for pseudo-rapidity dependent measurements of the charged multiplicity in the interval $\eta \leq 2.2$ which corresponds to $12.6^\circ < \theta < 167.4^\circ$ seen from the nominal interaction point. The cylindrical setup gives also the possibility of measuring azimuthal depen-

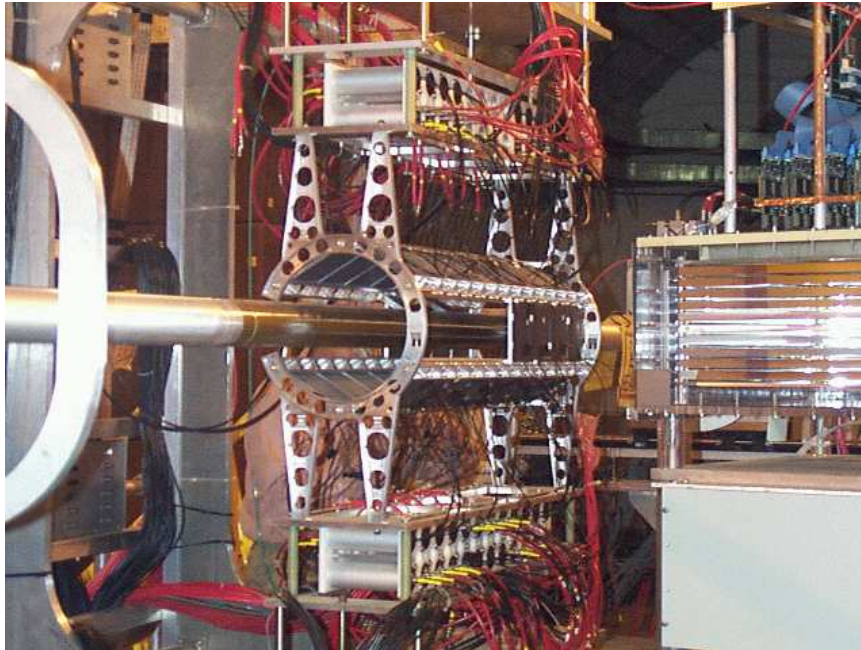


Figure 4.5: The Multiplicity Array(MA) placed around the beam pipe at the nominal interaction point(IP).

dence of the multiplicity distribution crucial in finding the reaction plane for elliptic flow analysis.

Beam-Beam Counters

The BBCs are located on either side of the event vertex at 219 cm from the nominal IP and very close to the beam pipe (see Fig. 4.6). They consist of two different sized Cherenkov radiators glued to photo-multiplier tubes. The small tubes are optimized so that they have a big probability to get single hits in heavy ion collisions while the big

tubes have a high probability of getting multiple hits useful for charged multiplicity measurements. The BBC tubes are placed at nominal pseudo-rapidities of 3.1, 3.4 and 3.6 but the coverage is in reality continuous and larger due to event vertex spread. Apart from the multiplicity measurements, due to its very good time resolution (\sim

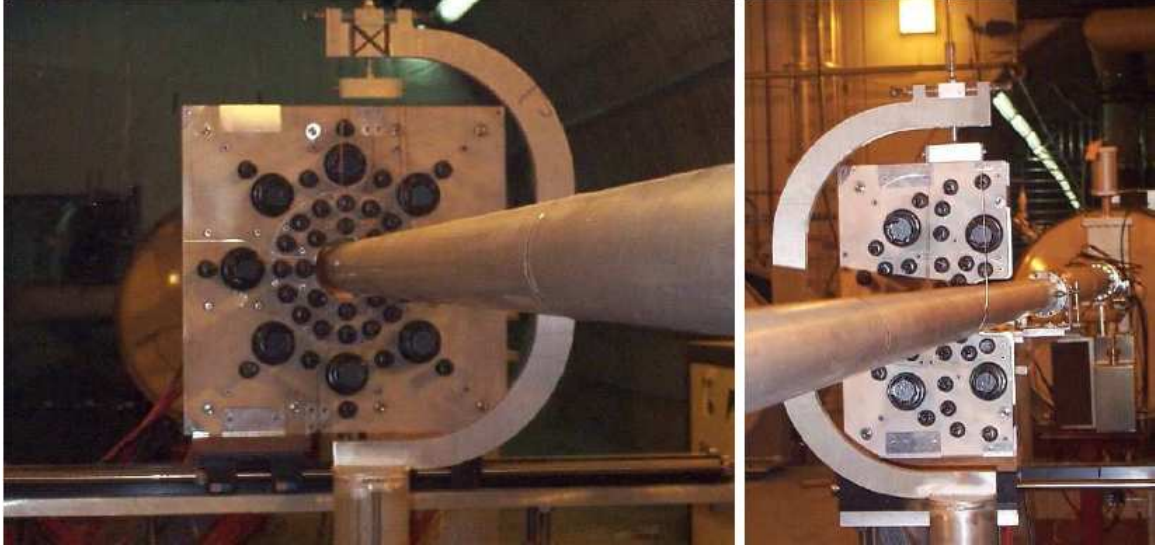


Figure 4.6: The Beam-Beam Counters (BBC) placed around the beam pipe at ± 219 cm from the nominal IP.

50ps) this detector provides a start time for time-of-flight measurements and a level 0 trigger. The event vertex position can also be determined with a 1.5 cm accuracy from the difference in arrival times of the fastest particles to reach the two arrays.

Zero-Degree Calorimeters

The ZDC detectors are common to all four RHIC experiments and they provide luminosity measurements. Their location is behind the DX RHIC magnets on both sides of the interaction vertex at about 18 m from the nominal IP (see Fig. 4.7). The ZDCs measure the total energy of spectator neutrons in a very narrow cone ($\theta \sim 2\text{mr}$) around the beam axis making them useful for collision centrality measurements and for providing a minimum bias trigger in peripheral events. The difference in arrival times of the spectator neutrons reaching the two arrays also gives an estimation of the event vertex.

4.2.2 The Spectrometers

The BRAHMS mobile spectrometers are placed on either side of the beam pipe, FS being in the interior of the RHIC ring while MRS is placed in the exterior of the RHIC ring. The MRS is placed so that it can measure particles around mid-rapidity ($|\eta| < 1.5$) while FS covers the forward rapidity region up to $\theta = 2.3^\circ$ or $\eta \sim 3.9$.

Mid-Rapidity Spectrometer

The MRS has a geometric acceptance of 6.5 msr and can be rotated in the range $30^\circ < \theta < 95^\circ$. The tracking is done by using two Time Projection Chamber detectors,



Figure 4.7: The Zero-Degree Calorimeters (ZDC) placed between the two beam pipes at 18 m on each side of the nominal IP.



Figure 4.8: Left: The Mid-Rapidity Spectrometer(MRS). From left to right, TPM1, D5, TPM1 and TOFW are visible in the picture. Right: The Forward Spectrometer(FS) photographed from the far end. The RICH detector is at the left of the picture and the magnets D4 and D3 (blue colored) are also visible.

TPM1 and TPM2, placed in front of and behind the D5 dipole magnet which is used for momentum measurement. The spectrometer also consists of two Time of Flight detectors, TOFW and TFW2, which are used for particle identification. Figure 4.8 left shows a photograph of the MRS.

Forward Spectrometer

The FS is a larger spectrometer than MRS due to the higher typical momentum measured at forward angles. It can be divided into two parts which can be rotated independently. The Front FS (FFS) can be rotated from 2.3° up to 30° while the Back FS (BFS) can be rotated from 2.3° up to only 15° due to limitations on the experimental hall size. The FS has an aperture of 0.8 msr. FS consists of four dipole magnets, D1-D4, for sweeping and analyzing charged particles emerging from the reaction, and five tracking chambers, T1-T5, for tracking and momentum measurements. T1 and T2 are TPCs while T3, T4 and T5 are Drift Chambers (DC). A photograph illustrating FS can be seen in figure 4.8 right.

The particle identification is based on two TOF hodoscopes, H1 and H2, and two Cherenkov detectors (C1 and RICH). H1 and H2 are composed of scintillator slats instrumented with two phototubes, one on either end. H1 is placed at 8.6m and H2 is placed at 19m distance from the nominal IP. The C1 detector is placed behind H1 and RICH is located at the back end of FS and is used for identifying high momentum particles.

4.2.3 Tracking components

Time Projection Chambers

The TPCs are used as three-dimensional tracking detectors. They are square boxes filled with gas mixtures which are ionized when charged particle pass through the detector volume. The electrons created along the particle trajectory drift towards the TPC anode wires due to an electric field which is uniform throughout most of the drift volume. In the strong electric field around the anode wires, the primary electrons trigger avalanches of secondary electrons which are collected by wires. The remaining, positive space charges (partially ionized atoms) induce mirror charges on the pads in the read out plane, which is the detected signal. A three-dimensional point is generated based on the pad, row and drift time (the drift velocity is constant).

The BRAHMS setup has four TPCs. Two of them belong to MRS (TPM1 and TPM2) and the other two are placed in FFS (T1 and T2). Their intrinsic position resolution is better than $400\mu\text{m}$ and the two-track resolution is better than 15mm. An illustration of a TPC can be seen in Fig. 4.9 left. The TPCs operate outside of the magnets fields which means that the local tracks are straight lines. TPM1 and TPM2 are placed in front and at the back of D5 in MRS. T1 and T2 are located in front and at the back of the D2 magnet.

Drift Chambers

The DCs, like the TPCs are also detectors with gaseous active volume. The DCs are wire chambers, each of them having three modules with 8-10 planes arranged in 4 different "views" which correspond to wire directions, x (horizontal), y (vertical), u and v ($\pm 18^\circ$ with respect to y). The combination of the 4 views gives unambiguous

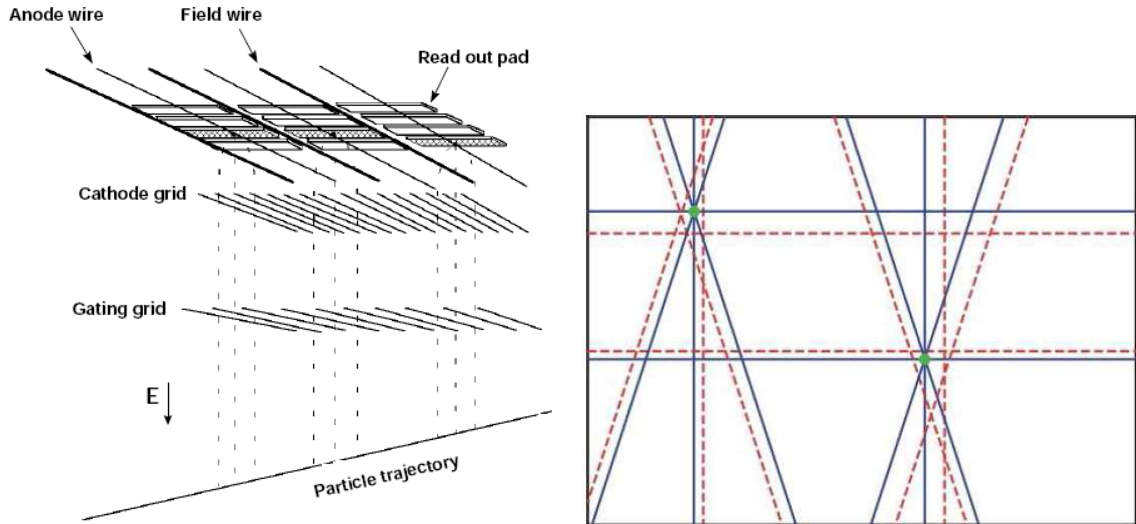


Figure 4.9: Left: Schematic picture of the TPC readout plane and electron drift lines. Right: DC shown from its front and views are x , y , u and v (intermediate angles). The two tracks visible (green dots) are defined by the intersection of the solid lines.

3-dimensional information about the track positions. A schematic picture of a DC is shown in Fig. 4.9 right. The position resolution achieved is $\sim 82\mu\text{m}$ and the two track resolution is 10mm. BRAHMS employ three DCs, all of them being located in the BFS arm (T3, T4 and T5). T3 and T4 are placed in front and at the back of the D3 magnet, while T5 is placed at the back of the D4 magnet.

Magnets

In order to make momentum measurements BRAHMS uses magnets placed in between two tracking devices. The charged particles are bent in the magnetic field of the magnet in the x - z plane and the deflection angle is measured with the help of the tracking chambers. The experimental setup has 5 dipole magnets, D1-D5. The D5 magnet is placed in the mid-rapidity spectrometer for measuring the relatively lower momentum charged particles emitted in this part of phase space. The D1-D4 magnet array are positioned in FS in order to select and characterize higher momentum particles.

4.2.4 PID devices

Time of Flight detectors

The TOF detectors are based on measuring time of flight of a particle from the vertex point to the detector. In order to achieve this, the TOF detectors rely on the BBCs to get the start time. Each of the TOF detectors consists of scintillator slats placed in a densely packed array so that dead zones are minimized. Each of the scintillators is coupled to a photo-tube (PMT) at each end that can provide timing and energy information. A photograph of TOFW and a schematic illustration of H1 are shown in Fig. 4.10. The timing resolution of the TOF detectors is 65 ps. By knowing the time of flight from the TOF detectors and the path length from tracking, the particle velocity can be determined. When the velocity and momentum are known, the particle mass

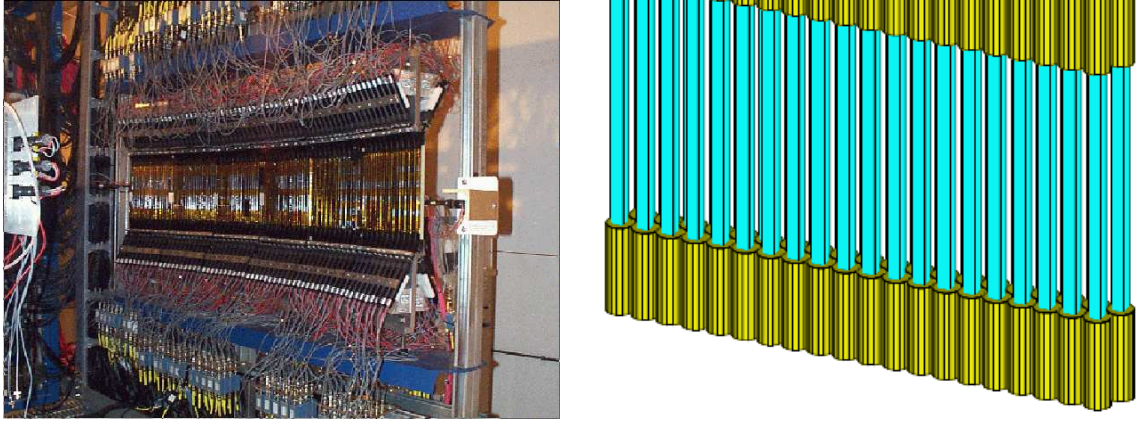


Figure 4.10: Left: Photograph of the Time of Flight Wall. Right: Schematic representation of H1 showing only the scintillator slats and the photo-tubes.

can be extracted, and particle identification is possible up to some momentum limits depending on the intrinsic timing resolution of the detectors and on the trajectory length.

BRAHMS uses four time of flight detectors. TOFW and TFW2 are placed at the back end of the MRS at 4.3 m from the nominal IP. The other two hodoscopes, H1 and H2, are positioned in FS, at the back of FFS and BFS, respectively. H1's position is at 8.7 m while H2 is located at 18.6 m from the interaction point.

Cherenkov detectors

The detection in this type of devices is based on measuring the Cherenkov light emitted by fast particles passing the sensitive volume. The Cherenkov detectors are filled with a gas having a very precisely controlled refractive index that sets the velocity threshold for measured particles. The particle velocity is obtained from the angle of the emitted Cherenkov photons, which is then used together with the track momentum for particle identification. BRAHMS is using two detectors of this type to extend the PID range in FS, C1 and RICH (see figure 4.11). C1 is placed behind H1 and is used to veto pions at a momentum higher than the H1 π/K separation threshold. RICH [179] is a ring imaging Cherenkov detector and is positioned at the back of FS at about 20 m from the nominal interaction point. It is designed mainly for high momentum particles. RICH has a focusing mirror at the back of the gas vessel which reflects Cherenkov light onto rings in the focal plane, which is highly segmented with PMT detectors. The ring radii measured in this way are dependent on the particle velocity, which again depends on mass and momentum, making identification possible.

4.2.5 Triggers

The triggers represent conditions which must be fulfilled in order for an event to be read-out and stored. They are applied from more reasons but the most important one is the need to define the minimum experimental signal that define a collision (minimum

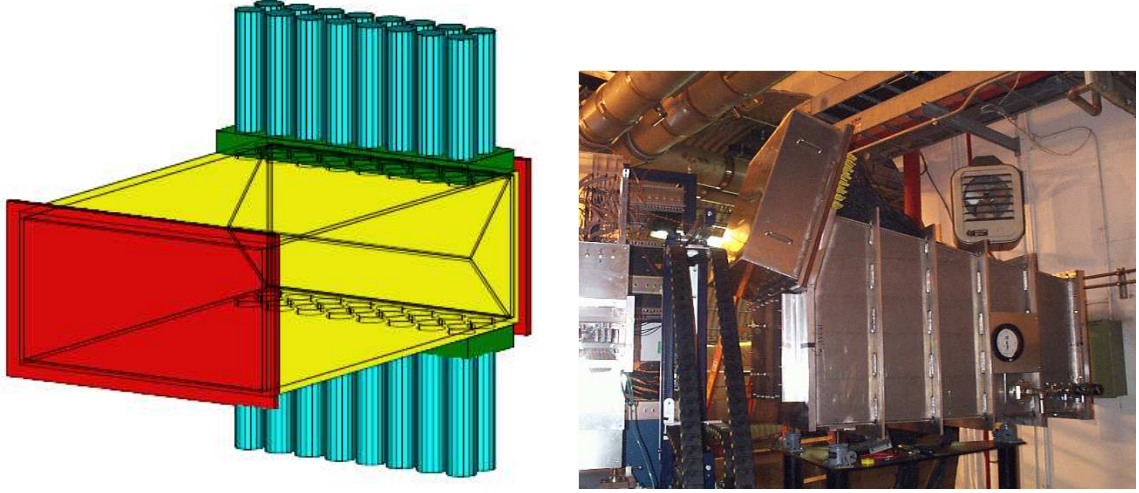


Figure 4.11: Left: The Cherenkov detector C1. Right: the Ring Imaging Cherenkov detector.

Trigger #	Condition	Description
1	$BBL \geq 1 + BBR \geq 1$	Min. bias in 0-30% centrality
2	Trig.1 + TR-FS + H1 + RC	FFS track trigger
3	ZDC + TR-MRS + TOFW	MRS track trigger
4	ZDC(wide) + RC	Min. bias in peripheral collisions
5	ZDC(CFD) + RC	Not used in this analysis
6	ZDC(CFD) + TR-FS + H1 + RC	FFS track trigger
7	Pulser	Pulser used for calibration
8	RHIC clock	Synchronization trigger

Table 4.1: Trigger definitions for the Au+Au at $\sqrt{s_{NN}} = 62.4$ GeV run.

bias condition). This is done by requiring coincident hits in the BB or ZDC arrays. The triggers are used also for the selection of "interesting" events with tracks in the spectrometer arms to be recorded on tape since a limited event rate can be handled by the Data Acquisition System (DAQ). For this purpose, scintillator trigger slats are mounted in front of both spectrometer arms. The optimization of data taking and the reduction of the recorded event rate to manageable values is done also through a set of scale-down factors corresponding to each trigger. The list of triggers used in the present analysis together with a short description is shown in table 4.1.

4.2.6 Acceptance

The solid angle seen by BRAHMS spectrometers is very small due to their design. However by changing the magnetic field and the angle of the spectrometers, BRAHMS can sweep a wide range of rapidities and momenta. Higher magnetic fields open the spectrometer to high momentum particles while lower fields open the spectrometer to smaller momentum particles. By changing the spectrometers angle, BRAHMS can shift also the rapidity window over a large interval (*e.g.* $0 \leq y \leq 3.9$ for pions). In figure 4.12 one can see the design acceptance of identified pions, kaons and protons with the BRAHMS experimental setup in the y - p_T space. The different colors and fill styles correspond to areas covered by specific PID detectors. In MRS, by using TOFW, the pions and kaons can be separated up to a full momentum of $\sim 2.5\text{GeV}/c$. The protons can be further separated up to $\sim 3.5\text{GeV}/c$. In FS, H2 can make π/K separation up to $\sim 5\text{GeV}/c$ due to a larger distance to the nominal IP than TOFW. The protons can be separated up to $\sim 8.5\text{GeV}/c$. The RICH detector extends the PID capabilities up to $\sim 20\text{GeV}/c$ for pions and kaons and up to $\sim 30\text{GeV}/c$ for protons.

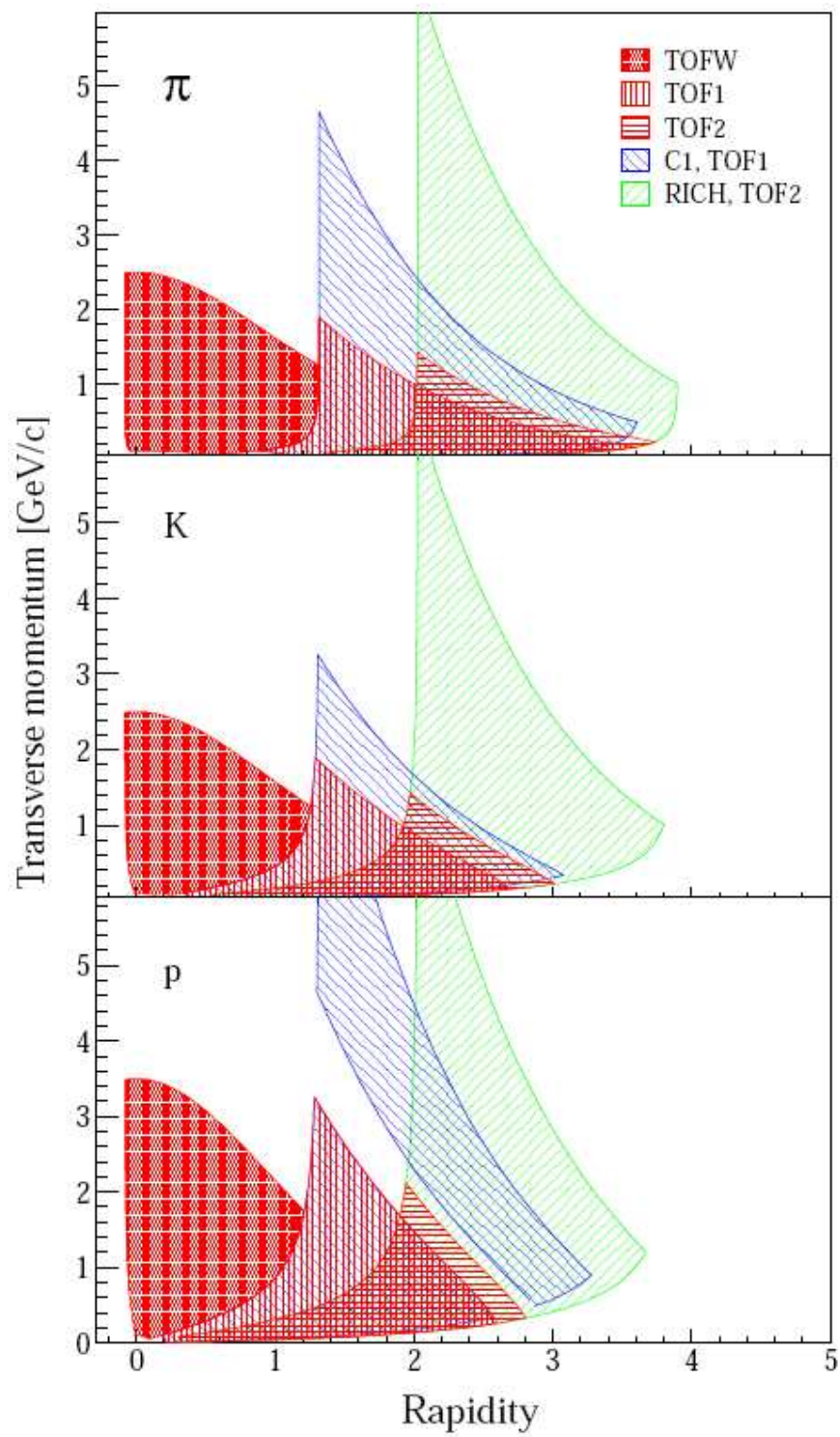


Figure 4.12: BRAHMS design acceptance for pions, kaons and protons.

Chapter 5

Data analysis

The data acquired by the Data Acquisition System (DAQ) during the experimental runs consists of energy and time signals from the detectors. The raw data must be processed in order to obtain the physical information. This chapter gives a detailed description of the data reconstruction with a focus on the particle identification methods employed.

5.1 Event characterization

5.1.1 Vertex determination

The collider experiments represent a huge step in energy for nuclear collisions due to the fact that all the beam energy from the laboratory frame is available in the center of mass system of the collisions. There are also some drawbacks to this, one of them being the fact that by trying to collide two beams, the collision coordinates are not fixed anymore like in the fixed-target experiments (SIS, AGS, SPS). At RHIC, the interval where the collisions take place is of the order of 1 m and is centered around a nominal interaction point (IP). The collisions coordinate (*vertex*) are defined relative to this point.

The acceptance of the Multiplicity Array is vertex dependent, and the event vertex is used to correct the event multiplicity measured with the MA, which in turn is crucial for defining the event centrality. The time-of-flight method for particle identification uses the collision coordinate together with the particle trajectory to determine the path length. In global tracking, the vertex is used to constrain tracking algorithms and also to select the primary tracks (particles emerging from the collision vertex).

The vertex measurements are done by using detectors placed on both sides of the IP, namely the Beam-Beam Counters and the Zero Degree Calorimeters. The difference in averaged arrival times from the detector arrays on both sides is used to calculate the position of the vertex as shown below:

$$Z_{\text{vertex}} = (\langle t_L \rangle - \langle t_R \rangle) \times \frac{c}{2} - Z_{\text{offset}}. \quad (5.1)$$

The particles are considered to travel with the speed of light (c). The $\langle t_{L,R} \rangle$ are the arrival times obtained from the left and right array, respectively, and Z_{offset} is an overall offset of the measurement.

The resolution of the vertex measurements and the offset can be studied by using the projection of the MRS tracks on the $y-z$ plane of the beam. The vertex resolution from BBC was studied for different tube configurations and is illustrated in figure 5.1. The

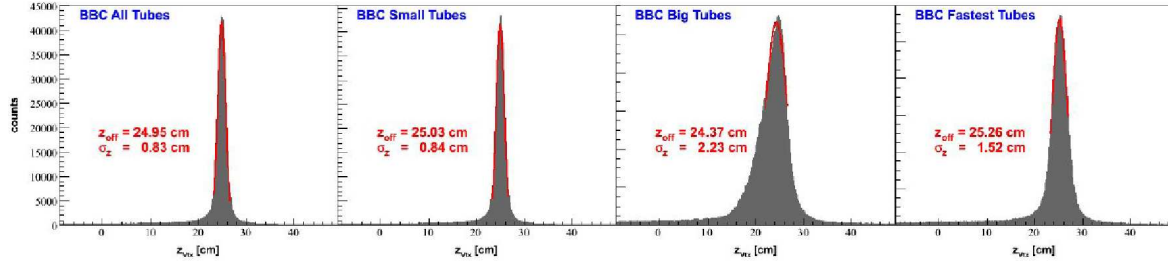


Figure 5.1: BBC vertex resolution and offset determined by small tubes, big tubes and fastest tubes. Picture taken from [180]

best resolution was found when the small tubes are used ($\sigma_z \sim 0.8$ cm) and the worst resolution is given by the big tubes ($\sigma_z \sim 2.2$ cm). However, all the methods are used

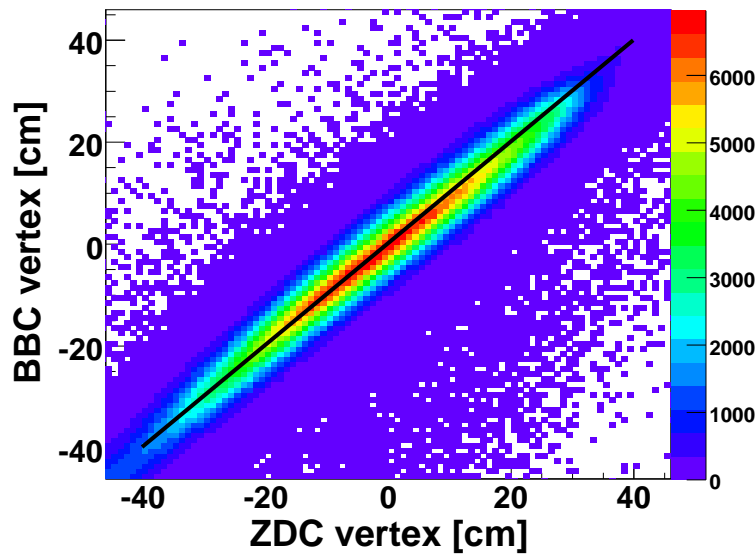


Figure 5.2: BBC and ZDC vertex measurements correlation.

in the analysis because in low multiplicity events (peripheral or low energy collisions) the small tubes have a smaller probability to get hits. This implies a slow decrease in vertex resolution towards peripheral collisions. ZDC detectors have 3 modules in both left and right arrays and use the same method in finding the vertex with a resolution of approximately 2-3 cm. A comparison between the vertex measurements from BBC and ZDC can be seen in figure 5.2. More detailed studies of the BBC calibrations and vertex measurements can be found in [4, 86].

Data selection

The collision vertex is varying in a wide interval but a cut is applied so that only events with a BBC vertex in the interval $-20 < Z_{BBC} < +20$ cm are selected. The choice of this narrow interval is due to the decrease of the MA detector efficiency far away from the nominal vertex and also due to the geometrical acceptance of the spectrometers.

5.1.2 Centrality determination

The impact parameter b of the nucleus-nucleus collisions is a very important piece of information because most of the physical observables (*e.g.* multiplicities, p_T spectra, flow, HBT radii) depend on it. In experiment however the impact parameter cannot be measured directly but it can be estimated indirectly by using its approximate correlation with observables like the number of produced charged particles or the number of spectator neutrons seen at beam rapidity. The left panel of figure 5.3 shows

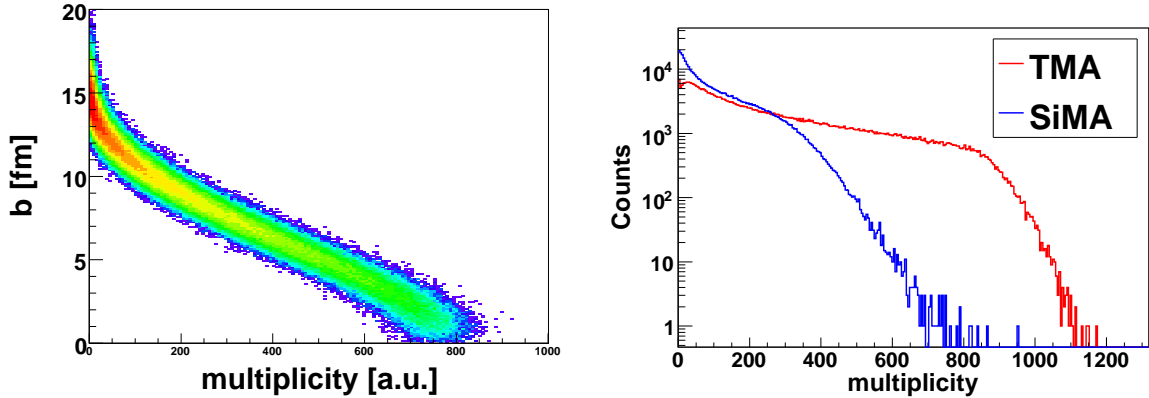


Figure 5.3: Left: Correlation between mid-rapidity charged particle multiplicity in the MA acceptance and impact parameter from Au+Au collisions at $\sqrt{s_{NN}} = 62.4$ GeV calculated using the AMPT model. Right: Charged particle multiplicity distribution measured with TMA and SiMA in minimum bias events (trigger 1).

a correlation between the charged particle multiplicity measured at mid-rapidity and the impact parameter in Au+Au collisions at $\sqrt{s_{NN}} = 62.4$ GeV calculated using the AMPT model briefly described in section 3.2. In order to estimate the centrality, BRAHMS is using the charged particle multiplicity measured with the MA detector in the pseudo-rapidity interval $|\eta| < 2.2$ (see right panel of figure 5.3). The charged particle distribution is then used to define centrality intervals in fractions of the total cross section seen by the minimum bias trigger. The most central events are the events with the highest multiplicities. The connection between a centrality interval and the impact parameter range probed is done by using a theoretical model (HIJING) together with a BRAHMS GEANT simulation. The impact parameter range corresponding to a centrality interval is dependent on the fraction from the total cross section covered by the minimum bias trigger and also on the theoretical model used.

Figure 5.4 shows the centrality distribution for Au+Au collisions at $\sqrt{s_{NN}} = 62.4$ GeV obtained by using two different minimum bias triggers. Ideally, if all the cross section would be covered, the two distributions should be independent on centrality. In reality, trigger 4 (ZDC) is less efficient in very central collisions because there are fewer single spectator neutrons which can be detected in the ZDC. In peripheral collisions, trigger 1 becomes inefficient because of the low charged particle multiplicity. Trigger 4 becomes also inefficient in peripheral collisions probably because part of the spectator neutrons which emerge from the reaction are bound in charged nuclear fragments and are deflected in magnetic fields. As a consequence, the experimental minimum bias trigger does not cover the full nucleus-nucleus reaction cross section meaning that the normalization constant for a no bias analysis is smaller than what it

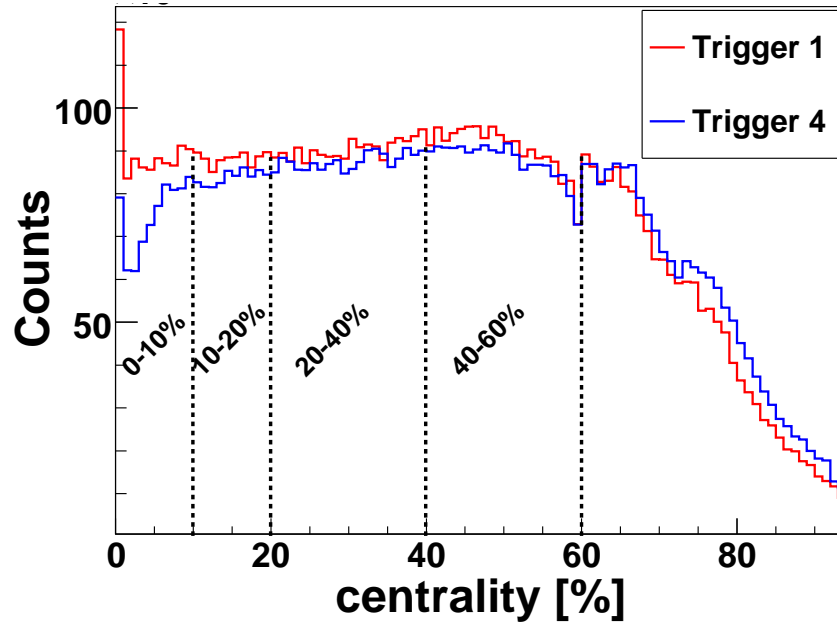


Figure 5.4: Centrality distribution using triggers 1 (BB) and 4 (ZDC).

should be. This always leads to higher yields than in reality. The minimum bias trigger inefficiency was estimated by using the HIJING model and a GEANT simulation of the BRAHMS trigger detectors. For the Au+Au at $\sqrt{s_{NN}} = 62.4$ GeV data set, the minimum bias trigger inefficiency was found to be $90 \pm 5\%$.

The number of participant nucleons, N_{part} , and the number of binary collisions, N_{coll} , can be also extracted from a Glauber-type theoretical model. These numbers are important when comparing observables in different centrality bins.

Data selection

The events selected for this analysis satisfy the minimum bias trigger and also the track trigger. The minimum bias trigger used is trigger 1 (as defined in Table 4.1) for events in the centrality range 0-30% and trigger 4 for events with centrality higher than 30%. The track trigger is trigger 2 for FS and trigger 3 for MRS. The centrality slices selected are shown in figure 5.4 and are 0-10%, 10-20%, 20-40% and 40-60%. The most peripheral events, with centrality higher than 60%, are not used in this analysis due to normalization problems raised by the minimum bias trigger inefficiency.

5.2 Tracking

Tracking is the process through which the hits registered by the TPC and DC devices are converted into particle trajectories. Every tracking device produces a local track which is then matched to another local track from the same event to construct a global track. Particle trajectories are then used for charge and momentum determination and also for species identification. The momentum and charge of the particles are determined with the help of magnets which deflect the charged particles in their magnetic field. The tracking algorithms are described in more detail in [4, 86, 19, 181, 182] and here we will give only a brief description.

5.2.1 Local tracking

Tracking chambers work by registering space-time coordinates of the hits due to passing charged particles which ionize the gas in the detector volume. The space coordinates are determined based on the chambers segmentation and by knowing the drift velocity of the electrons liberated by gas ionization. The hits obtained in this way are combined into track candidates using a "follow-your-nose" search algorithm (see figure 5.5) and are finally fitted to one or more linear trajectories. Local tracking is subject to the

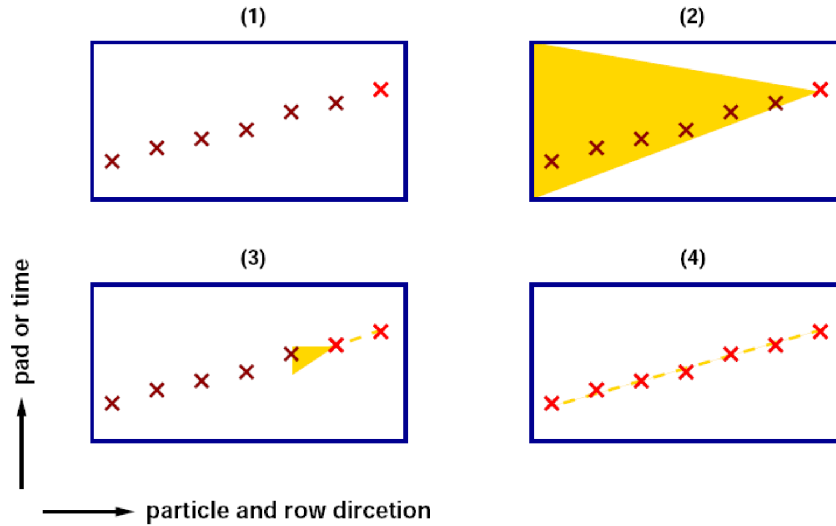


Figure 5.5: Illustration of the track finding algorithm. Picture taken from [4]

variation of many parameters which need to be carefully controlled and accounted for. The most important is the drift velocity which depends on the pressure of the gas and sometimes also on the position (*e.g.* non-uniformities may occur at the edges of the chambers).

5.2.2 Matching and global tracking

Matching

Tracking chambers can reconstruct many local tracks in a given event including background tracks not originating from the event vertex. In order to obtain global tracks and ensure background removal, a number of matching conditions must be imposed on the local tracks. Figure 5.6 shows schematically the geometry of the matching tracks in the $x - z$ plane. In the figure, two tracking chambers are placed in front and at the back of a magnet. In the $x - z$ plane, the local tracks are characterized by the angles θ_f (front) and θ_b (back) with respect to the z axis. The points F and B correspond to the intersections between the track and the effective front and back magnet edges, respectively. The magnetic field in the magnet is considered to have only the y component so the track is bent only in the $x - z$ plane. Inside the magnetic field, the $x - z$ projection of the trajectory is circular and outside is considered to be linear. The plane defined by the y axis and the normal to the $|FB|$ segment is the matching plane. The ψ_f and ψ_b are the angles made by the $|FB|$ segment with the front and back local tracks, respectively. The θ angle represents the deflection angle in the magnetic field and ω is the angle between the x axis and the matching plane.

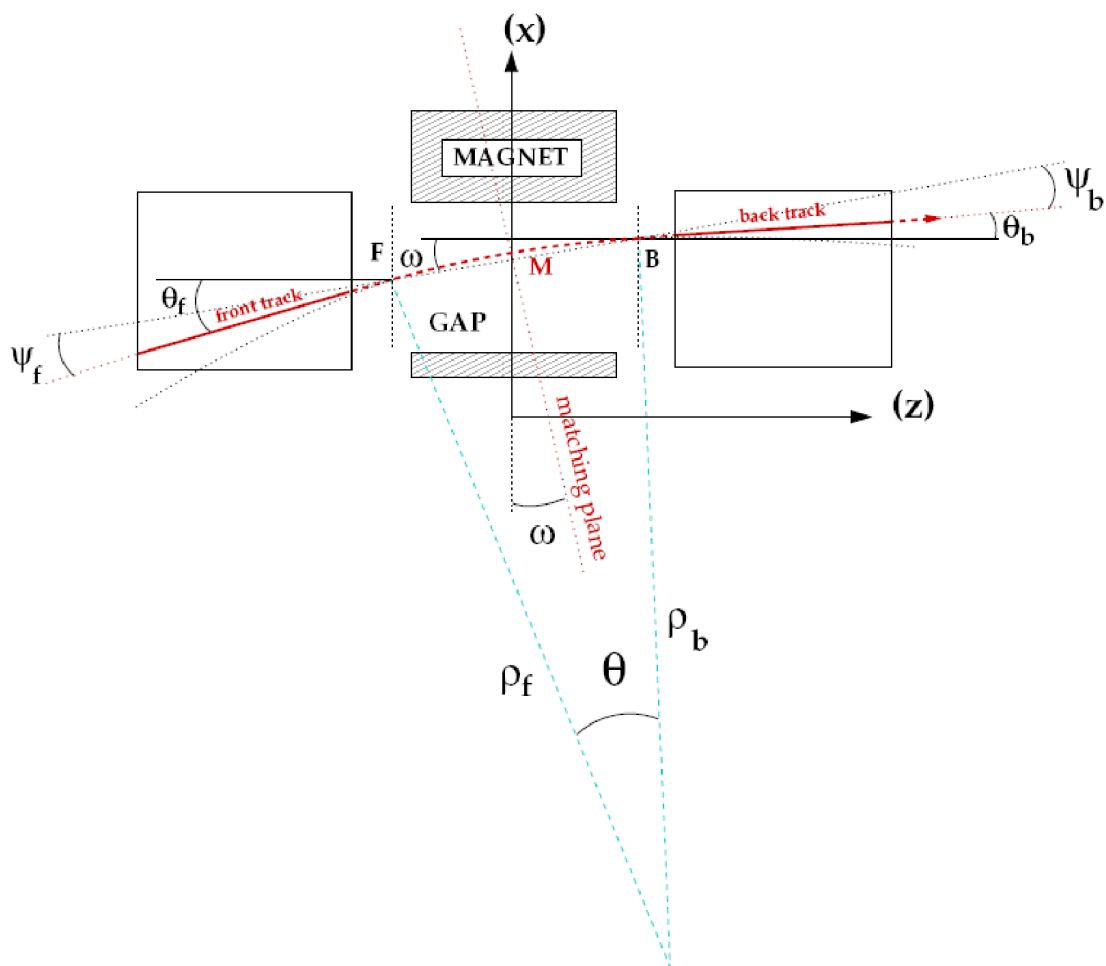


Figure 5.6: $x - z$ view of the matching geometry. F and B are the front and back points where the track enters and leaves the magnetic field. ψ_f and ψ_b are the angles between the local tracks and the FB line. These two angles should be equal if the local tracks match.

From figure 5.6 its easy to see that

$$\theta_f = \omega + \psi_f, \quad (5.2)$$

and

$$\theta_b = \omega - \psi_b. \quad (5.3)$$

After some simple geometrical reasoning follows that

$$\psi_f = \psi_b = \theta/2, \quad (5.4)$$

which gives the first matching condition: the ψ_f and ψ_b angles must be equal. Since the magnetic field has only a y component it means that the y slopes, α_y , of the two local tracks must also coincide. So the second matching condition is $\alpha_y^f = \alpha_y^b$. The third and last matching condition requires that the projections of the two local tracks on the matching plane, P_f and P_b , coincide with point M from figure 5.6. Thus the quantity $\Delta y = P_{f,y} - P_{b,y}$ is equal to zero for matching tracks. In real experimental conditions, the matching conditions cannot be met exactly due to finite tracking resolution, magnetic field approximations, rescatterings, geometrical imperfections etc. So the global tracks are selected based on a finite cut on the matching parameters, $\Delta\psi$, $\Delta\alpha_y$ and Δy , that can be expressed by the elliptical condition:

$$\left(\frac{\Delta y - \Delta y_{\text{offset}}}{\sigma_{\Delta y}}\right)^2 + \left(\frac{\Delta\alpha_y - \Delta\alpha_{y,\text{offset}}}{\sigma_{\Delta\alpha_y}}\right)^2 + \left(\frac{\Delta\psi - \Delta\psi_{\text{offset}}}{\sigma_{\psi}}\right)^2 < n_\sigma^2. \quad (5.5)$$

The quantities Δy_{offset} , $\Delta\alpha_{y,\text{offset}}$ and $\Delta\psi_{\text{offset}}$ are offsets while $\sigma_{\Delta y}$, $\sigma_{\Delta\alpha_y}$ and σ_{ψ} are the widths of the matching parameters distributions determined on a run by run basis. n_σ is the number of standard deviations used in the analysis cut.

Momentum determination

The momentum of the track is determined using the formula

$$\vec{p} = q\vec{B} \times \vec{r}, \quad (5.6)$$

where \vec{p} is the momentum vector, q the electric charge, \vec{B} the magnetic field and \vec{r} is the curvature of the particle trajectory due to the magnetic field. In our case, \vec{B} has only the y -component wich is considered to be uniform over the entire magnet. Since the trajectory will be curved only in the $x - z$ plane, equation 5.6 reduces to the scalar equation

$$p_{xz} = qB_y\rho, \quad (5.7)$$

where ρ is the radius of the circular trajectory in the $x - z$ plane and p_{xz} is the magnitude of the momentum vector projection on the $x - z$ plane. From figure 5.6 can be deduced that

$$\rho = \frac{|FB|}{2\sin(\theta/2)} \quad (5.8)$$

and

$$|FB| = \frac{\Delta L}{\cos\omega}, \quad (5.9)$$

where ΔL is the effective magnet gap length. By using equations 5.8 and 5.9 and after trigonometrical calculations, the radius of the trajectory curvature is obtained as a function of the magnet effective gap and local track $\theta_{f,b}$ angles.

$$\rho = \frac{\Delta L}{\sin\theta_f - \sin\theta_b}. \quad (5.10)$$

The $x - z$ component of the momentum becomes

$$p_{xz} = \frac{qB\Delta L}{\sin\theta_f - \sin\theta_b} \quad (5.11)$$

and the magnitude of the full momentum can be calculated by using the slope α_y of the track direction:

$$p = \frac{p_{xz}}{\sqrt{1 - \alpha_y^2}} \quad (5.12)$$

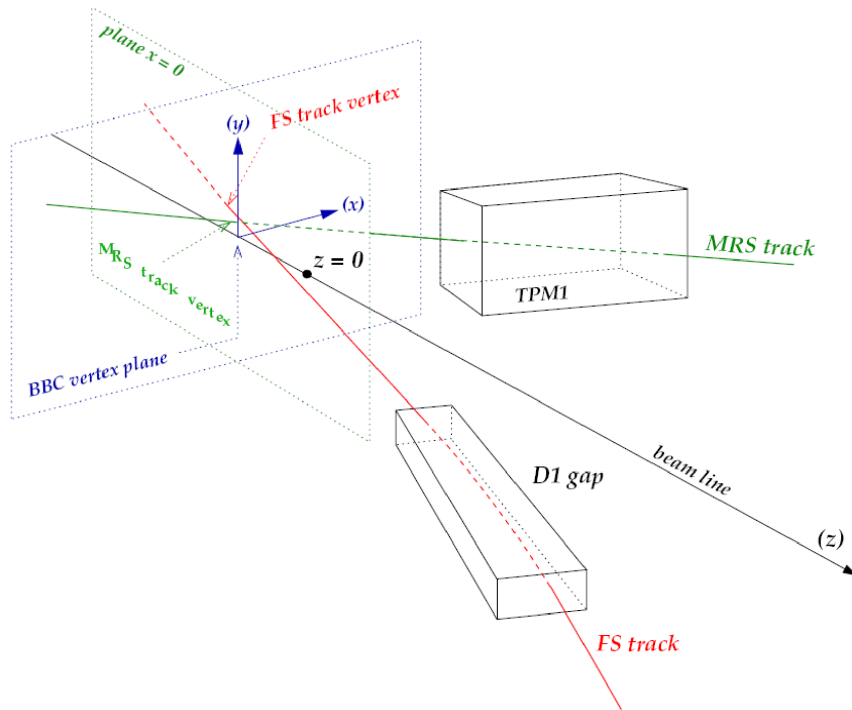


Figure 5.7: Track projection to the event vertex planes. For FS tracks, the plane is (x, y) with $z = Z_{BBC}$ and for MRS the plane is (y, z) with $x = 0$. Picture taken from [86].

Global tracking

After the matching and momentum determination is done, there can still be contaminations from poorly matched tracks and possibly background tracks. So each track is subject to a refitting procedure that involves its projection from the outmost tracking device towards the event vertex (see 5.7). In this procedure a χ^2 value is calculated to indicate the quality for each track as follows:

$$\chi^2 = \frac{(Z_{vtx}^{global} - Z_{vtx}^{proj})^2}{\sigma_{Z_{vtx}}^2} + \sum_{TN} \left(\frac{(x_{tr} - x_{proj})^2}{\sigma_x^2} + \frac{(y_{tr} - y_{proj})^2}{\sigma_y^2} + \frac{(\alpha_{y,tr} - \alpha_{y,proj})^2}{\sigma_{\alpha_y}^2} + \frac{(\theta_{tr} - \theta_{proj})^2}{\sigma_{\theta}^2} \right). \quad (5.13)$$

The quantity $Z_{\text{vtx}}^{\text{global}}$ is the event vertex position determined by the global detectors, $Z_{\text{vtx}}^{\text{proj}}$ is the projection of the track back to the $y - z$ plane containing the beam axis. The sum goes over all tracking chambers in a given spectrometer. The x and y are the coordinates of the track intersection with the tracking chamber entry plane, α_y and θ are defined in the same way as in the beginning of this section. The tr subscript refers to the track while **proj** refers to the projected value. The χ^2 value calculated in this way is used to cut loose tracks as described next.

5.2.3 Track cuts

The cuts on tracks are performed in order to remove background tracks or to remove tracks passing through specific parts of detectors and magnets.

Geometrical fiducial cuts

Fiducial cuts are applied both on magnet and on detector volumes. The cuts applied on the magnet gap volume ensure that the track matching efficiency is not affected by the magnet edges. The closest acceptable distance to the D5 magnet walls on the x direction is 1 cm, while on the y direction this is 0 (see left panel of figure 5.8). For the other magnets, D1-D4, the closest acceptable distance to the walls is set to 0 on both x and y directions.

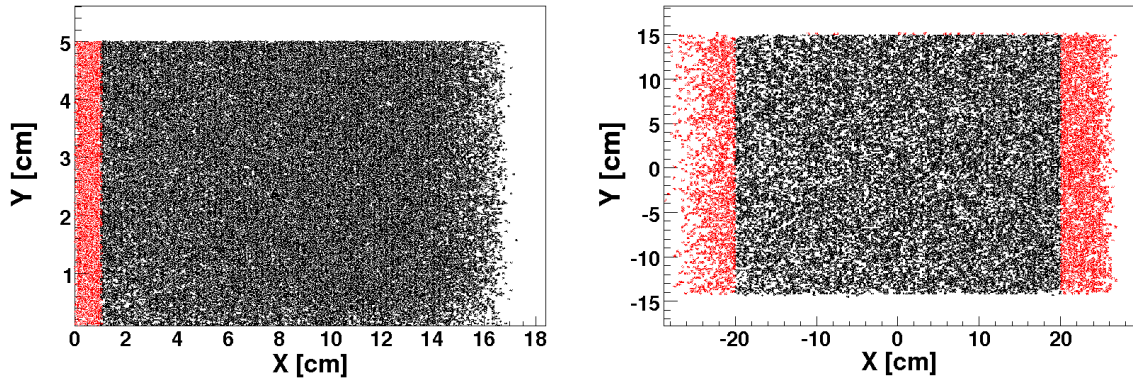


Figure 5.8: Left: Geometrical fiducial cut on D5 magnet. The x and y axis correspond to the distance of closest approach between a track and the magnet wall. The red dots represent the removed tracks. Right: Geometrical fiducial cut on the entrance window of the RICH detector. The x and y are the coordinates of the intersection between the projected T5 track and the RICH entry window plane in local RICH coordinates.

The cuts applied on detector volumes remove those parts which are inefficient or have a very low efficiency compared to the rest of the detector. A summary of the fiducial cuts applied on detector volumes is shown in Table 5.1. The cuts on TPM1 and TPM2 entrance windows remove the outer edges of the detector volumes which have very low tracking efficiency. The cut on the RICH entrance plane (see right panel of figure 5.8) is motivated by the low efficiency in ring reconstruction for tracks which enter RICH close to its edges.

All the geometrical cuts applied on the data are taken into account when the acceptance correction for the spectrometers is calculated.

Detector	Cut plane	X cut[cm]	Y cut[cm]
TPM1	front	[-13, +14]	none
TPM2	front	[-20, +22]	none
RICH	front	[-20, +20]	[-15, +15]

Table 5.1: Geometrical cuts on tracking detectors volumes applied in the analysis. There are no geometrical cuts on the other tracking stations because their efficiency is given as a function of the position of the track entry point.

Track quality cuts

After the tracking procedure and the geometrical cuts applied for every particle, some particles which do not originate directly from the collision may still survive (*e.g.* weak decay products). Since all the primary tracks must emerge from a very narrow region around the event vertex, a cut on the track projected vertex removes most of the secondary particles. The cut on the projected vertex is illustrated in figure 5.9 for both

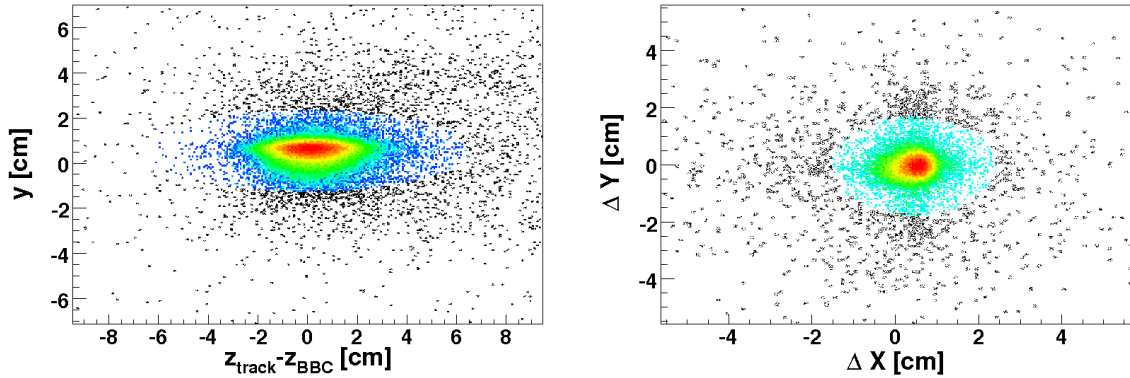


Figure 5.9: Track projection on the vertex plane $y - z$ for MRS tracks at 45 degrees (left) and $x - y$ for FS tracks at 4 degrees (right). The colored part represents the tracks which passed the elliptical cut.

MRS and FS tracks. MRS tracks are projected on the $y - z$ plane containing the beam pipe (z -axis). FS tracks are projected on the $x - y$ plane which intersects the beam pipe at the BBC global event vertex. The projection on each axis is compared with the BBC vertex, $0, 0, z_{vtx}$ in global coordinates, and the distribution of the difference is fitted with a gaussian. The offset and the width are extracted and used to apply an elliptical cut like this:

$$\left(\frac{\Delta y - y_{\text{offset}}}{\sigma_{\Delta y}}\right)^2 + \left(\frac{\Delta z - z_{\text{offset}}}{\sigma_{\Delta z}}\right)^2 \leq n_{\sigma}^2 \quad \text{for FS,} \quad (5.14)$$

$$\left(\frac{\Delta x - x_{\text{offset}}}{\sigma_{\Delta x}}\right)^2 + \left(\frac{\Delta y - y_{\text{offset}}}{\sigma_{\Delta y}}\right)^2 \leq n_{\sigma}^2 \quad \text{for MRS,} \quad (5.15)$$

where the n_{σ} value used in the analysis was 4. The offsets and widths are calculated on a run by run basis due to changes that might happen in the tracking chambers (*e.g.* drift velocity) and the exact (x, y) position of the beam.

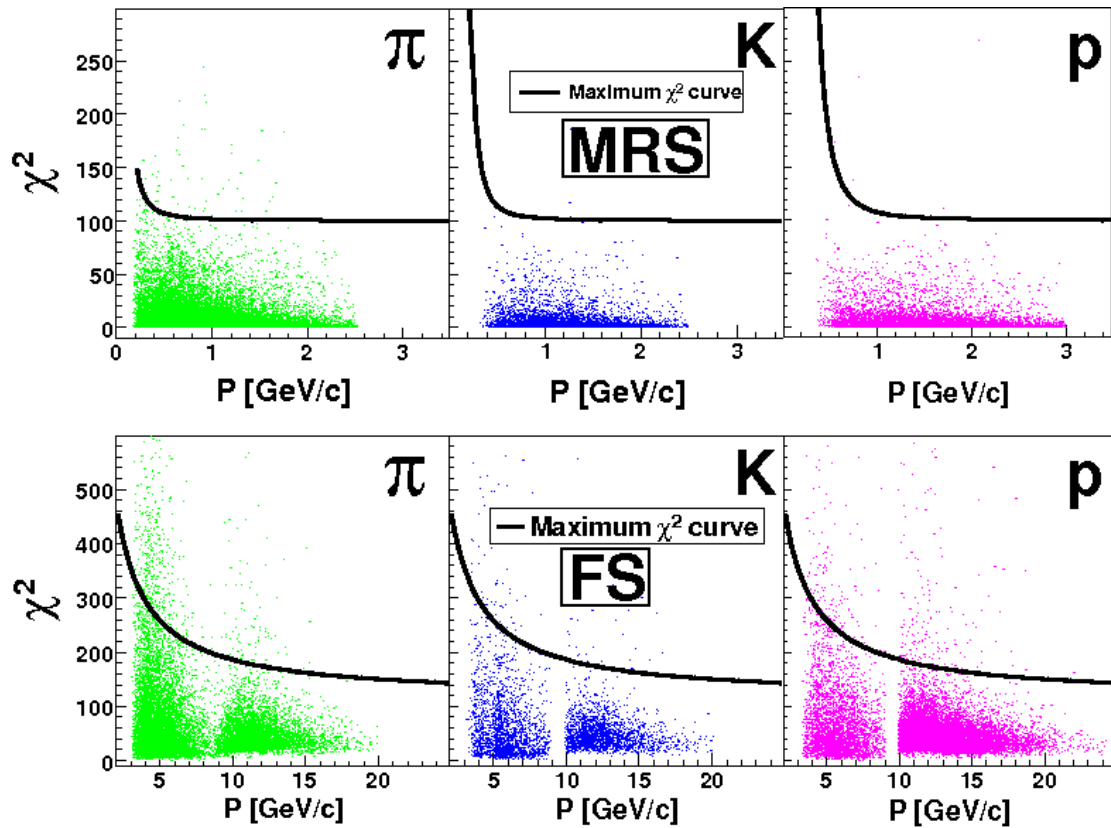


Figure 5.10: χ^2 dependence on momentum for identified particle species in MRS (top panels) and FS (bottom panels). The χ^2 is calculated based on the formula 5.13 from the global tracking section. The curves show the maximum allowed χ^2 for a given momentum.

Another cut which improves the track quality is the one performed on the χ^2 associated to each particle in the track refitting algorithm. The cut functions were constructed by fitting the mean χ^2 dependence on momentum with functions of the form $A + B/p$ for FS tracks and $A + (m_0^2 + p^2)B/p^4$ for MRS tracks. The B parameter is species dependent in MRS due to the strong variation with mass of the multiple scattering contribution to the χ^2 at low momentum. The condition imposed to a track at a given momentum p is obtained by multiplying the function value with an n factor. The values of the A , B and n parameters are given in Table 5.2.

Spectrometer	Specie	A	B	n
MRS	pion	10.0	0.165	10
MRS	kaon	10.0	0.183	10
MRS	proton	10.0	0.420	10
FS	all	28.5	180.0	4

Table 5.2: Parameters A , B and n used for the χ^2 cut functions.

5.3 Particle Identification

The particle identification (PID) is done by first matching the resolved tracks with valid hits in the PID detectors (ToF or Cerenkov detectors). After proper calibration, the PID detectors are able to measure the particle velocity which together with the momentum information leads to species identification. In this analysis, TOFW, H2 and RICH detectors were used for PID.

5.3.1 The time of flight PID

The time of flight PID can be done only after a track is assigned to a good hit slat in either TOFW(MRS) or H2(FS). The matching between tracks and slat hits and also the TOF calibration procedure are described in detail in reference [86]. The calibrated TDC signal produced by the hit slats together with the particle trajectory length gives the particle's velocity. Figure 5.11 shows the hits distribution from the time of flight detectors in $(p \times q, \beta^{-1})$ coordinates. The different particle species are clearly separated especially at low momentum ($p < 1.5$ GeV/ c in TOFW). The bands of hits have a non-zero width at a certain momentum, leading to overlapping between species at increasing momentum. This is due to uncertainties in flight time, t_{TOF} , momentum and trajectory length, L . The time of flight is mainly affected by the finite intrinsic time resolution of the TOF detector but also by the spread of the start time given by the BBC and by the uncertainties in the effective speed of light inside the slat's photomultiplier tube (PMT). The momentum and trajectory length are affected by the angular resolution of the tracking chambers and by the multiple scattering within the medium traversed by the tracks (air, detector materials).

The PID cuts used to separate charged particles can be in principle calculated as a function of momentum based on the knowledge of all the uncertainty sources. In the following the measured mass squared m^2 will be used instead of β^{-1} , because of the independence of the expected m^2 on momentum. The m^2 is experimentally obtained

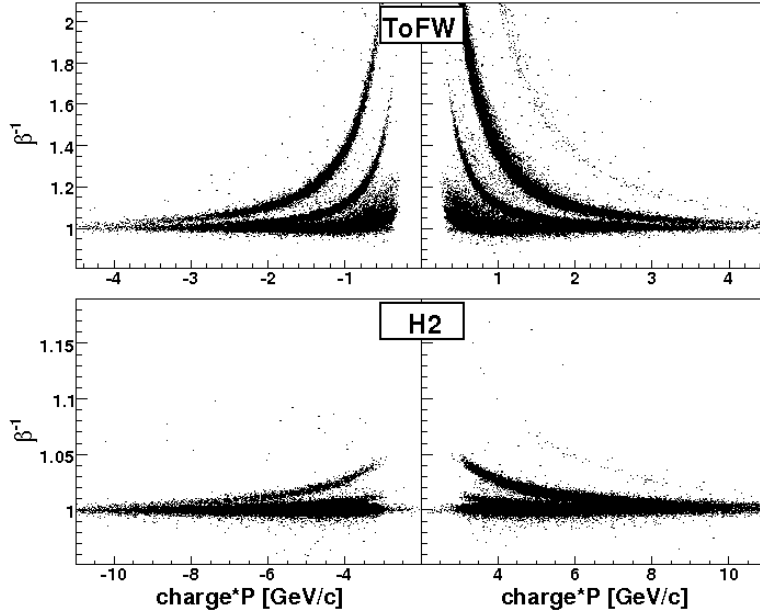


Figure 5.11: Inverse velocity (β^{-1}) as a function of momenta magnitude \times charge. The upper panels correspond to ToFW and the lower are for H2.

as follows:

$$m^2 = p^2 \left(\frac{1}{\beta^2} - 1 \right), \quad (5.16)$$

where $\beta = L/t_{TOF}$. The momentum dependent uncertainty on m^2 is given by the following equation [86]:

$$\sigma_{m^2}^2 = 4 \left[m^4 p^2 \sigma_{ang}^2 + m^4 \left(1 + \frac{m^2}{p^2} \right) \sigma_{mult}^2 + (m^2 + p^2)^2 \sigma_t^2 \right] \quad (5.17)$$

where σ_{ang} and σ_t are the intrinsic angular and time resolution; σ_{mult} is a quantity that takes into account multiple scatterings.

In this analysis the σ_{ang} , σ_t and σ_{mult} parameters are not extracted but instead the σ_{m^2} are found in narrow momenta ranges for each specie. In figure 5.12 the (m^2, p) scatter plots are shown for all settings that use TOFW and H2 for particle identification. At low momentum, $p < 0.5$ GeV/c, kaons and especially protons suffer multiple scatterings leading to a widening in the m^2 distribution (see upper panels in figure 5.12). At higher momenta, the multiple scatterings have smaller influence but the time resolution becomes important leading to the overlap of the different particle bands. The (m^2, p) scatter plot was divided into slices with equal momenta widths and each slice was projected onto the m^2 axis. The resulting histograms for each slice were fitted with the sum of three Gaussians function corresponding to pions, kaons and protons. At very low momentum, electrons and muons can also be in principle separated from pions as can be seen in figure 5.13. However their abundance relative to pions is less than 5% in the slice shown in figure 5.13 and decreases with increasing momentum. Electrons and muons become undistinguishable from pions at higher momenta so the yield of pions needs to be corrected for muons which are mistakenly identified as pions.

Figures 5.14 and 5.15 show examples of the m^2 distribution fitted for several momentum slices for TOFW and H2, respectively. The three Gaussian sum function is a

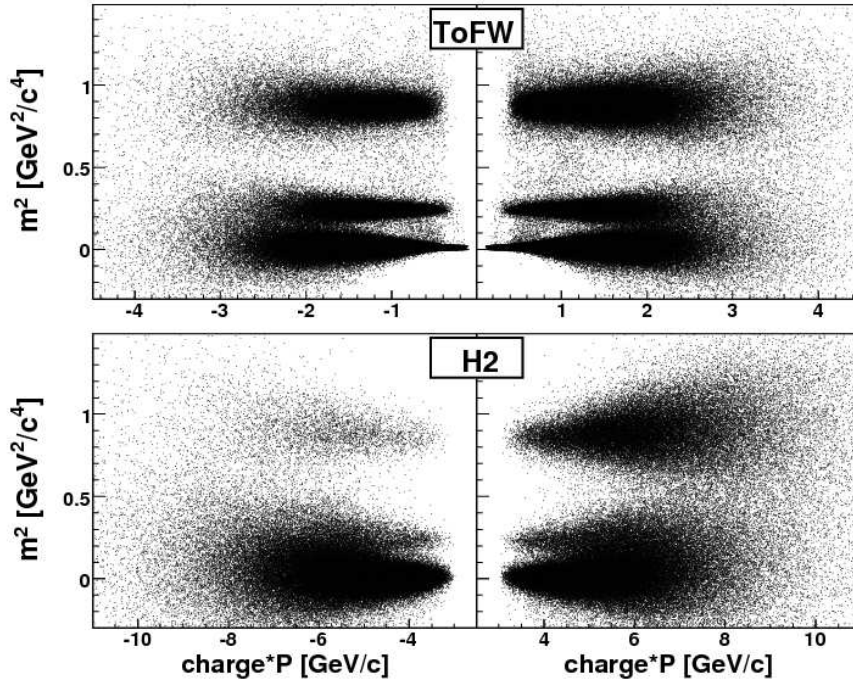


Figure 5.12: Measured m^2 as a function of momenta magnitude \times charge. The upper panels correspond to ToFW and the lower are for H2. In each panel, the particle bands centered around $m^2 \sim 0.9$, ~ 0.24 and ~ 0.02 correspond to protons, kaons and pions, respectively.

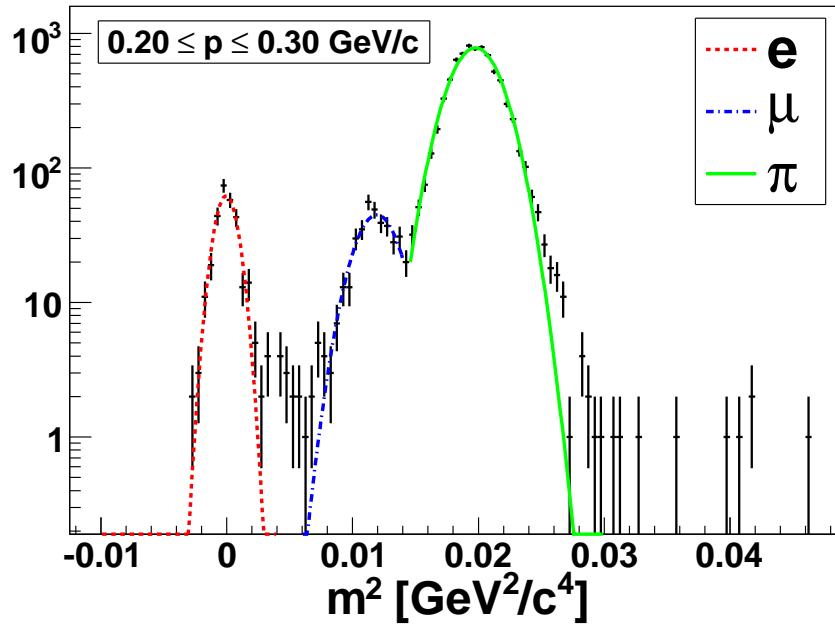
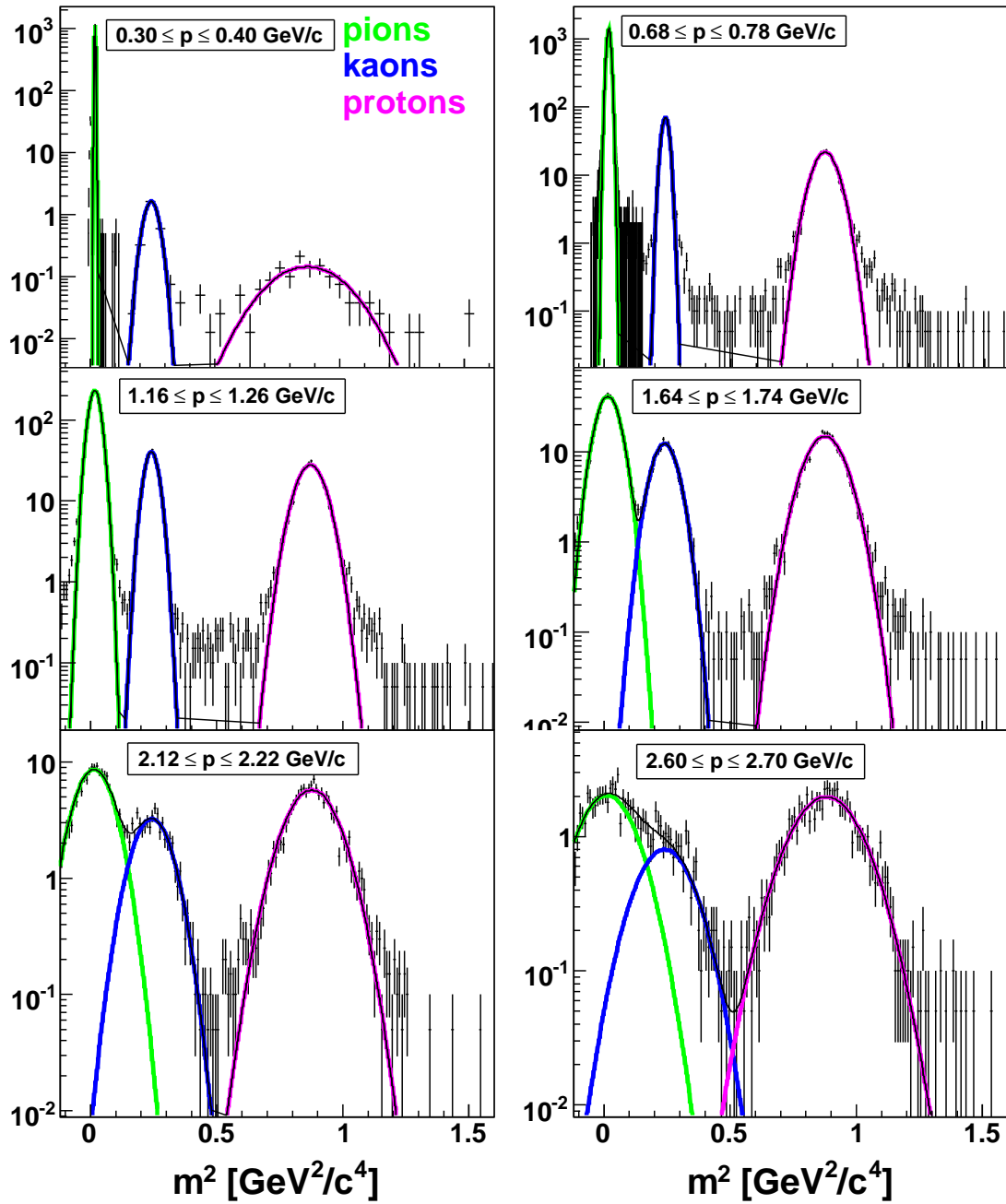


Figure 5.13: m^2 distribution for the momenta slice $0.2 < p < 0.3$ GeV/c. The electrons and muons are clearly visible around their theoretical m^2 value.

Figure 5.14: Fitted m^2 distributions in different momentum slices from TOFW.

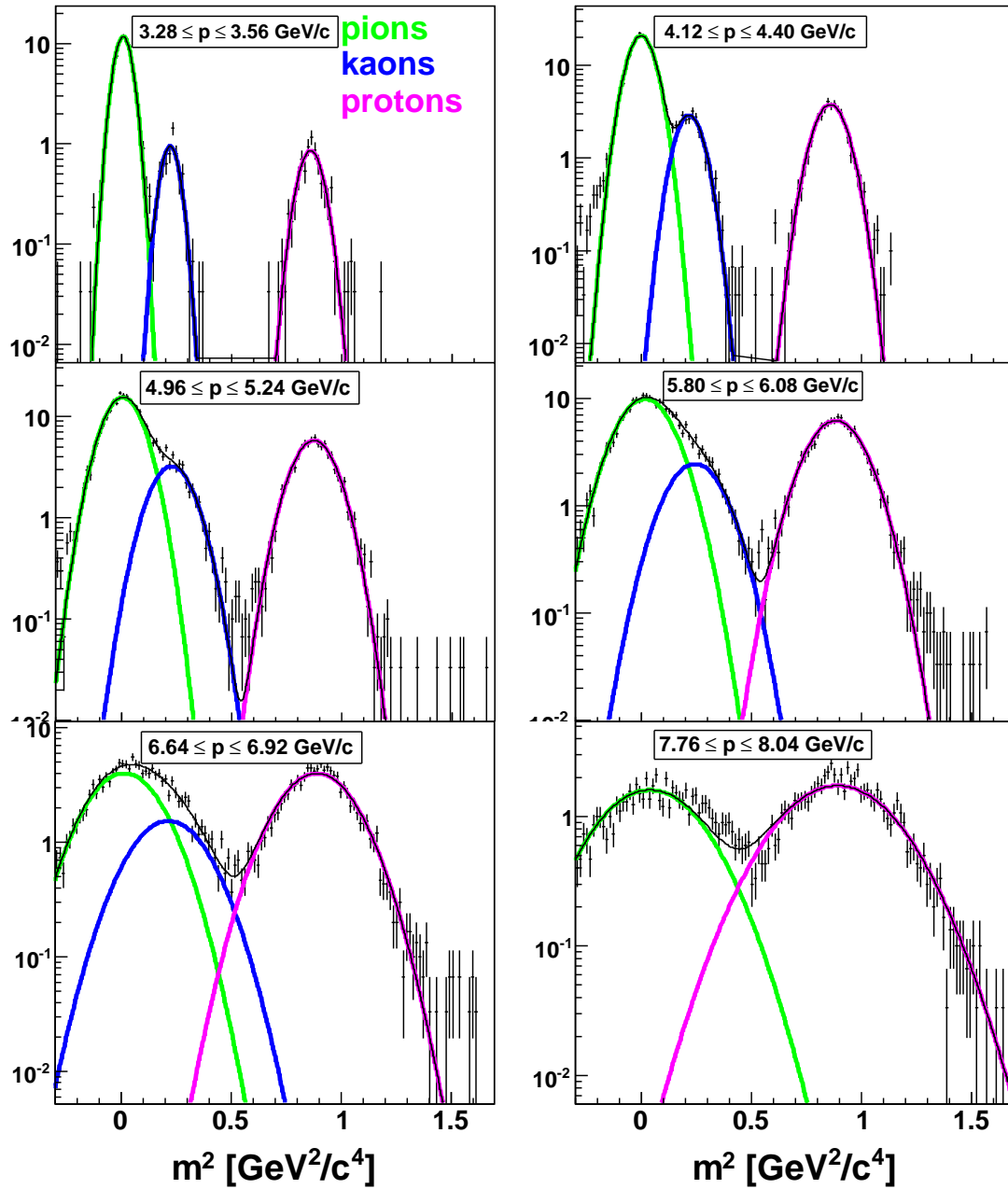


Figure 5.15: Fitted m^2 distributions in different momentum slices from H2.

9-parameter function which could make the fit unstable especially in higher momentum slices where the individual Gaussians overlap significantly. In order to avoid this, a series of limits are imposed on the fit parameters based on *a priori* information:

- The Gaussian centroids should be placed very close to the theoretical m^2 for each particle. The centroids can vary slowly with momentum due to imperfect calibrations but this can be allowed within some limits.
- At higher momentum (especially for H2), the multiple scattering term (σ_{mult}) gives a small contribution to the m^2 spread and the dominant term is σ_t which for a given path length depends only on particle velocity. As a consequence, in higher momentum slices the widths of the three gaussians corresponding to π , K and p can be constrained to have similar values.

The fit quality depends on statistics and on the degree of overlapping between different particles. The momentum dependence of the fitted parameters are illustrated in figures 5.16 and 5.17 for TOFW and H2, respectively. Gaussian centroids are shown in the upper panels. The widths of the Gaussians are shown as the y -errors of the centroid graphs. The Gaussians maxima are also shown in the bottom panels.

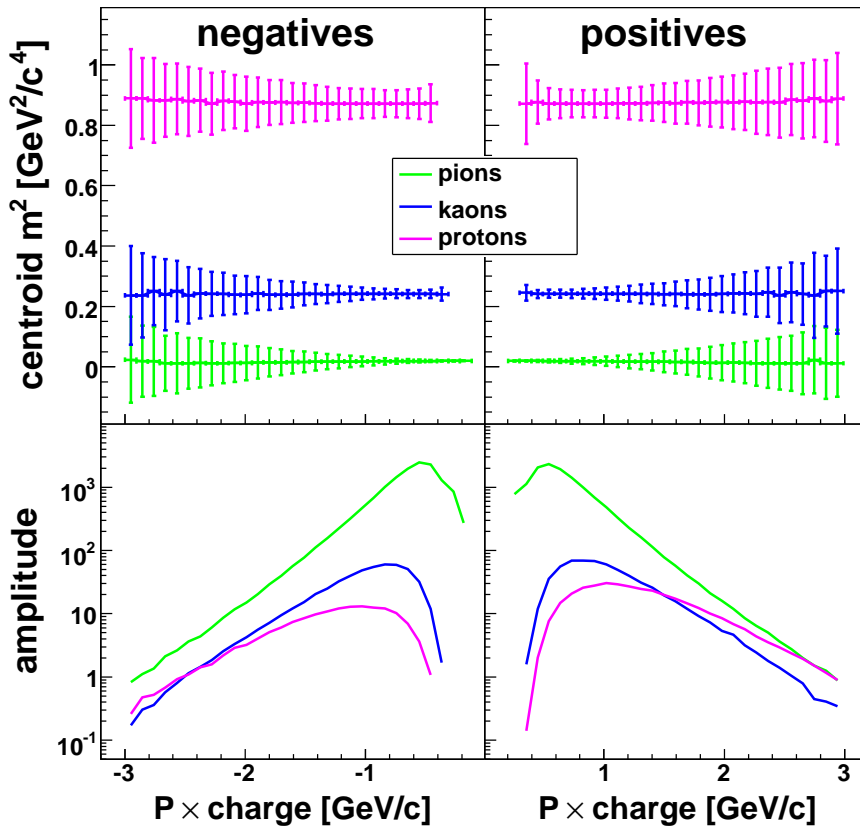


Figure 5.16: Fit parameters for TOFW obtained after fitting all slices. Top panels: centroids and Gaussian widths (the y -errors) for each particle. Bottom panels: Gaussian maxima(amplitude).

The fitted parameters in all of the momentum slices are linearly interpolated so that for every momentum a three-gaussian function can be obtained. The PID selection for a particle with a given p and m^2 is based on the following criteria:

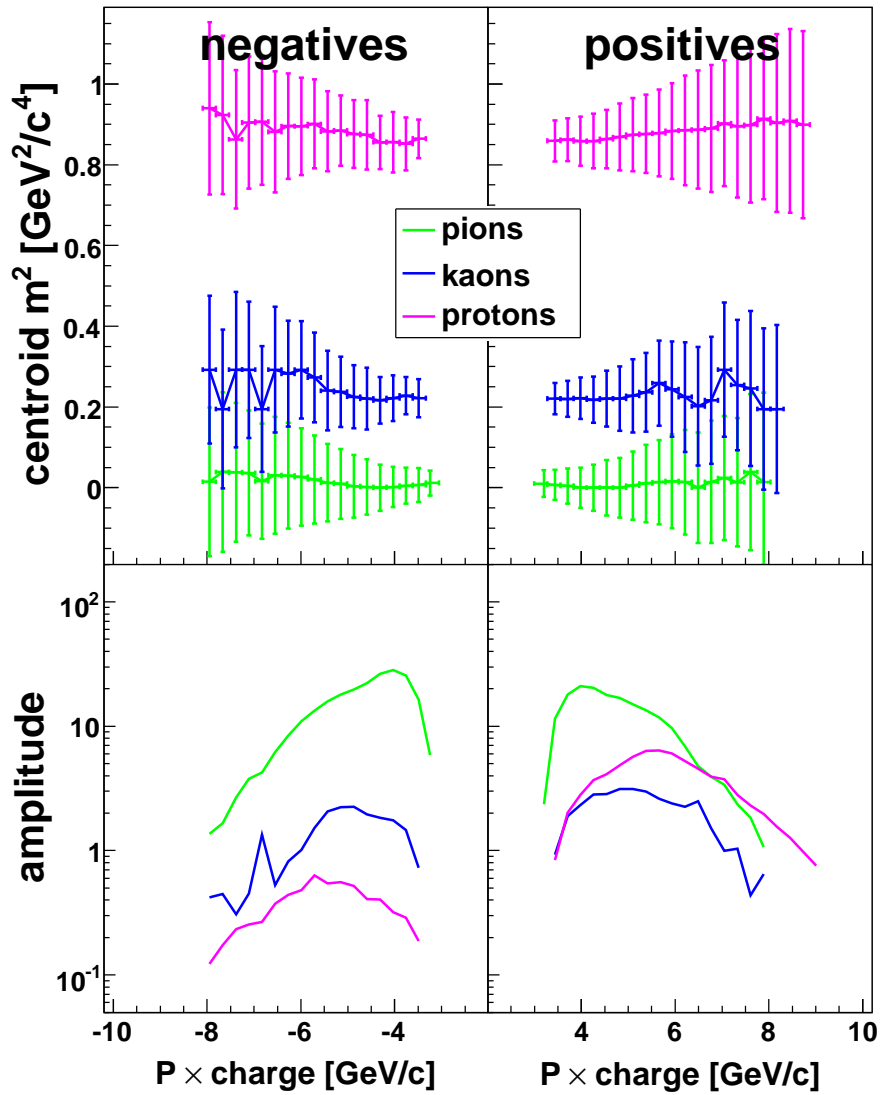


Figure 5.17: Fit parameters for H2 obtained after fitting all slices. Top panels: centroids and Gaussian widths (the y-errors) for each particle. Bottom panels: Gaussian maxima.

- The individual Gaussian corresponding to the candidate species must have the highest value.
- The particle m^2 must be within 3σ from the centroid corresponding to the candidate species.
- The level of contamination with the other species at a given m^2 must be less than a certain value. For this analysis, the maximum level of contamination was chosen to be 5%. For analyses where contamination with other species affects the measured observables, *e.g. elliptic flow, nuclear modification factors*, the contamination level can be decreased but this will lead to a decrease in the momentum range with valid PID.

At low momenta, *e.g.* $p \leq 1.5$ GeV/ c in TOFW, the first and second criteria are enough because all particle species are well separated. At higher momenta, the third criterion acts by rejecting the overlapping/contaminated m^2 intervals. The fraction from

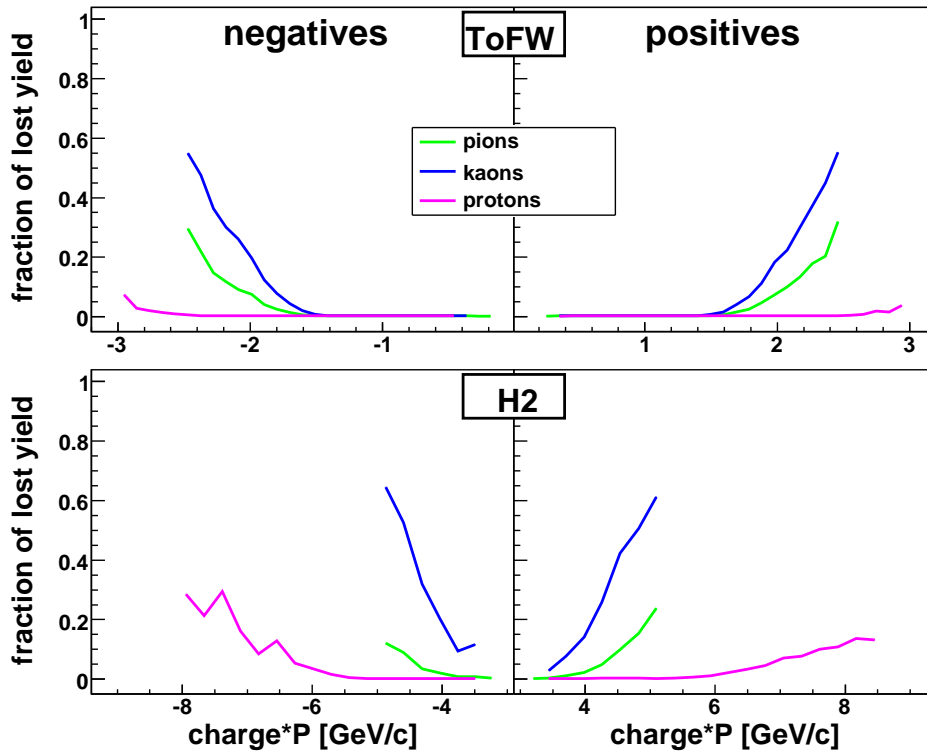


Figure 5.18: Fraction of the total yield lost due to PID cuts as a function of momentum \times charge.

the total yield lost due to this cut is species and momentum dependent as shown in figure 5.18. These fractions are calculated for each particle specie in every momenta slice using the expression

$$f_i(p) = \frac{L_i(p) - G_i(p)}{T_i(p)}, \quad i = \pi, K, p \quad (5.18)$$

where L_i (loss), G_i (gain) and T_i (total yield) can be calculated using the fitted Gaussian

functions $F_i(m^2; p)$:

$$L_i(p) = \int_{-\infty}^{m_{i,low}^2(p)} F_i(m^2; p) dm^2 + \int_{m_{i,high}^2(p)}^{+\infty} F_i(m^2; p) dm^2, \quad (5.19)$$

$$G_i(p) = \int_{m_{i,low}^2(p)}^{m_{i,high}^2(p)} F_{j \neq i}(m^2; p) dm^2 + \int_{m_{i,low}^2(p)}^{m_{i,high}^2(p)} F_{k \neq i}(m^2; p) dm^2, \quad (5.20)$$

$$T_i(p) = \int_{-\infty}^{+\infty} F_i(m^2; p) dm^2. \quad (5.21)$$

The j and k indexes refer to the species other than i . The quantities $m_{i,low}^2(p)$ and $m_{i,high}^2(p)$ are the m^2 cuts applied to identify a particle of specie i according to the criteria described. The quantity $L_i(p)$ is the yield of specie i lost due to the m^2 cuts while $G_i(p)$ is the yield gained due to the yield of other species, j and k , falling inside the m^2 cuts. The quantity $G_i(p)$ is controlled by the maximum contamination level accepted in the PID procedure. Finally, $T_i(p)$ is the total yield for a particle of specie i in the momentum slice centered on p .

5.3.2 The Cerenkov PID

The Cerenkov effect is used for PID by the RICH detector which focuses the light cones emitted by charged particles on a focal plane consisting of an array of photo-multiplier tubes. A detailed description of the detector and its PID capabilities can be found in [179, 19] Due to the detecting principle, only particles with velocities above the in-medium velocity of light, $v > c/n$, are detected. The Cerenkov threshold depends only on the particle specie through its mass and on the refractive index of the gas contained in the detector's active medium:

$$p_{\text{threshold}}^2 = \frac{m^2}{n^2 - 1}, \quad (5.22)$$

where m is the particle rest mass and n is the gas refractive index. For the present analysis the effective refractive index value used is $n = 1.001887$. A typical output generated by the PMT array is shown in the left panel of figure 5.19. The coordinates given by the fired PMTs are fitted with one or more circles and the radii are extracted. The ring reconstruction efficiency was calculated in [179] and is shown in the right panel of figure 5.19.

The expected ring radius r dependence on momentum can be derived from the Cerenkov angle θ_C

$$\theta_C = \arccos \left(\frac{1}{n} \sqrt{1 + \frac{m_0^2}{p^2}} \right) \quad (5.23)$$

by replacing θ_C with $\theta_C = \arctan(r/L_{foc})$. The following expression is obtained for the ring radius:

$$r = L_{foc} \tan \left\{ \arccos \left(\frac{1}{n} \sqrt{1 + \frac{m^2}{p^2}} \right) \right\}, \quad (5.24)$$

where L_{foc} is the focal length of the RICH spherical mirror. In figure 5.20, the Cerenkov radii versus momentum is shown for a low(red) and high(blue) field setting. The

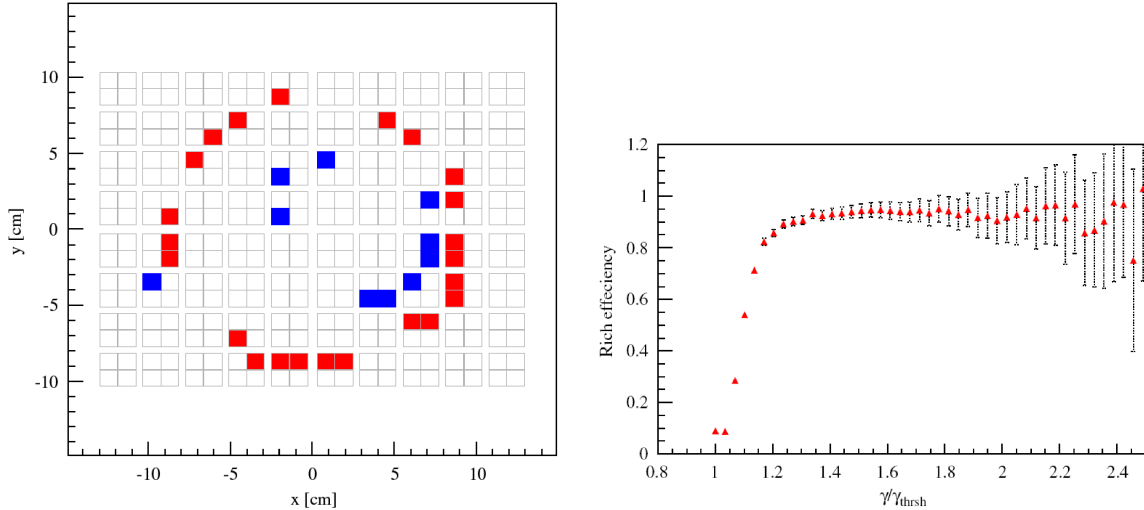


Figure 5.19: Left: Coordinates of the fired RICH PMTs in an event. The big ring has been produced by a 20 GeV/c pion. The smaller one was produced by a 17 GeV/c proton. The picture was taken from [179]. Right: RICH ring reconstruction efficiency as a function of $\gamma/\gamma_{\text{threshold}}$. The figure is taken from [179].

particle bands represent different particle species (labeled in the figure). The spread of the radii sets limits on the PID performance and is due to the limited precision on measuring the RICH rings and to momentum uncertainties. At momenta lower than 5 GeV/c, RICH can separate light particles like electrons and muons from pions. The pions and kaons can be clearly separated up to $p \sim 20$ GeV/c while the protons can be further identified up to $p \sim 30$ GeV/c.

RICH can be used for PID below the Cerenkov threshold also by using tracks which give a zero ring radius. Above the kaon Cerenkov threshold, $p_{th}^K \sim 8.0$ GeV/c, but below the proton threshold, $p_{th}^p \sim 15.3$ GeV/c, the only particles which can give a ring radius equal to zero are the protons or very rare higher mass particles (*e.g.* deuterons). As shown in figure 5.19, RICH ring reconstruction efficiency varies drastically close to the Cerenkov threshold. In consequence, the lower momentum bound for vetoed protons was chosen to be 10 GeV/c where the kaon ring reconstruction efficiency is saturated to the nominal value of 97%. The absolute and relative contamination of protons and anti-protons with pions and kaons due to the 3% RICH inefficiency are shown in figure 5.21. The data is from the FS settings 3(A/B)1723 in 0-10% most central events. The relative contamination for anti-protons is much higher than the one for protons due to their very different relative abundancies. Because the contamination correction depends on the species relative abundancies, it has also a small centrality dependence which was found to be always less than 10% for anti-protons and is negligible for protons.

Kaons can be also identified below the Cerenkov threshold in RICH provided that H2 PID information is available. All particles in the momentum interval $p_{th}^\pi < p < p_{th}^K$ with zero ring radius in RICH which are not identified as protons in H2 are vetoed as kaons. A valid hit in H2 is not required for the vetoed kaons so the contamination correction must take into account also H2 tracking efficiency. The yields of vetoed kaons have a significant contamination with protons and pions. The proton contamination comes mainly from the H2 tracking inefficiency and from protons which did not survive the PID cuts made in H2. The pion contamination comes from the RICH

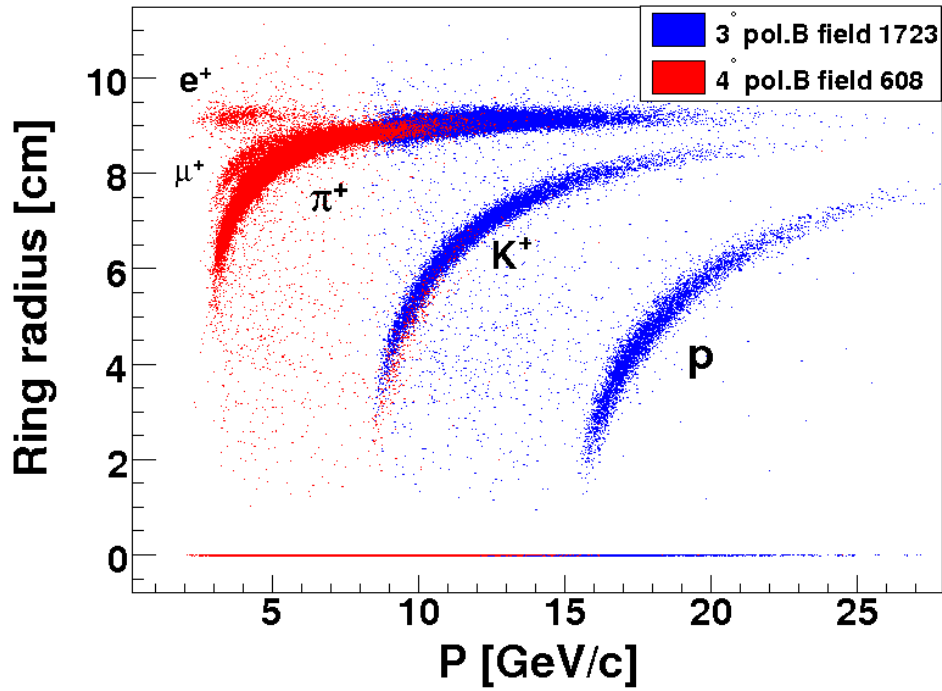


Figure 5.20: RICH ring radius as a function of momentum from two FS settings.

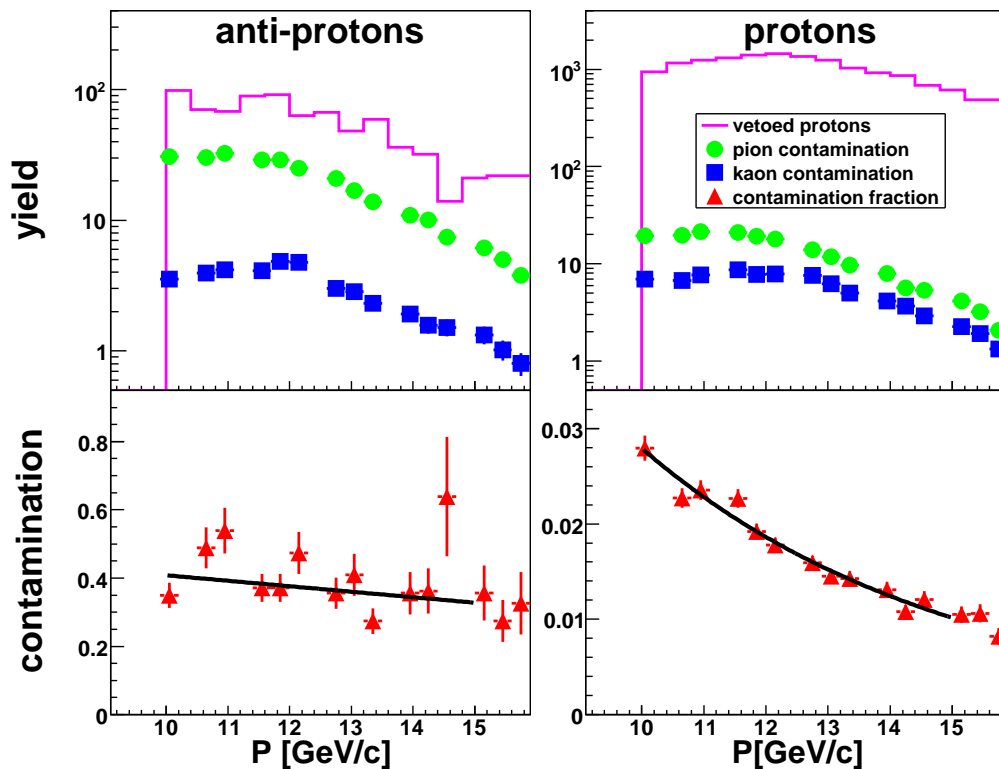


Figure 5.21: Top panels: Vetoed anti-protons (left) and protons (right) in RICH and estimated yields of contaminant pions and kaons. Bottom panels: Relative contamination with unresolved pions and kaons.

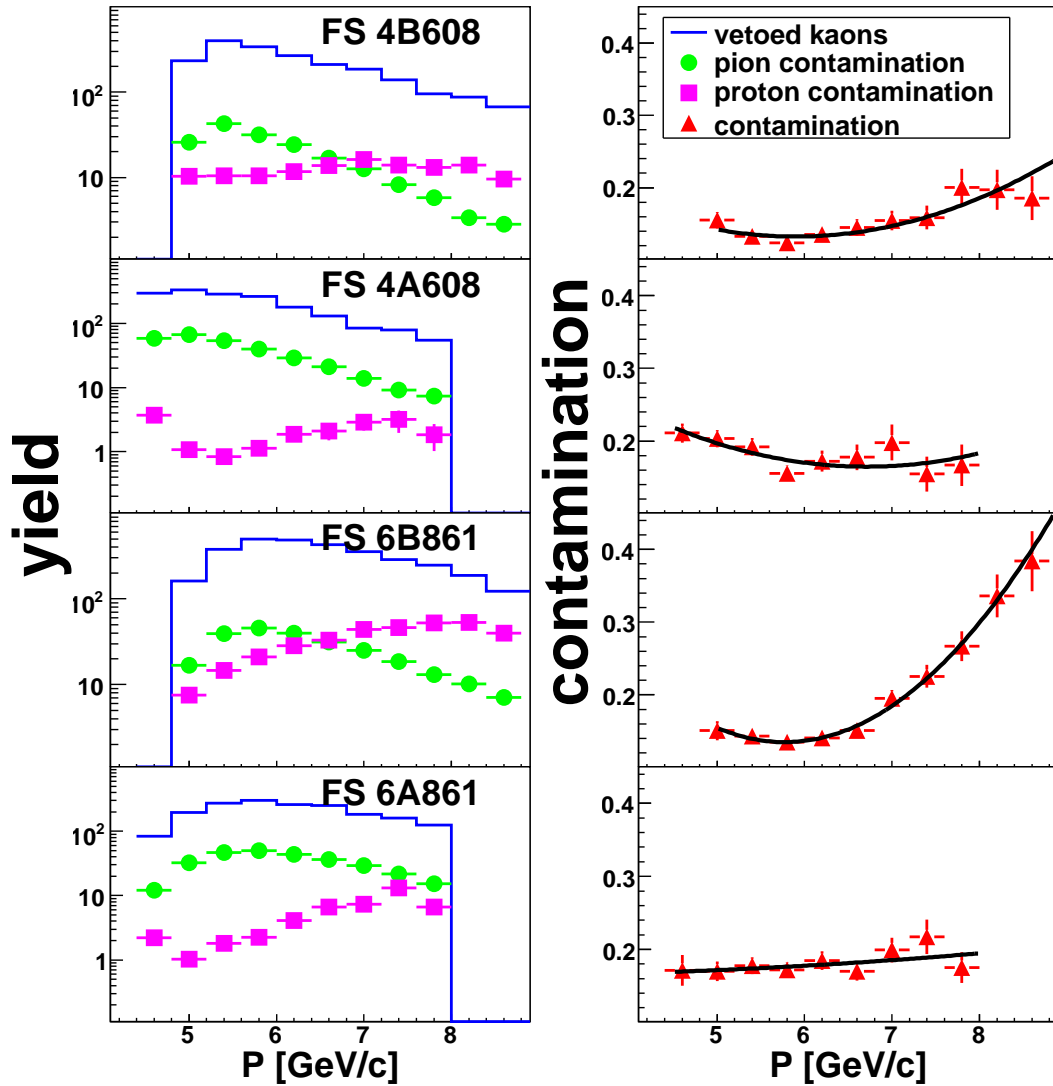


Figure 5.22: Left panels: Yields of vetoed (anti)kaons and estimated yields of contaminant protons and pions. Right panels: Relative contamination with unresolved protons and pions. The A polarity settings correspond to negatively charged particles while the B polarity settings correspond to the positives.

ring reconstruction inefficiency. The absolute and relative contaminations with protons and pions as a function of momentum are shown in figure 5.22 for 0-10% central events in low field FS settings at 4 and 6 degrees. At a given momentum, the relative contamination depends on the charge sign and on setting due to the different particle abundancies. The centrality dependence is less than 5% and was accounted for in the final results.

5.3.3 PID cuts

PID cuts are applied in order to select particles based on their species. In this analysis only pions, kaons and protons together with their anti-particles are identified. However, as it was shown above, in limited momentum intervals it is in principle possible to identify also electrons, muons and even deuterons [183].

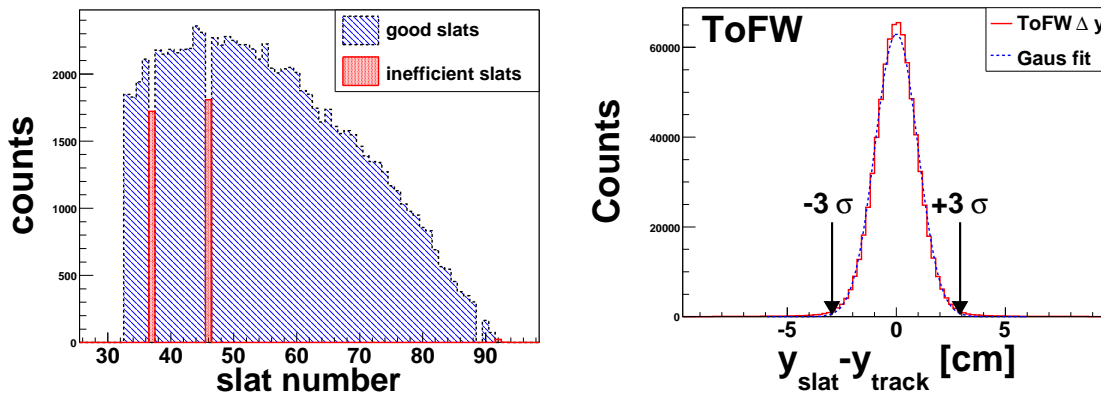


Figure 5.23: Left: Number of hits versus TOFW slat number in the 45 degrees setting at B polarity. Slats 37 and 46 (red areas) are removed from the analysis due to poor efficiency compared to neighbouring slats. Right: Distribution of $\Delta y = y_{slat} - y_{track}$ fitted with a gaussian.

Time of flight

Before using the PID procedure, all the TOF slats are checked for calibration and uniform efficiency. In the left panel of figure 5.23 the distribution of hits for each slat in TOFW for the 45 degrees setting at B polarity is shown. The overall dependence of the hits on the slat number is determined by the spectrometer acceptance and the angular distribution of tracks. The slats which have much less hits than the overall dependence are removed due to inefficiency (the case of slat 37 and 46 in the figure). The removal of TOF slats from analysis reduces the spectrometer acceptance and this is taken into account when the acceptance correction is calculated.

Every hit from the TOF detectors is checked for good consistency with the associated track projection. This is done by applying a 3σ cut on the difference between the y hit coordinate given by the time difference between the upper and lower PMT of the TOF slat and the one obtained by projecting the track on the slat volume (see right panel of figure 5.23). The cut ensures good matching between the TOF hit and track.

The conditions for identifying pions, kaons and protons are imposed on the (m^2, p) set of coordinates and the final result is shown in figure 5.24 for TOFW and H2. Because of finite time resolution, the separation power of the TOF detectors drops

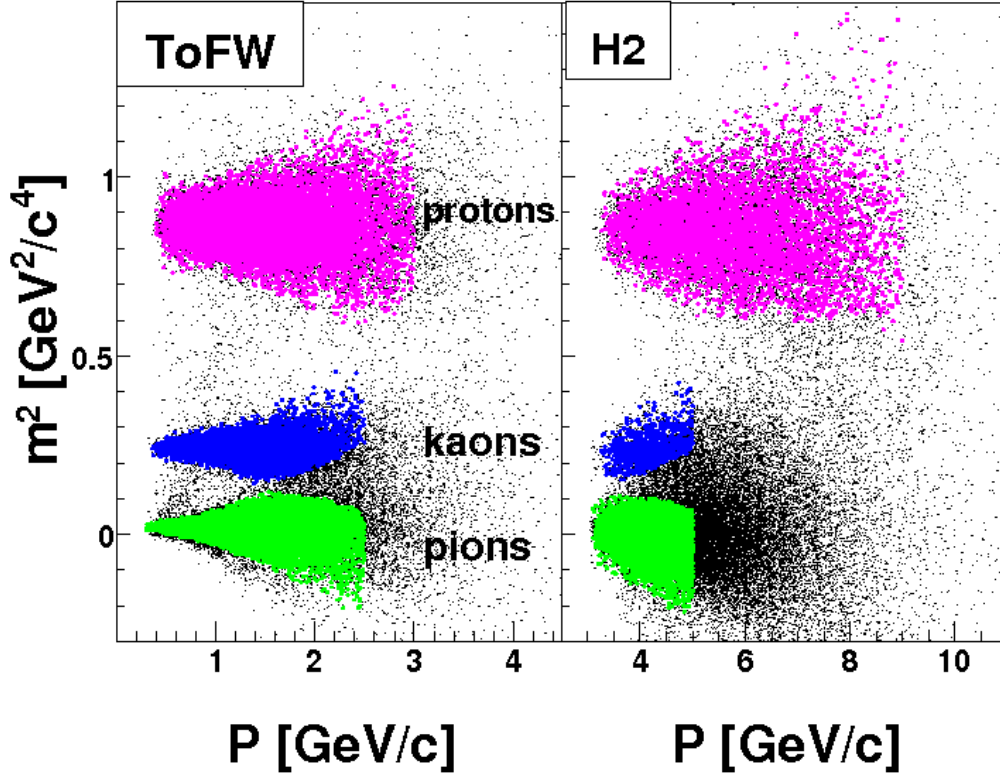


Figure 5.24: Identified pions, kaons and protons using TOFW and H2 hodoscopes.

with momentum leading to the necessity of making corrections for contamination with other species and for particles lost in the regions removed for too much overlapping (see figure 5.18 and equations 5.18-5.21). In TOFW, the pions and kaons start to overlap at $p \sim 1.5$ GeV/ c while in H2 the overlapping starts at $p \sim 3.0$ GeV/ c . The π/K separation is extended by the use of the contamination corrections up to ~ 2.5 GeV/ c in TOFW and ~ 5 GeV/ c in H2. The protons can be separated very well up to $p \sim 3$ GeV/ c in TOFW and up to $p \sim 9$ GeV/ c in H2.

RICH

RICH is used to identify high momentum particles where the TOF detectors usually lose their separation power. The cuts used in RICH to separate particles are illustrated in figure 5.25. The dashed curves are the expected radius dependence on momentum given in 5.24 for each particle species. The solid curves represent the PID cuts applied for particle separation and have the following form:

$$r_{\text{up}} = L \tan \left\{ \arccos \left(\frac{1}{n} \sqrt{1 + \frac{m^2}{(p + \delta p)^2}} \right) \right\} + \delta r, \quad (5.25)$$

$$r_{\text{low}} = L \tan \left\{ \arccos \left(\frac{1}{n} \sqrt{1 + \frac{m^2}{(p - \delta p)^2}} \right) \right\} - \delta r, \quad (5.26)$$

where δr is the RICH radius resolution and δp is the momentum resolution. The ring resolution is set to 0.45 cm while the momentum resolution is species dependent

and takes the values 0.4, 0.6 and 0.8 GeV/ c for pions, kaons and protons respectively. The above mentioned ring and momentum resolution values are just effective values sufficient for a very good species separation in this analysis. The pions and kaons can be separated using only these curves up to ~ 20 GeV/ c while protons are separated up to ~ 30 GeV/ c . Because the analyzed dataset does not have high field settings, it is not necessary to extend the π/K separation beyond 20 GeV/ c but in principle this can be done by using a technique similar to the one applied for TOF detectors in the overlapping regions.

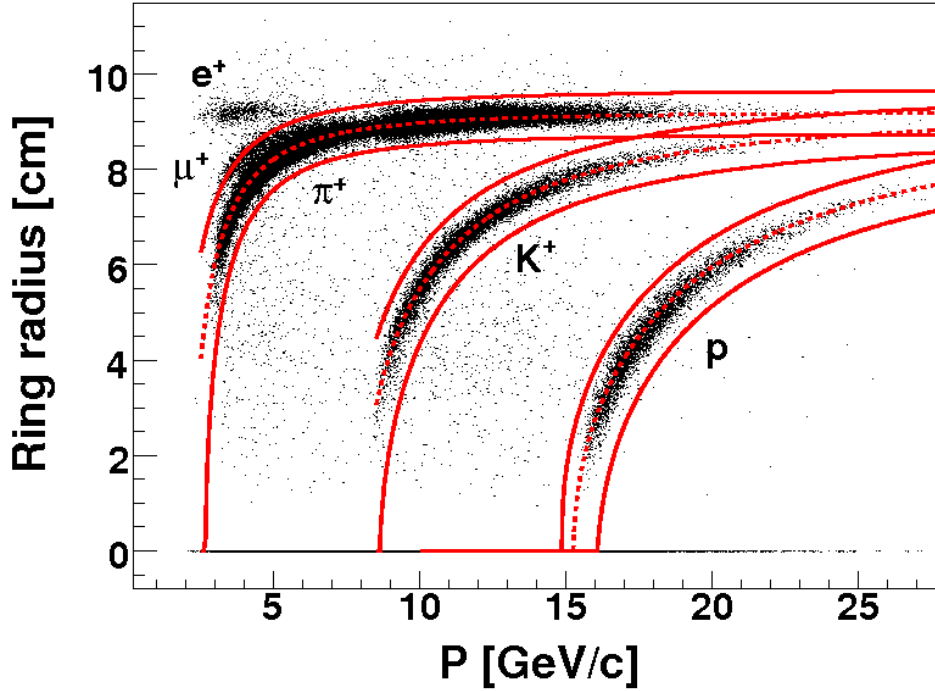


Figure 5.25: RICH ring radius versus momentum. The dashed lines show the expected $r(p)$ dependence while the continuous lines are based on momentum and radius uncertainties and show the cuts used for PID.

RICH is used also in veto mode to identify protons and kaons below the Cerenkov threshold. In the half field 3 degree settings, the tracks in the momentum interval $10 < p < 20$ GeV/ c which give a zero ring radius are vetoed as protons. In the low field 4 and 6 degree settings, the tracks with zero ring radius in the momenta interval $5 < p < 8$ GeV/ c which are not identified as protons in H2 are labeled as kaons. The veto identification method introduces significant amounts of contamination accounted for in section 5.3.2. The relative contamination correction is especially high for anti-protons which have a very small abundance.

5.4 Building spectra

The final outcome of the analysis is single-hadron invariant differential yields per event, or particle densities in rapidity y and transverse momentum p_T :

$$E \frac{d^3\sigma}{d^3p} = \frac{1}{2\pi p_T} \frac{d^2N}{dy dp_T}, \quad (5.27)$$

The azimuthal degree of freedom ϕ is integrated out for the purposes of this work but in an event-by-event analysis the yields depend also on ϕ due to the reaction plane anisotropy.

5.4.1 Corrections

The $d^2N/dydp_T$ is the yield of particles in a given phase space cell centered around y and p_T and is obtained by applying all the corrections to the raw yield like:

$$\left(\frac{d^2N}{dydp_T}\right)_{corrected} = \left(\frac{d^2N}{dydp_T}\right)_{raw} \times C(y, p_T). \quad (5.28)$$

The $C(y, p_T)$ factor is calculated as the product of all individual corrections: spectrometer acceptance, detector efficiencies and corrections due to cuts, contaminations, weak decays, multiple scatterings and hadronic absorption.

Tracking efficiency

Tracking efficiency was studied extensively in reference [184] and [185] by using the reference track method and the track embedding method, respectively.

The reference track method [184] was used for the FS tracking and consists in reconstructing a reference track by using $N - 1$ tracking chambers, where N is the total number of tracking chambers used in the analysis (T1-T5). The unused tracking chamber is then checked for a local track which should match the reference track. The tracking efficiency for the tracking chamber not used for the reconstruction of the reference track is calculated as:

$$\varepsilon = \frac{N_{\text{matched}}}{N_{\text{reference}}}. \quad (5.29)$$

The matching is done in the same way as for the momentum calculation described earlier in this chapter. Figure 5.26 (left panel) shows the calculated tracking efficiency for each tracking chamber by using the reference track method. The efficiency is calculated as a function of the X coordinate of the intersection point between the track and the detector entry window. In order that the calculated efficiencies be valid, the same cuts as in the real tracking analysis must be applied for the matching between the reference track and the local tracks from the studied chamber. The full FS tracking efficiency, taking into account all the detectors used (T1-T5) is calculated using

$$\varepsilon_{FS} = \varepsilon_{T1} \times [\varepsilon_{T2-T4} \times (1 - \varepsilon_{T3}) + \varepsilon_{T2-T3} \times \varepsilon_{T3}] \times \varepsilon_{T4} \times \varepsilon_{T5}, \quad \text{if T3 is used,} \quad (5.30)$$

or

$$\varepsilon_{FS} = \varepsilon_{T1} \times \varepsilon_{T2-T4} \times \varepsilon_{T4} \times \varepsilon_{T5}, \quad \text{if T3 is not used,} \quad (5.31)$$

where ε_{T2-T4} is the efficiency of T2 obtained based on T4-T2 matching and ε_{T2-T3} is the efficiency of T2 obtained based on T3 - T2 matching. The relatively complicated formula of calculating the full FS tracking efficiency ε_{FS} is due to the fact that there is no magnet between the T2 and T3 chambers which leaves the use of the relatively less efficient T3 optional (only if it improves the spectrometer tracking efficiency). Tracking efficiency depends also on occupancy and particular conditions of every setting so ε_{FS} was determined separately for every setting. The tracking efficiency dependence on centrality was found to be negligible for the Au+Au collisions at $\sqrt{s_{NN}} = 62.4$ GeV and only the dependence on the x coordinate of the entry window was considered.

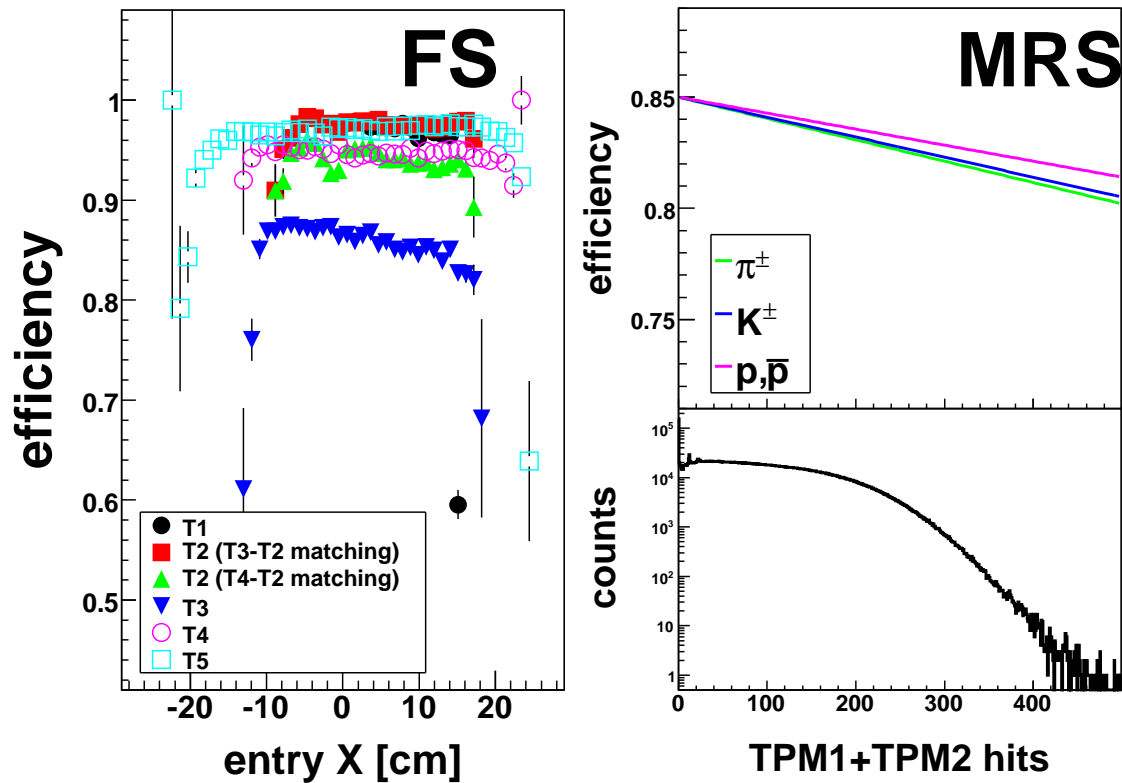


Figure 5.26: Tracking efficiency for individual tracking chambers in FS at 4 degrees (left) and overall MRS tracking efficiency (right panels). In FS, the tracking efficiency is given as a function of the X coordinate of the track intersection with the detector's entry window. In MRS, the tracking efficiency is given as a function of the number of hits in TPM1 and TPM2 detectors.

The track embedding method was used for TPCs [185] and consists in including simulated tracks with well defined momentum into the real data. The simulated tracks are digitized and embedded into raw event data and the tracking software is run normally. The tracking efficiency is calculated as the ratio between the number of successfully reconstructed tracks and the number of embedded tracks and is found to be a function of the hit occupancy in the TPCs (see right panel of figure 5.26). This method was used for MRS tracking and it was found that the efficiency drops linearly with increasing TPC occupancy.

PID detectors efficiency

PID efficiency refers to the fraction of primary tracks intersecting the PID detectors that are associated with a valid hit.

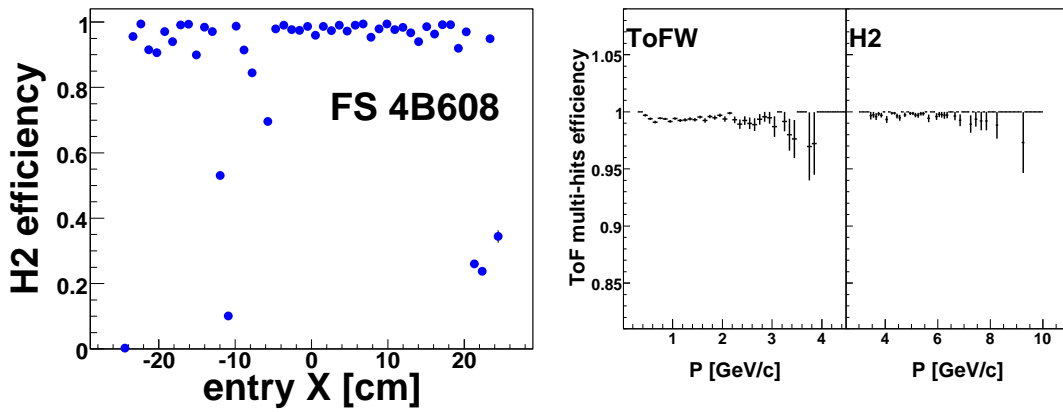


Figure 5.27: Left: Track + TOF hit matching efficiency for H2 as a function of the X coordinate of the track intersection with the detector front plane. Right: TOF detectors efficiency due to multiple hits for TOFW (left) and H2 (right).

For TOF detectors, the inefficiency is due to tracks depositing too little energy in the slats, normally because of edge effects. Also, some tracks are lost due to multiple hits in the same slat since the tracks associated to the same hit are removed in the analysis. The slat efficiency is estimated as the ratio between the number of tracks associated to a valid TOF hit and the number of valid tracks traversing the volume of a TOF slat. The TOFW slat efficiency was found to be approximately constant around 98%. The slat efficiency for H2 is shown in the left panel of figure 5.27 as a function of the hit X coordinate which can be directly connected to the a slat number. The very low efficiency X intervals correspond to dead or inefficient slats which were removed from analysis. The inefficiency due to multiple tracks hitting the same TOF slat, which were removed from analysis, was estimated to be less than 1% in both TOFW and H2. Right panel of figure 5.27 shows the multiple hits efficiency (1-inefficiency) as a function of momentum.

RICH efficiency was studied in detail in reference [179] and was found to be approximately constant beyond a velocity threshold which depends on the particle species and the refractive index of the gas used as active medium. Between the Cerenkov threshold and the saturation limit the RICH efficiency varies strongly from zero to the maximum efficiency. A calculation of RICH efficiency as a function of the normalized Lorentz factor γ made for protons is shown in figure 5.19. For this analysis, only mo-

momentum intervals where the RICH efficiency is saturated to a maximum of 97% are used, meaning $p > 3$ GeV/ c for pions and $p > 10$ GeV/ c for kaons. Protons with a good ring but with momenta close to threshold are used together with the vetoed protons which do not produce a ring. In this case a contamination correction due to the unresolved pions and kaons is required.

TOF PID cuts correction

TOF PID separates particle species with a 3σ confidence only up to certain momentum limits. This was discussed in section 5.3.1. Beyond this limits, the condition that the contamination with other species be less than 5% imposed momentum dependent cuts on m^2 which reduces the real yield (see figure 5.18). The correction due to this loss is calculated as $Y_{corr}^i(p) = Y_{PID}^i(p)/(1 - f_i(p))$ where Y_{corr} is the corrected yield, Y_{PID} is the yield obtained after applying the PID cuts and f_i is the fraction of lost yield due to cuts defined in equation 5.18 and shown in figure 5.18 as a function of momenta. The index i refers to the particle species π , K and p .

RICH veto contamination corrections

RICH was used in veto mode to identify protons and kaons as explained in section 5.3.2. The momentum p dependent contamination fraction of vetoed protons $F^{p,\bar{p}}(p)$ with unresolved pions and kaons in the momentum range $10 < p < 20$ GeV/ c was estimated as

$$F^{p,\bar{p}}(p) = \frac{C^{\pi^\pm}(p) + C^{K^\pm}(p)}{Y^{p,\bar{p}}(p)} = \frac{1 - \varepsilon_{RICH}}{\varepsilon_{RICH}} \times \frac{Y^{\pi^\pm}(p) + Y^{K^\pm}(p)}{Y^{p,\bar{p}}(p)}, \quad (5.32)$$

where ε_{RICH} is the RICH maximum efficiency (97%), $Y^{\pi^\pm}(p)$ is the yield of identified pions, $Y^{K^\pm}(p)$ is the yield of identified kaons and $Y^{p,\bar{p}}(p)$ is the yield of vetoed (anti)protons. The contamination factor was estimated for the 3 degrees settings and is shown in figure 5.21. The uncorrected yield of (anti)protons is multiplied with the factor $(1 - F^{p,\bar{p}})$ to get the corrected yield.

The contamination fraction for vetoed kaons through the mixed H2+RICH veto PID method is shown in figure 5.22 and was calculated as follows:

$$F^{K^\pm}(p) = \frac{C^{\pi^\pm}(p) + C^{p,\bar{p}}(p)}{Y^{K^\pm}(p)}, \quad (5.33)$$

where the pion contamination $C^{\pi^\pm}(p)$ due to RICH inefficiency is calculated in the same way as in equation 5.32 and the contamination with protons $C^{p,\bar{p}}(p)$ is estimated as

$$C^{p,\bar{p}}(p) = \varepsilon_{H2}(p) \times \left(\frac{1}{1 - f_p(p)} - 1 \right) \times Y^{p,\bar{p}}(p). \quad (5.34)$$

The factor $(1/(1 - f_p(p)) - 1)$ accounts for the lost protons due to the H2 PID cuts, ε_{H2} is the H2 PID efficiency and $Y^{p,\bar{p}}(p)$ is the uncorrected yield of identified protons in H2.

Correction for rescatterings

Charged particles emerging from a collision have a flight length of a few meters inside the MRS spectrometer and up to 20 meters in the FS spectrometer where these can

suffer secondary interactions like weak decays (kaons and pions), scatterings in the air or materials and absorption. All these phenomena must be taken into account and cor-

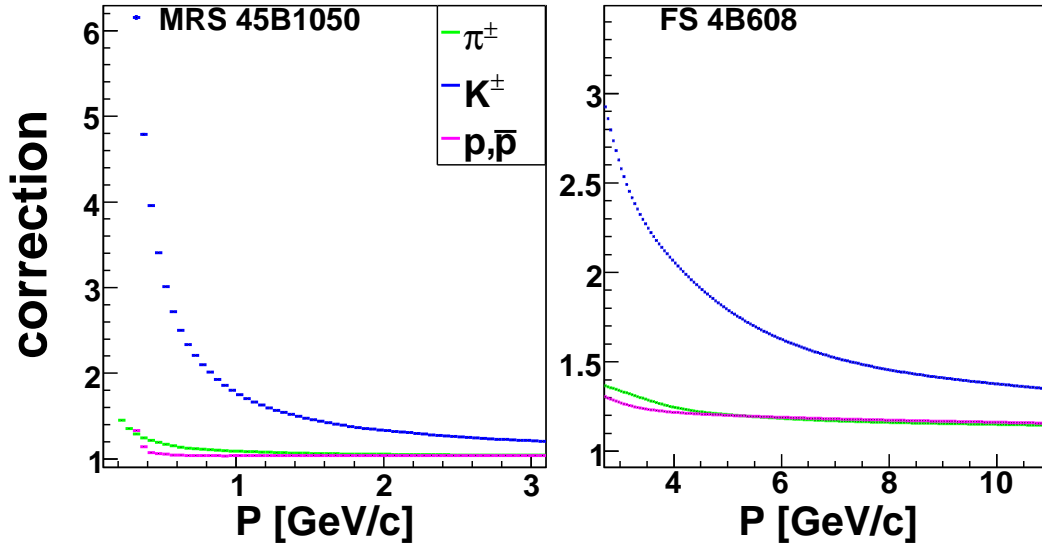


Figure 5.28: Correction for decays, multiple scatterings and hadronic absorption for the MRS setting 45B1050 (left) and the FS setting 4B608 (right).

rected for when constructing the final invariant yields. To calculate these corrections, a GEANT simulation of the entire experimental setup was used. Charged particles from the species of interest are generated in a wide momentum range. These tracks are then transported through the experimental setup with phenomena like energy loss, decays, absorption and rescatterings turned on and finally digitized to mimic the real data. The resulting tracks are analyzed like the real data with the same track quality cuts. The ratio between the number of good reconstructed tracks passing the same cuts as in the data and the number of thrown tracks is used to correct the final spectrum. Figure 5.28 shows the momentum dependent correction factor applied to the data. Kaons have the highest correction due to their relatively small decay length. This correction accounts also for the lost particles due to the χ^2 cut on tracks and also for the muons mistakenly identified as pions.

Feed-down correction

The identified particle yields obtained after all the analysis can still contain a sizeable amount of products from weakly decaying particles with decay lengths of the order of the spectrometer size, like K^0 , Λ , Σ , Ξ or Ω . Since not all the decays happen before detectors and not all products fall in the spectrometer acceptance, it is crucial to estimate the fraction of measured particles which have their origin in weak decays. To do this, a GEANT simulation was used where weakly decaying particles (only K_S^0 and $\Lambda + \Sigma$) with realistic momenta distributions were used [76]. Particles were tracked through the entire experimental setup and the same analysis cuts were applied.

The yield of K^0 particles was estimated to amount to the average between K^+ and K^- and it was found that the overall contamination of pion yields with products from K_S^0 decay is 4% in MRS and 6% in FS. The correction was implemented by using the above mentioned contamination values without momentum dependence.

The Λ yields were estimated by assuming that $\Lambda/p = \bar{\Lambda}/\bar{p} = 0.9$ [26] in central Au+Au collisions at $\sqrt{s_{NN}} = 200$ GeV over the entire rapidity interval covered experimentally. The fraction of pions originating in Λ weak decays was found to be $< 1\%$ due to the strong momentum kick which usually takes the pions out of the spectrometer acceptance and primary particle cuts. It was estimated that most of the $\Lambda - \Sigma$ decay protons survive the analysis cuts and fall in the spectrometer acceptance ($\sim 90\%$ in MRS and $\sim 80\%$ in FS [26]). However, no feed-down correction was applied to the (anti-)proton spectra obtained in this analysis.

In the case of charged kaons, the contamination with products from long lived weakly decaying hadrons is negligible since only the decay of the rare Ω baryons can produce kaons.

Acceptance correction

The BRAHMS spectrometers have a very small geometrical aperture which needs to be corrected for in order to obtain the final yields. The acceptance correction is calculated for each spectrometer angle and magnetic field setting by throwing a flat distribution of particles in momentum p , polar angle θ and azimuthal angle ϕ [4, 86, 19, 186]. The particles are transported through the entire spectrometer and are checked to satisfy all the geometrical cuts imposed on real data (geometrical fiducial cuts on magnets and detectors, missing TOF slats). The acceptance correction for a given phase space cell is calculated as:

$$A(y, p_T) = \frac{\text{accepted particles } (y, p_T)}{\text{thrown particles } (y, p_T)} \times \frac{\Delta\phi}{2\pi}, \quad (5.35)$$

where $\Delta\phi$ is the width of the interval in azimuthal angle where particles are thrown which must be chosen wide enough so that the spectrometer aperture be well inside. The momentum and θ interval are also selected around the spectrometer acceptance to improve the simulation efficiency.

The spectrometer geometrical acceptance depends on the collision vertex Z_{vtx} because the polar $\Delta\theta$ and azimuthal $\Delta\phi$ apertures of the spectrometer are changing with Z_{vtx} so the acceptance correction is calculated in small vertex intervals. For this analysis, acceptance correction maps were calculated in 5 cm wide vertex intervals between -20 cm and +20 cm. The analysis of the data is also done in such a way that (y, p_T) maps of yields are generated for every 5 cm vertex interval.

The phase space coordinates used are the rapidity y and transverse momenta p_T but the acceptance maps can be generated in the same way using different coordinates and their combinations like transverse mass m_T , Feynman x_F , pseudo-rapidity η , etc. Figure 5.29 shows the acceptance correction for the vertex interval $[0, +5]$ cm in all spectrometer settings available for this work. The low acceptance edges visible in the figure for all settings are due to the continuous nature of the acceptance edges which intersect partially the finite size bins of the acceptance histograms. These bins are removed from the analysis. The iso-momentum curves shown in the figure illustrate the maximum momentum for the PID methods used.

Normalization

After all the analysis and corrections, the final yields must be divided by the total number of events taken into consideration in the analysis. This is obtained from the number of all events satisfying the minimum bias trigger and the analysis bias (*e.g.*

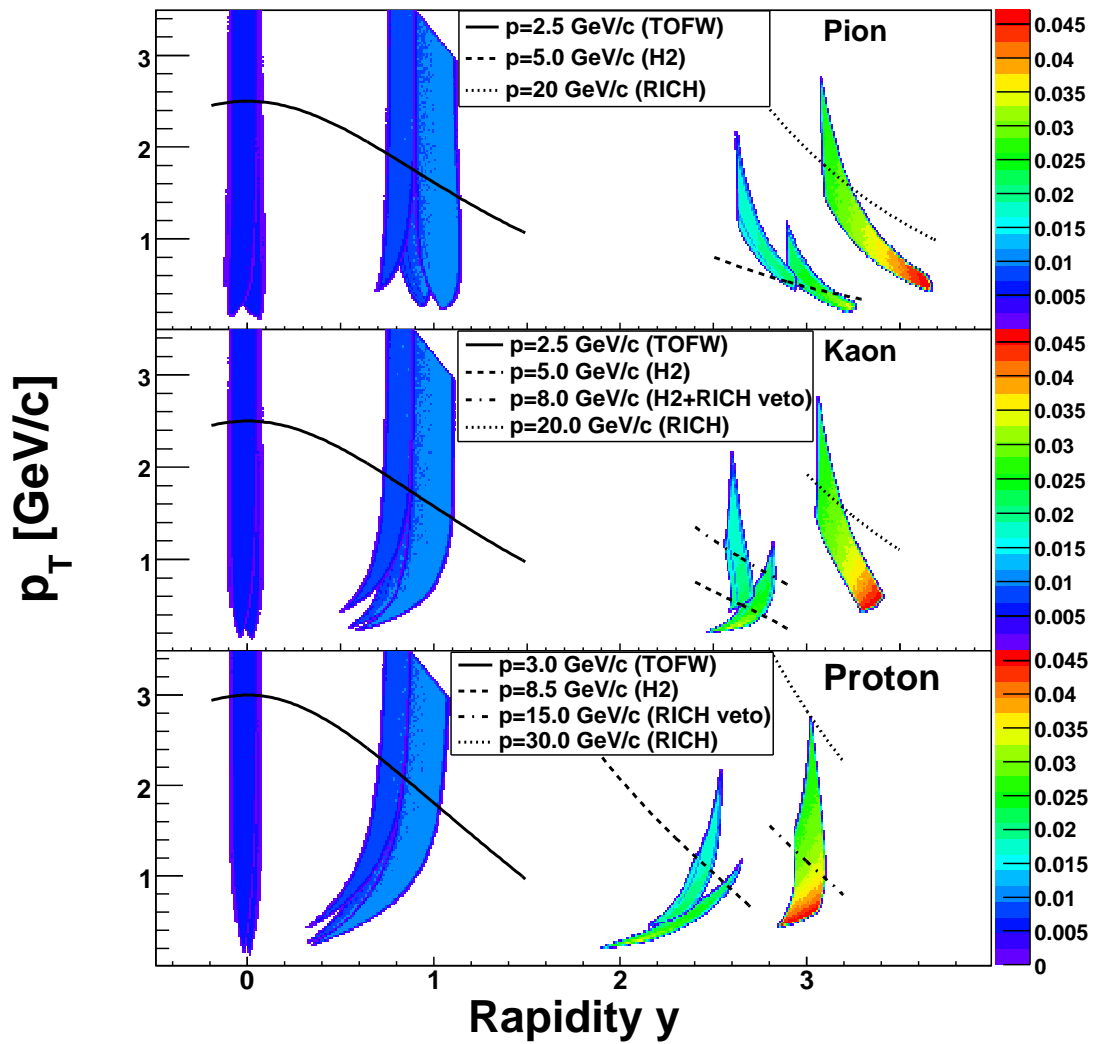


Figure 5.29: Acceptance correction in the vertex interval $[0,+5]$ cm for pions (top), kaons (middle) and protons (bottom) in the (y, p_T) space. The curves indicate the maximum momentum for the different PID methods used in this analysis.

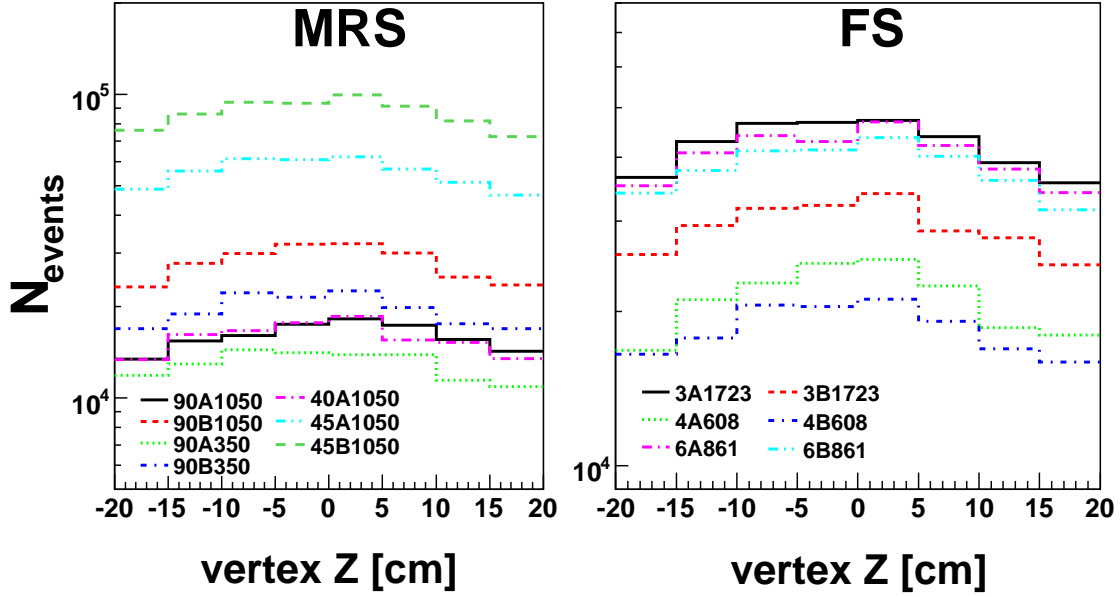


Figure 5.30: Normalization constants for 0-10% central Au+Au collisions in all settings and all vertex bins used in this work.

centrality and vertex range). Since the events satisfying the minimum bias but not the track trigger are interesting only for normalization, these are downscaled so that only a fraction of them are recorded. In order to obtain the normalization constant N_{events} for a given vertex interval i_Z and a given centrality class the following formula must be used:

$$N_{\text{events}}(i_Z) = \sum_r N_{\text{events}}^{\text{min-bias}}(r; i_Z) \times S(r), \quad (5.36)$$

where the summation goes over the run number r , $N_{\text{events}}^{\text{min-bias}}(r; i_Z)$ is the number of minimum bias events from run r in the vertex interval i_Z and $S(r)$ is the scale-down factor for run r . The normalization constants for all the settings used in MRS and FS are shown in figure 5.30.

5.4.2 Merging spectra

Final invariant spectra in a given setting and vertex interval can be obtained from the (y, p_T) maps of yields, corrections and acceptance as [4, 86, 19]

$$\frac{1}{2\pi p_T} \frac{d^2 N}{dy dp_T}(y, p_T) = \frac{1}{2\pi p_T} \times \frac{1}{N_{\text{events}}} \times \frac{1}{\delta y \delta p_T} \times \frac{C(y, p_T)}{A(y, p_T)} \times Y(y, p_T), \quad (5.37)$$

where δy and δp_T are the bin sizes of the (y, p_T) histograms, $C(y, p_T)$ is the product of all the necessary corrections for the (y, p_T) cell, $A(y, p_T)$ is the spectrometer acceptance and $Y(y, p_T)$ is the raw yield of particles surviving all the analysis cuts.

Combining vertex intervals for one setting

In order to improve statistics and also to extend the phase space coverage, the spectra obtained in the available vertex intervals for a given setting are merged. The resulting

invariant yield can be calculated as the sum [4, 86, 19]

$$Y(y, p_T; s) = \sum_{i_Z} Y(y, p_T; i_Z, s), \quad (5.38)$$

and

$$\frac{1}{\text{Corr}(y, p_T; s)} = \sum_{i_Z} \frac{1}{\text{Corr}(y, p_T; i_Z, s)} \quad (5.39)$$

where

$$\text{Corr}(y, p_T; i_Z, s) = \frac{C(y, p_T)}{N_{\text{events}}(i_Z, s)A(y, p_T; i_Z, s)}. \quad (5.40)$$

The corrections other than acceptance and normalization do not depend on the vertex bin. The summed invariant yield can be obtained as follows:

$$\frac{1}{2\pi p_T} \frac{d^2 N}{dy dp_T}(y, p_T; s) = \frac{1}{2\pi p_T} \times \frac{1}{\delta y \delta p_T} \times \text{Corr}(y, p_T; s) \times Y(y, p_T; s). \quad (5.41)$$

Combining settings

Combining data from more spectrometer settings is necessary to expand the rapidity and p_T ranges since one spectrometer setting covers a relatively small area in phase space.

Spectrometer	Angle[°]	Polarity	Current[A]
MRS	90°	A	1050
MRS	90°	B	1050
MRS	90°	A	350
MRS	90°	B	350
MRS	45°	A	1050
MRS	45°	B	1050
MRS	40°	A	1050
FS	6°	A	861
FS	6°	B	861
FS	4°	A	608
FS	4°	B	608
FS	3°	A	1723
FS	3°	B	1723

Table 5.3: Spectrometer settings used in this analysis. The current values correspond to the current intensity in the D5 magnet (MRS) and D1 magnet (FS).

A list of all spectrometer settings used in this analysis is given in table 5.3. The average invariant yield of a number of settings in a given $y - p_T$ cell is obtained as [4, 86, 19]:

$$\left\langle \frac{d^2 N}{dy dp_T} \right\rangle = \frac{\sum_s \frac{d^2 N}{dy dp_T}(s) \times W(y, p_T, s)}{\sum_s W(y, p_T, s)}, \quad (5.42)$$

where $W(y, p_T, s)$ acts as a weight and is defined as $W(y, p_T, s) = 1/\text{Corr}(y, p_T; s)$. In this way, settings with high corrections contribute less to the average. In figure 5.31

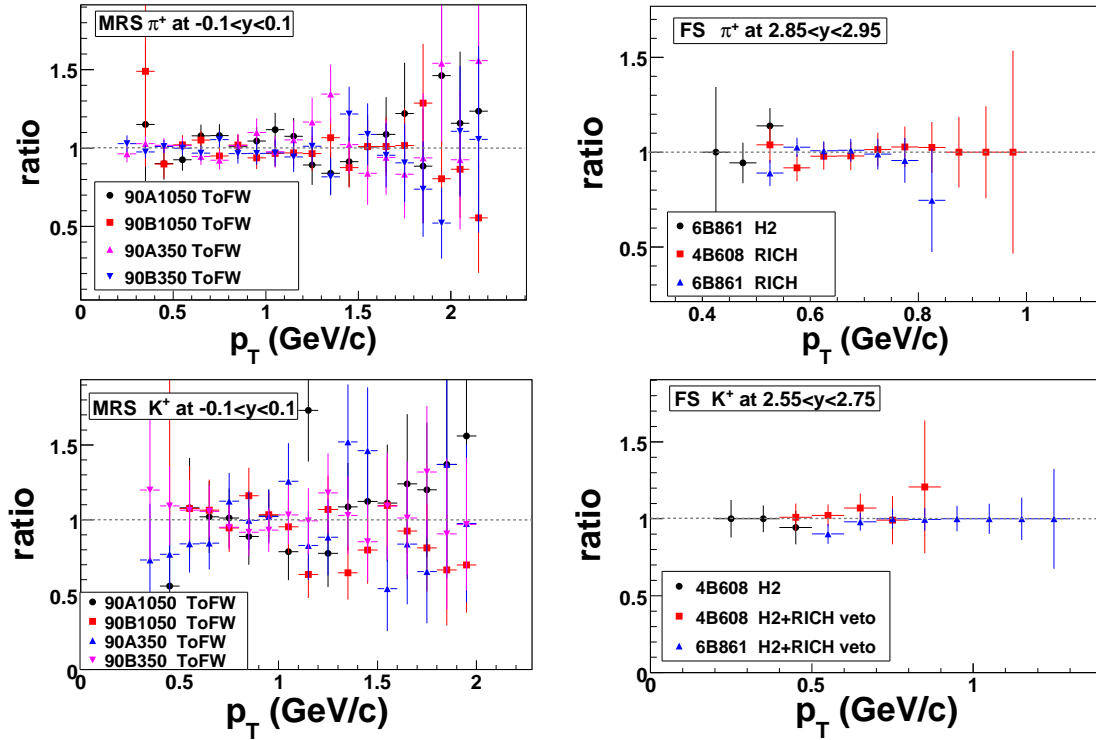


Figure 5.31: Consistency check between the settings and PID methods used for π^+ (top panels) and K^+ (bottom panels) in MRS (left panels) and FS (right panels). The ratio is the yield of a given setting divided by the average given by all settings contributing.

comparisons between different overlapping settings and their average are shown for pions and kaons.

Its important to note that the summation in equation 5.42 is made only over those settings which have non-zero acceptance and thus, non-zero weight, in the considered (y, p_T) cell.

Chapter 6

Experimental results

Invariant yields obtained from the data analysis described in Chapter 5 are presented here for 0-10% central Au+Au collisions. The spectra are fitted with different functions to obtain p_T integrated yields and spectral information like average p_T and inverse slopes T_{eff} . Anti-particle to particle and K/π ratios are constructed using the dN/dy values. The sources of systematic errors are also discussed.

6.1 Invariant spectra

Invariant differential yields, $\frac{1}{2\pi p_T} \frac{d^2N}{dy dp_T}$, were constructed for each available spectrometer setting and were corrected for geometrical acceptance, tracking and PID efficiency, contamination, in-flight weak decays, feed-down from weakly decaying particles (only pions) and multiple scattering effects. The resulting (y, p_T) map is shown in figure 6.1. The available spectrometer settings allowed a p_T coverage down to $p_T \sim 0.25$ GeV/ c for pions and no less than 0.35 GeV/ c for kaons. The (anti)protons were measured down to $p_T \sim 0.3$ GeV/ c in the 4 and 6 degree FS settings but in the other settings the p_T coverage was poorer. The protons and anti-protons identified in MRS with a full momentum smaller than $p = 0.6$ GeV/ c were rejected from the analysis due to strong effects from multiple scatterings.

The invariant p_T spectra were extracted in several rapidity intervals by projecting the two-dimensional differential yield map on the p_T axis. In figure 6.2, the spectra obtained from the available (y, p_T) range for pions are shown. The centers of the rapidity windows are given on the figure. The widths of these intervals are $\Delta y = 0.2$ in MRS settings ($y \leq 1$) and generally $\Delta y = 0.1$ in the FS intervals. The reason for having thinner slices at forward rapidity is the strong rapidity dependence of yields in a given p_T bin. Wider slices in FS are used only when there are constraints from limited statistics or covered p_T range.

6.1.1 Fitting spectra

For extracting the integrated yields and spectral information, the spectra obtained in the available rapidity intervals were fitted with different functions. Figures 6.2, 6.3 and 6.4 show the fitted spectra for pions, kaons and (anti)protons, respectively, from 0-10% central Au+Au collisions. The functions used in the plots are power laws for pions and m_T exponential functions for kaons and protons. The fitting functions used in this analysis are defined in table 6.1.

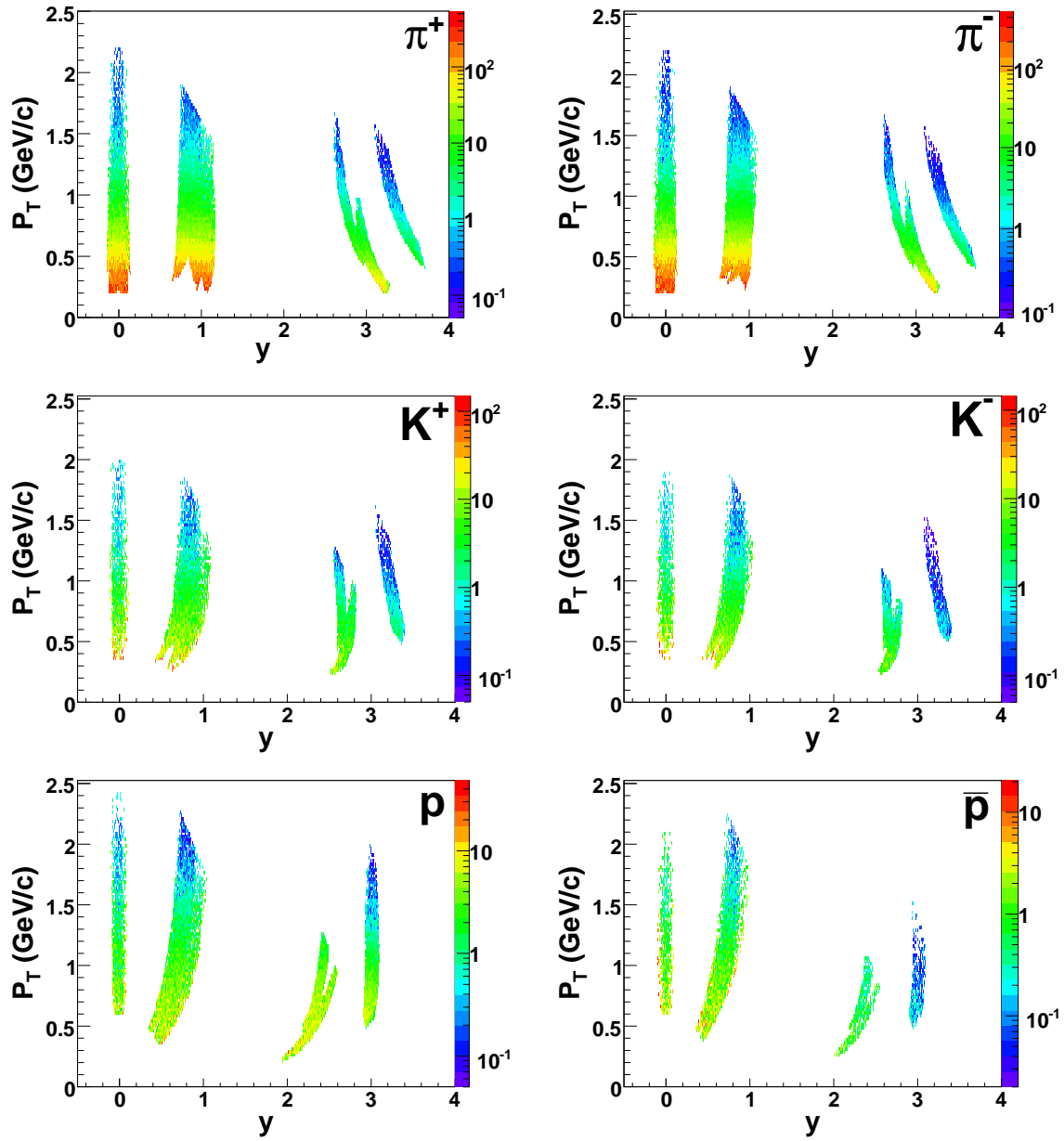


Figure 6.1: Invariant differential yield map in rapidity y and transverse momentum p_T for identified pions, kaons, protons and their corresponding anti-particles from 0-10% central Au+Au collisions at $\sqrt{s_{NN}} = 62.4$ GeV.

Name	Definition	Parameters
Power law in p_T	$A \times (1 + p_T/p_0)^{-n}$	A, p_0, n
Exponential in m_T	$A \times \exp(-m_T/T_{\text{eff}})$	A, T_{eff}
Boltzmann in m_T	$A \times m_T \times \exp(-m_T/T)$	A, T

Table 6.1: Functions used to fit the invariant differential spectra.

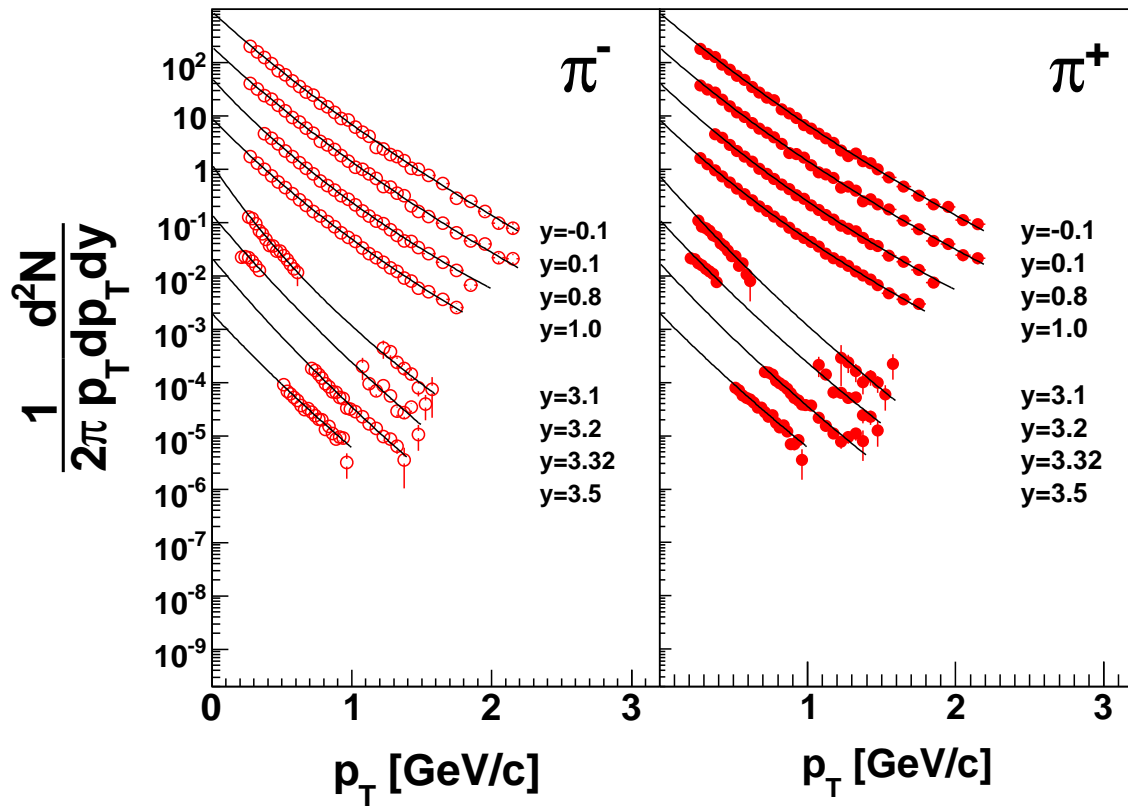


Figure 6.2: Pion invariant spectra from 0-10% central Au+Au collisions at $\sqrt{s_{NN}} = 62.4$ GeV fitted with power law functions. Only spectra from rapidity windows with good enough coverage are shown. The spectra are multiplied with a 0.2^n factor where $n = 0, 1, 2, \dots$, for better visibility.

Since the spectrometer acceptance does not allow measurements at very low p_T , all the integrated dN/dy yields obtained have an amount of extrapolation into the p_T intervals outside acceptance and a systematic error due to the choice of fitting function. This uncertainty is largest for pions because of the low average p_T for this species. In order to estimate the extrapolation uncertainty, both a power law distribution and an m_T exponential were used to fit the pion spectra. Of these two, the power law

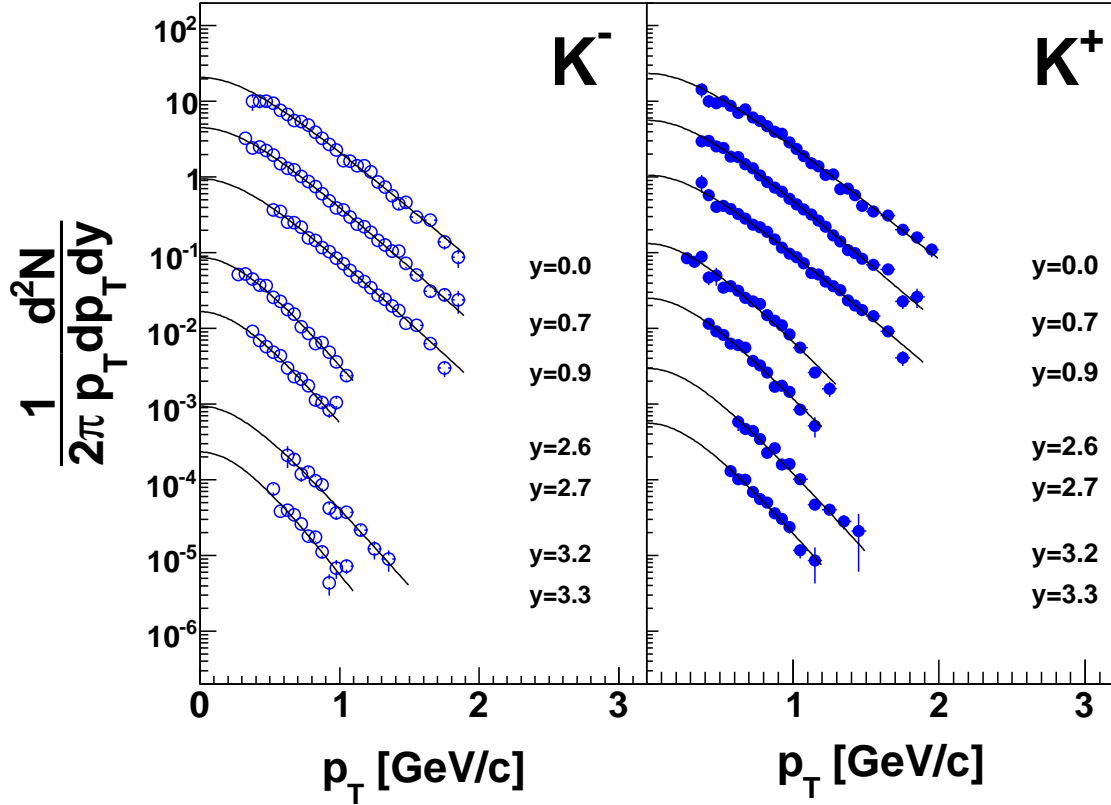


Figure 6.3: Kaon invariant spectra from 0-10% central Au+Au collisions at $\sqrt{s_{NN}} = 62.4$ GeV fitted with m_T exponential functions. The spectra are multiplied with a 0.2^n factor where $n = 0, 1, 2, \dots$, for better visibility.

distribution gives the best fit to the experimental results over the observed momentum range (see figure 6.5), and at very low p_T is in agreement with the measurements made by the PHOBOS collaboration at $y = 0.8$ and with $p_T < 0.1$ GeV/c [187]. In the case of the m_T exponential, the spectra cannot be described over the entire p_T range so the fit range was limited to $p_T < 1$ GeV/c. Also, the fitted inverse slope parameters and the average p_T manifest a dependence on the fit range which is believed to be due to the many resonances that give a strong contribution to the pion spectra at low p_T . Kaon and proton spectra are equally well fitted with m_T exponentials and Boltzmann distributions. Figure 6.5 shows the fit quality for the spectra from a mid-rapidity slice and a forward rapidity slice for π^+ , K^+ and protons.

Inverse slope parameters were extracted from fits with thermal model inspired m_T exponential functions. These parameters can be interpreted as an effective temperature T_{eff} of the spectra. The pion spectra do not have a thermal shape due to significant contributions from resonance decays, a fact that is believed to make the m_T exponential fit less successful. So in order to extract the T_{eff} parameters for pions, the fit was

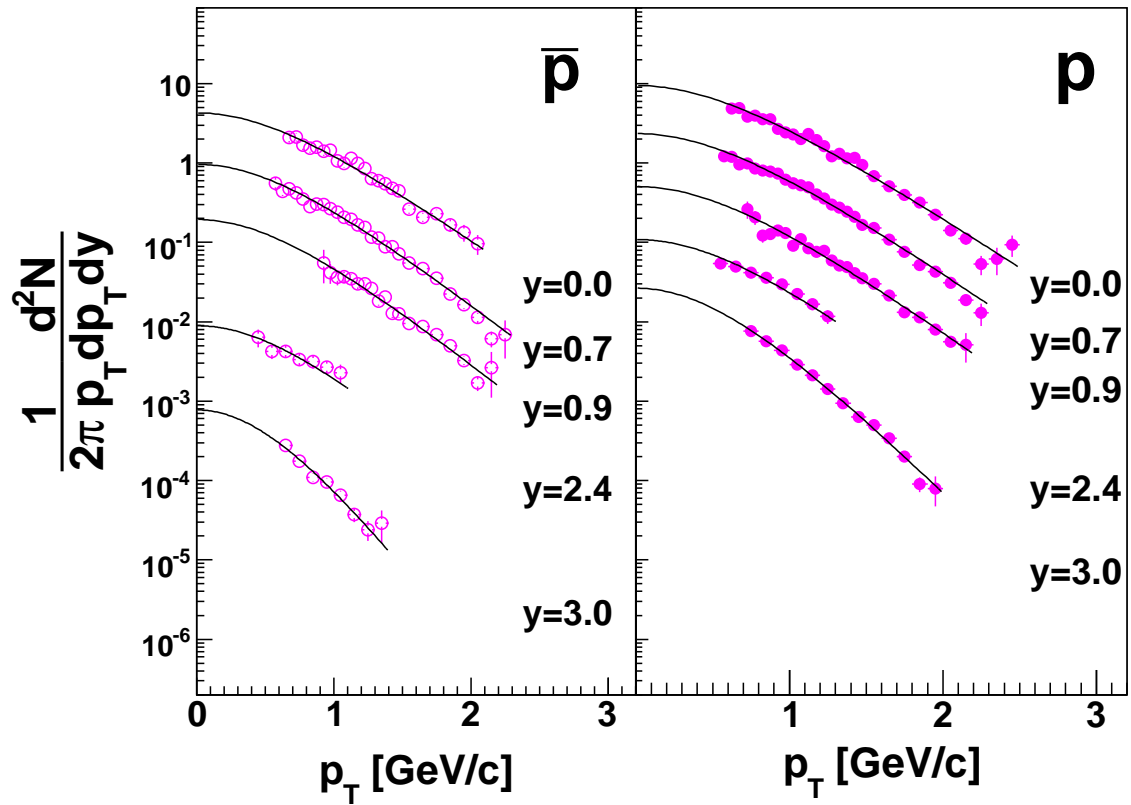


Figure 6.4: Proton and anti-proton invariant spectra from 0-10% central Au+Au collisions at $\sqrt{s_{NN}} = 62.4$ GeV fitted with m_T exponential functions. The spectra are multiplied with a 0.2^n factor where $n = 0, 1, 2, \dots$, for better visibility.

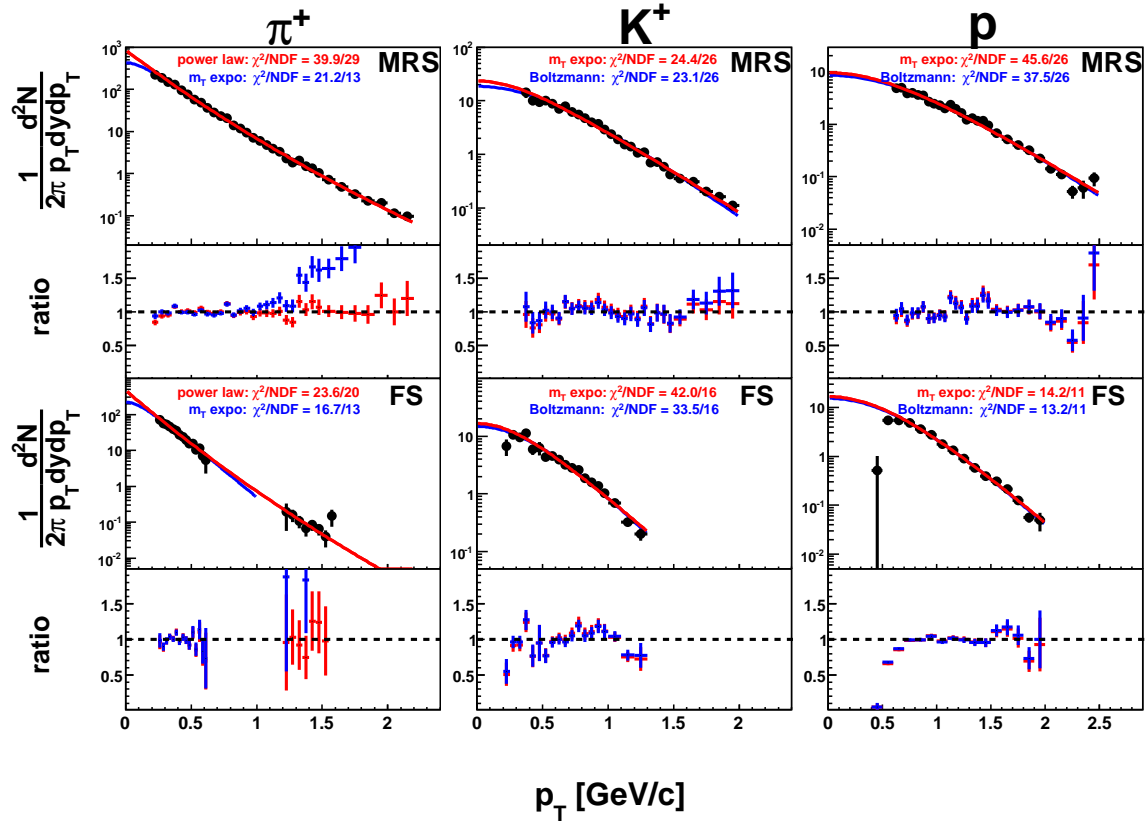


Figure 6.5: Invariant spectra for π^+ , K^+ and protons fitted with different functions and the ratios between spectra and fitted functions. The top two rows are MRS spectra at $y = 0$ and the bottom two rows are FS spectra at $y = 3.1$ (π^+), $y = 2.6$ (K^+) and $y = 3.0$ (p). The colors correspond to the fit functions.

performed only up to $p_T = 1$ GeV/ c . Figure 6.6 shows the extracted inverse slope

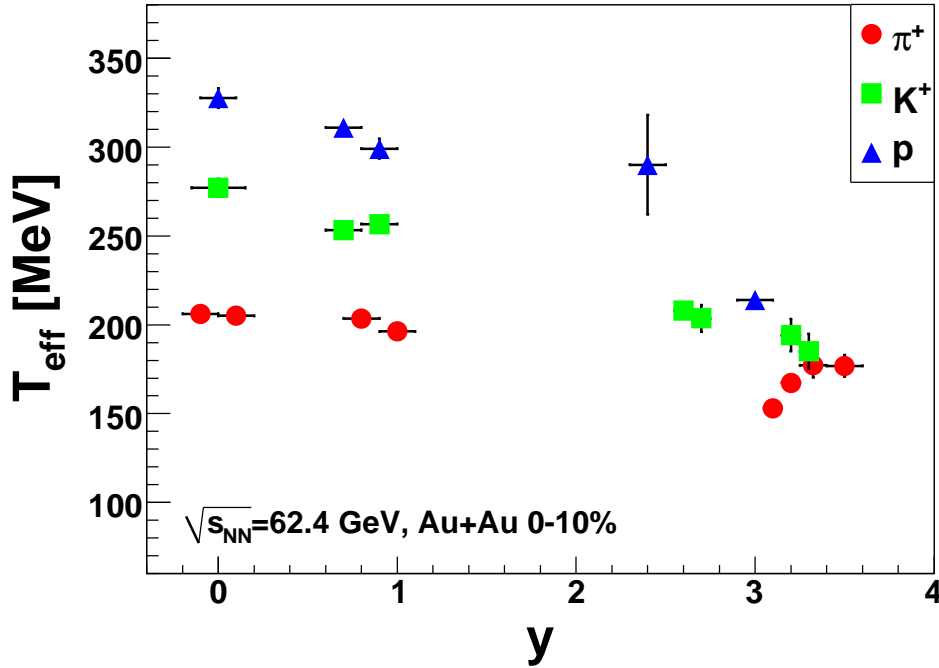


Figure 6.6: Inverse slope parameters T_{eff} versus rapidity obtained from fitting invariant spectra with m_T exponential functions. The error bars are statistical errors only.

parameters with rapidity for π^+ , K^+ and protons. The error bars shown in the figure represent just the statistical errors given by the fit procedure. There is an overall drop of T_{eff} with increasing rapidity which is stronger for heavier particles. The pion effective temperatures behaviour with rapidity shows some irregularities at rapidities higher than 3 due to the change in the p_T interval covered. Effective temperatures for pions are lower in low p_T intervals and increase towards high p_T due to the power-law shape of the spectra.

The mean transverse momentum $\langle p_T \rangle$ can also be extracted from the fitted functions using the formula

$$\langle p_T \rangle = \frac{\int_0^\infty p_T (2\pi p_T) f(p_T) dp_T}{\int_0^\infty (2\pi p_T) f(p_T) dp_T}. \quad (6.1)$$

where $f(p_T)$ are the fit functions defined in table 6.1. It is obvious that $\langle p_T \rangle$ is dependent on the function chosen for the fit so in figure 6.7 these are shown accompanied by the variance due to the fit function choice (shaded squares). The average p_T values show a decrease with rapidity as seen above for the inverse slopes, demonstrating that these observables are strongly correlated. The reasons for the rapidity behaviour of $\langle p_T \rangle$ and effective temperatures T_{eff} will be discussed in the next chapter.

6.1.2 p_T integrated yields

Particle integrated yields for the rapidity intervals defined in the previous section are obtained by extrapolating the spectra to the full p_T range by using the fit functions. The fit functions are defined in such a way that the dN/dy is proportional to the A parameter shown in table 6.1. This procedure, described in [4], gives the possibility of

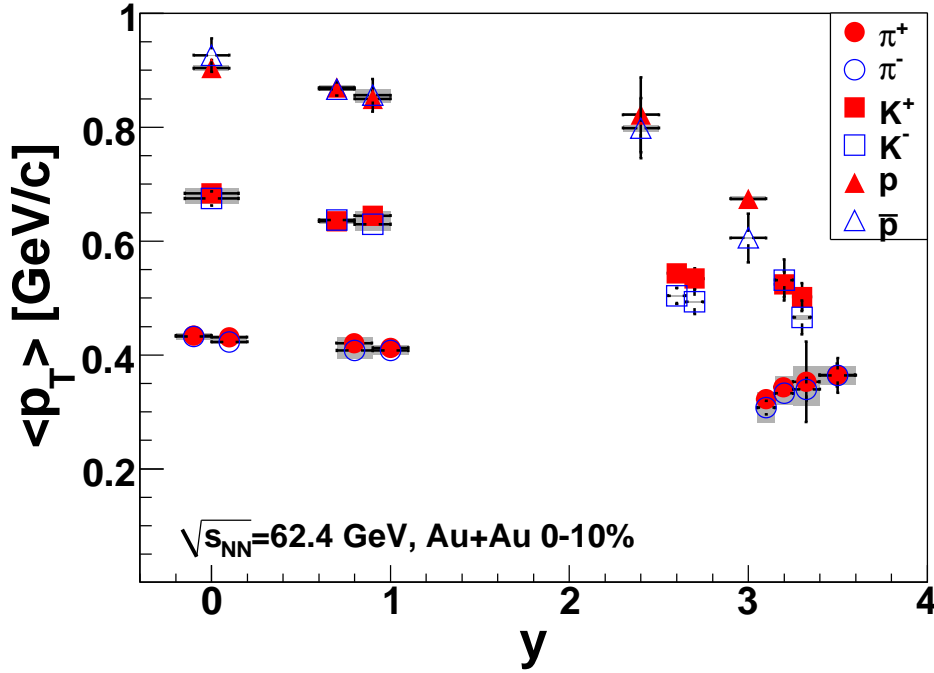


Figure 6.7: Average transverse momentum $\langle p_T \rangle$ for π^\pm , K^\pm , p and \bar{p} as a function of rapidity. The error bars are statistical errors. The shaded boxes represent systematic errors due to the choice of fitting function.

extracting the statistical error for the integrated yield in a rigorous way by using the fitting algorithm. As shown in figure 6.5, the fit functions can disagree significantly in the experimentally uncovered low p_T range which creates an uncertainty for the extracted dN/dy values. The yield uncertainty is usually high when the fraction of the total yield covered is small and also when the covered p_T range is not wide enough to constrain the fit well. Thus not all available rapidity slices were chosen to extract dN/dy . In tables 6.2, 6.3 and 6.4, the extrapolated yields from the fit functions used are given for pions, kaons, protons and anti-protons. It is clear that in the case of pions the p_T coverage is crucial for constraining the results. The fiducial ratio (F.R.) listed

y	dN/dy power law		dN/dy m_T expo		p_T [GeV/c]	F.R.[%]
	π^+	π^-	π^+	π^-		
-0.10	202.0±3.3	207.7±3.8	183.9±2.3	187.4±2.6	0.25 - 2.2	68
0.10	215.2±4.3	216.4±3.8	193.7±2.9	195.7±2.5	0.25 - 2.2	68
0.80	208.9±3.7	220.3±4.6	175.5±1.6	178.5±1.8	0.35 - 2.0	48
1.00	207.2±2.4	214.6±2.3	180.1±1.2	186.1±1.2	0.25 - 1.8	65
3.10	58.8±1.7	69.6±3.6	50.9±1.0	53.0±1.0	0.25 - 1.6	55
3.20	48.7±1.2	56.2±1.2	45.8±1.1	52.6±1.1	0.20 - 1.5	65
3.32	37.4±15.6	42.4±4.0	25.5±3.2	27.7±3.1	0.70 - 1.4	8
3.50	24.8±2.0	24.3±3.7	20.3±1.2	19.9±1.0	0.50 - 1.0	20

Table 6.2: Extrapolated dN/dy values for charged pions. The given errors are statistical only. F.R.(fiducial ratio) is the fraction of the total yield covered by the experimental data.

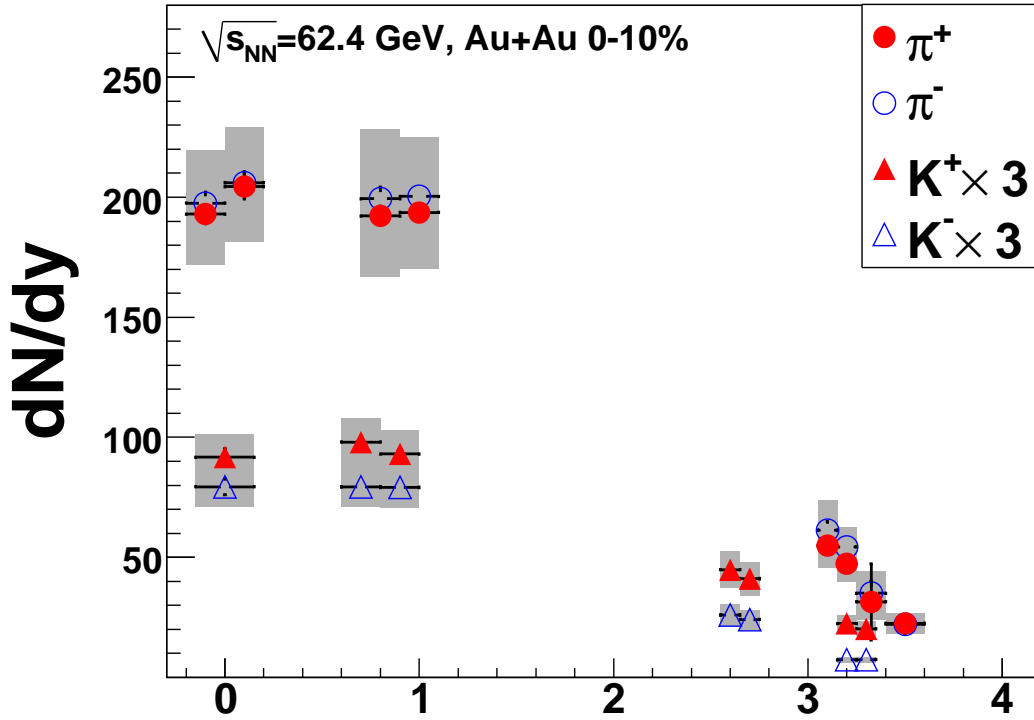


Figure 6.8: p_T integrated yields (dN/dy) as a function of rapidity for identified charged mesons. The error bars are statistical errors. The shaded boxes represent all systematical errors added in quadrature. The pion yields are corrected for pions originating from weak decays.

y	dN/dy m_T expo		dN/dy Boltzmann		p_T [GeV/c]	F.R. [%]
	K^+	K^-	K^+	K^-		
0.00	31.4 ± 0.85	27.2 ± 0.79	29.7 ± 0.81	25.7 ± 0.75	0.35 - 2.00	75
0.70	33.5 ± 0.45	27.0 ± 0.36	31.8 ± 0.43	25.9 ± 0.34	0.30 - 1.90	80
0.90	32.1 ± 0.60	27.5 ± 0.61	30.0 ± 0.57	25.3 ± 0.56	0.35 - 1.90	75
2.60	15.2 ± 0.38	8.76 ± 0.27	14.8 ± 0.37	8.57 ± 0.26	0.25 - 1.30	78
2.70	14.0 ± 0.38	8.16 ± 0.25	13.4 ± 0.37	7.91 ± 0.24	0.35 - 1.20	60
3.20	7.80 ± 0.66	2.53 ± 0.32	7.16 ± 0.59	2.32 ± 0.29	0.60 - 1.50	32
3.30	6.93 ± 0.37	2.53 ± 0.20	6.55 ± 0.35	2.41 ± 0.19	0.50 - 1.20	34

Table 6.3: Extrapolated dN/dy values for charged kaons. The errors are statistical only. F.R. (fiducial ratio) is the fraction of the total yield covered by the experimental data.

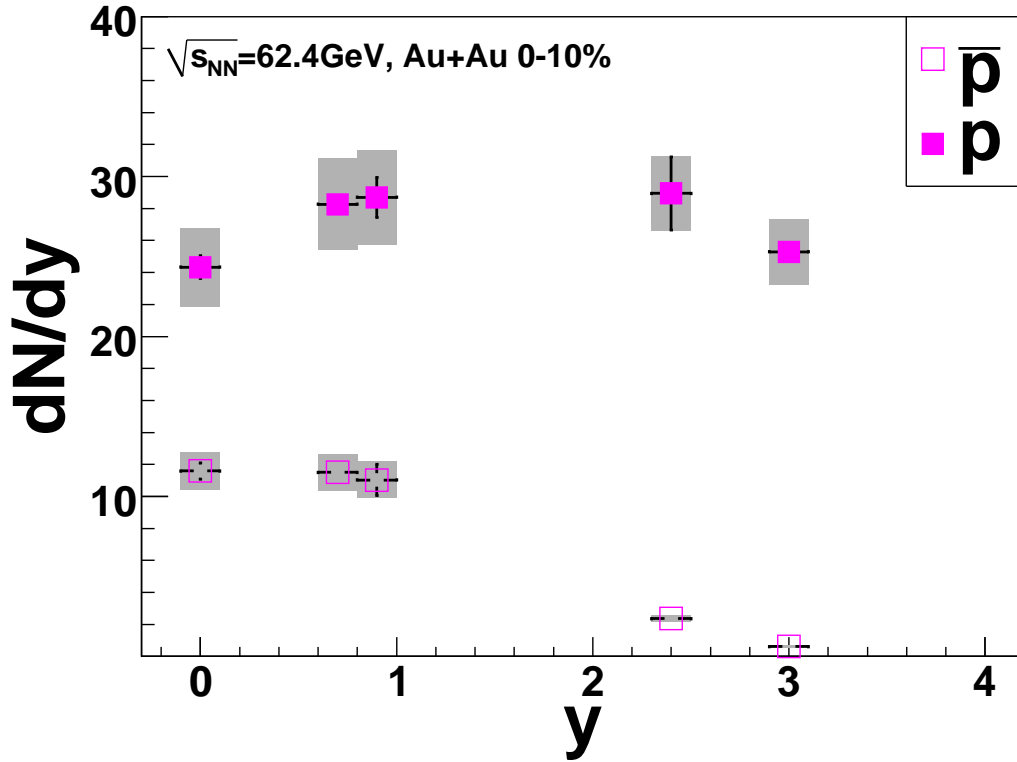


Figure 6.9: p_T integrated yields (dN/dy) as a function of rapidity for identified protons and anti-protons. The error bars are statistical errors. The shaded boxes represent all systematical errors added in quadrature. No feed-down corrections applied.

y	dN/dy m_T expo		dN/dy Boltzmann		p_T [GeV/c]	F.R. [%]
	p	\bar{p}	p	\bar{p}		
0.00	24.7 ± 0.51	11.8 ± 0.37	24.0 ± 0.50	11.4 ± 0.36	0.60 - 2.50	65
0.70	28.7 ± 0.29	11.7 ± 0.51	27.9 ± 0.28	11.3 ± 0.17	0.55 - 2.30	68
0.90	29.4 ± 0.91	11.4 ± 0.71	28.0 ± 0.86	10.7 ± 0.66	0.70 - 2.20	54
2.40	29.2 ± 1.63	2.39 ± 0.18	28.7 ± 1.60	2.34 ± 0.18	0.50 - 1.30	58
3.00	25.7 ± 0.39	0.62 ± 0.04	24.9 ± 0.38	0.61 ± 0.04	0.70 - 2.00	40

Table 6.4: Extrapolated dN/dy values for charged protons and anti-protons. The errors are statistical only. F.R.(fiducial ratio) is the fraction of the total yield covered by the experimental data.

in these tables is calculated as

$$\text{F.R.} = \frac{\int_{p_T^{\min}}^{p_T^{\max}} f(p_T) dp_T}{\int_0^{\infty} f(p_T) dp_T} \quad (6.2)$$

where $f(p_T)$ is the fit function and p_T^{\min} and p_T^{\max} are the fit limits. F.R. is dependent on the fit function so in the tables an average between the two functions used is shown.

The resulting dN/dy distributions, taking the average of the two functional forms used in fitting each species, are shown in figures 6.8 and 6.9. The shaded boxes represent all systematic errors, including fit function choice, added in quadrature. The error bars represent the statistical errors as an average of the statistical errors from the two fit functions.

6.2 Ratios

6.2.1 Anti-hadron to hadron ratios

Extrapolated particle yields are used to calculate anti-particle to particle ratios. Most

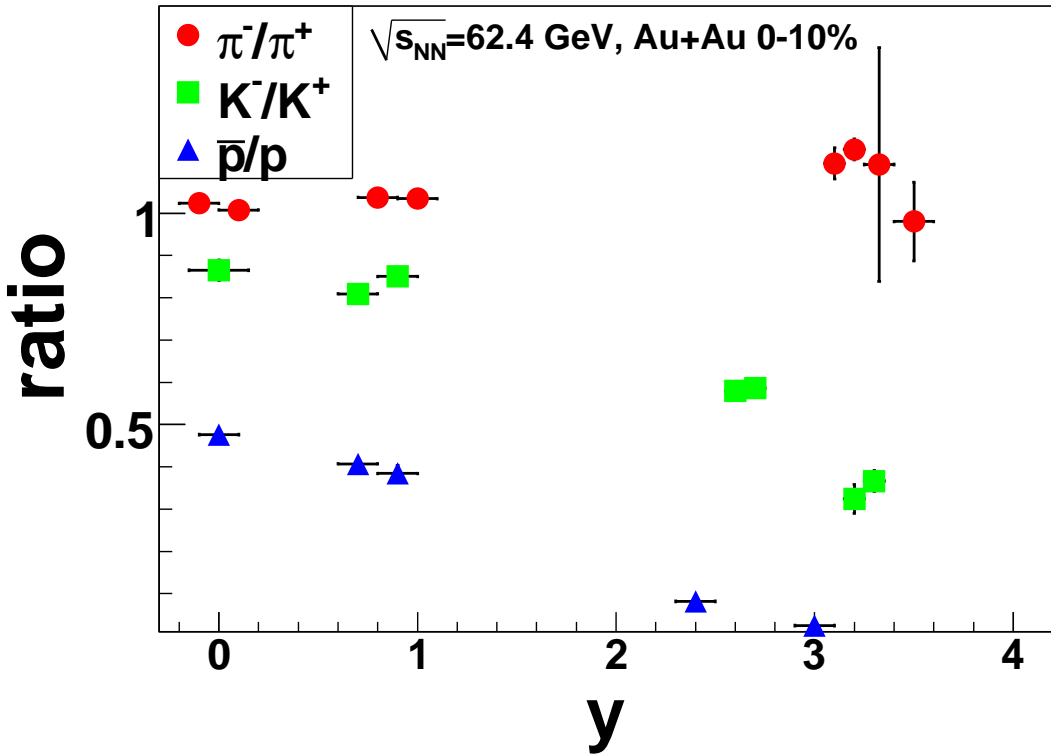


Figure 6.10: Anti-particle to particle ratios as a function of rapidity. The error bars show statistical errors only.

of the systematic errors cancel here due to the fact that efficiencies, cuts and most of the corrections are the same for particles and their anti-particles. Some exceptions exist in the case of contamination corrections, explained in section 5.4.1, which have uncertainties that depend on statistics and relative abundancies. This is especially the case for the \bar{p}/p ratio at $y = 3$ where the yield of anti-protons is ~ 0.6 and the

contamination with pions and kaons unresolved in RICH is $\sim 50\%$. The contamination correction is big and strongly dependent on the RICH ring efficiency, unlike the corresponding correction for protons which amounts to less than 3%.

Only the dN/dy values from the best fitting function were used for the like ratios. The power law is used for the π^-/π^+ ratio while for kaons and protons the chosen function is the m_T exponential. Calculated anti-hadron to hadron ratios as a function of rapidity are shown in figure 6.10. The error bars are statistical only.

6.2.2 K/π ratios

Due to the limited (y, p_T) regions covered by the spectrometer settings, pions and kaons do not always share the same rapidity intervals, especially at forward rapidities. In the analyzed dataset, at forward rapidities, extrapolated yields dN/dy for pions are available only at $y > 3.0$ while for kaons yields have been extracted at $y = 2.6, 2.7, 3.2$ and 3.3 . In order to calculate K/π ratios, the pion yields were interpolated using two methods. The procedure is illustrated in figure 6.11. For the first method, the data

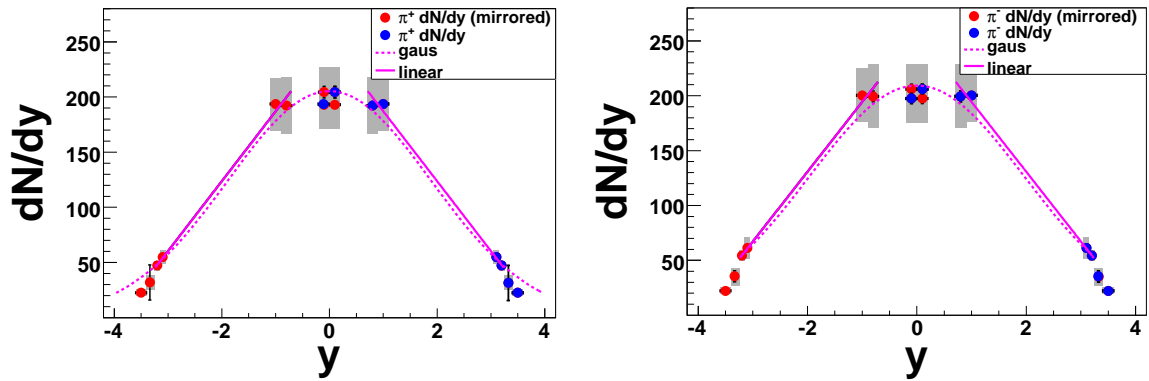


Figure 6.11: Rapidity distributions of the dN/dy yields for π^+ (left) and π^- (right) interpolated using a linear and gaussian fit.

points from rapidity $y = 0.8$ and $y = 1.0$ together with the points at $y = 3.1$ and $y = 3.2$ are fitted with a linear function. For the second one, all available dN/dy points are used for a fit with a Gaussian. Additionally, the data points were weighted in the fit procedure according to their fiducial ratio (F.R.) given in table 6.2. The two methods give approximately the same result in the interpolated interval, and in the following the linear interpolation was used to extract pion yields at $y = 2.6, 2.7$ and 3.0 . In order to calculate the K/π at $y = 3.0$ also, a linear interpolation between the closest points ($y = 2.7$ and $y = 3.2$) was necessary also for kaons. The reason to have a K/π ratio at $y = 3.0$ where we have proton data will be discussed in detail in the next chapter. The resulting K/π ratio rapidity distribution is shown in figure 6.12. The error bars are statistical while the shaded boxes represent systematical errors mainly from choice of the fit function.

6.3 Systematic errors

There are multiple sources of systematical errors which must be taken into account for the final results. The uncertainties from normalization, tracking efficiency, PID

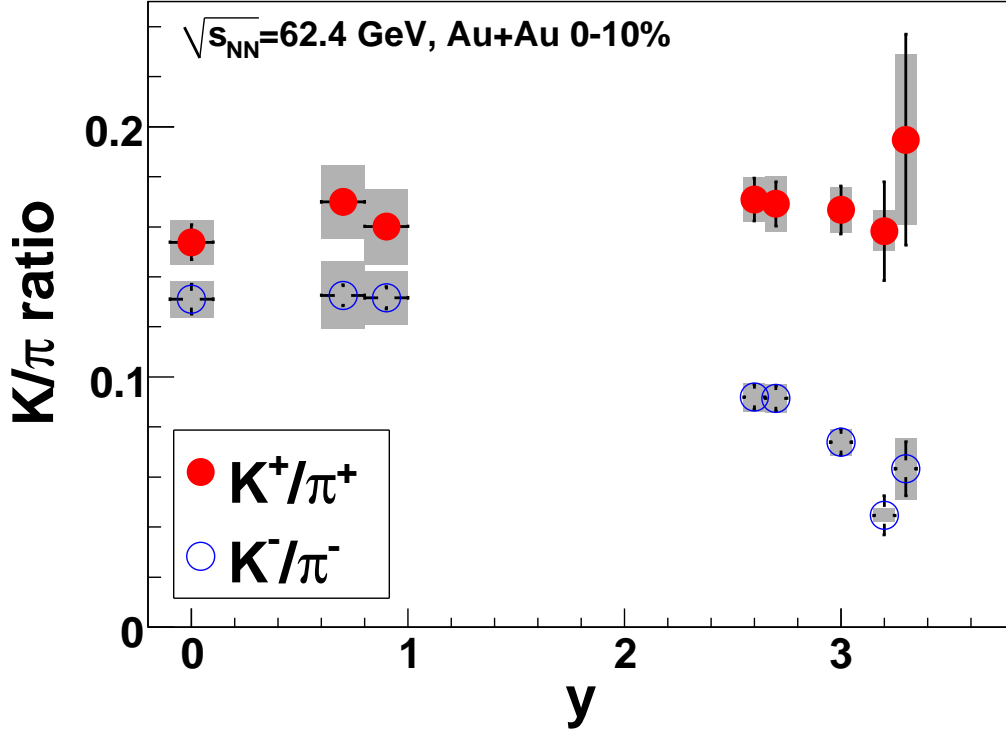


Figure 6.12: K/π ratios versus rapidity. The error bars are statistical errors. The shaded boxes represent systematical errors.

efficiency and other corrections are estimated to be $\sim 8\%$. This uncertainty can be checked by looking at the overall agreement between the particle spectra obtained from different settings at the same rapidity and transverse momentum. Figure 5.31 shows that, within statistical errors, the spectra obtained from the different settings employed in this analysis are consistent with a $\sim 10\%$ systematic error. A comparison for the charged pion spectra at mid-rapidity between this work and the results obtained by STAR Collaboration [188] for 0-10% central Au+Au collisions is illustrated in figure 6.13. The pion spectra from STAR is corrected for feed-down from weak decays of K^0 and Λ while the BRAHMS data is not. Taking into account that the estimated contribution from weak decays into the pion yields was roughly estimated for BRAHMS at mid-rapidity to be $\sim 4\%$ it is easy to see that there is a very good agreement between the BRAHMS and STAR results. The contamination correction for RICH vetoed particles has also an uncertainty due to limited statistics and RICH efficiency uncertainty. For a maximum RICH efficiency of 97% and a variation of $\pm 0.5\%$, the systematic uncertainty due to the contamination correction was estimated to be $\sim 2\%$ of the total yield for K^\pm ($y = 2.6, 2.7$) and $\sim 6\%$ for anti-protons ($y = 3.0$).

The systematical errors on the extrapolated yields depend on the choice of fit function. For pions, the difference in yields between power law and m_T exponential ranges from 10% in MRS ($y < 1.5$) up to $\sim 20\%$ in FS. For kaons and protons, the yields obtained with m_T exponentials and Boltzmann distribution are always less than 5% apart.

Most of the systematic errors cancel in the anti-particle to particle ratios with the exception of systematic errors due to the contamination correction for RICH vetoed particles. This affects only the K^-/K^+ ratio at $y = 2.6$ and $y = 2.7$, and the \bar{p}/p ratio

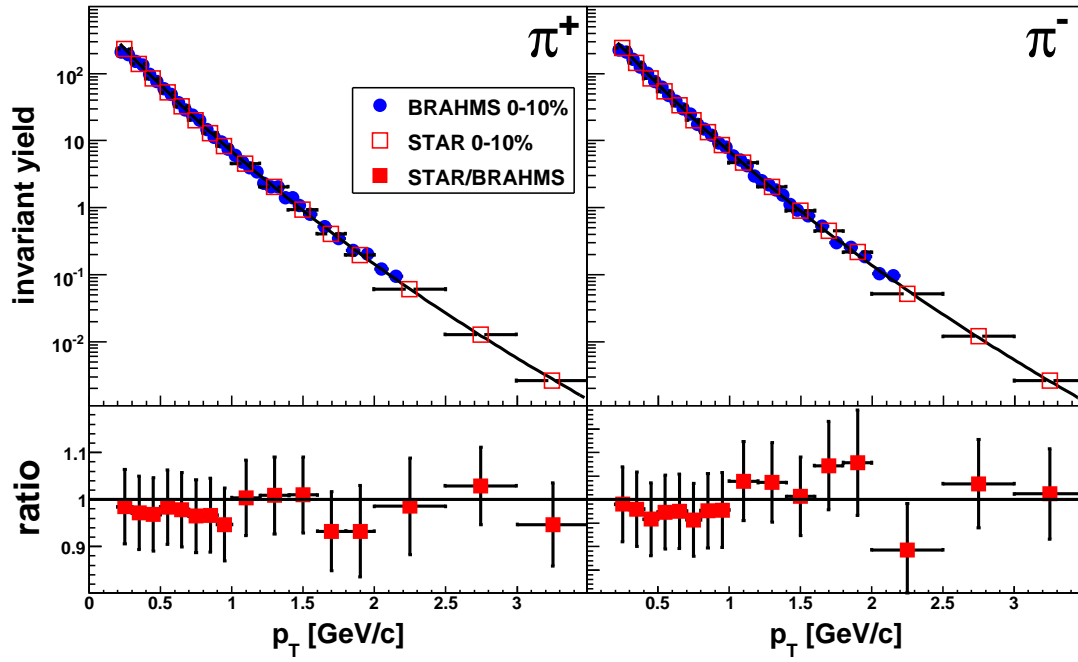


Figure 6.13: Top: Invariant p_T spectra for charged pions in 0-10% central Au+Au collisions at $\sqrt{s_{NN}} = 62.4$ GeV from this analysis at $|y| < 0.2$ (blue solid circles) and from STAR Collaboration at $|y| < 0.5$ (red open squares) [188]. The curves are power law fits to BRAHMS data. BRAHMS data is not feed-down corrected. Bottom: Ratio between STAR data and the power law fit to BRAHMS data. Error bars show the systematic and statistical uncertainties on STAR data points.

at $y = 3.0$. The K/π ratios systematic uncertainty includes the systematic errors due to yield extrapolation and due to the contamination correction.

Chapter 7

Discussions and comparisons

In this chapter, the experimental results obtained as described in the previous chapters are discussed in the context of already existing data together with comparisons to theoretical models.

7.1 Simulation procedures

7.1.1 HYDroynamics plus JETs

HYDJET++ was described in section 3.3 and here just the simulation procedures are described.

The code was run separately for each of the centrality bins available in the data by using the relative impact parameter ranges shown in table 7.1. The rest of the

	0-10%	10-20%	20-40%	40-60%
b_{\min}/R_{Au}	0.0	0.72	1.02	1.46
b_{\max}/R_{Au}	0.72	1.02	1.46	1.79

Table 7.1: HYDJET++ relative impact parameter ranges used for each centrality bin.

parameters, were found by using data from central collisions or phenomenological extrapolations as described in the next section.

In order to compare calculated yields with data, the same conditions regarding the feed-down from weak decays were applied. Since the pion data is corrected for feed-down from K^0 s and Λ s, all pions from the HYDJET++ output originating from these weakly decaying resonances are discarded. For constructing the proton yields, 90% of the protons originating from Λ and Σ baryon decay were counted for comparison with data.

7.1.2 Ultra Relativistic Quantum-Molecular Dynamics (UrQMD)

The UrQMD model was used to generate Au+Au events at an energy of $\sqrt{s_{NN}} = 62.4$ GeV and with impact parameters in the range $0 < b < 16$ fm. The simulation was carried out up to the time $t = 100$ fm/ c when all the strong resonances have decayed and most of the particles have frozen out. The unstable particles which survive after times higher than 100 fm/ c are decayed by using an "after-burner" program which uses the

large table of resonances and decays from the SHARE model [128]. The decays of the long lived weakly decaying particles are not performed. In the experimental analysis, the pions are corrected for feed-down from its weakly decaying highest contributors, K^0 and $\Lambda + \Sigma$. The experimental proton yields are not corrected for feed-down so in order to compare the UrQMD proton yields with data it is assumed that most of the decay protons from Λ and Σ baryons (90% in MRS and 80% in FS) are detected as primary protons in experiment (see section 5.4.1).

In order to determine the event centrality, the charged particle multiplicity in the pseudo-rapidity range $|\eta| < 2.2$ was used so that it matches with the experimental centrality definition which uses the Multiplicity Array detector. Only events with at least one inelastic collision were considered. Experimentally, the BRAHMS minimum bias trigger for the Au+Au at $\sqrt{s_{NN}} = 62.4$ GeV does not cover the full inelastic cross-section (only 90% as mentioned in the analysis chapter) but this is taken into account when the centrality is calculated so it is possible to compare to model calculations for the centrality intervals considered in this analysis. The impact parameter distributions generated with the UrQMD model and the distributions corresponding to the various centrality bins are shown in the left panel of figure 7.1.

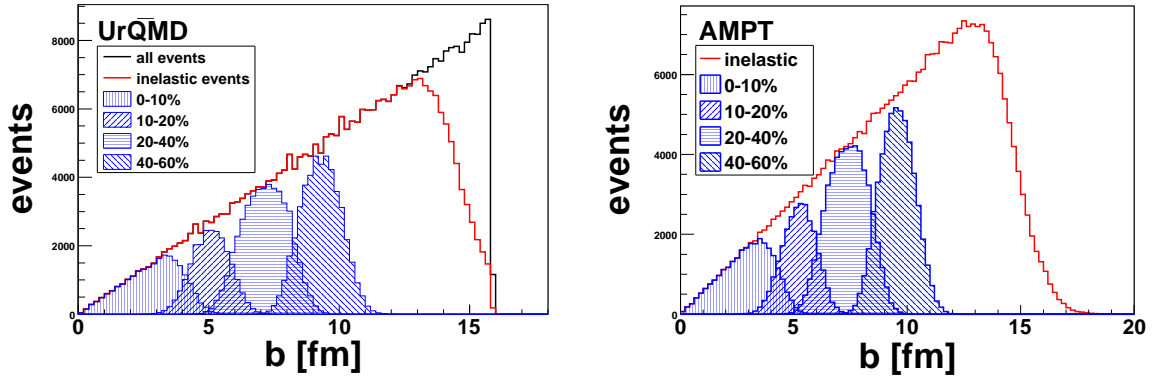


Figure 7.1: Impact parameter b distribution for the events generated with UrQMD and AMPT. The hashed areas represent the impact parameter distributions for the centrality bins considered in this analysis.

7.1.3 A Multi-Phase Transport model (AMPT)

The AMPT model was used to generate events in the impact parameter range $0 < b < 20$ fm. In this model all the unstable particles are decayed with the exception of the long lived weakly decaying particles which are saved in the output. BRAHMS results for pions are corrected for feed-down from long lived particles so no additional work on the AMPT output was necessary to get the pion yields. For protons the same assumptions were used as for the UrQMD model (see previous section).

The centrality selection was made also in the same way as for UrQMD. The impact parameter distributions for the centrality classes selected in the analysis are shown in the right panel of figure 7.1. It can be observed that the number of inelastic events follows the normal quadratic dependence on the impact parameter up to $b \sim 2r_{Au} \sim 13$ fm for both UrQMD and AMPT. At higher impact parameters, the ratio between inelastic events and the total number of events decreases smoothly from 1 at $b = 13$ fm to zero at $b \sim 20$ fm for AMPT. The UrQMD model has an internal impact parameter

threshold which did not allow the calculation of events with impact parameters higher than $b \sim 16$ fm although the inelastic cross-section is still non-zero. However, as can be seen in the figure, the impact parameter interval $16 < b < 20$ fm has little contribution to the total inelastic cross-section so the selection of the central and semi-central centrality classes is not significantly affected.

7.2 Thermal fit of the mid-rapidity data using HYDJET++

The soft part of the HYDJET++ is a statistical model with a hydro inspired freeze-out parametrization. This type of model is often used to fit the experimental data available and not to make predictions. In the following section, the model input parameters will be tuned to data and a few comparisons will be made. The effective volume

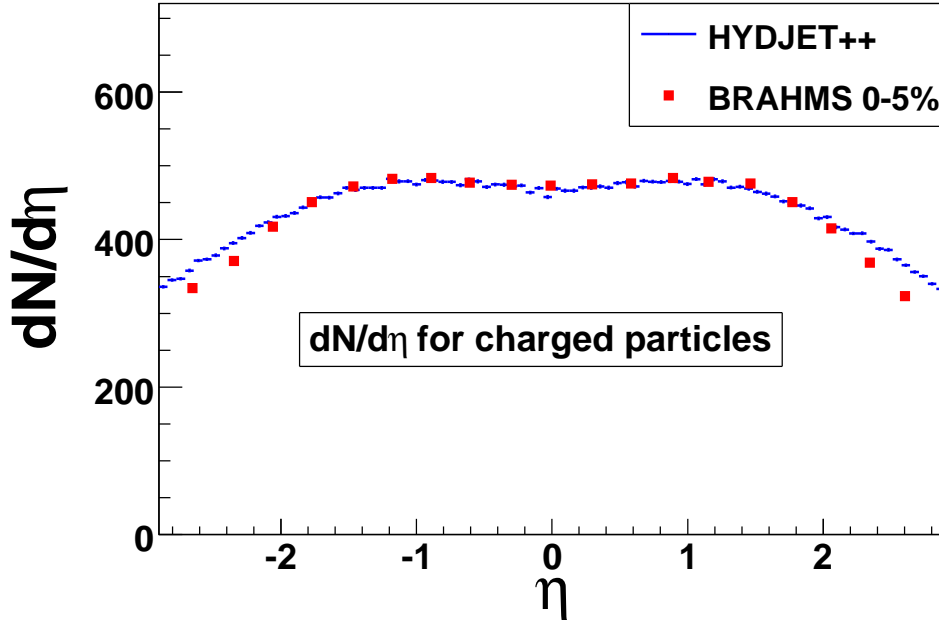


Figure 7.2: Charged particle pseudo-rapidity density in 0-5% central Au+Au collisions obtained with HYDJET++ and compared to BRAHMS results [189]. The parameters used are explained in the text.

of the fireball, V_{eff} , is fixed by using the experimental charged particle distribution. Figure 7.2 shows a good agreement between the calculated $dN/d\eta$ distribution and the experimental data from BRAHMS in the 5% most central collisions [189]. The chemical and thermal freeze-out temperatures used were $T^{ch} = 165$ MeV and $T^{th} = 100$ MeV as obtained in section 3.3 with the same model but for the top RHIC energy. Chemical potentials, μ_B, μ_S and μ_Q were obtained from an interpolation of chemical potentials obtained at SIS, AGS, SPS and top RHIC energies [190] and were fixed to $\mu_B = 72.5$ MeV, $\mu_S = 17.5$ MeV and $\mu_Q = 0.0$ MeV for all centrality classes. A good agreement between the anti-particle to particle ratios calculated in the model and data has been found (see figure 7.3). In order for the K/π ratios to be described, the strangeness suppression factor, γ_S , was set to 0.75. Similar fits to the Au+Au

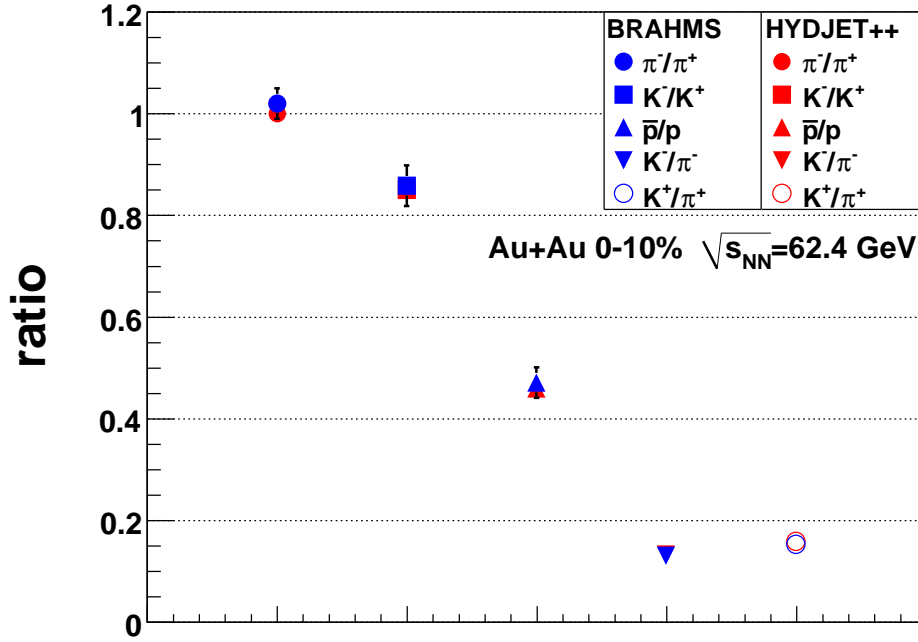


Figure 7.3: Particle ratios at $y = 0$ in 0-10% central Au+Au collisions at $\sqrt{s_{NN}} = 62.4$ GeV. The data is from this work. HYDJET++ parameters are the same as the ones used for figure 7.2 with the exception of the impact parameter range.

collisions at $\sqrt{s_{NN}} = 62.4$ GeV were performed in [93] with a thermal equilibrium model and the results obtained for the freeze-out temperatures and chemical potentials were $T^{ch} \sim 155$ MeV, $T^{th} \sim 100$ MeV, $\mu_B \sim 62$ MeV and $\mu_s \sim 7$ MeV while the strangeness suppression ratio extracted was $\gamma_S \sim 0.8$. In the above cited work, the chemical potential for charged kaons was taken to be $\mu = \mp\mu_q \pm \mu_s$ for K^- and K^+ respectively, where $\mu_q = \mu_B/3$ is the quark chemical potential. Hence the K^-/K^+ ratio can be expressed as $K^-/K^+ \approx \exp[(-2\mu_B/3 + 2\mu_s)/T^{ch}]$. In this work, the chemical potential for charged kaons is taken as $\mu = 0 \times \mu_B \mp \mu_s$ for K^- and K^+ respectively which leads to $K^-/K^+ \approx \exp(-2\mu_s/T^{ch})$. The obvious connection between the two strangeness potentials is $\mu_s = \mu_B/3 - \mu_s$ where μ_s is from the present analysis. The equivalent μ_s from reference [93] would be $\mu_s = 62/3 - 7 = 14$ MeV which is close to the value we extracted from the parametrization of world data given in [190].

The transverse flow velocity was fixed with the help of data on invariant spectra at mid-rapidity (see figure 7.4). The best agreement for spectrum slopes was found when the maximum transverse flow rapidity parameter ρ_u^{\max} , defined in section 3.3.3, was set to 0.95. This value is slightly lower than the one found for the central Au+Au collisions at the maximum RHIC energy ($\rho_u^{\max}(200\text{GeV}) = 1.1$, see table 3.1). The list of parameters fixed using the data mentioned above are listed in table 7.2. Invariant spectra of pions and kaons are described well over the entire p_T range covered experimentally. The proton spectrum is slightly overestimated but the slope seems to be close to the data.

In figure 7.5, the average transverse momentum $\langle p_T \rangle$ calculated at $y = 0$ is shown for each particle in comparison to the data. A good agreement with the data is observed for all species, which supports the transverse flow generated by the hydrodynamic expansion of the fireball. The $\langle p_T \rangle$ for particles originating from jets are also shown in the figure. It seems that the average transverse momentum for jet particles follows a

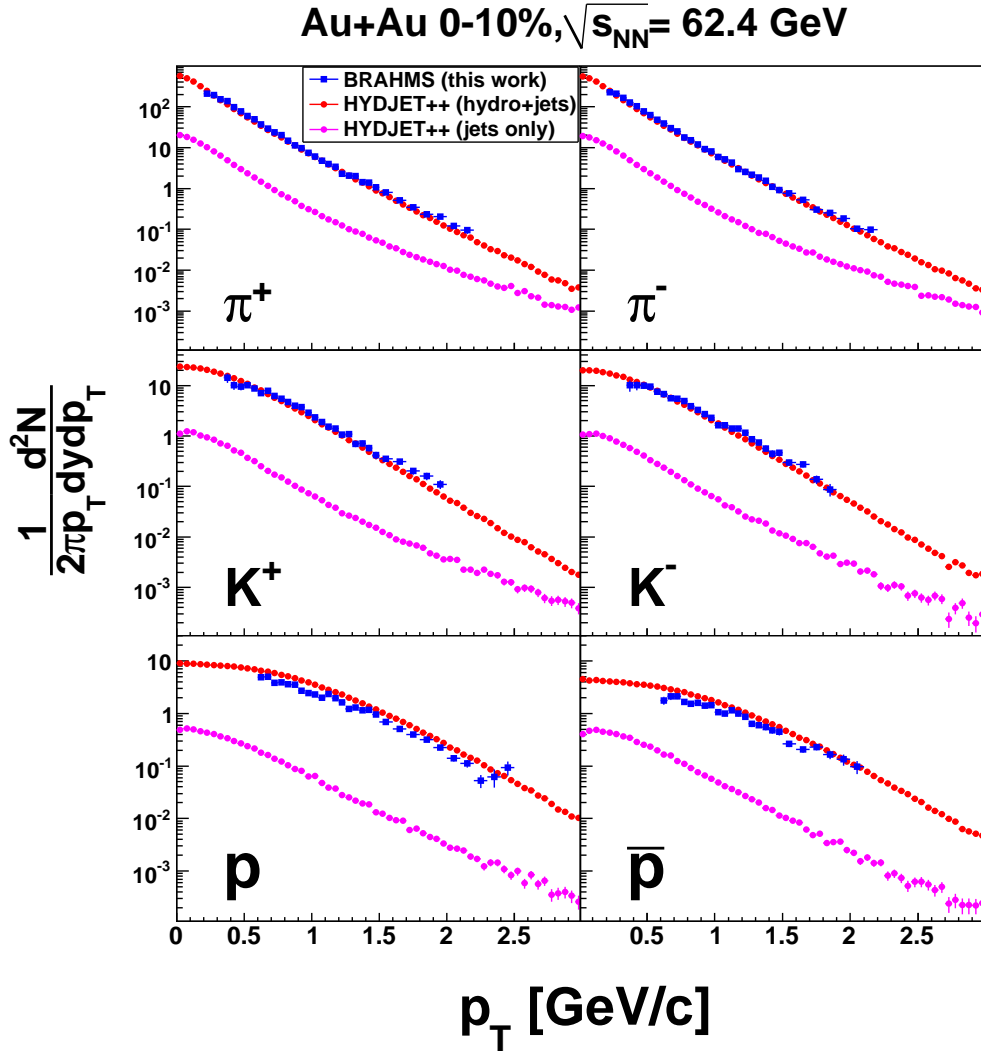


Figure 7.4: Invariant spectra at $y = 0$ in 0-10% central Au+Au collisions at $\sqrt{s_{NN}} = 62.4$ GeV. Comparison of HYDJET++ output with BRAHMS data from this work.

$\mu_{\pi^+}^{\text{eff th}} [\text{MeV}]$	$\tau [\text{fm}/c]$	$\Delta\tau [\text{fm}/c]$	$R(b=0) [\text{fm}]$	$\rho_u^{\text{max}}(b=0)$
90	8.0	2.0	9.0	0.95

Table 7.2: HYDJET++ parameters common to all centrality bins. Freeze-out temperatures are the same as the ones used for Au+Au collisions at $\sqrt{s_{NN}} = 200$ GeV, namely $T^{\text{ch}}=165$ MeV and $T^{\text{th}} = 100$ MeV. Chemical potentials are also constant and are given in the text.

different dependence on mass w.r.t. to the particles in the fireball.

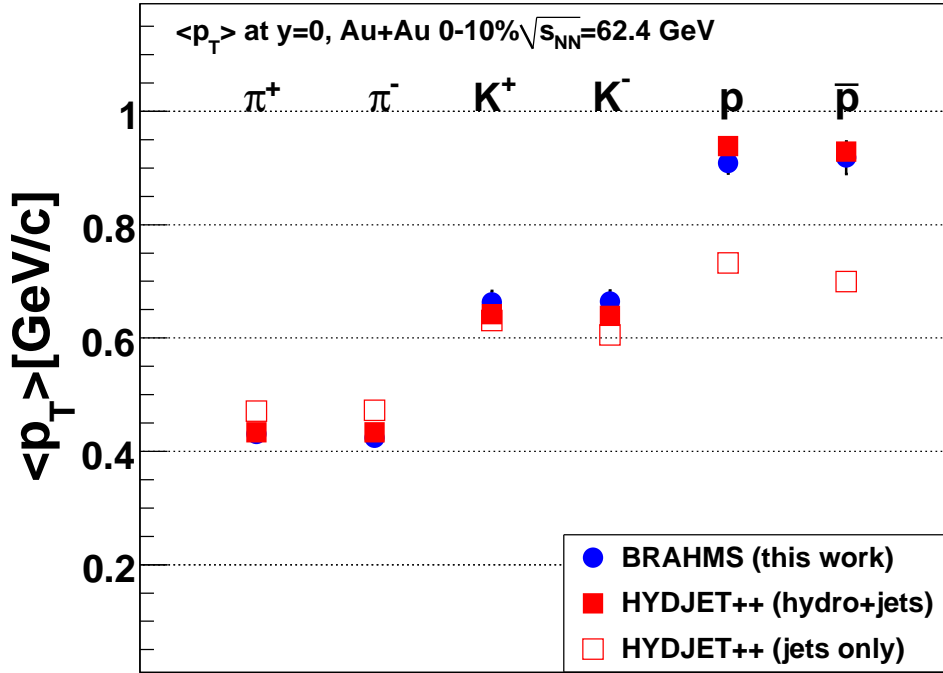


Figure 7.5: Average $\langle p_T \rangle$ for π^\pm , K^\pm , p and \bar{p} in 0-10% Au+Au collisions at $\sqrt{s_{NN}} = 62.4$ GeV.

The HYDJET++ model was run also for semi-peripheral collisions as mentioned in section 7.1.1. All the parameters used for central collisions were kept constant with the exception of the strangeness suppression factor which is necessary to fit the strange to non-strange particle ratios. The justification of the γ_S factor being smaller than 1 is based on the possibility of strangeness chemical non-equilibrium and on the canonical suppression due to exact strangeness conservation which leads to a reduction of multiplicity of open strange hadrons [191, 192]. Figure 7.6 illustrates the centrality dependence of the anti-particle to particle ratios (left) and K/π ratios at mid-rapidity. The anti-particle to particle ratios are constant w.r.t. centrality as expected since the chemical potentials used as input were kept constant. For K/π ratios, the γ_S factors used were 0.75, 0.7, 0.65 and 0.6 for the centrality bins 0-10%, 10-20%, 20-40% and 40-60% respectively.

The parameters for the hard part of HYDJET++ were not fixed based on the 62 GeV data due to lack of statistics at high p_T . However, the parameters found at $\sqrt{s_{NN}} = 200$ GeV were used with the exception of the p_T^{min} parameter which was reduced from 3.4 GeV/c to 2.8 GeV/c. A list of input parameters for the hard part of HYDJET++ is shown in table 7.3. In figure 7.4 the jet contribution to the invariant

Shadowing	E_{loss}	p_T^{min} [GeV/c]	$T_{QGP}^{initial}$ [MeV]	τ_{QGP} [fm/c]
off	rad. & coll.	2.8	300	0.4

Table 7.3: Input parameters for the hard part of HYDJET++

spectrum is shown for each particle species. In HYDJET++ it was found that at

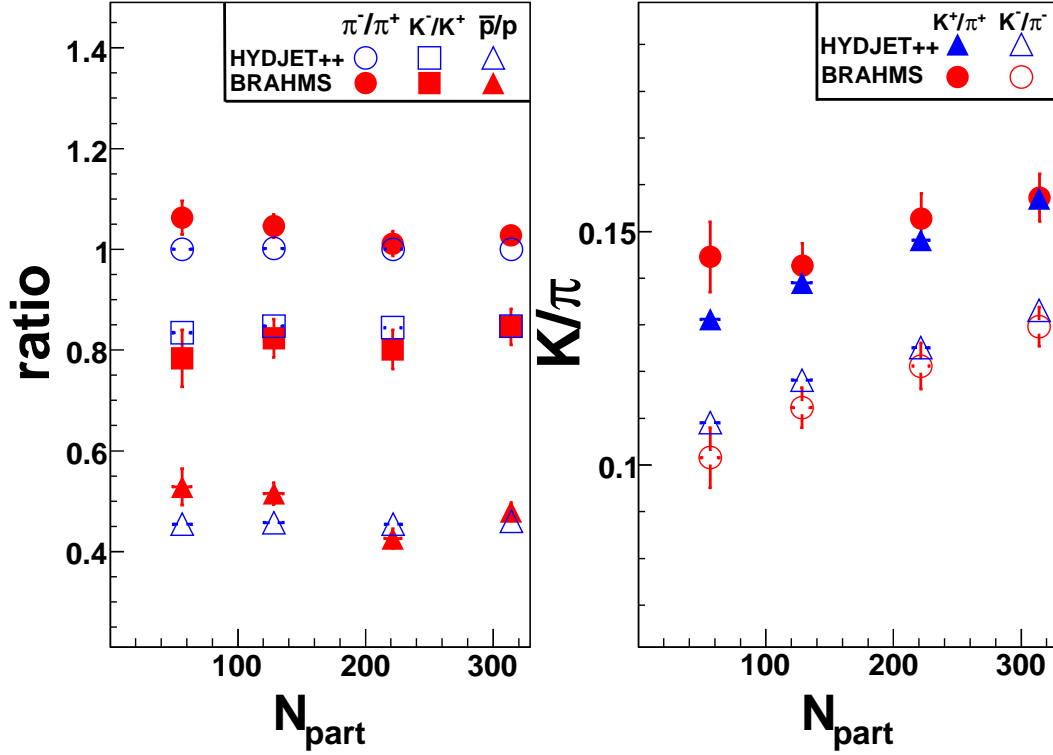


Figure 7.6: Particle ratios as functions of centrality at mid-rapidity. Left: anti-particle to particle ratios; right: K/π ratios.

$\sqrt{s_{NN}} = 200$ GeV jets contribute as much as $\sim 15\%$ to the total yields (see figure 3.9). At 62.4 GeV this contribution was found to be less than 5% with the current parameters.

7.3 Particle production in central Au+Au collisions

In this section, the production of charged pions and kaons in central Au+Au collisions at $\sqrt{s_{NN}} = 62.4$ GeV is investigated using the two microscopical transport models described earlier, UrQMD and AMPT.

7.3.1 Integrated yields (dN/dy)

In figure 7.7 the model calculations are compared to the experimental dN/dy rapidity distributions of pions and kaons. At mid-rapidity, UrQMD overestimates the pion yields by almost 20% while AMPT gives a slightly smaller rapidity density than found experimentally. A reason for this could be the fact that UrQMD slightly overestimates the baryon stopping, allowing more energy for particle production, while AMPT underestimates it as can be seen from the net-proton distribution shown in figure 7.9. UrQMD uses a continuous spectrum of high mass resonances and also a big number of reaction channels which also might lead to an increased pionic yield [96]. Both models overestimate the forward rapidity pion yield. The model calculations agree better with the observed kaon yields, with the most significant discrepancy occurring at forward rapidity for the negative charge state. The bottom panel of figure 7.7 shows the ra-

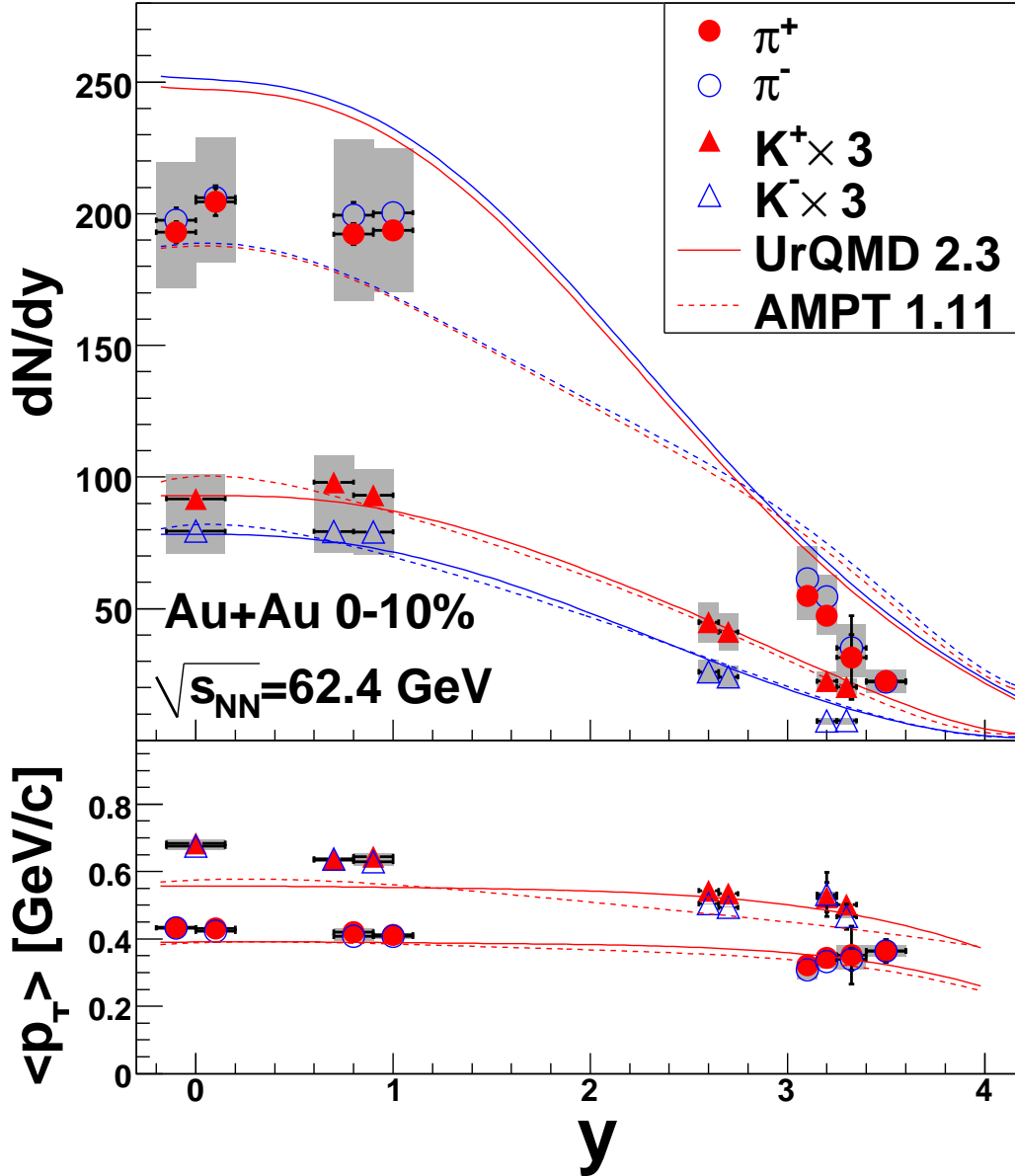


Figure 7.7: Upper panel: dN/dy as a function of rapidity for π^\pm and K^\pm from 0-10% central Au+Au collisions at $\sqrt{s_{NN}} = 62.4$ GeV. The curves are model calculations, solid lines are for UrQMD and dashed lines for AMPT. For both models, the curves assigned to each particle species follow the same order as the data. Bottom panel: $\langle p_T \rangle$ dependence on y . The curves are model calculations for π^+ and K^+ .

rapidity dependence of the average transverse momentum $\langle p_T \rangle$ for pions and kaons. For pions, $\langle p_T \rangle \sim 0.43$ GeV/c at $y = 0$ and decreases to ~ 0.32 GeV/c at $y > 3.0$ while for kaons, $\langle p_T \rangle$ drops from ~ 0.65 GeV/c at $y = 0$ to ~ 0.5 GeV/c at $y = 3.2$. The slight decrease of average p_T towards forward rapidity might indicate a decrease of the radial flow. Both model calculations underestimate the data at mid-rapidity especially for kaons but seem to describe data better at forward rapidity.

7.3.2 Particle ratios

Figure 7.8 shows the rapidity-dependent anti-hadron to hadron integrated yield ratios for pions, kaons and protons. The proton and anti-proton yields used to calculate the \bar{p}/p ratio are obtained in the present analysis. As mentioned in section 5.4.1 the (anti-)proton yields are not corrected for feed-down from hyperons (see also [193]). The π^-/π^+ ratio is approximately equal to unity at mid-rapidity and consistent with a small rising at forward rapidity probably due to isospin effects. The kaon and proton ratios at mid-rapidity ($K^-/K^+ \sim 0.85$, $\bar{p}/p \sim 0.45$) are lower than the corresponding ones measured at the top RHIC energy [29]. The lower K^-/K^+ ratio at mid-rapidity is due to the significantly higher net-baryon content which enhances production mechanisms other than pair creation. At forward rapidity, a decrease of the kaon ratio to a value of

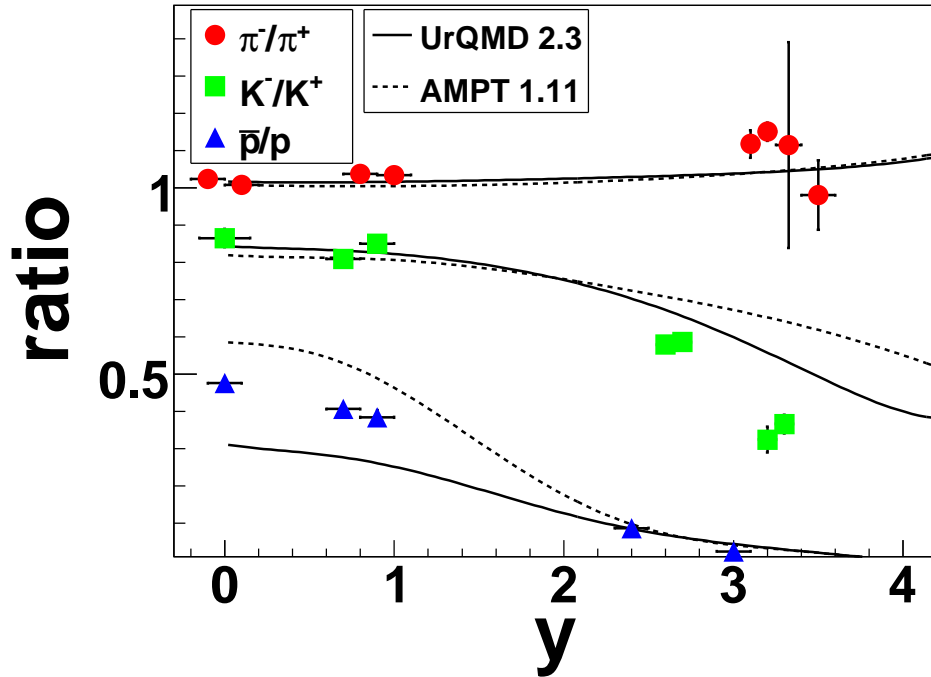


Figure 7.8: Anti-particle to particle ratios as a function of rapidity in 0-10% central Au+Au collisions at $\sqrt{s_{NN}} = 62.4$ GeV. The solid lines are UrQMD calculations and dashed lines are AMPT calculations. For both models, the top curve is for the π^-/π^+ ratio, the middle one for the K^-/K^+ ratio and the bottom one for the \bar{p}/p ratio.

~ 0.35 at $y = 3.3$ is observed. From a microscopical point of view, possible explanations include the competition between Λ baryons and K^- mesons for the available strange quarks and associated production (e.g., $N + N \rightarrow p + \Lambda + K^+$) which increases the number of positive kaons. Both of these mechanisms depend on the net-baryon content

and, consequently, lead to a decrease of the K^-/K^+ ratio at forward rapidity. The \bar{p}/p ratio decreases significantly with rapidity, reaching $\bar{p}/p = 0.087 \pm 0.003$ at $y = 2.4$ and $\bar{p}/p = 0.024 \pm 0.001$ at $y = 3$. The net-proton dependence on rapidity is

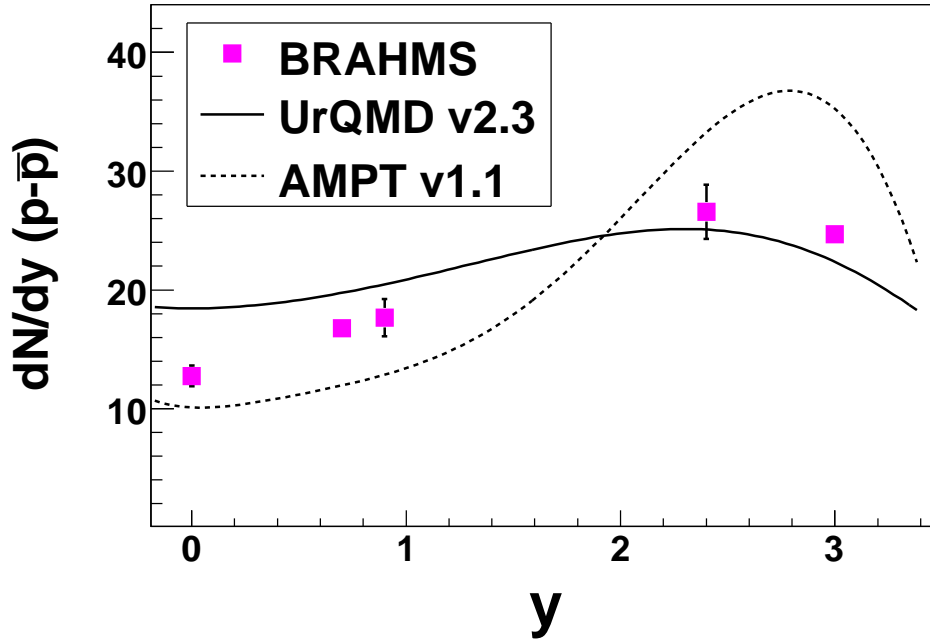


Figure 7.9: Net protons as a function of rapidity. The data is from this work. Curves are calculations for central Au+Au collisions using UrQMD (solid line) and AMPT (dashed line).

shown in figure 7.9 together with comparisons to the two transport models employed. Both models estimate correctly the rapidity range of the fragmentation peak but give different average rapidity losses. The average rapidity loss in central Au+Au collisions at $\sqrt{s_{NN}} = 62.4$ GeV was estimated from data to be $\delta y = 2.01 \pm 0.16$ (see reference [193]).

In figure 7.10 the rapidity dependence of the K/π ratio is shown. As described in section 6.2.2, some of the points were obtained by interpolating the integrated yields between closest measured points. The K^+/π^+ ratio was found to be 0.154 ± 0.011 at mid-rapidity and is almost constant as a function of rapidity. The K^-/π^- ratio has a value of 0.131 ± 0.010 at mid-rapidity and shows a steep decrease for $y > 2.5$ with a value of ~ 0.06 at $y = 3.2$. The different rapidity dependence of the positive and negative charge K/π ratios is similar to, but somewhat more pronounced than that found in central Au+Au collisions at $\sqrt{s_{NN}} = 200$ GeV [76]. The two model calculations give quite different results. The AMPT model agrees well with the K/π data points with the exception of the forward rapidity K^+/π^+ values which are underestimated. The UrQMD calculation for the K^+/π^+ is in qualitative agreement with the shape of the rapidity distribution, although underestimating the magnitude of the ratio. In this model, a large number of scattering channels results in enhanced associated production of strange particles in the baryon rich matter formed at forward rapidity. However, UrQMD correspondingly predicts an excess production of pions, leading to the model systematically under-predicting the absolute values of the K/π ratio. Also, both models severely underpredict the large splitting between the positive and the negative K/π ratios. Lower energy data shows a similar behaviour between the K^+/π^+ ratio and the

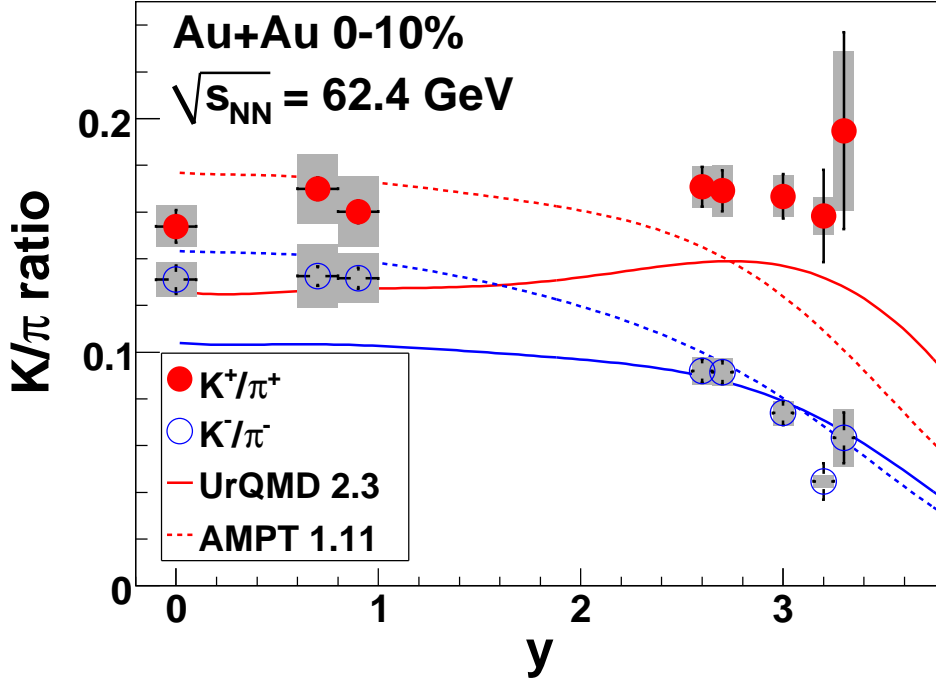


Figure 7.10: Rapidity dependence of the K/π ratios in 0-10% central Au+Au collisions at $\sqrt{s_{NN}} = 62.4 \text{ GeV}$. The circles are data from the present work. The curves are UrQMD (solid lines) and AMPT (dashed lines) calculations. The upper curves for both models are for the K^+/π^+ ratio and the lower ones are for K^-/π^- .

proton rapidity density (see figure 7.11). At AGS top energy, $\sqrt{s_{NN}} = 4.8 \text{ GeV}$, where the dominant strangeness creation mechanism is the hadronic associated production, the K^+/π^+ ratio has a comparable value with the one found at mid-rapidity at top SPS energy and at RHIC energies. At SPS and RHIC there are new competing production mechanisms like pair production which grow in relative contribution with collision energy but one can still see the effects of the associated channels especially at forward rapidity where the net-baryon content is high and the influence of the midrapidity fireball drops.

The excitation function of the K/π ratios in nucleus-nucleus collisions is shown in figure 7.12. Both 4π and the mid-rapidity ratios, obtained in this work follow the trend of the existing data. From highest SPS energy up to the highest energy RHIC data, the K^+/π^+ ratio tends to saturate while the K^-/π^- monotonically increases with energy, almost reaching the value of its positive counterpart at 200 GeV. It can also be noted that the difference between the K^+/π^+ ratio and the K^-/π^- ratio at RHIC energies is higher for the integrated yields than for the mid-rapidity yields. This is due to the non-negligible influence of the higher net-baryon content from the forward rapidities which produces the splitting of K^\pm/π^\pm ratios even at top RHIC energy.

Figure 7.13 shows the dependence of the K/π ratios on the \bar{p}/p ratio. BRAHMS data points are obtained in this work in different rapidity slices at the same energy, $\sqrt{s_{NN}} = 62.4 \text{ GeV}$, while the SPS points are obtained at mid-rapidity in central Pb+Pb collisions at $\sqrt{s_{NN}} = 6.3, 7.6, 8.8, 12.3$ and 17.3 GeV . The curves are calculations from UrQMD (thick lines) and AMPT (thin lines) for central Au+Au collisions at $\sqrt{s_{NN}} = 62.4 \text{ GeV}$. In the case of UrQMD we show also calculations for central Au+Au collisions at $\sqrt{s_{NN}} = 200 \text{ GeV}$ and central Pb+Pb collisions at $\sqrt{s_{NN}} = 17.3 \text{ GeV}$. In Au+Au

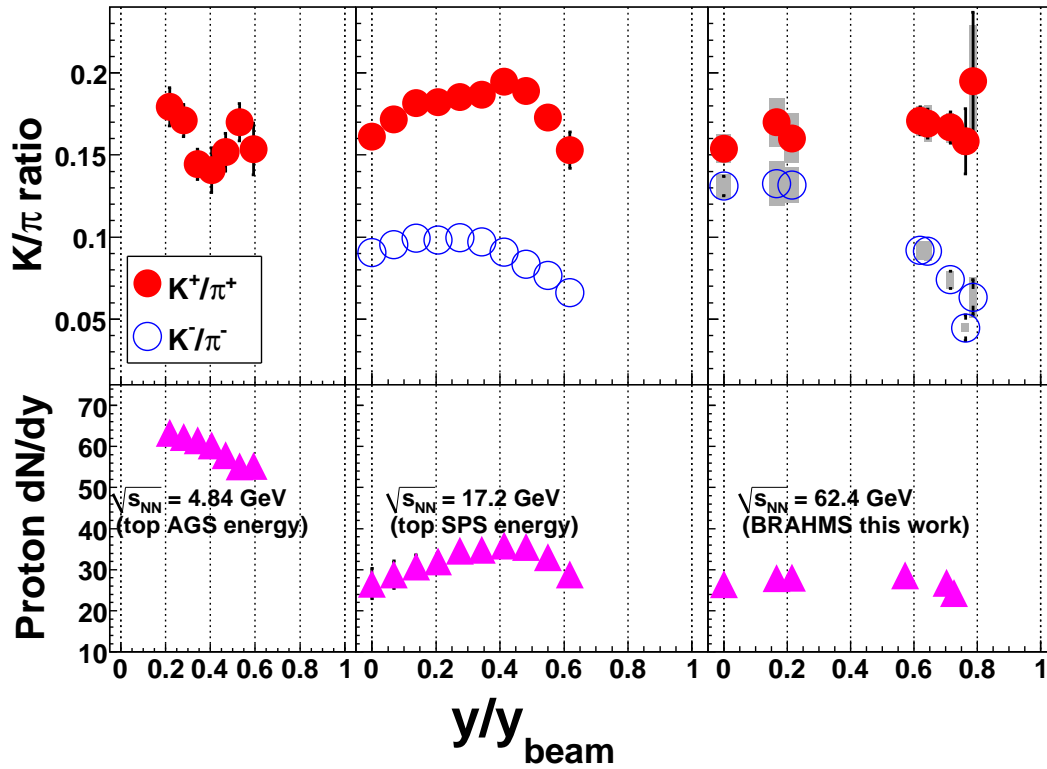


Figure 7.11: K/π ratios and proton dN/dy from central nucleus-nucleus collisions as a function of the normalized rapidity. Data is from Au+Au collisions at AGS top energy, 4.84 GeV, [81, 87], Pb+Pb collisions at 17.3 GeV at SPS [194] and Au+Au collisions at 62.4 GeV from this work.

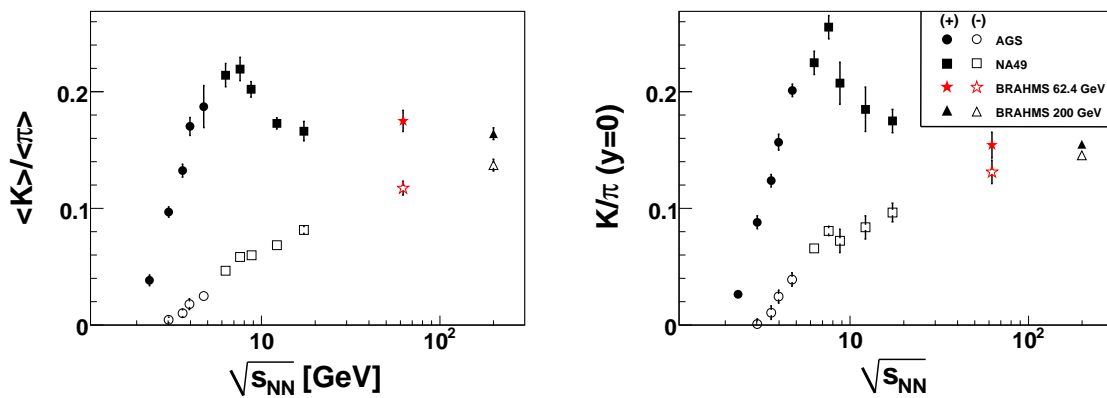


Figure 7.12: K/π ratios calculated using 4π yields (left) and mid-rapidity yields (right) as a function of energy. The star symbols are obtained in this work by fitting the rapidity densities of pions and kaons with a Gaussian and using the integral. Solid symbols are for the positive ratios and open symbols are for the negative ones.

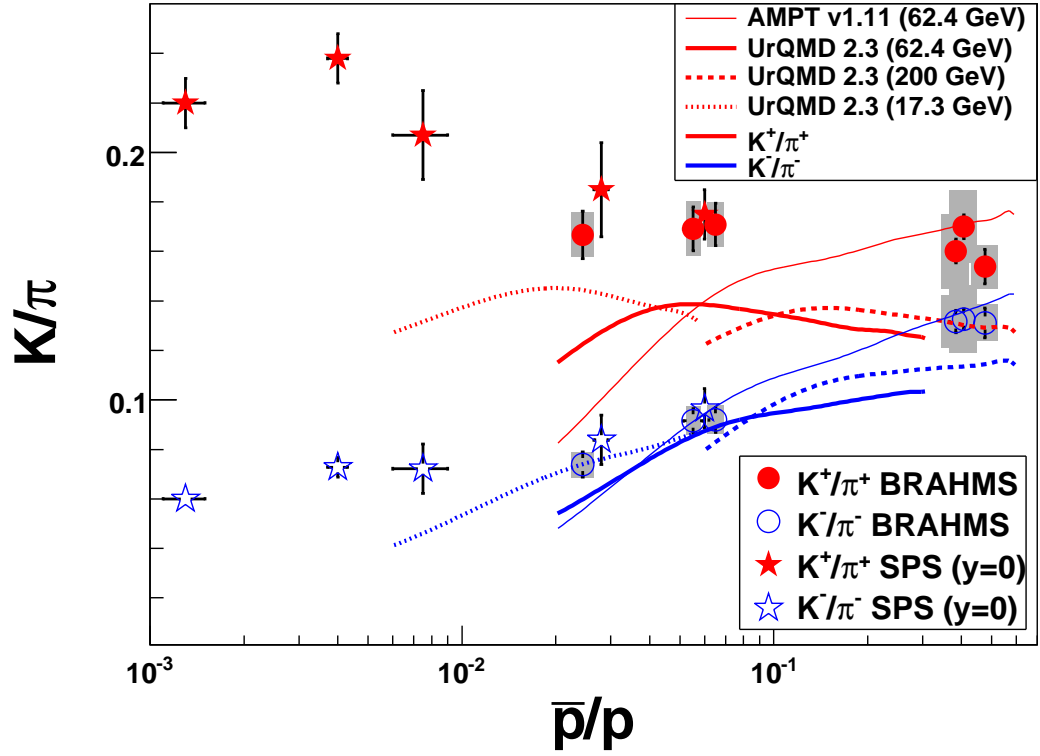


Figure 7.13: K/π ratios as functions of the \bar{p}/p ratio. The circles are data from 0-10% central Au+Au collisions at $\sqrt{s_{NN}} = 62.4$ GeV and the stars are results measured at mid-rapidity in the SPS experiments at different energies [195]. Filled symbols represent the positive ratio and the open ones represent the negative ratio. The curves are UrQMD (thick lines) and AMPT (thin lines) calculations for central A+A collisions at $\sqrt{s_{NN}} = 200, 62.4$ and 17.3 GeV for UrQMD and $\sqrt{s_{NN}} = 62.4$ for AMPT. Red curves are for the positive ratio while blue ones are for the negative ratio.

collisions at 62.4 GeV, the fragmentation peak is estimated to be in the interval $2.5 < y < 3.3$ [193] with a net-proton density of ~ 30 and \bar{p}/p ratio values in the same range as the ones measured at mid-rapidity at $\sqrt{s_{NN}} = 12.3$ and 17.3 GeV. Comparing the SPS and RHIC results, a common dependence of the K/π ratios on the \bar{p}/p ratio is observed. If we look at models we see that none of them manage to get the dependence of the K/π ratios observed in the data. However, if we use UrQMD calculations from more energies and we exclude the lowest \bar{p}/p part, where the K/π ratios drop (due to approaching beam rapidity, small local system size, etc.), then we make the same observation as in the data: K/π ratios depend approximately only on the \bar{p}/p ratio and not on energy.

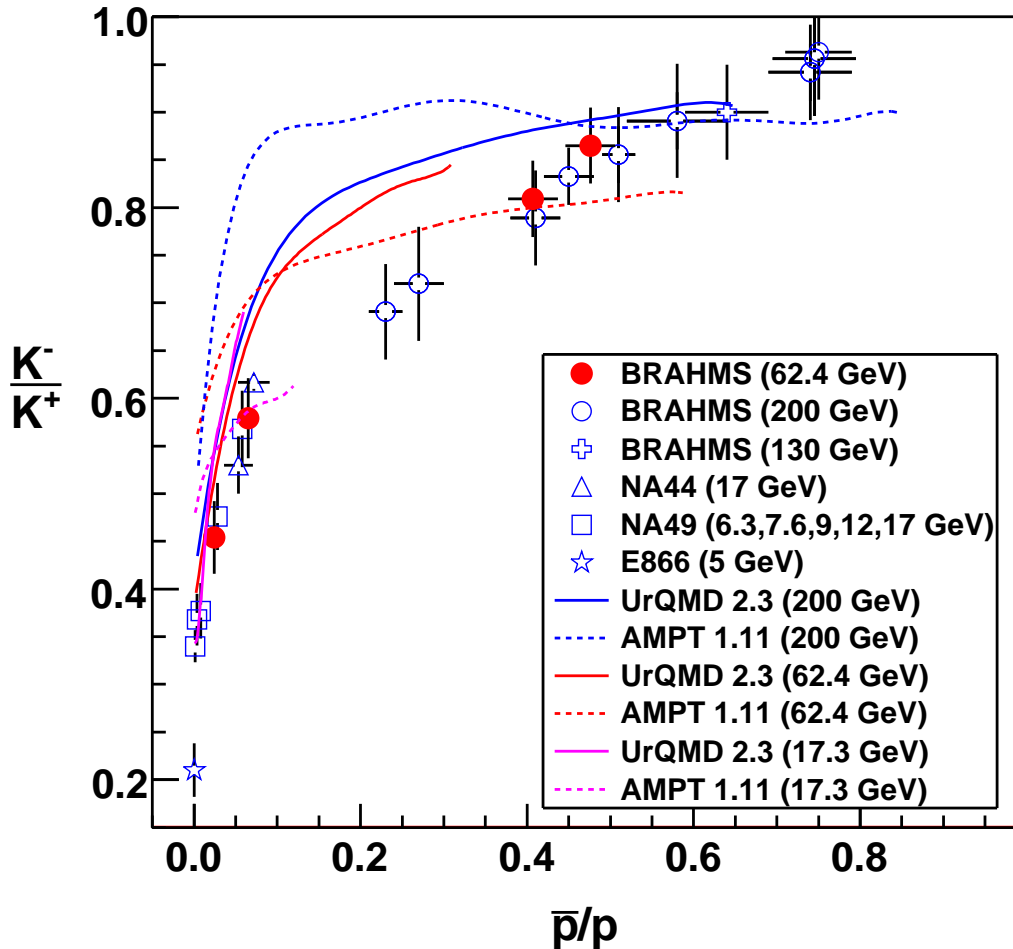


Figure 7.14: K^-/K^+ ratio dependence on the \bar{p}/p ratio. The solid circles are from 0-10% central Au+Au collisions at $\sqrt{s_{NN}} = 62.4$ GeV obtained in this work. The open symbols are BRAHMS data from ref. [29] and lower energy data from [82, 196, 197, 64, 88, 198]. The error bars represent statistical and systematic errors. The curves are calculations with UrQMD (solid lines) and AMPT (dashed lines) for central Au+Au collisions at $\sqrt{s_{NN}}=62.4$ GeV (red in online version) and $\sqrt{s_{NN}}=200$ GeV (blue) and central Pb+Pb collisions at $\sqrt{s_{NN}}=17.3$ GeV (magenta).

The K^-/K^+ ratio exhibits a similar dependence on the \bar{p}/p ratio (see figure 7.14) for data spanning energies from $\sqrt{s_{NN}} = 5$ GeV to $\sqrt{s_{NN}} = 200$ GeV. The calculations made with UrQMD(solid line) and AMPT(dashed line) for central nucleus-nucleus

collisions at $\sqrt{s_{NN}} = 200, 62.4$ and 17.3 GeV do not reproduce the dependence of the K^-/K^+ ratio on the \bar{p}/p ratio which seems to be universal over a large energy range. However, UrQMD calculations at the three energies give similar rapidity-dependent K^-/K^+ ratios in the common interval of \bar{p}/p values. The same behaviour was observed above for K/π ratios and is due to the local chemical equilibration of the system reached via secondary rescatterings including formation, decay and regeneration of many high mass resonance states [94, 96].

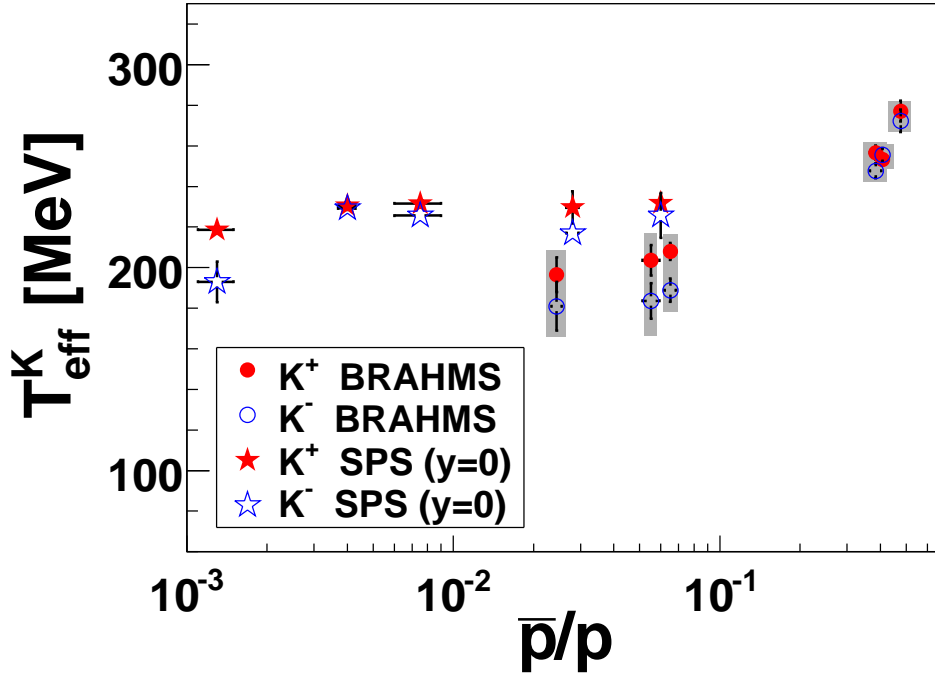


Figure 7.15: Inverse slopes (T_{eff}) for kaons as a function of the \bar{p}/p ratio. The BRAHMS points are from 0-10% central Au+Au collisions at $\sqrt{s_{NN}} = 62.4$ GeV (this analysis) at different rapidities while the SPS points are from mid-rapidity at different energies [195]. The error bars represent statistical errors and the shaded boxes represent systematic errors.

The effective temperature of the spectra for positive and negative kaons measured at forward rapidity in this work's dataset are ~ 20 MeV smaller than the ones measured at mid-rapidity in SPS experiments at the same \bar{p}/p ratio, albeit consistent within the error bars (see figure 7.15). The difference in inverse slopes might also be due to the radial flow velocity which is expected to depend on the local system size and multiplicity. The local system size is approximated by the pion rapidity density and is found to be ~ 100 at $y = 2.6$ (from interpolations, see figure 7.7) in this work while at $\sqrt{s_{NN}} = 17.3$ GeV at mid-rapidity and the same \bar{p}/p ratio is ~ 170 [82]. Also, in this work at $y = 3.0$, the pion rapidity density is ~ 70 (see figure 7.7) while at $\sqrt{s_{NN}} = 12$ GeV at mid-rapidity is ~ 140 [82].

In a chemical analysis, the \bar{p}/p ratio has an approximate correspondence with the baryo-chemical potential through the formula $\bar{p}/p = \exp(-2\mu_B/T)$ for a given freeze-out temperature T . Hence if T is the same in the two cases, this would imply that the local system formed at high rapidity at RHIC (62.4 GeV) is chemically equivalent with the system formed at the higher SPS energies at mid-rapidity, both being controlled by the baryo-chemical potential, which also fixes the strangeness potential at a given T . A

rapidity dependent baryo-chemical potential μ_B has been suggested in thermal models like [199]. Together with a strangeness chemical potential μ_S fixed by the requirement of net local strangeness density this reproduces the universal dependence of K^-/K^+ and K/π ratios on \bar{p}/p . However a fit of thermal statistical parameters to data do not give useful information on the underlying microscopic dynamics.

7.4 Centrality dependent particle production

In figure 7.16 we show the centrality dependence of the average transverse momentum for the identified particles at $y = 0$ (left) and forward rapidity (right). The number of participant nucleons (N_{part}) are estimated using a Glauber HIJING calculation as described in [200]. At mid-rapidity, in the N_{part} range probed by using Au+Au and Cu+Cu collisions, the $\langle p_T \rangle$ increases with increasing system size and centrality of the collision. This together with the particle mass ordering suggests the presence of effects

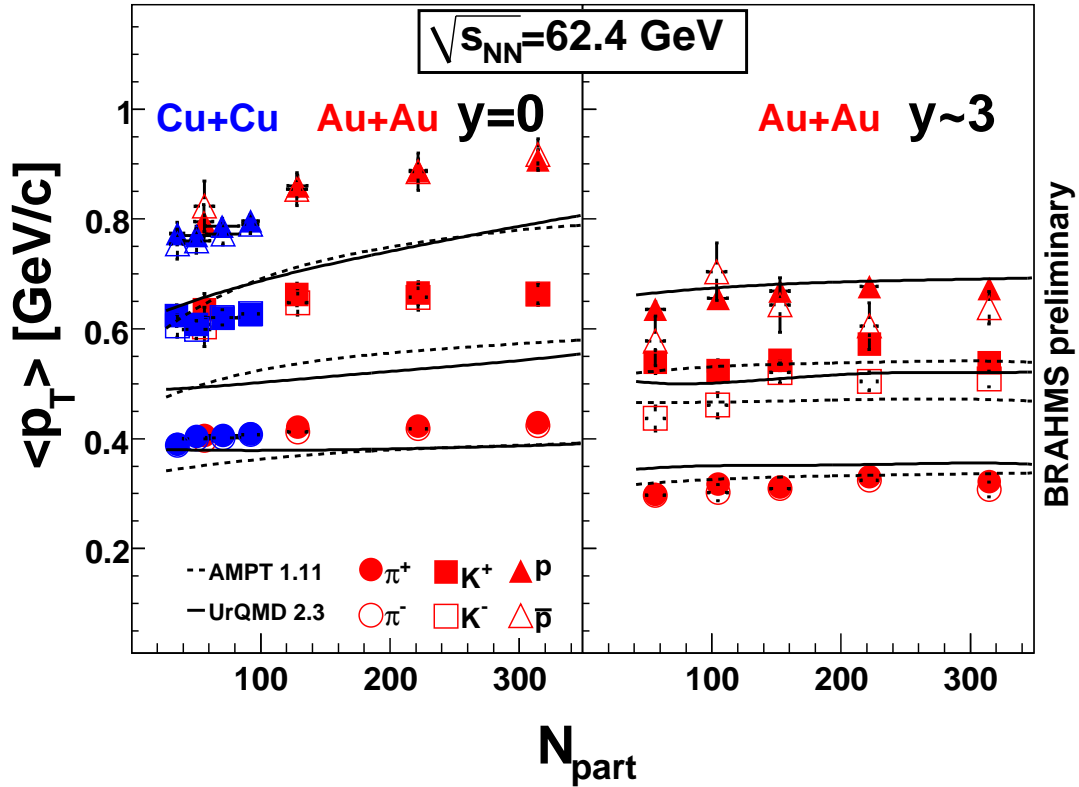


Figure 7.16: Average p_T for identified particles as a function of the number of participants. The data at mid-rapidity (left panel) is from Au+Au (red) and Cu+Cu (blue) collisions at $\sqrt{s_{NN}} = 62.4$ GeV and the data at forward rapidity (right panel) is from Au+Au collisions only. The curves are model calculations with AMPTv1.11 [142] (dashed line) and UrQMDv2.3 [95] (solid line). The curves respect the same mass hierarchy as in the data.

like transverse radial flow due to the pressure developed during the collision. There are however other effects which can contribute also to the observed values of the transverse momenta like jets, k_{\perp} broadening or rescatterings in the hadronic phase. At forward rapidity, $y \sim 3$, much smaller values of the $\langle p_T \rangle$ were measured especially for protons

and kaons but the same mass ordering as in mid-rapidity is kept. Also, there is no or little dependence of $\langle p_T \rangle$ on centrality in contrast to mid-rapidity. The curves in figure 7.16 represent the theoretical calculations with AMPT (dashed lines) and UrQMD (solid lines). The results of the calculations keep the same mass ordering as in the data both at mid-rapidity (left panel) and forward rapidity (right panel). At mid-rapidity, both models give the right system size dependence but underestimate the absolute values of the average transverse momentum. The calculations at forward rapidity shows a better agreement with the data with the exception of the proton average p_T calculated with AMPT, which underpredicts the results.

The change of chemical conditions with centrality can be studied with the help of anti-particle to particle ratios of the integrated dN/dy yields. The errors due to efficiencies are cancelled in these ratios while the systematic errors due to extrapolations at low p_T approximately cancel also. The mid-rapidity anti-particle to particle ratios are shown in the left panel of figure 7.17. The π^-/π^+ ratio is approximately 1 independent of centrality or colliding system. Within the statistical errors, the measured K^-/K^+ ratio stays constant with centrality. The \bar{p}/p ratio shows a significant decrease from p+p results towards central Au+Au which is consistent with larger baryon stopping in central nucleus-nucleus collisions. The theoretical calculations made with the UrQMD and AMPT models agree with the data for π^-/π^+ and K^-/K^+ ratios. The calculations for \bar{p}/p ratio seem to follow the trend of the data but the absolute values are not well understood.

In the right part of figure 7.17 we show the anti-particle to particle ratios measured at forward rapidity. The π^-/π^+ ratio measured at $y = 3.1$ is independent of centrality and keeps a value slightly above 1 in agreement with the theoretical models that indicate a small isospin effect at this rapidity. The K^-/K^+ ratio ($y = 2.7$) is also independent of centrality but at a value smaller than at mid-rapidity presumably due to the high net baryon content which favours the associated production of K^+ . Contrarily to the dependence shown at mid-rapidity, the \bar{p}/p ratio measured at $y = 3.0$ increases with centrality and is consistent with the larger stopping in central nucleus-nucleus collisions which shifts the initial protons towards mid-rapidity. The models seem to describe qualitatively well this trend.

In the left panel of figure 7.18 we show the K/π ratios measured at mid-rapidity in p+p, Cu+Cu and Au+Au collisions as a function of the number of participant nucleons. The error bars are statistical only. Both positive and negative measured ratios increase with increasing system size. It can also be observed that the K/π ratios measured in peripheral Au+Au reactions are smaller than the ones measured at the same number of participants but in central Cu+Cu collisions. This observation was also made at SPS energies and interpreted as being due to the different mean number of N+N collisions per projectile [91]. The theoretical calculations shown are made only for Au+Au collisions over the entire N_{part} interval covered by nucleus-nucleus data. Thermodynamic models explain the increase of the K/π ratios with the system size based on the transition from the canonical to grand-canonical ensemble [191, 192] (see also the discussion in section 7.2). There are also models which suggest that the medium formed after the collision is made of a thermally equilibrated core and a corona which is a superposition of N+N sub-collisions in which the strangeness production is suppressed [79]. The AMPT calculations made for Au+Au collisions seem to describe the trend of the data but overestimate the absolute values. UrQMD predicts flat centrality dependence at $y = 0$ inconsistent with the data. The absolute values of these ratios are also underestimated mainly due to disagreements in the estimation of

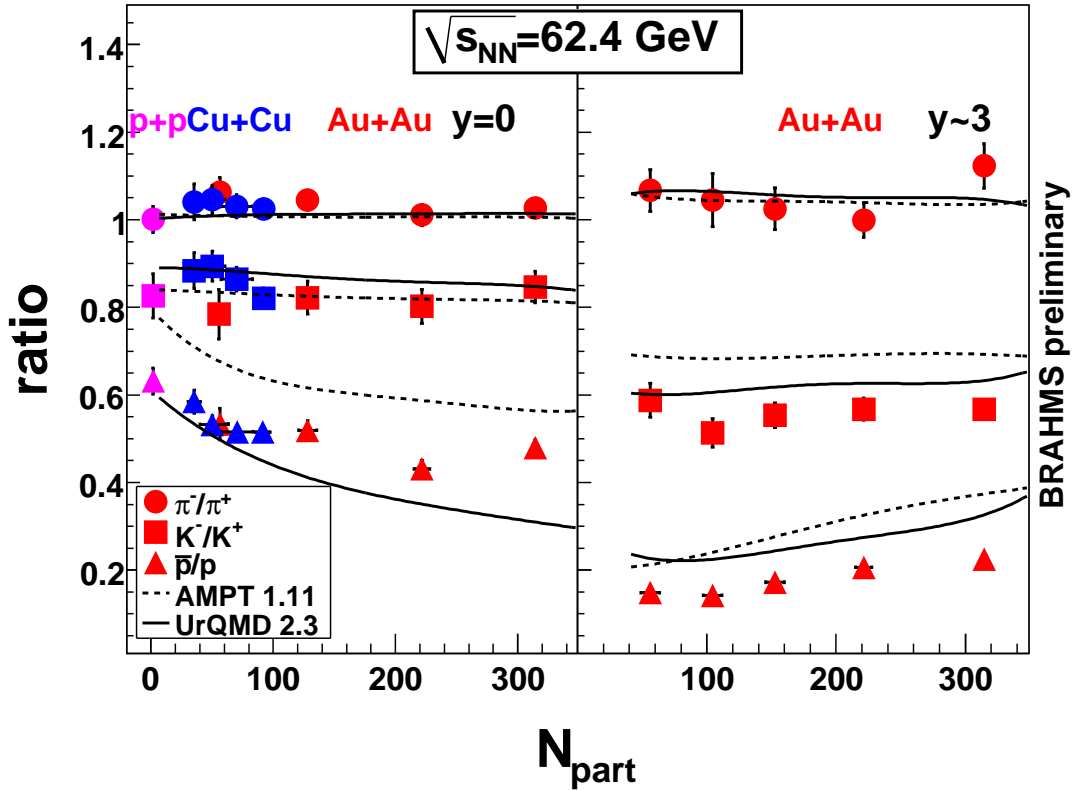


Figure 7.17: Anti-particle to particle ratios as a function of the number of participants at mid-rapidity (left panel) and forward rapidity (right panel). The data at mid-rapidity includes BRAHMS results from Au+Au (red), Cu+Cu (blue) and p+p (magenta) collisions at $\sqrt{s_{\text{NN}}} = 62.4$ GeV. At forward rapidity only Au+Au results are used. The π^-/π^+ ratio is from $y = 3.1$, K^-/K^+ ratio is from $y = 2.7$ and \bar{p}/p is from $y = 3.0$. The \bar{p}/p ratio at $y = 3.0$ was multiplied with a factor of 10 for convenience. The curves are model calculations using AMPT (dashed line) and UrQMD (solid line).

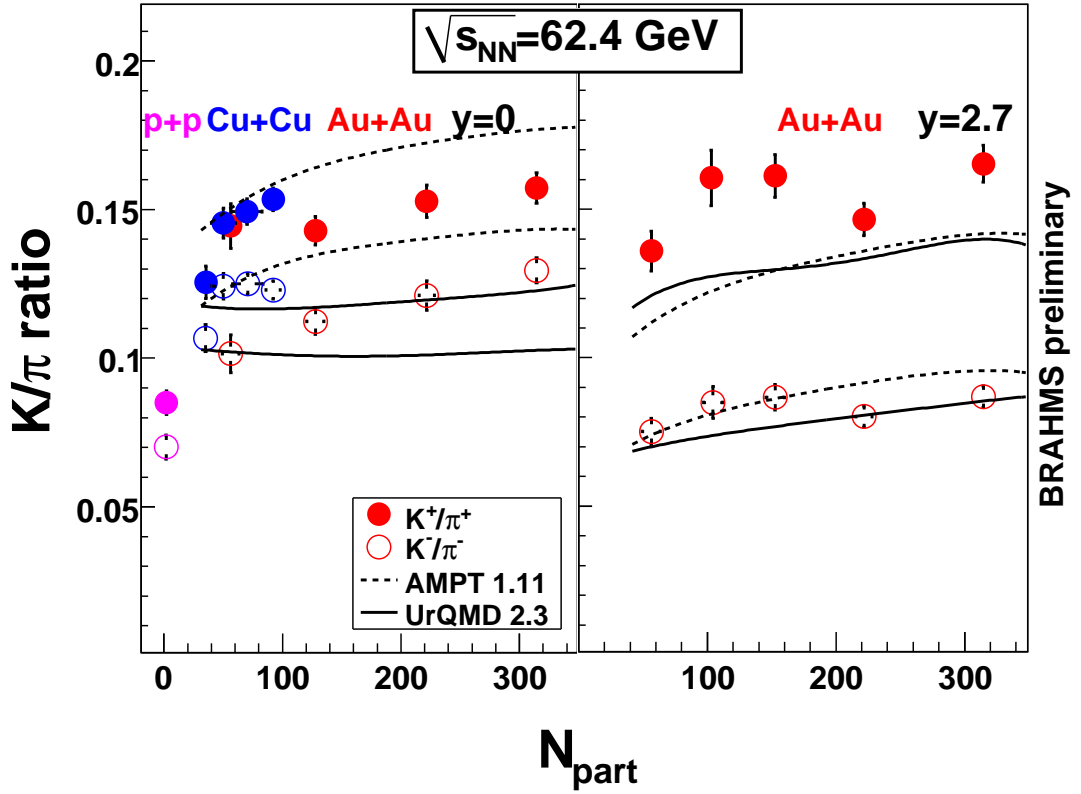


Figure 7.18: K/π ratios dependence on the number of participant nucleons at mid-rapidity (left panel) and forward rapidity (right panel). The data at mid-rapidity includes BRAHMS results from Au+Au (red), Cu+Cu (blue) and p+p (magenta) collisions at $\sqrt{s_{NN}} = 62.4$ GeV. At forward rapidity only Au+Au results are used. The curves are model calculations with AMPT (dashed line) and UrQMD (solid line). The upper curve is for the K^+/π^+ ratio and the lower curve is for the K^-/π^- ratio.

the pion yields (see figure 7.7). The forward rapidity K/π ratios measured in Au+Au collisions at $y \sim 3$ are shown in the right panel of figure 7.18. The K^+/π^+ and K^-/π^- ratios show the same dependence on centrality as at mid-rapidity but the negative ratio has much smaller values. The rapidity dependence of these ratios has a splitting behaviour towards forward rapidity which was also observed on a smaller scale in Au+Au collisions at $\sqrt{s_{NN}} = 200$ GeV [76]. The theoretical calculations with both models give a good agreement with the K^-/π^- results while the K^+/π^+ is slightly underestimated, illustrating again that the models fail to reproduce the magnitude of the difference between the positive and negative K/π ratios at forward rapidity.

Chapter 8

Summary and conclusions

In this thesis we tried to characterize a few aspects of the rich field of relativistic heavy ion collisions at intermediate and high energies.

In chapter 2 we used two different microscopic string models, UrQMD and QGSM, to study the formation and evolution of the locally equilibrated matter in the central zone of heavy ion collisions at energies spanning from $\sqrt{s_{NN}} \sim 4$ GeV up to 17.3 GeV. The calculations were performed both in the cubic central cell of fixed volume $V = 5 \times 5 \times 5 \text{ fm}^3$ and for the instantly expanding volume of homogeneous energy density. To decide whether or not equilibrium is reached we used a traditional approach based on the fulfillment of the conditions of kinetic, thermal and chemical equilibrium. Both models favor the formation of equilibrated matter for a period of about $10 \text{ fm}/c$ in which the matter expands isentropically with constant entropy per baryon. The square of the speed of sound c_s^2 has been found to vary in UrQMD from 0.13 at AGS to 0.15 at SPS energies and in QGSM from 0.11 at AGS to 0.15 at SPS. In both models the rise in c_s^2 slows down at $\sqrt{s_{NN}} \sim 9$ GeV.

Chapter 3 describes the HYDJET++ model as a superposition of the soft, hydro-type state and the hard state resulting from multi-parton fragmentation. Both states are treated independently. The hard part is an NN collision generator called PYQUEN which modifies the "standard" jet event obtained with the PYTHIA generator and includes radiative and collisional energy loss for partons. Initial state effects like shadowing are included also. The soft part is the thermal hadronic state generated on the chemical and thermal freeze-out hypersurfaces obtained from the parametrization of relativistic hydrodynamics. We found that this model gives a good description of soft observables at top RHIC energy, like the p_T spectrum, elliptic flow and HBT correlations. The hard part of the model describes well the high- p_T spectrum at top RHIC energy and also the nuclear modification factors calculated using PYTHIA as reference for p+p collisions.

In the experimental part of the thesis we measured the transverse momentum spectra and inclusive invariant yields of identified charged particles in Au+Au collisions at $\sqrt{s_{NN}} = 62.4$ GeV over a wide rapidity range which includes the nuclear fragmentation region. The yields at mid-rapidity have values close to the ones observed at RHIC at $\sqrt{s_{NN}} = 200$ GeV but the anti-particle to particle ratios for kaons and protons are smaller. At forward rapidity $y > 2.0$, the anti-particle/particle yields for kaons and protons have a steep decrease while being approximately centrality independent. The rapidity dependence of the K/π ratio depends on charge, which is understood in microscopical models (*i.e.* UrQMD) as resulting from the associated production mechanisms in a baryon rich medium, which enhances the fraction of s quarks ending up in hyper-

ons, thus depleting the K^- yield. Also, we observe in central nucleus-nucleus collisions a common dependence of the particle ratios (K/π , K^-/K^+) and kaon spectra inverse slopes on the baryo-chemical potential, whether measured for different energies at mid-rapidity at SPS, or at different rapidities at $\sqrt{s_{NN}} = 62.4$ GeV. The baryo-chemical potential interval covered at forward rapidity extends to high values but not quite high enough to probe the horn structure in the K^+/π^+ ratio excitation function. In the calculations made with UrQMD and AMPT models, K/π ratios are not well reproduced for large baryo-chemical potential found either at high rapidity or mid-rapidity at lower energies. Also, the universal dependence of the K^-/K^+ on the \bar{p}/p ratio is not well explained in the approach of microscopic transport models although calculations with UrQMD at different energies shows some hints of universal behaviour.

The average p_T has been shown to increase with system size at mid-rapidity for all studied particle species while being approximately centrality independent at rapidity $y \sim 3$. The $\langle p_T \rangle$ calculated for different species increases also with the particle rest mass. The π^-/π^+ and K^-/K^+ ratios are independent of the number of participants in the covered centrality range both at mid- and forward-rapidity. The \bar{p}/p ratio at mid-rapidity decreases with increasing system size while at $y \sim 3$ it increases which is consistent with higher baryon stopping in larger colliding systems. Finally, it has been shown that the K/π ratios are higher in more central collisions both at mid-rapidity and forward rapidity. The positive and negative K/π ratios have similar values at mid-rapidity and show an increasing difference as a function of rapidity at all centralities due to the high net-baryon content. Also, at the same number of participants, it has been observed that the central Cu+Cu collisions produce higher amounts of strangeness than peripheral Au+Au collisions.

HYDJET++ model was used to fit the charged particle distribution, invariant spectra and ratios at mid-rapidity in the most central bin. A good agreement with the data was found for a chemical freeze-out temperature of 165 MeV and a thermal decoupling temperature of 100 MeV. The chemical potentials μ_B and μ_S were found to be $\mu_B = 72.5$ MeV and $\mu_S = 17.5$ MeV in the approach of the thermal model. A strangeness suppression factor of $\gamma_S = 0.75$ was necessary to describe the K/π ratios at mid-rapidity in central collisions. This factor was found to decrease down to 0.6 in the most peripheral bin analyzed (40-60%). The experimental p_T coverage of the invariant spectra is not enough to constrain the jet contribution but from parameters extrapolated from the 200 GeV data it was found that this is less than 5% at 62.4 GeV.

Bibliography

- [1] ATLAS Webpage at KEK. <http://atlas.kek.jp/sub/photos/Physics/PhotoPhysicsSM.html>
- [2] Particle Data Group, <http://pdg.lbl.gov/>
- [3] S. Bethke, *Nucl.Phys.Proc.Suppl.* **121** (2003) 74
- [4] P. H. L. Christiansen, PhD thesis, Niels Bohr Institute, 2003
- [5] E. Shuryak, *Phys.Lett.* **B78** (1978) 150
- [6] R. Pisarski, *Phys.Lett.* **B110** (1982) 110
- [7] S. Damjanovic *et al.*, NA60 Collaboration, *Eur.Phys.J.* **C49** (2007) 235
- [8] F. Karsch, *Nucl.Phys.* **A698** (2002) 199
- [9] Z. Fodor, S. D. Katz, *JHEP* **0203** (2002) 014, arXiv: hep-lat/0106002
- [10] P. de Forcrand, O. Philipsen, *Nucl.Phys.* **B642** (2002) 290
- [11] R. Hagedorn, *Nuovo Cim.Suppl.* **3** (1965) 147
- [12] M. Stephanov, "Phase diagram of QCD", Plenary talk at the 20th International Conference on Ultra-Relativistic Nucleus-Nucleus Collisions, Jaipur, India, 4-10 February 2008
- [13] F. Becattini, "Strangeness production from SPS to LHC", Plenary talk at the 20th International Conference on Ultra-Relativistic Nucleus-Nucleus Collisions, Jaipur, India, 4-10 February 2008
- [14] Y. Aoki, G. Endrodi, Z. Fodor, S.D. Katz, K.K. Szabo, *Nature* **443** (2006) 675
- [15] P. B. Munzinger, J. Stachel, *J.Phys.* **G28** (2002) 1971
- [16] CERN-NA49 Collaboration, <http://na49info.web.cern.ch/na49info/>
CERN-NA61 Collaboration, <https://na61.web.cern.ch/na61/>
- [17] GSI Facility for Antiproton and Ion Research (FAIR), <http://www.gsi.de/fair/>
- [18] JINR Nuclotron-based Ion Collider fAcility (NICA), <http://nica.jinr.ru/>
- [19] C. Joergensen, PhD thesis, Niels Bohr Institute, 2004
- [20] I. Arsene *et al.*, BRAHMS Collaboration, *Phys.Rev.Lett.* **93** (2004) 242303
- [21] D. Kharzeev, E. Levin, L. McLerran, *Phys.Lett.* **B561** (2003) 93

- [22] K.J. Eskola, V.J. Kolhinen, C.A. Salgado, *Eur.Phys.J.* **C9** (1999) 61;
K.J. Eskola, V.J. Kolhinen, P.V. Ruuskanen, *Nucl.Phys.* **B535** (1998) 351
- [23] M. Hirai, S. Kumano, M.Miyama, *Phys.Rev.* **D64** (2001) 034003
- [24] L. Frankfurt, V. Guzey, M. Strikman, *Phys.Rev.* **D71** (2005) 054001
- [25] K. Tywoniuk, I.C. Arsene, L. Bravina, A.B. Kaidalov, E. Zabrodin, *Phys.Lett.* **B657** (2007) 170
- [26] I. G. Bearden *et al.*, BRAHMS Collaboration, *Phys.Rev.Lett.* **93** (2004) 102301
- [27] I. Arsene *et al.*, BRAHMS Collaboration, *Nucl.Phys.* **A757** (2005) 1
- [28] J.D. Bjorken, *Phys.Rev.* **D27** (1983) 140
- [29] I.G. Bearden *et al.*, BRAHMS Coll., *Phys.Rev.Lett.* **90** (2003) 10
- [30] C. Y. Wong, Introduction to high-energy heavy ion collisions. World Scientific (1994)
- [31] J. Kapusta, P. Lichard, D. Siebert, *Nucl.Phys.* **A544** (1992) 485
P.V. Ruuskanen, *Nucl.Phys.* **A544** (1992) 169
- [32] S. Turbide, C. Gale, E. Frodermann, U. Heinz, *Phys.Rev.* **C77** (2008) 024909
- [33] A. Adare *et al.* (PHENIX Collaboration), arXiv:0804.4168v1 [nucl-ex]
- [34] P.V. Ruuskanen, *Nucl.Phys.* **A522** (1991) 255
- [35] A. Adare *et al.* (PHENIX Collaboration), *Phys.Lett.* **B670** (2009) 313
- [36] S. Afanasiev *et al.* (PHENIX Collaboration), arXiv:0706.3034[nucl-ex], submitted to *Phys.Rev.Lett.*
- [37] I.C. Arsene, L. Bravina, A.B. Kaidalov, K.Tywoniuk, E. Zabrodin, *Phys.Lett.* **B660** (2008) 176
- [38] A. Adare *et al.* (PHENIX Collaboration), *Phys.Rev.Lett.* **101** (2008) 082301
- [39] T. Matsui, H. Satz, *Phys.Lett.* **B178** (1986) 416.
- [40] K. Tywoniuk, L. Bravina, A. Capella, E.G. Ferreira, A.B. Kaidalov, E. Zabrodin, *J.Phys.* **G35** (2008) 104156
- [41] A. Andronic, P. Braun-Munzinger, K. Redlich, J. Stachel, *Nucl.Phys.* **A789** (2007) 334
- [42] J.D. Bjorken, *Report No. Fermilab-Pub-82/59-THY*, 1982.
- [43] M. Gyulassy, M. Plümer, *Phys.Lett.* **B243** (1990) 432
- [44] X.N. Wang, M. Gyulassy, *Phys.Rev.Lett.* **68** (1992) 1480
- [45] I. Arsene *et al.* (BRAHMS Collaboration), *Phys.Rev.Lett.* **91** (2003) 072305
- [46] J. Adams *et al.* (STAR Collaboration), *Phys.Rev.Lett.* **91** (2003) 072304

- [47] J.W. Cronin *et al.*, *Phys.Rev.* **D11** (1975) 3105
- [48] I. Arsene *et al.* (BRAHMS Collaboration), *Phys.Rev.Lett.* **93** (2004) 242303
- [49] C. Adler *et al.*, STAR Collaboration, *Phys.Rev.Lett.* **90** (2003) 82302
- [50] A. Adare *et al.* (PHENIX Collaboration), *Phys.Rev.* **C78** (2008) 014901
- [51] P.M. Chesler, L.G. Yaffe, *Phys.Rev.* **D78** (2008) 045013
- [52] B. Betz, M. Gyulassy, D.H. Rischke, H. Stöcker, G. Torrieri, *J.Phys.* **G35** (2008) 104106
- [53] J. Adams *et al.*, (STAR Collaboration), *J.Phys.* **G32** (2006) L37
- [54] J. Bielcikova for the STAR Collaboration, "High- p_T results from STAR - what did we learned", Presented at the "High- p_T physics at LHC 2009" workshop, Prague, 4-7 february 2009.
- [55] A. Poskanzer, "History of flow analysis methods", LBL, <http://rnc.lbl.gov/Poskanzer/>
- [56] A. Adare *et al.* (PHENIX Collaboration), *Phys.Rev.Lett.* **98** (2007) 162301
- [57] P. Romatschke, U. Romatschke, *Phys.Rev.Lett.* **99** (2007) 172301
- [58] B. Alver *et al.* (PHOBOS Collaboration), arXiv:nucl-ex/0702036
- [59] J. Adams *et al.* (STAR Collaboration), *Phys.Rev.Lett.* **92** (2004) 062301
- [60] P. Kovtun, D.T. Son, A.O. Starinets, *Phys.Rev.Lett.* **94** (2005) 111601
- [61] J. Rafelski, B. Müller, *Phys.Rev.Lett.* **48** (1982) 1066
- [62] F. Antinori *et al.* (NA57 Collaboration), *J.Phys.* **G32** (2006) 427
- [63] A. Andronic, P. Braun-Munzinger, J. Stachel, *Nucl.Phys.* **A772** (2006) 167
- [64] C. Alt *et al.*, NA49 Coll., *Phys.Rev.* **C77** (2008) 024903
- [65] M. Gazdzicki, D. Röhrich, *Z.Phys.* **C71** (1996) 55
- [66] M. Gazdzicki, M.I. Gorenstein, *Acta Phys.Polon.* **B30** (1999) 2705
- [67] E. Laermann, O. Philipsen, *Ann.Rev.Nucl.Part.Sci.* **53** (2003) 163, arXiv:0303.042[hep-ph]
- [68] P. de Forcrand, S. Kim, O. Philipsen, *PoS LAT* (2007) 178, arXiv:0711.0262[hep-lat]
- [69] Z. Fodor, S.D. Katz, *JHEP* **0404** (2004) 50
- [70] S. Ejiri, C.R. Allton, S.J. Hands, O. Kaczmarek, F. Karsch, E. Laermann, C. Schmidt, *Prog. Theor. Phys. Suppl.* **153** (2004) 118.
- [71] V.D. Toneev, E.G. Nikonov, B. Friman, W.N. Nörenberg, K. Redlich, *Eur.Phys.J.* **C23** (2004) 399.

- [72] I.C. Arsene, L.V. Bravina, W. Cassing, Yu.B. Ivanov, A. Larionov, J. Randrup, V.N. Russkikh, V.D. Toneev, G. Zeeb, D. Zschesche, *Phys.Rev.* **C75** (2007) 034902
- [73] G. Torrieri, submitted to *J.Phys.* **G**, arXiv:0901.0221[nucl-th].
- [74] J.L. Klay *et al.* (E895 Collaboration), *Phys.Rev.* **C68** (2003) 054905.
- [75] R. Stock, *Phys.Rep.* **135** (1986) 259.
- [76] I. G. Bearden *et al.*, BRAHMS Collaboration, *Phys.Rev.Lett.* **94** (2005) 162301
- [77] R.D. Field, R.P. Feynman, *Phys.Rev.* **D15** (1977) 2590
- [78] T. Sjöstrand, *Comp.Phys.Comm.* **39** (1986) 347.
- [79] F. Becattini *et al.*, *Phys.Rev.* **C69** (2004) 024905.
P. Bozek, *Acta Phys.Polon.* **B36** (2005) 3071.
C. Hohne *et al.*, *Phys.Lett.* **B640** (2006) 96.
K. Werner *et al.*, *Phys.Rev.Lett.* **98** (2007) 152301.
- [80] L. Ahle *et al.*, E802 Coll., *Phys.Rev.* **C57** (1998) 466
- [81] L. Ahle *et al.*, E802 Collaboration, *Phys.Rev.* **C58** (1998) 3523
- [82] S.V. Afanasiev *et al.*, NA49 Coll., *Phys.Rev.* **C66** (2002) 054902
- [83] L. Ahle *et al.* (E866 Collaboration), *Nucl.Phys.* **A661** (1999) 472.
- [84] L.Ahle *et al.* (E866/E917 Collaboration), *Phys.Lett.* **B490** (2000) 53.
- [85] L.Ahle *et al.* (E866/E917 Collaboration), *Phys.Rev.* **C60** (1999) 044904.
- [86] D. Ouerdane, PhD thesis, Niels Bohr Institute, 2003
- [87] L. Ahle *et al.*, E802 Collaboration, *Phys.Rev.* **C59** (1999) 2173
- [88] C. Alt *et al.*, NA49 Coll., *Phys.Rev.* **C73** (2006) 044910
- [89] M. Gazdzicki *et al.* (NA49 Collaboration), *J.Phys.* **G30** (2004) S701
- [90] L. Ahle *et al.*, E866 and E917 Collaborations, *Phys.Lett.* **B476** (2000) 1.
- [91] C. Hohne *et al.*, NA49 Collaboration, *Nucl.Phys.* **A715** (2003) 474.
- [92] F. Sikler *et al.*, NA49 Collaboration, *Nucl.Phys.* **A661** (1999) 45c.
- [93] B. I. Abelev *et al.*, STAR Collaboration, arXiv:0808.2041[nucl-ex]
- [94] L. V. Bravina, I. Arsene, J. Bleibel, M. Bleicher, G. Bureau, A. Faessler, C. Fuchs, M. S. Nilsson, H. Stocker, K. Tywoniuk, E.E.Zabrodin, *Phys.Rev.* **C78** (2008) 014907
- [95] S.A. Bass, M. Belkacem, M. Bleicher, M. Brandstetter, L. Bravina, C. Ernst, L. Gerland, M. Hofmann, S. Hofmann, J. Konopka, G. Mao, L. Neise, S. Soff, C. Spieles, H. Weber, L.A. Winkelmann, H. Stöcker, W. Greiner, C. Hartnack, J. Aichelin, N. Amelin, *Prog.Part.Nucl.Phys.* **41** (1998) 225
M. Bleicher, E. Zabrodin, C. Spieles, S.A. Bass, C. Ernst, S. Soff, L. Bravina, M. Belkacem, H. Weber, H. Stöcker, W. Greiner, *J. Phys.* **G25** (1999) 1859.

- [96] H. Petersen, M. Bleicher, S. A. Bass, H. Stöcker, arXiv:0805.0567[hep-ph]
- [97] N.S. Amelin, L.V. Bravina, *Sov.J.Nucl.Phys.* **51** (1990) 133; *Yad.Fiz.* **51** (1990) 211;
N.S. Amelin, L.V. Bravina, L.P. Csernai, V.D. Toneev, K.K. Gudima, S.Yu. Sivoklov, *Phys.Rev.* **C47** (1993) 2299.
- [98] W. Henning, *Nucl.Phys.* **A734** (2004) 654.
- [99] J. Cleymans, K. Redlich, *Phys.Rev.* **C60** (1999) 054908.
- [100] Z.D. Lu, A. Faessler, C. Fuchs, E.E. Zabrodin, *Phys.Rev.* **C66** (2002) 044905; *J. Phys.* **G28** (2002) 2127.
- [101] L.V. Bravina, M.I. Gorenstein, M. Belkacem, S.A. Bass, M. Bleicher, M. Brandstetter, M. Hofmann, S. Soff, C. Spieles, H. Weber, H. Stöcker, W. Greiner, *Phys.Lett.* **B434** (1998) 379.
- [102] L.V. Bravina, E.E. Zabrodin, M.I. Gorenstein, S.A. Bass, M. Belkacem, M. Bleicher, M. Brandstetter, C. Ernst, M. Hofmann, L. Neise, S. Soff, H. Weber, H. Stöcker, W. Greiner, *Phys.Rev.* **C60** (1999) 024904.
- [103] L.V. Bravina, M. Brandstetter, M.I. Gorenstein, E.E. Zabrodin, M. Belkacem, M. Bleicher, S.A. Bass, C. Ernst, M. Hofmann, S. Soff, H. Stöcker, W. Greiner, *J.Phys.* **G25** (1999) 351;
L.V. Bravina, E.E. Zabrodin, M.I. Gorenstein, S.A. Bass, M. Belkacem, M. Bleicher, M. Brandstetter, C. Ernst, Amand Faessler, W. Greiner, S. Soff, H. Stöcker, H. Weber, *Nucl.Phys.* **A661** (1999) 600c.
- [104] L.V. Bravina, E.E. Zabrodin, S.A. Bass, M. Bleicher, M. Brandstetter, A. Faessler, C. Fuchs, W. Greiner, S. Soff, H. Stöcker, *Phys.Rev.* **C63** (2001) 064902;
L.V. Bravina, E.E. Zabrodin, S.A. Bass, A. Faessler, C. Fuchs, M.I. Gorenstein, W. Greiner, S. Soff, H. Stöcker, H. Weber, *Nucl.Phys.* **A698** (2002) 383c;
L.V. Bravina, E.E. Zabrodin, S.A. Bass, M. Bleicher, M. Brandstetter, A. Faessler, C. Fuchs, M.I. Gorenstein, W. Greiner, S. Soff, H. Stöcker, *J.Phys.* **G27** (2001) 421.
- [105] L.V. Bravina, I. Arsene, M.S. Nilsson, K. Tywoniuk, E.E. Zabrodin, *J.Phys.* **G32** (2006) S213;
L.V. Bravina, I. Arsene, M.S. Nilsson, K. Tywoniuk, E.E. Zabrodin, M. Bleicher, H. Stöcker, W. Greiner, *Int.J.Mod.Phys.* **E16** (2007) 777.
- [106] J. Bleibel, G. Burau, A. Faessler, C. Fuchs, *Nucl.Phys.* **A767** (2006) 218.
- [107] J. Bleibel, G. Burau, A. Faessler, C. Fuchs, *Phys. Rev.* **C76** (2007) 024912;
J. Bleibel, G. Burau, C. Fuchs, *Phys. Lett.* **B659** (2008) 520.
- [108] B. Andersson, G. Gustafson, B. Nilsson-Almqvist, *Nucl.Phys.* **B281** (1987) 289.
- [109] V. Gribov, *Sov.Phys.JETP* **26** (1968) 414, *Zh.Eksp.Theor.Fiz.* **53** (1967) 654;
L.V. Gribov, E.M. Levin, M.G. Ryskin, *Phys.Rep.* **100** (1983) 1.
- [110] C. Pajares, Yu.M. Shabelski, *Relativistic Nuclear Interactions* (Russia, Moscow, 2007);
A.B. Kaidalov, *Surveys in High Energy Phys.* **13** (1999) 265.

- [111] E. Fermi, *Prog.Theor.Phys.* **5** (1950) 570.
- [112] L.D. Landau, *Izv.Akad.Nauk SSSR, Ser.Fiz.* **17** (1953) 51 (in Russian); S.Z. Belenkij, L.D. Landau, *Nuovo Cimento Suppl.* **3** (1956) 15.
- [113] M. Berenguer, C. Hartnack, G. Peilert, H. Stöcker, W. Greiner, J. Aichelin, A. Rosenhauer, *J.Phys.* **G18** (1992) 65.
- [114] M. Belkacem, M. Brandstetter, S.A. Bass, M. Bleicher, L. Bravina, M.I. Gorenstein, J. Konopka, L. Neise, C. Spieles, S. Soff, H. Weber, H. Stöcker, W. Greiner, *Phys.Rev.* **C58** (1998) 1727.
- [115] L.V. Bravina, E.E. Zabrodin, S.A. Bass, M. Bleicher, M. Brandstetter, S. Soff, H. Stöcker, W. Greiner, *Phys.Rev.* **C62** (2000) 064906.
- [116] L.D. Landau, E.M. Lifshitz, *Statistical Physics* (Pergamon, Oxford, 1980).
- [117] E. Shuryak, *Sov.J.Nucl.Phys.* **16** (1973) 395; *Yad.Fiz.* **16** (1972) 707.
- [118] R. S. Bhalerao, J.-P. Blaizot, N. Borghini, J.-Y. Ollitrault, *Phys.Lett.* **B627** (2005) 49.
- [119] A. Adare *et al.* (PHENIX Collaboration), *Phys.Rev.Lett.* **98** (2007) 162301.
- [120] Y. Aoki, Z. Fodor, S. D. Katz, K. K. Szabo, *JHEP* **0601** (2006) 089.
- [121] M. Bleicher, J. Aichelin, *Phys.Lett.* **B530** (2002) 81.
- [122] L.V. Bravina, I.N. Mishustin, N.S. Amelin, J.P. Bondorf, L.P. Csernai, *Phys.Lett.* **B354** (1995) 196.
- [123] L.V. Bravina, I.N. Mishustin, J.P. Bondorf, A. Faessler, E.E. Zabrodin, *Phys.Rev.* **C60** (1999) 044905.
- [124] S. Ejiri, F. Karsch, E. Laermann, C. Schmidt, *Phys.Rev.* **D73** (2006) 054506.
- [125] G. Boyd, J. Engels, F. Karsch, E. Laermann, C. Legeland, M. Lutgemeier, B. Petersson, *Nucl.Phys.* **B469** (1996) 419
- [126] Z. Fodor, S.D. Katz, K.K. Szabo, *Phys.Lett.* **B568** (2003) 73
- [127] M. Gluck, E. Reya, M. Stratmann, W. Vogelsang, *Phys.Rev.* **D63** (2001) 094005
- [128] G. Torrieri, S. Steinke, W. Broniowski, W. Florkowski, J. Letessier, J. Rafelski, *Comput.Phys.Commun.* **167** (2005) 229
- [129] A. Kisiel, T. Taluc, W. Broniowski, W. Florkowski, *Comput.Phys.Commun.* **174** (2006) 669
- [130] T. Hirano, K. Tsuda, *Phys.Rev.* **C66** (2002) 054905
- [131] X.N. Wang, M. Gyulassy, *Phys.Rev.* **D44** (1991) 3501
- [132] R.J. Glauber, *Phys.Rev.* **130** (1963) 2529
- [133] L.D. McLerran, R. Venugopalan, *Phys.Rev.* **D49** (1994) 2233

- [134] L.D. McLerran, R. Venugopalan, *Phys.Rev.* **D59** (1999) 094002
- [135] B. Zhang, *Comput.Phys.Commun.* **109** (1998) 193
- [136] T. Csorgo, B. Lorstad, *Phys.Rev.* **C54** (1996) 1390
- [137] E. Schnedermann, J. Sollfrank, U. Heinz *Phys.Rev.* **C48** (1993) 2462
- [138] F. Cooper, G. Frye, *Phys.Rev.* **D10** (1974) 186
- [139] C. Anderlik, L.P. Csernai, F. Grassi, W. Greiner, Y. Hama, T. Kodama, Z.I. Lazar, V.K. Magas, H.Stoecker, *Phys.Rev.* **C59** (1999) 3309
- [140] B.A. Li, C.M. Ko, *Phys.Rev.* **C52** (1995) 2037
- [141] H. Sorge, H. Stocker, W. Greiner, *Nucl.Phys.* **A498** (1989) 567
- [142] B. Zhang, C.M. Ko, B.A. Li, Z.-wei Lin, *Phys.Rev.* **C61** (2000) 067901
- [143] K. Goulianos, *Phys.Rep.* **101** (1983) 169
- [144] A.H. Mueller, J. Qiu, *Nucl.Phys.* **B268** (1986) 427
- [145] T. Sjostrand, S. Mrenna, P. Skands, *JHEP* **0605** (2006) 026
- [146] N.S. Amelin, R. Lednicky, T.A. Pocheptsov, I.P. Lokhtin, L.V. Malinina, A.M. Snigirev, Iu.A. Karpenko, Yu.M. Sinyukov, *Phys.Rev.* **C74** (2006) 064901
- [147] N.S. Amelin, R. Lednicky, I.P. Lokhtin, L.V. Malinina, A.M. Snigirev, Iu.A. Karpenko, Yu.M. Sinyukov, I. Arsene, L. Bravina, *Phys.Rev.* **C77** (2008) 014903
- [148] I.P. Lokhtin, L.V. Malinina, S.V. Petrushanko, A.M. Snigirev, I. Arsene, K. Tywoniuk, *Comput.Phys.Commun.* **180** (2008) 779.
- [149] S.V. Akkelin, P. Braun-Munzinger, Yu.M. Sinyukov *Nucl.Phys.* **A710** (2002) 439
- [150] I.P. Lokhtin, A.M. Snigirev, *Eur.Phys.J.* **C45** (2006) 211
- [151] S.R. de Groot, W.A. van Leeuwen, Ch.G. van Weert, Relativistic kinetic theory. Principles and Applications, North-Holland Publishing Company, Amsterdam-New York-Oxford, 1980
- [152] Yu.M. Sinyukov, S.V. Akkelin, A.Yu. Tolstykh, *Nukleonika* **43** (1998) 369
- [153] J. Sollfrank, M. Gazdzicki, U.W. Heinz, J. Rafelski, *Z.Phys.* **C61** (1994) 659
- [154] Yu.M. Sinyukov, *Z.Phys.* **C43** (1989) 401
- [155] J. Adams *et al.*, STAR Collaboration, *Phys.Rev.Lett.* **92** (2004) 112301
- [156] P.F. Kolb, J. Sollfrank, U.W. Heinz, *Phys.Lett.* **B459** (1999) 667
- [157] U.A. Wiedemann, *Phys.Rev.* **C57** (1998) 266
- [158] W. Broniowski, A. Baran, W. Florkowski, *AIP Conf.Proc.* **660** (2003) 185

- [159] J. Adams *et al.*, STAR Collaboration, *Phys.Rev.* **C72** (2005) 014904
- [160] S.S. Adler *et al.*, PHENIX Collaboration, *Phys.Rev.Lett.* **91** (2003) 072301
- [161] J.D. Bjorken, *Fermilab publication Pub-82/29-THY* (1982)
- [162] E. Braaten, M. Thoma, *Phys.Rev.* **D44** (1991) 1298
- [163] I.P. Lokhtin, A.M. Snigirev, *Eur.Phys.J.* **C16** (2000) 527
- [164] R. Baier, Yu.L. Dokshitzer, A.H. Mueller, D. Schiff, *Phys.Rev.* **C60** (1999) 064902
- [165] R. Baier, Yu.L. Dokshitzer, A.H. Mueller, D. Schiff, *Phys.Rev.* **C64** (2001) 057902
- [166] I.P. Lokhtin, A.M. Snigirev, *Phys.Lett.* **B440** (1998) 163
- [167] B.B. Back *et al.*, PHOBOS Collaboration, *Phys.Rev.Lett.* **91** (2003) 052303
- [168] B.I. Abelev *et al.*, STAR Collaboration, *Phys.Rev.Lett.* **97** (2006) 152301
- [169] V.N. Gribov, *Sov.Phys.JETP* **29** (1969) 483
- [170] L. Frankfurt, V. Guzey, M. Strikman, *Phys.Rev.* **D71** (2005) 054001
- [171] K.J. Eskola, V.J. Kolhinen, C.A. Salgado, *Eur.Phys.J* **C9** (1999) 61
- [172] M. Hirai, S. Kumano, M. Miyama, *Phys.Rev.* **D64** (2001) 034003
- [173] A. Aktas *et al.*, H1 Collaboration, *Eur.Phys.J.* **C48** (2006) 715
- [174] <http://www.bnl.gov/rhic/>
- [175] <http://www.star.bnl.gov/>, K.H. Ackermann *et al.*, STAR Collaboration, *Nucl.Instr.Meth.* **A499** (2003) 624
- [176] <http://www.phenix.bnl.gov/>, K. Adcox *et al.*, PHENIX Collaboration, *Nucl.Instr.Meth.* **A499** (2003) 469
- [177] <http://www.phenix.bnl.gov/>, B.B. Back *et al.*, PHOBOS Collaboration, *Nucl.Instr.Meth.* **A499** (2003) 603
- [178] <http://www4.rcf.bnl.gov/brahms/WWW/>, M.Adamczyk *et al.*, BRAHMS Collaboration, *Nucl.Instr.Meth.* **A499** (2003) 437
- [179] R. Debbe, C.E. Jorgensen, J. Olness, Z. Yin, *Nucl.Instr.Meth.* **A570** (2007) 216
- [180] C. Ristea, PhD thesis, Niels Bohr Institute, 2007
- [181] J. I. Joerdre, PhD thesis, University of Bergen, 2005
- [182] R. Karabowicz, Master's thesis, Jagiellonian University
- [183] C. Nygaard, Master's thesis, Niels Bohr Institute, 2007
- [184] P. Staszal, BRAHMS analysis notes 27, 29, 34 and 38
- [185] T. M. Larsen, Master thesis, University of Oslo, 2002

- [186] B. H. Samset, PhD thesis, University of Oslo, 2006
- [187] B. B. Back *et al.*, PHOBOS Coll., *Phys.Rev.* **C77** (2007) 024910
- [188] B. I. Abelev *et al.*, STAR Collaboration, *Phys.Lett.* **B655** (2007) 104
- [189] P. Staszelski *et al.*, BRAHMS Collaboration, *Nucl.Phys.* **A774** (2006) 77
- [190] J. Cleymans *et al.*, *Phys.Rev.* **C73** (2006) 034905
- [191] J. Rafelski, M. Danos, *Phys.Lett.* **B97** (1980) 279
- [192] R. Hagedorn, K. Redlich, *Z.Phys.* **C27** (1985) 541
- [193] H. Dalsgaard *et al.*, BRAHMS Coll., *Int.J.Mod.Phys.* **E16** (2007) 7; I. Arsene *et al.*, BRAHMS Coll., submitted to PLB, arXiv:0901.0872
- [194] M. Gazdzicki *et al.*, NA49 Collaboration, Compilation of NA49 results.
- [195] M. Mitrovski *et al.*, NA49 Coll., *J.Phys.* **G32** (2006) S43
- [196] L. Ahle *et al.*, E866 Coll., *Phys.Rev.Lett.* **81** (1998) 2650
- [197] M.van Leeuwen *et al.*, NA49 Coll., *Nucl.Phys.* **A715** (2003) 161
- [198] I.G. Bearden *et al.*, NA44 Coll., *Phys.Rev.* **C66** (2002) 044907
- [199] F. Becattini, J.Cleymans, *J.Phys.* **G34** (2007) S959
- [200] I. Arsene *et al.*, BRAHMS Collaboration, *Phys.Rev.* **C72** (2005) 014908
Phys.Rev. **C71** (2005) 044906